

Sheffield Hallam University

A study of the microstructural and mechanical properties of novel spring steels.

HARRIS-POINTER, Cheryl Faye.

Available from the Sheffield Hallam University Research Archive (SHURA) at:

<http://shura.shu.ac.uk/19763/>

A Sheffield Hallam University thesis

This thesis is protected by copyright which belongs to the author.

The content must not be changed in any way or sold commercially in any format or medium without the formal permission of the author.

When referring to this work, full bibliographic details including the author, title, awarding institution and date of the thesis must be given.

Please visit <http://shura.shu.ac.uk/19763/> and <http://shura.shu.ac.uk/information.html> for further details about copyright and re-use permissions.

LEARNING
CITY CAMPUS, POND STREET,
SHEFFIELD, S1 1WB.

101 585 614 4



REFERENCE

ProQuest Number: 10697065

All rights reserved

INFORMATION TO ALL USERS

The quality of this reproduction is dependent upon the quality of the copy submitted.

In the unlikely event that the author did not send a complete manuscript and there are missing pages, these will be noted. Also, if material had to be removed, a note will indicate the deletion.



ProQuest 10697065

Published by ProQuest LLC (2017). Copyright of the Dissertation is held by the Author.

All rights reserved.

This work is protected against unauthorized copying under Title 17, United States Code
Microform Edition © ProQuest LLC.

ProQuest LLC.
789 East Eisenhower Parkway
P.O. Box 1346
Ann Arbor, MI 48106 – 1346

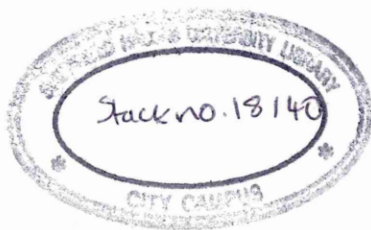
A study of the microstructural and mechanical properties of novel spring steels

Cheryl Faye Harris-Pointer

**A Thesis submitted in partial fulfilment of the requirements of
Sheffield Hallam University
for the degree of Doctor of Philosophy**

April 1998

**Collaborating organisation
Pandrol International, Worksop, U.K.**



Preface

This thesis is submitted in partial fulfilment of the requirements of Sheffield Hallam University for the degree of Doctor of Philosophy. It contains a detailed account of research carried out between May 1993 to June 1996 in the Materials Research Institute, Sheffield Hallam University under the supervision of Dr J. Cawley, Dr I Wadsworth, Mr B Marshall and Prof. B. Pickering. Except where acknowledgement and reference has been made, this work is, to the best of my knowledge original and has been carried out independently. No part of this thesis has been, or is currently being submitted for any degree or diploma at Sheffield Hallam, or any other university.

Acknowledgements

The author would like to sincerely thank the following people and collaborating establishments for their helpful discussions and advice during the period of study:-

- Dr J Cawley, and Prof. B Pickering, Materials Research Institute, Sheffield Hallam University.
- The Sponsor Company:- Pandrol International Ltd for funding this project.
- The staff at Pandrol International Ltd for their help and guidance, in particular Mr B Marshall, Mr R Larke, Mr P Hewlett, Mr I Presley and Mr A Williams.
- The staff of the materials research institute, in particular, Mr P. Slingsby, Mr T. Hudson. Ms C. Shaw, Dr I. Wadsworth, Dr B. Lewis and Mr S. Creasey.
- The staff of the School of Engineering at Sheffield Hallam University for their help in the preparation of test pieces.
- Mr S. Ryalls at Swindon Laboratories, Rotherham, for his help on cold rolling and plastic deformation of test pieces.
- Mr B Encliffe and Mr D Tame at Sheffield Testing Laboratories, Nursery St. Sheffield.

Finally, I would like to thank my husband, Richard, for his constant support and encouragement throughout this programme of research.

Abstract

This work is concerned with track spring components manufactured by Pandrol from a SiMn alloy in the quenched and tempered condition. For many years low to medium carbon based spring steel has been manufactured via an oil quench temper route producing components with suitable mechanical and microstructural properties. The current problem facing the spring manufacturer with the traditional heat treatment route involve a number of technical issues including a sensitivity to temper embrittlement and susceptibility to stress corrosion cracking. In addition, economic factors and component handling problems led Pandrol to seek solutions via the manufacturing process and materials selection.

A programme of research was therefore proposed to identify a possible replacement alloy system and production route which could exclude the costly tempering operation and instil a degree of production control.

The initial program of work involved the examination of several alloy systems based loosely around three separate microstructures, i.e. a fully pearlitic, bainitic and martensitic microstructure. In turn, each alloy was examined and assessed with respect to their suitability for the industrial application given their mechanical properties.

From the initial research, a selected number of promising alloy systems were examined further, namely a chromium molybdenum alloy, salt bath quenched to produce a bainitic microstructure, a water quenched low carbon chromium and low carbon boron martensitic type alloy. The low carbon boron alloy was considered the most promising, with similar mechanical properties in both the plain bar and clip form compared to the existing Pandrol alloy. However, concern was raised over the amount of plastic deformation (permanent set) suffered by a clip component whilst in service. In response to this, the use of cold work was examined to further strengthen the microstructure with notable success.

On identifying several possible alternative alloy systems to replace the existing oil quenched and tempered variant, the second stage of this research work concentrated on understanding the degree and type of microstructural strengthening involved on each particular alloy system. The effect of plastic deformation in each alloy type was also thoroughly investigated via transmission electron microscopy / true stress strain analysis and an attempt was made to relate microstructural changes to obtained mechanical properties. In addition the work hardening characteristics of the tempered microstructure were investigated, and compared to the straight through hardened variants.

Qualitative Transmission Electron Microscopy studies confirmed that dislocation density / mobility played a crucial role in determining the work hardening rate.

This project has studied the phenomena of work hardening in body centred cubic materials in the through hardened and untempered condition. A series of novel alloys have been developed with strengths equal to or above an oil quenched and tempered counterpart. However, these new alloys do not require a temper treatment thereby removing the risk of temper embrittlement. A clearer understanding of the work hardening characteristics has been developed through an assessment of the work hardening coefficient of these material variants.

Further Studies

As part of the course of study, I attended the following conferences and workshops combined with a number of informal research seminars presented at Sheffield Hallam University by academic staff from the Materials Research Institute and the School of Engineering.

- Bainite and Accicular Ferrite. Conference held at Institute of Materials, Carlton House Terrace, London, 14 December 1993.
- New Aspects of microstructures in modern low carbon high strength steels. Conference held at Tokyo University, Japan, (Japanese iron and Steel Institute) 29 Nov. to 1 December 1993.
- Quality steel - Advances in process technologies to meet customer requirements, SMEA conference, Sheffield University, 3-4 April 1995
- Post graduate course:- "Crystallography", presented by Dr. J. Cawley, Materials Research Institute, (eight week course)
- Post graduate course:- "High strength steels", presented by Dr. A Smith, School of Engineering, Sheffield Hallam University, (eight week course)
- Post graduate research course:- "Materials under load", presented by Dr. A Fletcher, School of Engineering, Sheffield Hallam University, (eight week course).
- Post graduate research course:- " Electron microscopy and diffraction techniques", presented by Prof. J. Tichmarsh, Materials Research Institute, Sheffield Hallam University.
- Post graduate research meeting:- Fatigue failure investigations, presented by Prof. J. Atkinson.
- Excel, Microsoft word course, Sheffield Hallam University.
- Training:- Philips XL40 Scanning Electron Microscope, Materials Research Institute, Sheffield Hallam University, (P. Slingsby)
- Training:- Philips CM20 Transmission Electron Microscope, Materials Research Institute, Sheffield Hallam University (Dr. J Cawley, Dr I. Wadsworth)

Contents

Preface.	i
Acknowledgements.	ii
Abstract.	iii
Additional Studies.	iv
Contents.	v
Chapter 1:- Introduction to spring steel, research aims and objectives.	1
1.1 Spring steel definitions and general property requirements.	1
1.2 Specific spring manufacturing : The Pandrol clip.	2
1.3 Spring steel manufacturing problems.	6
1.4 Research aims and Objectives.	6
1.5 Program of work.	7
1.5.1 Eutectoid microstructure.	8
1.5.2 Bainitic microstructure.	8
1.5.3 Martensitic microstructure.	9
1.5.4 Mixed martensite-bainite microstructure.	9
Chapter 2:-Eutectoid literature review.	11
2.1 Eutectoid microstructure.	11
2.1.1 Eutectoid transformation.	11
2.1.2 The effect of alloying additions on eutectoid transformation.	13
2.1.3 The effect of alloying elements on eutectoid transformation rate.	14
2.1.4 Effect of prior austenite grain size on eutectoid microstructure.	16
2.1.5 Strengthening mechanisms for eutectoid steels.	17
2.1.5.1 Grain size / pearlite colony size and morphology.	17
2.1.5.2 Microalloy additions.	18
2.1.6 Determination of optimum transformation temperature.	19
2.1.6.1 Determination of interlamellae spacing and distribution.	20
Chapter 3:-Bainite microstructure literature review.	23
3.1 The bainite transformation.	23
3.1.1 Bainite start temperature.	24
3.2 Bainite structure characterisation.	25
3.2.1 Upper bainite.	26
3.2.2 Lower bainite.	28
3.2.2.1 Precipitation within the lower bainite ferrite plate.	30

3.2.2.2 Precipitation between lower bainite ferrite platelets.	31
3.3 Transition temperature between upper and lower bainite.	31
3.4 Crystallography of bainite.	33
3.4.1 Bain region definition.	34
3.5 Crystallography of carbide precipitation in bainite.	35
3.5.1 Orientation relationship of cementite.	37
3.5.2 Orientation relationship of epsilon carbide.	38
3.5.3 Orientation relationship of eta carbide.	38
3.5.4 Orientation relationship of chi carbide.	39
3.6 Structure property relationships in the bainitic microstructure.	39
3.6.1 Hardness.	40
3.6.2 Proof strength.	40
3.6.3 Proof strength / ultimate tensile strength ratio.	43
3.6.4 Ductility.	43
3.6.5 Toughness.	45
3.7 Ideal chemistry and cooling procedure for bainite.	47
Chapter 4:-Martensitic microstructure literature review.	50
4.1 The martensitic transformation.	50
4.1.1 Lattice deformation or "Bain" strain.	51
4.1.2 Lattice invariant deformation.	52
4.1.3 Martensite start / finish temperature determination.	53
4.1.4 Auto tempered martensite formation.	56
4.1.5 Retained austenite formation.	56
4.2 Hardenability assessment.	58
4.2.1 Definition and test methods.	58
4.2.2 The ideal critical / critical diameter.	58
4.2.3 Assessment of ideal critical diameter.	59
4.2.4 Boron and hardenability.	62
4.3 Crystallography of martensite.	64
4.4 Crystallography of carbides in martensite.	64
4.5 Strengthening of martensite.	65
4.6 Optimising mechanical properties.	66
4.6.1 Strength and stress corrosion cracking.	66
4.6.2 Quench cracking.	67
4.7 Tempering of martensite.	68
4.7.1 Stages of tempering.	69
4.7.2 Temper embrittlement.	70

Chapter 5:-Dislocation theory, strengthening mechanisms and stress strain modelling.	72
5.1 Introduction: dislocations and strength.	72
5.1.1 The dislocation.	72
5.1.2 Burgers vector and burgers circuit.	73
5.2 Movement of dislocations via slip.	75
5.2.1 Slip planes and directions in a bcc and fcc lattice.	77
5.2.2 Perfect dislocation in the fcc lattice.	80
5.2.3 Shockley partial dislocation in the fcc lattice.	80
5.2.4 Dislocations in bcc lattice.	82
5.3 Movement of dislocations via twinning.	83
5.4 Nucleation of twins during deformation.	84
5.5 Strain (work) hardening.	85
5.5.1 Interstitial / substitution atom - dislocation interaction.	86
5.5.2 Precipitate - dislocation interactions.	88
5.5.3 Grain boundary - dislocation interactions.	91
5.5.4 Dislocation intersections and forests.	92
5.5.5 Dislocation reaction to form sessiles - bcc structures.	93
5.5.6 Dislocation multiplication.	94
5.5.6.1 Frank-Reed source.	94
5.5.6.2 Multiplication by multiple cross glide.	96
5.5.6.3 Grain boundary sources.	97
5.6 Strain hardening rate and exponent.	98
5.6.1 Determination of strain hardening rate from hardness.	100
5.7 The deformed microstructure.	101
5.7.1 Stored Energy in the deformed microstructure.	103
Chapter 6:-Experimental procedure.	104
6.1 Alloy selection procedure.	104
6.1.1 Precipitation strengthened eutectoid pearlite.	104
6.1.2 Air cooled bainitic microstructure.	105
6.1.3 Martensitic and martensite-bainite microstructure.	106
6.2 Thermal treatment.	106
6.2.1 Clip thermal treatment.	107
6.3 Mechanical treatments.	109
6.3.1 Strain hardening under the tensile test.	109
6.3.2 Strain hardening of the Pandrol clip.	110
6.3.2.1 Load deflection of the Pandrol clip.	110
6.3.2.2 Underpressing of the Pandrol clip.	111
6.3.3 Plain strain cold rolling of strip.	111

6.3.3.1 Determination of minimum reduction per pass.	112
6.4 Hardness measurements.	113
6.5 Tensile testing.	114
6.5.1 Tensile testing of formed clip.	114
6.5.2 Tensile testing of bar and strip material.	115
6.6 Toe load testing of formed clip.	116
6.7 Fatigue testing of formed clip.	117
6.8 Charpy "V" notch impact testing.	118
6.9 Optical microscopy.	118
6.10 Scanning electron microscopy.	118
6.10.1 EDS digital line scanning.	119
6.11 Transmission electron microscopy.	120
6.11.1 Sample preparation.	120
6.11.2 Calculation of correct magnification and TEM camera constant.	121
6.11.3 Determination of image / diffraction pattern rotation.	124
6.11.4 Determination of orientation relationship.	125
6.12 X-ray diffraction technique for the assessment of retained austenite.	126
6.12.1 Sample preparation.	126
6.12.2 XRD- calculation of retained austenite.	127
Chapter 7:- Optimisation of alloy system.	129
7.1 Introduction.	129
7.2 Eutectoid alloy system results.	129
7.2.1 Normalised (continuously air cooled) pearlite results.	129
7.2.2 Isothermally treated pearlite results.	131
7.3 Bainitic alloy system results.	133
7.3.1 0.4% carbon bainite results.	133
7.3.2 0.48% carbon, 1¼ Cr Mo bainite alloy results.	136
7.4 Martensitic alloy system results.	139
7.4.1 Chromium / nickel alloy system results.	139
7.4.2 Boron martensite alloy system results.	142
7.5 Preliminary discussion:- Which alloy?	144
7.5.1 Unsuitable alloy systems.	144
7.5.2 Promising alloy systems.	145
7.5.2.1 1.25% Cr Mo bainitic alloy system.	145
7.5.2.2 Cr Ni martensite alloy system.	147
7.5.2.3 Carbon boron martensite alloy system.	147

Chapter 8:-Clip results and additional mechanical results of boron alloy.	149
8.1 Tensile results of plain bar.	149
8.2 Tensile and impact properties of specimens from formed clip.	152
8.3 Toe load results from “virgin” clips.	154
8.3.1 Toe load results of work hardened clip.	155
8.4 Load deflection results of “virgin” clips.	156
8.4.1 Load deflection results of work hardened clips.	158
8.5 Microstructural results.	160
8.6 Fatigue results.	162
Chapter 9:-Microstructural evaluation of optimum alloy systems	164
9.1 Morphological studies of 1.25 Cr Mo alloy system.	164
9.1.1 Optical microscopy.	164
9.1.2 Segregation analysis results using scanning electron microscopy.	167
9.1.3 Transmission electron microscopy.	170
9.2 Morphological studies of 0.25% carbon / 0.5% chromium alloy system.	178
9.2.1 Optical microscopy.	178
9.2.2 Transmission electron microscopy.	180
9.3 Morphological studies of 0.3% carbon boron alloy system.	189
9.3.1 Optical microscopy.	189
9.3.2 Transmission electron microscopy.	191
9.4 Morphological studies of 0.3% carbon boron alloy system tempered at 250°C.	197
9.4.1 Optical microscopy.	197
9.4.2 Transmission electron microscopy.	200
9.5 Morphological studies of 0.3% carbon boron alloy system tempered at 400°C.	207
9.5.1 Optical microscopy.	207
9.5.2 Transmission electron microscopy.	209
9.6 Precipitate size distribution and identification,	216
9.6.1 Precipitate size distribution.	216
Chapter 10:-Mechanical evaluation of optimum alloy systems.	219
10.1 Mechanical evaluation of 1.25 mass% Chromium molybdenum alloy system.	219
10.1.1 Tensile and hardness test results..	219
10.1.1.1 Comparison of 0.2% proof strength and shape of flow curves.	221

10.1.2 Determination of work hardening during the tensile test..	222
10.1.2.1 Work hardening rate from the gradient of the flow curve.	222
10.1.2.2 Work hardening rate from power law relationships.	223
10.1.3 Determination of strengthening from cold rolling procedure.	226
10.2 Mechanical evaluation of 0.5 mass% Chromium 0.25 mass% carbon alloy system.	229
10.2.1 Tensile and hardness test results.	229
10.2.1.1 Comparison of 0.2% proof strength and shape of flow curves.	231
10.2.2 Determination of work hardening during the tensile test.	232
10.2.3 Determination of strengthening from cold rolling procedure.	233
10.3 Mechanical evaluation of 0.3 mass% carbon, boron alloy system.	236
10.3.1 Tensile and hardness test results.	236
10.3.1.1 Comparison of 0.2% proof strength and shape of flow curves.	238
10.3.2 Determination of work hardening during the tensile test.	239
10.3.3 Determination of strengthening from cold rolling procedure.	241
10.4 Mechanical evaluation of 0.3 mass% carbon, boron alloy tempered at 250°C.	243
10.4.1 Tensile and hardness test results.	243
10.4.1.1 Comparison of 0.2% proof strength and shape of flow curves.	243
10.4.2 Determination of work hardening during the tensile test.	245
10.4.3 Determination of strengthening from cold rolling procedure.	247
10.5 Mechanical evaluation of 0.3 mass% carbon, boron alloy tempered at 400°C.	249
10.5.1 Tensile and hardness test results.	249
10.5.1.1 Comparison of 0.2% proof strength and shape of flow curves.	251
10.5.2 Determination of work hardening during the tensile test.	251
10.5.3 Determination of strengthening from cold rolling procedure.	253
10.6 Summary of mechanical results from optimum alloy systems.	255
10.6.1 True stress strain results (proof and ultimate tensile strength).	255
10.6.2 Hardness results summary and comparison.	261
10.6.3 Deformation strengthening from the cold rolling procedure.	263
10.6.4 Work hardening results summary from the tensile test.	266

Chapter 11:- Discussion .

11.1 Basic microstructural strengtheners in optimum alloy system.	269
11.2 Microstructural observations, mechanical property relationships.	281
11.2.1 The 1.25 mass% chromium molybdenum alloy.	281
11.2.2 The 0.5 mass% chromium 0.25 mass% carbon alloy.	293
11.2.3 The 0.3 mass% carbon boron alloy system.	301
11.2.4 The 0.3 mass% carbon boron alloy (tempered at 250°C) system.	309
11.2.5 The 0.3 mass% carbon boron alloy (tempered at 400°C) system.	316
11.3 Discussion Summary	323

Chapter 12:- Conclusions. 324

Appendix. 326

References. 333

Chapter 1

Introduction to spring steel, research aims and objectives.

1.1 Spring steel definition and general property requirements

The ability of a material to absorb energy when deformed elastically and to return it when unloaded is called resilience (Dieter¹). Certain types of steel that perform such a task are commonly referred to as spring steel, to which this research work is based upon.

The basic mechanical properties required for spring steel include a high tensile strength, coupled with a high proof to ultimate tensile strength ratio to facilitate a high modulus of resilience (Dieter¹). A good fatigue strength is also essential, hence a certain amount of material toughness is also required. Additionally if the component is to be placed in an aggressive atmosphere, resistance to stress corrosion cracking is important. To meet this criteria, careful control of alloy chemistry and heat treatment regime is essential.

Traditionally medium carbon, silicon / manganese steels and more recently chromium containing steels have been employed to manufacture a wide range of springs from automotive leaf and coils to the railway track retaining clips which are pertinent to this work. These materials are used in the oil quenched and tempered condition ensuring adequate tensile, hardness and fatigue properties.

Historically the alloy chemistry was specified to promote adequate hardenability, but at low cost, hence the use of a basic silicon manganese grade. It has long been known that silicon improves the relaxation resistance of springs (Keysor², Kenneford and Ellis³). The beneficial effects of other alloying additions, such as manganese (for hardenability), chromium and molybdenum (for better ductility and surface finish) have also been reported since as early as 1946 (Keysor²) and 1950 (Kenneford and Ellis³).

The strengthening by precipitation of alloy carbides of chromium, molybdenum, vanadium etc. often referred to as secondary hardening is also well known (Kuo⁴, Honeycombe and Seal⁵, Pickering⁶).

In order to reduce production costs, today's spring manufacturer seeks to obtain the most competitively priced steel bar available. Often some of the steel stock will have been produced via the electric arc method where the charge consists of scrap metal. The Achilles heal in the use of a cheaper alloy source is from the continual rise in residuals (namely Cu, Sn Sb), thereby exasperating the temper embrittlement problem (Ritchie⁷, Low et. al.⁸).

One additional industrial practice used to impart some degree of strength into the spring was a process known as Scragging. This entailed incorporating a small amount of plastic deformation into the spring to raise the yield strength and proof to ultimate tensile strength ratio. Such a practice was believed to have been carried out at many spring manufacturers, although was not required at Pandrol, since the proof strength obtained was quite sufficient.

1.2 Specific spring manufacturing:- The Pandrol Clip.

The Pandrol clip was developed as a load bearing spring for the rail track industry. The design of this clip has varied somewhat over the years (figure 1 and 2), however the types of alloy together with the heat treatment process remained more or less the same. Figure 3 shows an "e" type clip within the rail configuration. Rail clips are driven into a shoulder support (attached to the sleeper) with insulating rubber pads placed underneath the clip toe for added shock absorption. Typical demands placed on the clip material include high strength enabling achievement of high load bearing capacities and low permanent set values when placed into the sleeper assembly. Hence the clip must be able to withstand a high degree of loading before the onset of substantial plastic deformation, which is partly achieved by careful alloy selection.

A medium carbon, silicon manganese grade is currently used in the manufacture of the Pandrol spring clip, specified to a 251A58 grade (see table 1).

Table 1:- Alloy chemistry used at Pandrol in the manufacture of railtrack clips

C	Si	Mn	P/S	Cr	Mo	Ni/Cu	Sn
0.52-0.57	1.7-2.1	0.8-1.0	0.035 max	0.2-0.3	0.02-0.06	0.3 max	0.035 max

Figure 1:- The “e” type and “PR” type clip

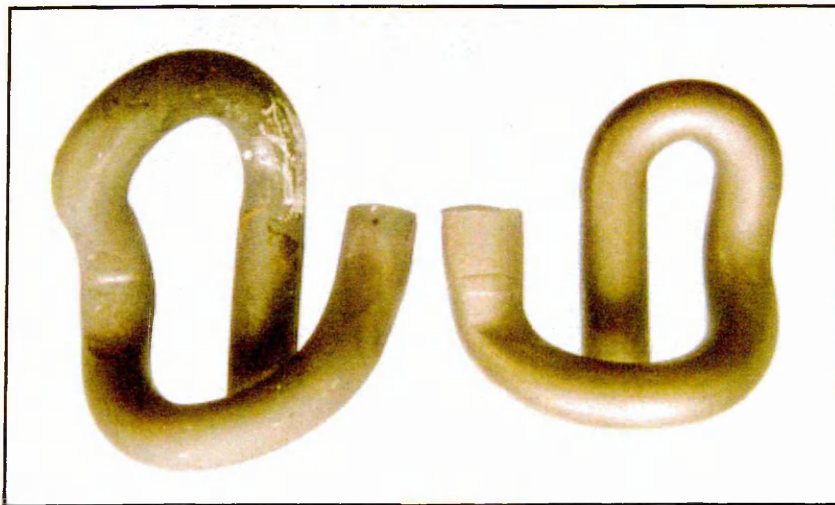


Figure 2:- The most recently developed fast clip

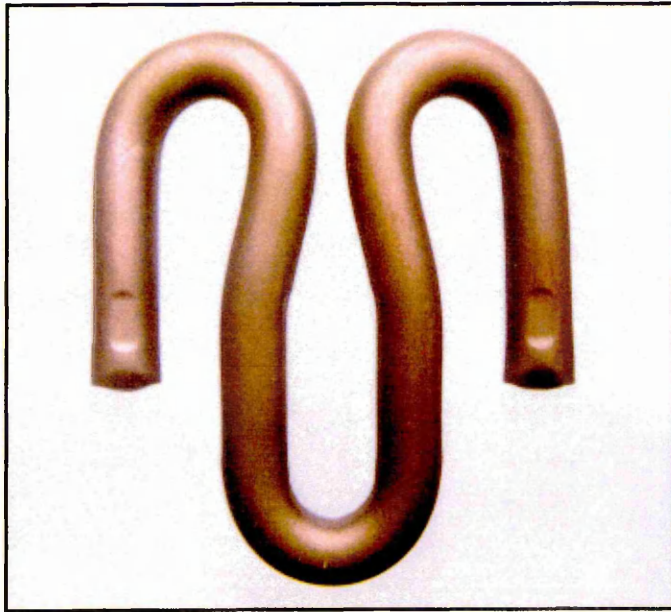
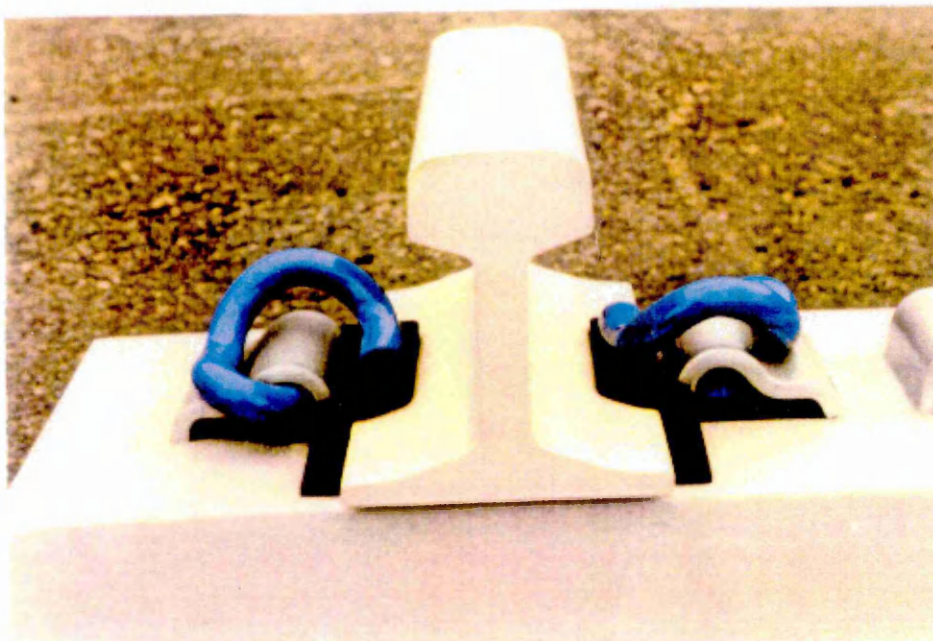


Figure 3:- The “e” type clip in shoulder and sleeper assembly

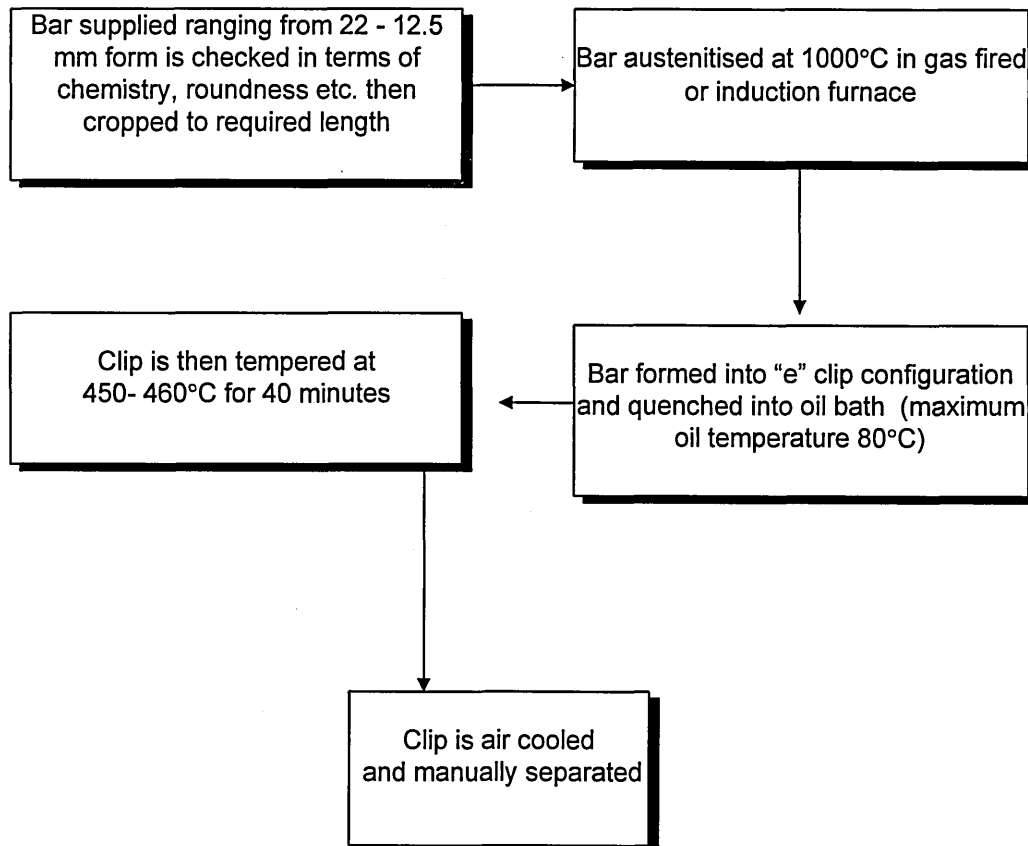


To produce a component with ideal mechanical properties utilising one of the given alloy systems, careful production control is essential. Figure 4 shows a typical production cycle for the Pandrol “e” type clip. The clip is austenitised to a critical temperature range where grain growth / hot working resistance is optimised. After an oil quench and temper treatment the microstructure consists of tempered martensite with ideal mechanical properties as noted in table 2.

Table 2: Summary of current material properties used at Pandrol

0.2% Proof strength (MPa)	Ultimate tensile strength (MPa)	Elongation %	Reduction in area %	Charpy Impact (J)
1250	1500	10-15	30-40	10-12

Figure 4:- The production route for Pandrol ‘e’ clip



1.3 Spring steel manufacture problems

During the past few years there has been a significant rise in clip manufacture from chromium containing steel. A major problem arises from the fact that such steels can contain large amounts of deleterious elements i.e. Sb, P, As, Sn from excessive recycling. This inexorable rise in residual alloy content draws the alloy system into the temper embrittlement regime. Additionally the silicon manganese grades are difficult to manufacture with respect to cleanness with the inevitable loss of toughness and fatigue life.

One further consideration is that the actual heat treatment procedure to produce the spring clip is expensive and not particularly environmentally friendly with the necessity for an oil quench. It has also become apparent that the temper operation means "loss of control" of the clip which has made the possibility of robotics control unrealisable. Alternatively a simple water quench or air cool route has the possibility of allowing full robotics control and hence a significant step forward in manufacturing production methods.

1.4 Research aims and objectives

The aims and objectives of the research work can be summarised as follows

- To develop microstructures which are resistant to temper embrittlement.
- To establish novel cooling techniques to avoid the necessity for tempering.
- To develop processes which can be implemented as industrial practice.
- To avoid the environmental consequences of oil quenching.
- To reduce overall processing costs and use of energy.

The primary objective of this work was therefore to investigate the possibility of utilising novel alloy chemistry and cooling regimes to produce alternative structures that enhance the base properties and eliminate or reduce the need for tempering, thus solving the intangible problem of temper embrittlement.

The alloy systems investigated were based on a quenched lower carbon martensitic microstructure, a medium carbon chromium molybdenum bainitic microstructure, and a precipitation strengthened eutectoid pearlitic microstructure. Additionally the role of work hardening was considered as a means of increasing the overall strength of the material. This process has been used in the spring industry for some time (scragging) even though it is generally accepted that body centred cubic metals do not appreciably work harden.

In order to fully utilise the application of cold work to increase alloy strength, first it was necessary to gain an understanding of the microstructural changes that took place during cold work as well as the influence of additional strengthening mechanisms such as precipitates and grain boundaries. Changes in microstructure can then be related to deformation amounts, chemistry and thermal treatments, which in turn are intimately related to mechanical properties. Fundamental alloy aims and objectives are summarised as follows.

- To assess the influence of cold work on a range of microstructures.
- To assess the influence of additional strengthening mechanisms.
- To identify and relate microstructure to mechanical properties.
- Describe the stress strain behaviour in terms of documented models.
- Understand the correlation between industrial requirements and laboratory results.

1.5 Program of work

The program of work involved the examination of three separate microstructures, and to assess their suitability for the industrial application given their mechanical properties in both the as received and clip form. Promising alloy systems were then strengthened further by the application of small amounts of cold work using a rolling mill and therefore assuming plain strain conditions.

Mechanical property evaluation included hardness and stress strain measurement, with comparisons of the plastic stress strain behaviour between tested alloy systems and existing models detailed in the literature. Microstructure was identified utilising optical and electron microscopy. A summary of the program of work is given in figure 5. A detailed program of research on each microstructure is given in the following sub-sections.

1.5.1 Eutectoid microstructure

The eutectoid alloy system chemistry was carefully controlled to generate strengthening from fine grain size and precipitates. The cooling regime was also controlled to facilitate the formation of fine pearlite lamella structure. The microstructure together with mechanical properties were examined to assess their suitability for the industrial application.

1.5.2 Bainitic microstructure

From an extensive literature review of continuous cooling transformation diagrams it was possible to determine the chemistry required to produce a bainitic microstructure over a relatively wide range of air cooling regimes.

Upper, lower or a mixed bainitic microstructure was formed depending on the cooling rates employed, with microstructure identified by optical and electron microscopy. The mechanical strength of the lower bainite structure was found to come close to industrial requirements, with additional strengthening observed after cold work. Hence a detailed investigation was carried out to assess the effect of cold work on a lower bainite microstructure and to relate this to obtained mechanical properties.

To ensure that a lower bainite microstructure was obtained for advanced mechanical and microstructural study, an isothermal salt bath treatment was adopted instead of the rather unpredictable accelerated air cool.

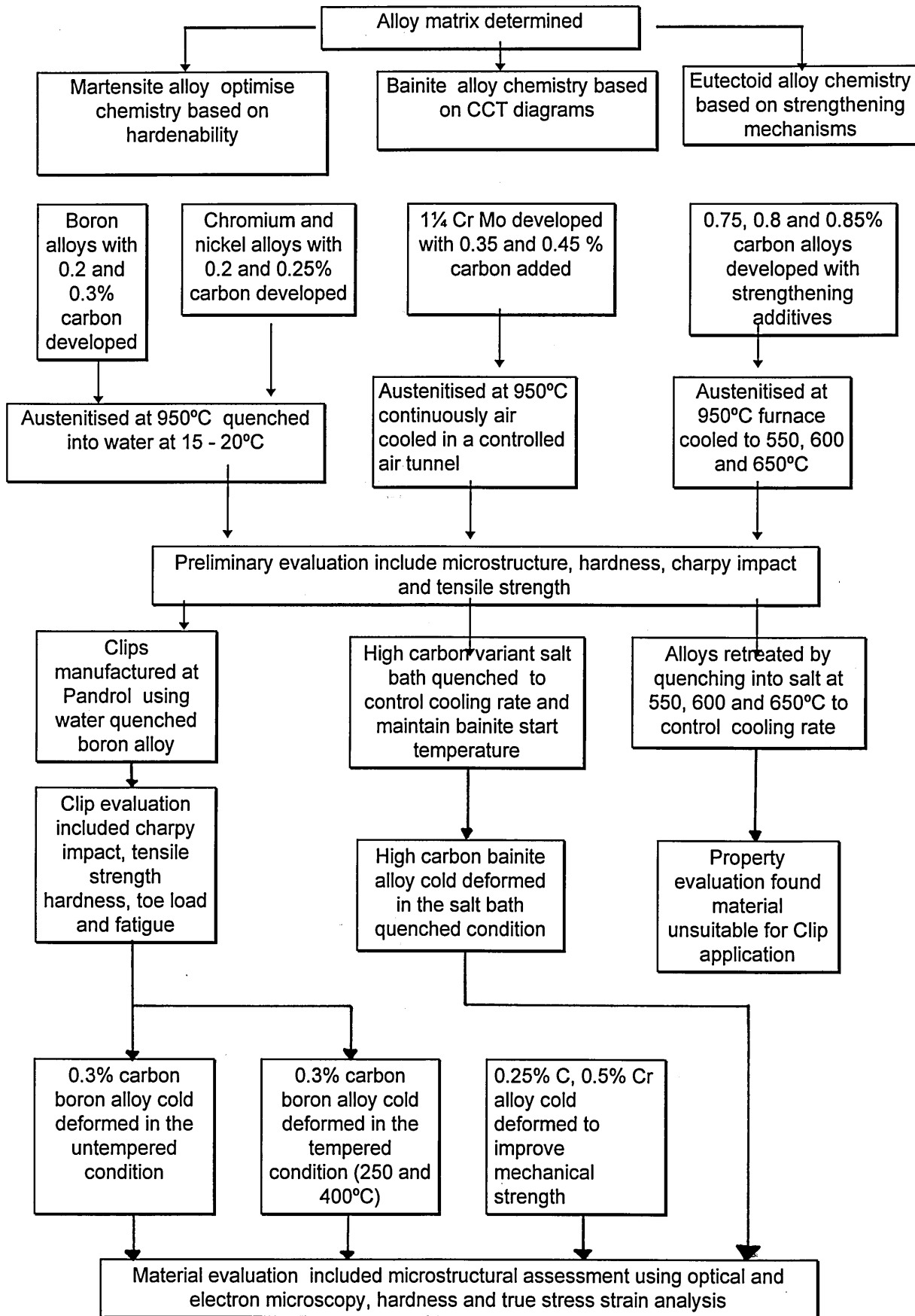
1.5.3 Martensitic microstructure

After a simple water quench from austenitisation at 950°C, and small amounts of cold work the boron alloy systems possess a martensitic microstructure with mechanical properties superior to the oil quenched and tempered microstructure. The program of work therefore included the assessment of work hardening as a means of further strengthening the martensite structure, especially since there appears to be little reference to this in the literature for b.c.c structures. Since the carbon content of this alloy system was quite low hence martensite start temperature (M_s) quite high, it was expected that auto tempered carbides would form. The effect of carbides on the overall strength and work hardening characteristics was then investigated further by creating a series of tempered alloy systems. The mechanical properties and microstructure of auto tempered, and “manually” tempered alloys in the work hardened and unworked condition were assessed. Additionally, because the water quenched boron martensite alloy properties were comparable to industrial requirements, a series of Pandrol “e” clips were made using the production route of straight water quench. The cold work (scragging) operation was also included as a means of increasing the strength of the product further, the amount of work required was determined from a series of clip tensile results.

1.5.4 Mixed martensite - bainite microstructure

The chemistry of the 0.5Cr / 0.75% Ni alloy systems were carefully designed to facilitate the formation of martensite on water quenching. However, due to segregation problems, this alloy system was found to contain significant amounts of lower bainite with martensite even after a relatively severe water quench. This microstructure provided an interesting median of the “pure” boron alloy martensite and 1¼Cr Mo bainite series and the mechanical properties and microstructure of the mixed bainite-martensite microstructure in the unworked and work hardened condition were assessed.

Figure 5:- Program of research



Chapter 2

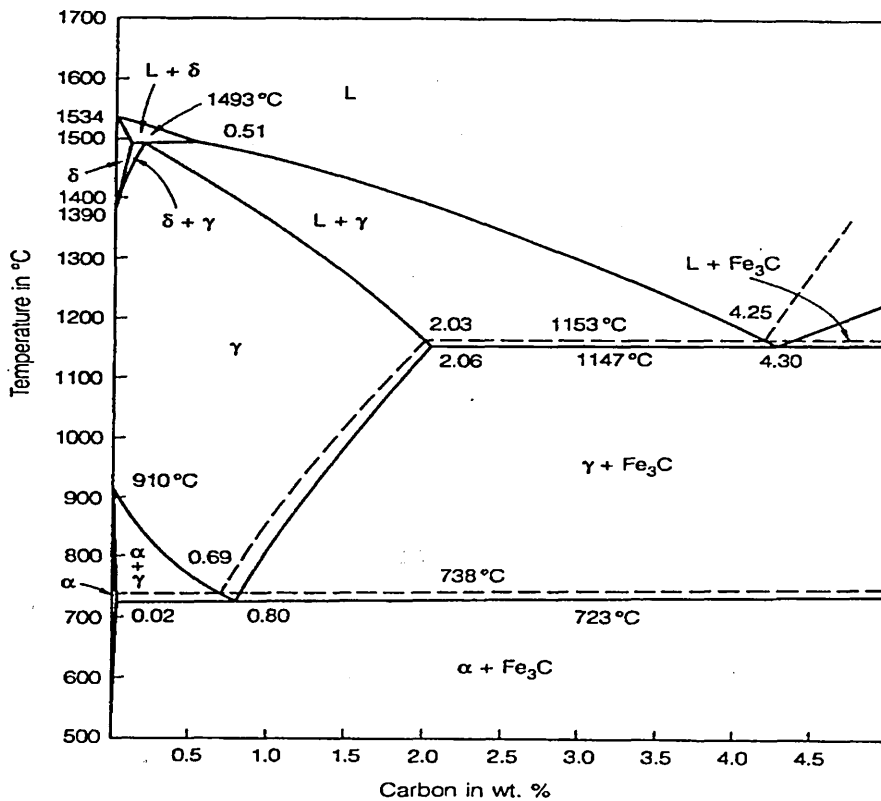
Eutectoid microstructure: Literature Review

2.1 Eutectoid Microstructure

2.1.1 Eutectoid transformation

Figure 6 shows the iron carbon equilibrium diagram, at high temperatures, for example 900°C and at low carbon concentrations, the microstructure consists of a single phase, known as austenite (γ). This phase is a solid solution of carbon in a face centred cubic iron lattice, and on moderate cooling the austenite decomposes into ferrite and cementite phases, ferrite being the body centred cubic allotropic form of iron which has very restricted solubility for carbon. The resultant ambient temperature microstructure is dependant on the carbon content of the steel and quench rate (Honeycombe⁹).

Figure 6:- The iron carbon equilibrium diagram



Consider a hypoeutectoid steel (i.e. steels with less than the eutectoid composition of 0.8 mass % carbon), cooling from 950°C under equilibrium conditions, (i.e. slow cool). Ferrite will begin to form when the temperature falls below the A_3 temperature and because of the very low carbon content of the ferrite, the austenite solid solution is enriched in carbon. As the temperature approaches the A_1 eutectoid temperature (723°C in Fe-C alloys), the remaining enriched austenite will then decompose to give ferrite and cementite aggregate known as pearlite. (the eutectoid reaction). Thus the hypo-eutectoid steel would comprise of a two phase microstructure, pro-eutectoid ferrite and lamellae ferrite and cementite (eutectoid pearlite). The relative proportions of each phase depends upon the carbon content of the alloy system, and is determined by applying the lever rule on the iron carbon phase diagram. In contrast, a steel having a hyper-eutectoid composition (carbon content above the eutectoid composition) would start to transform during cooling when the temperature falls below the A_{cm} line. Decomposition of austenite would start by the nucleation and growth of cementite, usually in the form of a fine cementite network around austenite grain boundaries. As cementite is formed, gradual depletion of carbon in the remaining austenite ensues, hence as the eutectoid temperature is approached, the composition of the carbon depleted austenite also approaches the eutectoid composition. Finally at the eutectoid temperature, the eutectoid reaction occurs where the remaining austenite will decompose into the lamellae eutectoid pearlite structure comprising of ferrite and cementite. The final microstructure thus consists of a network of pro-eutectoid cementite along the prior austenite grain boundaries with a pearlite inset (Krauss¹⁰). A steel having the eutectoid composition would contain neither pro-eutectoid ferrite or pro-eutectoid cementite under equilibrium conditions, but would show a fully pearlitic microstructure. On cooling from the austenite phase field, the austenite solid solution would remain unchanged, until at the eutectoid temperature, the entire austenitic microstructure would decompose to give a lamellae eutectoid of ferrite and cementite i.e. pearlite (Krauss¹⁰, Gladman¹¹).

2.1.2 The effect of alloying additions on eutectoid transformation

Additions of alloying elements influence both the eutectoid reaction temperature and the eutectoid composition with respect to carbon (Rayson¹²). Elements such as manganese and nickel lower the eutectoid temperature and also decrease the carbon content of the eutectoid composition. In contrast, a molybdenum content greater than 4 wt.% increases the eutectoid temperature and the carbon content of the eutectoid composition (Bain and Paxton¹³), In slowly cooled hypoeutectoid steels the proportions of ferrite and pearlite will therefore be changed by the presence of alloying elements such as manganese or chromium, both which would increase the proportion of pearlite (Gladman¹¹).

The effects of alloys on these changes have been summarised by Bain and Paxton¹³ and are illustrated in figures 7a and 7b.

Figure 7a:- The effect of alloying elements on the eutectoid temperature
(Bain and Paxton¹³ 1961)

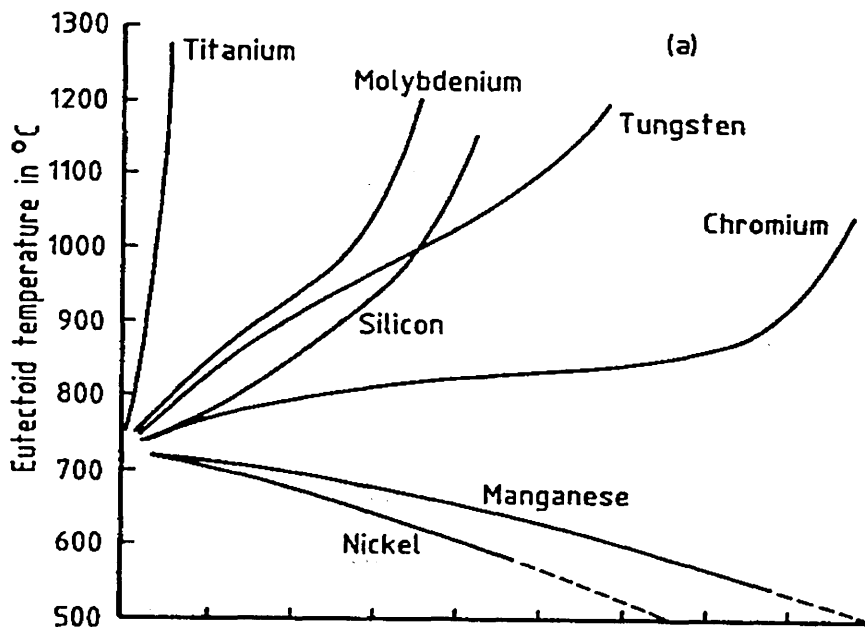
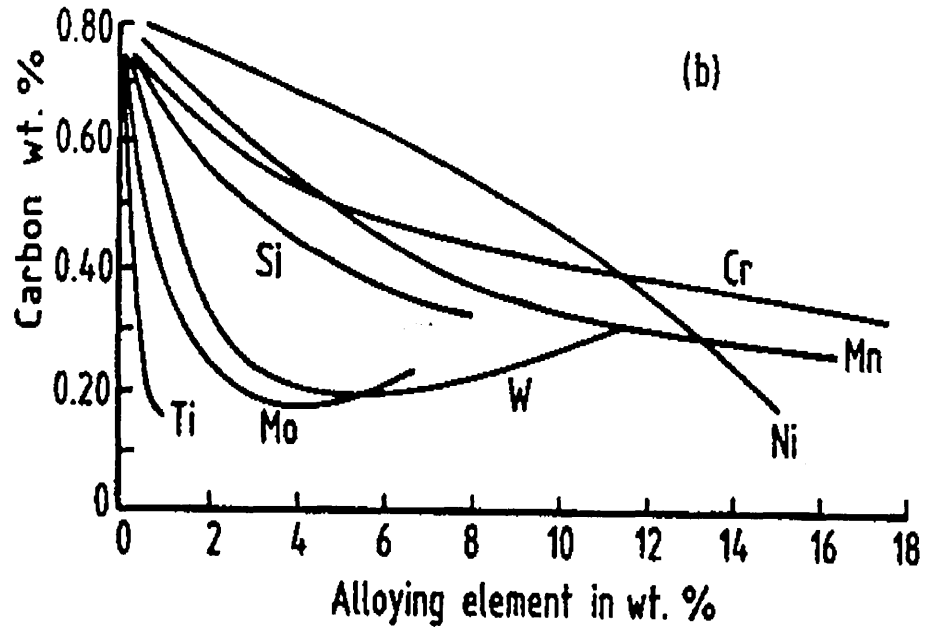


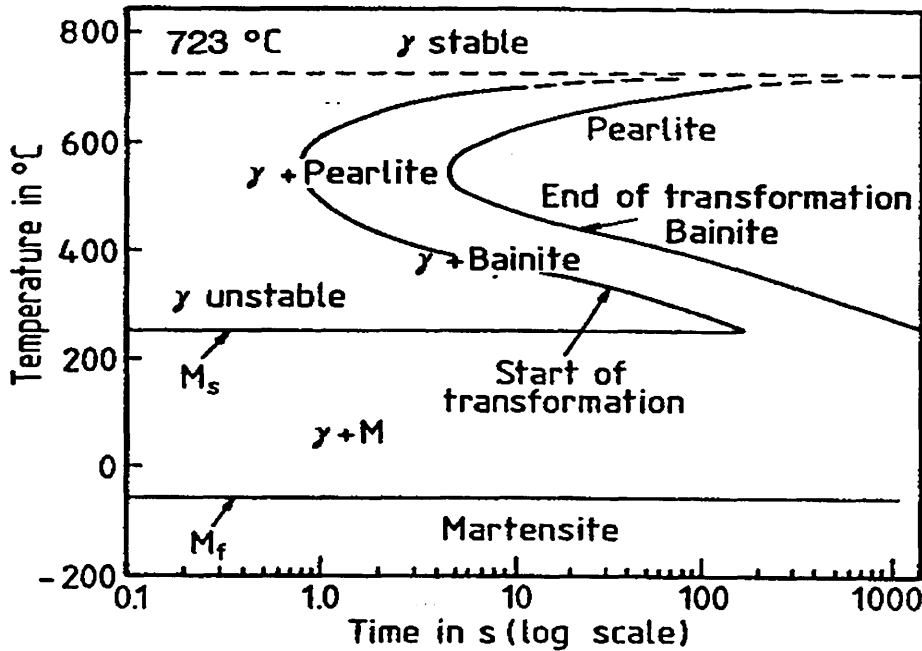
Figure 7b:- The effect of alloying elements on the eutectoid composition
(Bain and Paxton¹³ 1961)



2.1.3 Effect of alloying elements on eutectoid transformation rate

Nearly all common alloying elements, for example chromium, manganese and nickel retard the isothermal transformation temperature i.e. transformation requires longer times (Gladman¹¹). In terms of microstructure, the addition of small amounts of alloying elements produce a similar effect as increasing the cooling rate. Figure 8 shows the isothermal transformation diagram for a eutectoid steel. The addition of alloying elements pushes this curve (figure 8) to the right, in addition to any effect they may have on the eutectoid transformation temperature.

Figure 8:- Isothermal transformation diagram for a eutectoid steel
(after Gladman¹¹).



When optimum alloy concentrations are achieved the transformation will be sufficiently suppressed hence continuous cooling transformation will begin with high nucleation rate but low growth rate. The end result is a eutectoid microstructure with fine pearlite grains (colonies). The pearlite lamellae themselves will be also reduced in thickness as a result of the lower transformation temperature (Garbarz¹⁴, Marder and Bramfitt¹⁵).

Mehl¹⁶ proposed the following type of relationship between the interlamellae spacing (s) and the transformation temperature:-

$$s = K \exp \left(\frac{Q}{\alpha R T} \right) \quad (2.1)$$

Where K and α are constants, Q is the activation energy and T is the temperature in Kelvin.

Alloy additions however, must be kept to an optimum level since increasing the alloy content beyond this may cause the formation of alloy carbides, for example Cr_7C_3 or Cr_{23}C_6 for high chromium additions. Also high alloy additions may retard the austenite transformation to an extent where bainite or martensite forms. For example the effect of excess manganese additions was studied by Samuel and Hussein¹⁷ who reported that a 12% Mn addition to a steel with 0.8% carbon transformed at 350°C, with a bainitic microstructure.

Hence, the effects on the eutectoid microstructure of relatively small additions of manganese, nickel or chromium would be to reduce the pearlite colony size and interlamellae spacing of the pearlite. However such changes would only be observed under conditions of continuous cooling. Under isothermal transformation conditions, the use of alloy additions may in fact cause coarser interlamellae spacing to be formed at given transformation temperature (Pelissier et al.,¹⁸ McIvor¹⁹).

2.1.4 Effect of prior austenite grain size on eutectoid microstructure

The effect of the austenite grain size in the transformation characteristics and kinetics of eutectoid steels are well established. A coarser austenite grain size retards the isothermal transformation and depresses the transformation temperature during continuous cooling (pushes the nose of the time temperature transformation diagram to the right) (Gladman¹¹, Nadkarni et. al.²⁰). The overall effect is to decrease the interlamellae spacing of the pearlite, however the effect on pearlite colony size is not as straight forward. At very slow cooling rates, a coarse austenite grain size may give a coarse pearlite colony size. At faster cooling rates however, the depression of the transformation temperature is increasingly influential, hence finer pearlite colonies are obtained (Krauss¹⁰, Ridley²¹).

At even faster cooling rates, near to the critical cooling rate at which martensite can form as opposed to pearlite, coarse grained austenite will encourage the formation of low temperature transformation product, i.e. bainite and martensite (Krauss¹⁰). Grain refining additives such as aluminium, titanium and vanadium which form nitrides and inhibit grain growth, produce opposite effects because of the grain refinement which they introduce, hence it is expected that from this fine austenitic grain size fine pearlite colony size are obtained (DeMeo and Subramanian²², Garbarz¹⁴). However, it is important to carefully control the amount of grain refinement additive, since excess of that needed for refinement precipitation will incur hardenability problems (Gladman¹¹).

2.1.5 Strengthening mechanisms for eutectoid steels

To strengthen the eutectoid microstructure essentially means to provide obstacles to the movement of dislocations. Examples of strengthening mechanisms pertinent to the pearlitic microstructure may include grain / pearlite colony boundaries, interlamellae spacing and precipitates (Pickering²³).

2.1.5.1 Grain size / pearlite colony size and morphology

A detailed study by Gladman et al.²⁴ of the relationships between the microstructure and properties of medium to high carbon steels was carried out and included an assessment of the separate effects of the ferrite grain size, the pearlite fraction, the pearlite colony size, the interlamellae spacing and the cementite lamellae thickness, in addition to solid solution strengthening effects and precipitation hardening. This work concluded that low carbon steels containing a high degree of pro-eutectoid ferrite benefit from strengthening mechanisms such as solid solution strengthening and a fine ferrite grain size.

However as the carbon content was increased up to the eutectoid composition the strength of the alloy becomes markedly dependant on the pearlite content and its morphological characteristics.

Early work on the effects of interlamellae spacing (Gensamer et al.²⁵), on the yield strength of pearlite showed a negative linear relationship between strength and the logarithm of the interlamellae spacing, but other workers have since suggested an inverse relationship between strength and the interlamellae spacing or the square root of that spacing (Pickering²³). There is no evidence that the pearlite colony size influences the strength of pearlite directly (Gladman¹¹), however there is literature to suggest that the pearlite colony size effects toughness (Krauss²⁶, Hyak and Bernstein²⁷). It was found that the pearlite colony size in eutectoid steels has a very similar effect on the impact transition temperature to that of the ferrite grain size in low carbon steels (Gladman¹¹, Pickering²³). This is as expected since a growing crack is probably deflected / impeded by a pearlite colony or ferrite grain boundary in exactly the same manner.

To date it appears that the general view is that the strength of steel consisting of a near or fully pearlitic microstructure is dominated by the interlamellae spacing, whereby maximum strength is obtained with fine interlamellae spacing (Gladman¹¹, Pickering²³).

In contrast, the strength of a hypo-eutectoid steel would depend upon a wider range of parameters such as the ferrite grain size and amount of solid solution strengthening (Pickering²³, Honeycombe⁵, Pickering and Gladman²⁸). The amount and morphology of the pearlite component would also require consideration especially in steels approaching the eutectoid composition (Pickering²³).

2.1.5.2 Microalloy additions

One further strengthening mechanism pertinent to hypo-eutectoid steel and eutectoid steel is the addition of certain elements which combine with carbon or nitrogen to form small particles (Pickering²³, Ashby²⁹).

This technique is commonly known as micro alloying, and can improve the strength of the alloy quite dramatically (Garbarz¹⁴).

Nitride forming elements such as aluminium, vanadium and titanium can be used in medium to high carbon steels (Gladman¹¹). Carbide forming micro alloying elements such as niobium and vanadium are also used, however niobium is restricted to low carbon steels because of its limited solubility in austenite (Gladman¹¹, Pickering²³). The micro alloying additions have other functions in these steels, for example grain size control using titanium produces very fine titanium nitride particles which are capable of inhibiting austenite grain growth at temperatures up to about 1300°C (George and Irani,³⁰ Pickering³¹). Grain growth is important in that it affects not only the ferrite grain size but also the pearlite colony size and hence the toughness of the alloy (Gladman¹¹).

2.1.6 Determination of optimum transformation temperature

To obtain optimum mechanical properties from a precipitation strengthened eutectoid steel, (for example a vanadium bearing eutectoid) it is important that the transformation from austenite to pearlite is carried out at a temperature which facilitates fine interlamellae spacing together with a dispersion of fine precipitates to pin dislocations (DeMeo and Subramanian²²). If the austenite pearlite reaction was allowed to take place at high temperatures where nucleation is limited but growth is rapid, then the resultant microstructure would consist of coarse vanadium carbides / inter-lamellae spacing.

However if the pearlite reaction took place at a low temperature (utilising a faster cooling rate), although the interlamellae spacing would be much reduced hence favourable, a loss in overall strength would be observed since at lower temperatures no vanadium carbide precipitation would take place. In this instance the strengthening mechanism would therefore be from the morphology of the pearlite colony (Gladman¹¹).

It can be concluded that to obtain optimum mechanical properties from a precipitation strengthened pearlitic steel, it is necessary to apply a cooling rate which allows transformation to take place at the optimum temperature. The resultant microstructure would consist of a large dispersion of fine vanadium carbides together with a pearlitic matrix whose inter-lamellae spacing would be relatively fine.

2.1.6.1 Determination of interlamellae spacing and distributions

The determination of interlamellae spacing is important in evaluating metallurgical changes, controlling overall product quality, and for prediction of product properties (Brogran and McIvor³², Marder and Bramfitt¹⁵, Kavishe and Baker³³).

The most versatile and most widely used technique is probably that involving the examination of shadowed carbon replicas taken from fully or partially transformed specimens, in which measurements are made on electron micrographs or on the fluorescent screen of the microscope (Ridley et al.³⁴) The distance measured is usually of the average minimum observed spacing (λ_0), taken from several pearlite colonies, or the mean intercept spacing (\bar{l}). The former parameter is a perpendicular distance across two consecutive lamellae i.e. ferrite and cementite, while the mean intercept spacing is an average distance across two successive lamellae taken from random test lines. The true spacing does not have a constant value, but its distribution of spacing about a mean true value (λ_0), with the difference between minimum and mean true spacing dependant on system type and transformation temperature (Ridley³⁴).

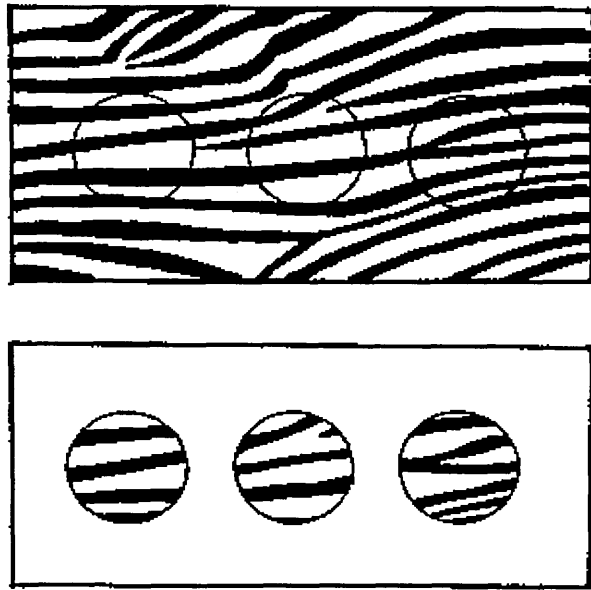
Methods available for determining the minimum, true random and apparent spacing are reviewed by Reti et.al³⁵, who suggests that the best method for determining the mean true spacing is to first calculate the mean random spacing.

This is because on calculating true interlamellae spacing value, variations in the spacing within the pearlite colony and the sectioning plane effect must be accounted for. Fowler³⁶ has reviewed Reti / Vander Voorts technique and found that problems encountered when determining the random spacing i.e. difficulty in determining fine lamellae and tedious lamellae counting are elevated with automatic image analysis. This technique involves examining metallographic specimens using a scanning electron microscope and photomicrographs are made of pearlite colonies at a magnification of 10,000X. which are then scanned into the digital memory of an integrated image analysis system.

To separate the lamellae into discrete countable fields, a mask image is electronically superimposed over the image of the photomicrograph. This mask is composed of a circular test pattern of fifteen windows through which several random orientations of the lamellae are observable for counting. The diameter of the circular window multiplied by the number of windows is the total true line test length. Standard image analysis functions automatically count the numbers of lamellae appearing in the windows. The count data is used to calculate the mean random spacing and from this the mean true interlamellae spacing is derived (illustrated in figure 9).

The distribution of true interlamellae spacing has also been studied by several authors (Roosz et. al.³⁷, Roosz and Gacsi³⁸, Vander Voort and Roosz³⁹) using stereological methods based on electron metallographic procedures. By generalising and extending this method a computational procedure is also available providing an additional way to approach the solution (Reti⁴⁰).

Figure 9:- System for calculating the lamellae thickness / spacing (Fowler³⁶)



Chapter 3

Bainitic Microstructure literature review

3.1 The bainite transformation

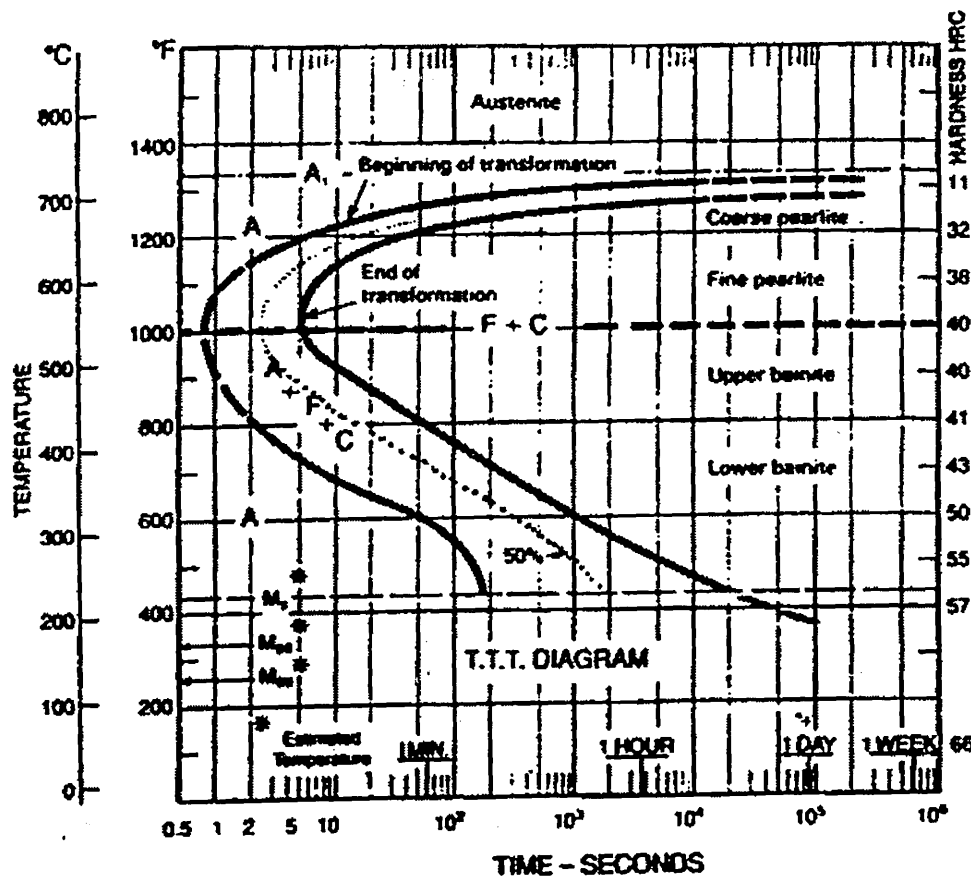
The bainite microstructure is formed on cooling from austenite between the temperature ranges at which pearlite and martensite form. Bainite consists of B.C.C laths and cementite, however the transformation mechanism produces a microstructure significantly different with respect to pearlite. (Krauss¹⁰)

Pearlite formation is controlled by diffusion mechanisms, where carbon diffusion and transfer of iron atoms across the austenite-pearlite interface define the colony of pearlite. Bainite however forms at lower temperatures, where even short range iron atom transfer is suppressed. As a result bainitic ferrite is nucleated by a co-operative iron atom shear mechanism (Christian and Edmonds⁴¹), with the resultant microstructure consisting of lath or plate like ferrite as opposed to the lamellar morphology of pearlite and pro-eutectoid ferrite. The smaller carbon atom however is still able to diffuse somewhat, therefore various temperature dependent cementite particles are formed alongside the bainitic lath. In contrast to pearlite, the cementite particles are not continuous, leading to a metallographic definition of bainite as a structure consisting of a non lamellar array of ferrite and cementite (Aaronson⁴²). The aggregates of bainitic platelets are often referred to as sheaves (Aaronson and Wells⁴) and the individual platelets are sometimes called sub-units. A cluster of platelets which form a sheaf is also sometimes called a packet of bainite because under light microscopy, fully transformed grains of austenite appear to be divided into discrete regions (i.e. "packets").

3.1.1 Bainite start temperature

Figure 10 shows a TTT diagram for a steel with 0.79 mass% carbon and 0.76 mass% manganese content (Krauss¹⁰). Curves for the beginning and end of the bainite (and pearlite) transformation are shown with the horizontal broken line marking the transition between pearlite and bainite formation. There is a temperature above which bainite does not form, called the B_s (bainite start) temperature, which has been demonstrated using hot stage light microscopy (Bhadashia⁴⁴).

Figure 10: TTT diagram for a 0.79 mass.% C, 0.76 mass.% Mn steel (Krauss¹⁰, "American Society for metals 1985)



Empirical equations have been developed to express the bainite start temperature as a function of the steel chemistry, the most widely used is due to Steven and Haynes⁴⁵ who determined the B_s temperature for a range of steels covering the composition ranges:-

Carbon	0.1-0.55	Nickel	0.0-5.0
Silicon	0.1-0.35	Chromium	0.0-3.5
Manganese	0.2-1.7	Molybdenum	0.0-1.0

and found that:-

$$B_s (\text{°C}) = 830 - 270W_C - 90W_{Mn} - 37W_{Ni} - 70W_{Cr} - 83W_{Mo} \quad (3.1)$$

where W_i = weight % of element i which is in solid solution in austenite

3.2 Bainite structure characterisation

Two morphologies of non lamellar ferrite cementite aggregate form in medium carbon steels (Mehl⁴⁵; Hehemann⁴⁶).

a) Upper bainite forms in the temperature range below that in which pearlite forms. Like pearlite fine aggregates of ferrite and carbide are developed, however “feathery” aggregates of laths or needle like ferrite particles with cementite precipitated in the inter-lath regions parallel to the long axis are developed (Christian and Edmonds⁴¹).

b) Lower bainite is formed at lower temperatures, (just above M_s) where the diffusion of carbon is limited. Fine carbides precipitate within the ferrite laths as well as at lath boundaries and the lath width is also reduced with decreasing temperature (Krauss¹⁰).

Some authors also characterise the difference between upper and lower bainite based on whether the transformation is above or below approximately 350°C (Matas and Hehemann⁴⁸), although Pickering⁴⁹ has shown that this distinction is not universally applicable (see figure 10). Additionally, attempts have been made to model the transition from upper to lower bainite based on the hypothesis that bainitic ferrite grows with the supersaturation of carbon in solid solution. The theory involves the comparison between the time required to reject the excess carbon into the residual austenite versus the time required to obtain a detectable degree of cementite precipitation in the bainitic ferrite. (Takahashi and Bhadeshia⁵⁰).

An important characteristic of bainitic microstructures, especially relevant to their mechanical properties, is the nature and extent of carbide precipitation. In the following two subsections, the carbide precipitation reaction is discussed in relation to the transformation mechanism of bainite.

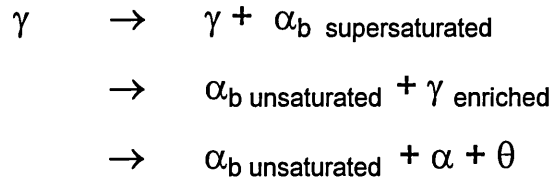
3.2.1 Upper bainite

As a consequence of the transformation to bainite, austenite enveloped between platelets of upper bainite becomes enriched in rejected carbon. The carbide phase associated with upper bainite precipitates from carbon enriched residual austenite and is nearly always cementite (Wever and Mathieu⁵¹, Lyman and Troiano⁵², Hultgren⁵³, Austen and Schwartz⁵⁴)

If the carbon concentration of the residual austenite exceeds the value given by the extrapolated $\gamma / (\gamma + \theta)$ phase boundary shown in figure 11, then cementite precipitation from the enriched austenite lying adjacent to the platelets of bainitic ferrite becomes thermodynamically possible (Kriesement and Wever⁵⁵). It is also assumed that bainite growth stops when the carbon concentration of the austenite exceeds the T'_0 phase boundary, and will only continue when carbon concentration drops i.e. on precipitation.

Hence the overall sequence is growth of bainitic ferrite, rejection of carbon to form cementite, back to growth of bainitic ferrite. When the temperature is below T_c however, subject to kinetics, carbide precipitation and growth of upper bainite is expected simultaneously.

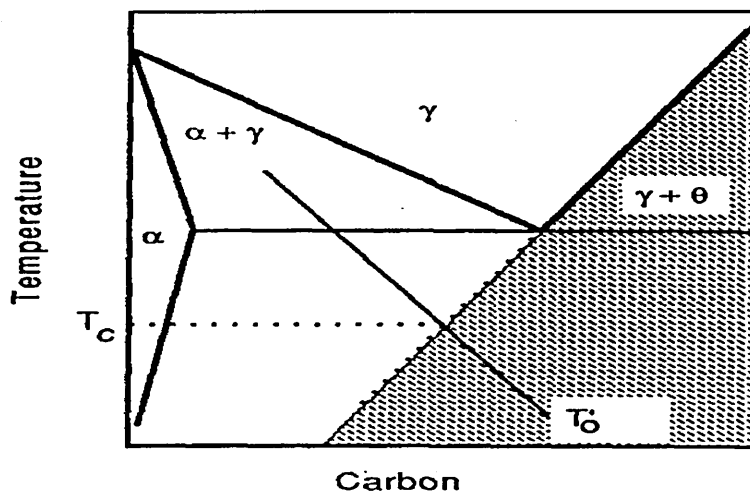
The sequence of reactions are summarised as follows, α refers to the secondary ferrite which forms as the carbide precipitates from residual austenite (Bhadeshia⁴⁴):-



T'_o = Temperature at which γ and α of the same composition have the same free energy also accounting for the stored energy of ferrite.

T_c = Temperature below which cementite can in principle precipitate in association with upper bainitic ferrite.

Figure 11:- Schematic illustration of the thermodynamic condition which has to be satisfied before cementite may precipitate from the austenite (Bhadashia⁴⁴)



As noted previously the formation of cementite or other carbides leads to a reduction of the carbon concentration in the residual austenite, thereby permitting the growth of a further amount of ferrite (denoted α). The mechanism of this secondary ferrite reaction is not well understood.

Sandvik⁵⁶ has proposed that the decomposition of the residual austenite involves the displacive formation of a triclinic carbide, and the subsequent formation of a small amount of bainitic ferrite. Whilst Nakamura and Nagakura⁵⁷ have suggested that cementite nucleates directly on the ferrite / austenite grain boundary. They also proposed that the secondary ferrite, which they denote as bainite, grows martensitically from the carbide depleted austenite.

In planar sections, the cementite particles in upper bainite appear parallel to the traces of habit planes of the bainitic ferrite platelets. Fisher⁵⁸ described these particles as irregular ribbons in three dimensions particularly in bainite formed at elevated temperatures. Additionally the precipitation of cementite from supersaturated austenite is probably initiated at austenite grain boundaries, hence these carbides will be relatively coarse and detrimental to the mechanical properties, especially toughness in high strength steels (Pickering²³).

3.2.2 Lower bainite

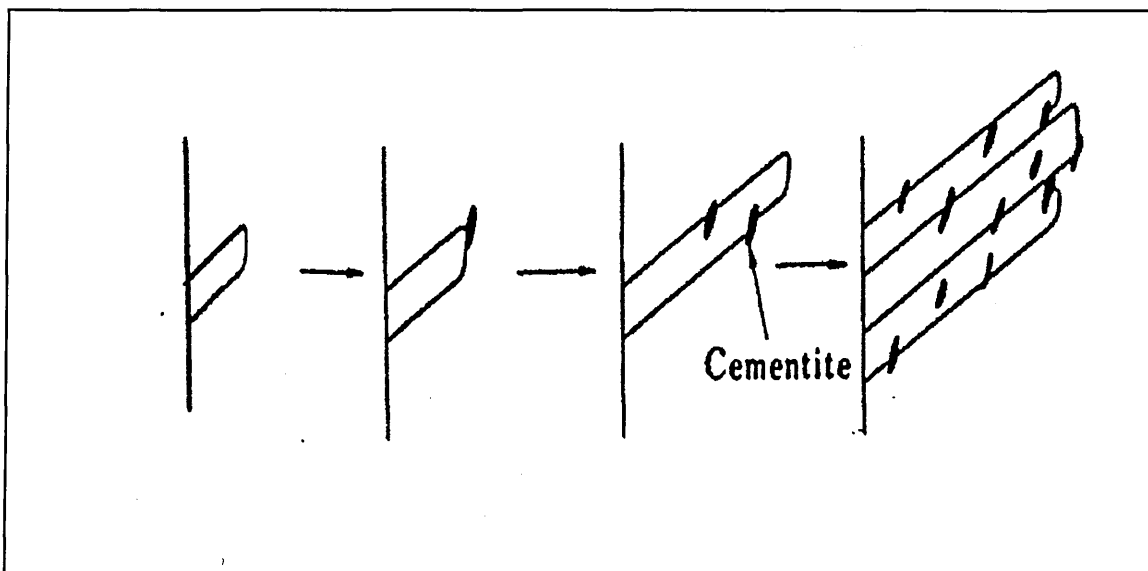
Lower bainite consists of a non lamellar aggregate of ferrite and two kinds of carbides. (Bhadashia⁴⁴). As with upper bainite there is some precipitation of carbide from the enriched austenite between the bainite plates. However there is also a fine dispersion of carbides (ϵ - carbide or cementite) within the ferritic plates (discussed in section 3.2.2.1).

Spanos et. al⁵⁹ proposed a mechanism for the formation of lower bainite sheaves based on TEM observations on specimens of Fe-C ~ 2% Mn alloys which contain relatively low (30%) volume fractions of bainite. The mechanism, summarised in figure 12, involves the following stages:-

- 1) Precipitation of a nearly “carbide free ferrite spine”.
- 2) Sympathetic nucleation of “secondary ferrite” plates usually only one side and at an angle of approximately 55 to 60° to the initiating spine.
- 3) Precipitation of carbides in the austenite at the α/γ boundary forming gaps between adjacent “secondary ferrite plates”
- 4) Annealing then fills gaps with further growth of ferrite and additional carbide precipitation causing the sheaf to lose its original serrated appearance not far behind its leading edges.

Annealing out ferrite : ferrite boundaries formed by lateral impingement of adjacent “secondary plates” further contributes to the appearance of lower bainite sheaves as monolithic ferrite plates containing embedded carbides. The ferrite spine corresponds to the smooth side of lower bainite plates first observed by Oblak and Hehemann⁶⁰ and subsequently reported by other authors (Yada and Ooka⁶¹).

Figure 12:- Schematic representation of the mechanism of carbide precipitation suggested by Ohmori et. al⁶²



The alternative theory summarised by Christian and Edmonds⁴¹ suggests that lower bainite forms first as supersaturated ferrite, and that precipitation within this ferrite is then a subsequent stage of the reaction. The precipitation within the ferrite laths is then a result of relief precipitation (Ko and Cottrell⁶³) or in-situ precipitation once a sub unit of bainite has ceased to grow, where because of increased driving force and low mobility of the carbon atom, diffusion to austenite is limited.

3.2.2.1 Precipitation within the lower bainite ferrite plate

Carbides found within any given bainitic ferrite plate usually occur in a single crystallographic orientation. Cementite carbides have the longest axes inclined at 60° to the “growth direction” of the ferrite platelets (ASTM, Irvine and Pickering⁶⁴, Speich⁶⁵, Shimizu and Nishyama⁶⁶, Shimizu et al.⁶⁷,). This angle quoted however varies as a function of the plane section, it has been shown that for lower bainite ferrite the cementite precipitates on the (112)_α so that the true angle between the α and the cementite habit plane normal is approximately 57°(Bhadashia⁴⁴).

Early experimental work using Curie point measurements and dilatometry gave indirect indications that ε-carbide as well as cementite was associated with lower bainite, (Wever and Lange⁶⁸, Allen et. al⁶⁹. Antia et al⁷⁰). Austin and Swartz⁷¹ first identified the presence of ε-carbide (Fe_{2.4}C) in lower bainite and since then similar results have been reported by several investigators. (Matas and Hehemann⁴⁸, Deliry⁷², Pomey⁷³, Oblak and Hehemann⁶⁰).

Bhadashia⁴⁴ has considered the available data and has concluded that the average carbon content of the alloy system needs to be greater than 0.55wt% for ε-carbide formation. Since the partitioning of carbon into the residual austenite depletes the bainitic ferrite too rapidly to permit any appreciable precipitation of this carbide. The exception to this rule are nickel containing steels which are believed to enhance the precipitation of ε-carbide (Miihkinen and Edmonds⁷⁴).

Additionally η -carbide (Fe_2C) has also been observed in lower bainitic ferrite obtained by transforming the austenitic matrix of a high silicon cast iron (Franetovic et al.⁷⁵).

3.2.2.2 Precipitation between lower bainite ferrite platelets

The precipitation of carbides within the bainitic ferrite plate by the decomposition of the carbon into a mixture of cementite and ferrite is identical to the precipitation of carbides in the upper bainite microstructure. However, because some of the carbon is already tied up in the form of carbides within the ferrite lath, a reduced amount of interplate cementite is observed (Hehemann⁴⁷). An important consequence of this is that lower bainite often has a higher toughness than upper bainite even though it is usually the stronger of the two.

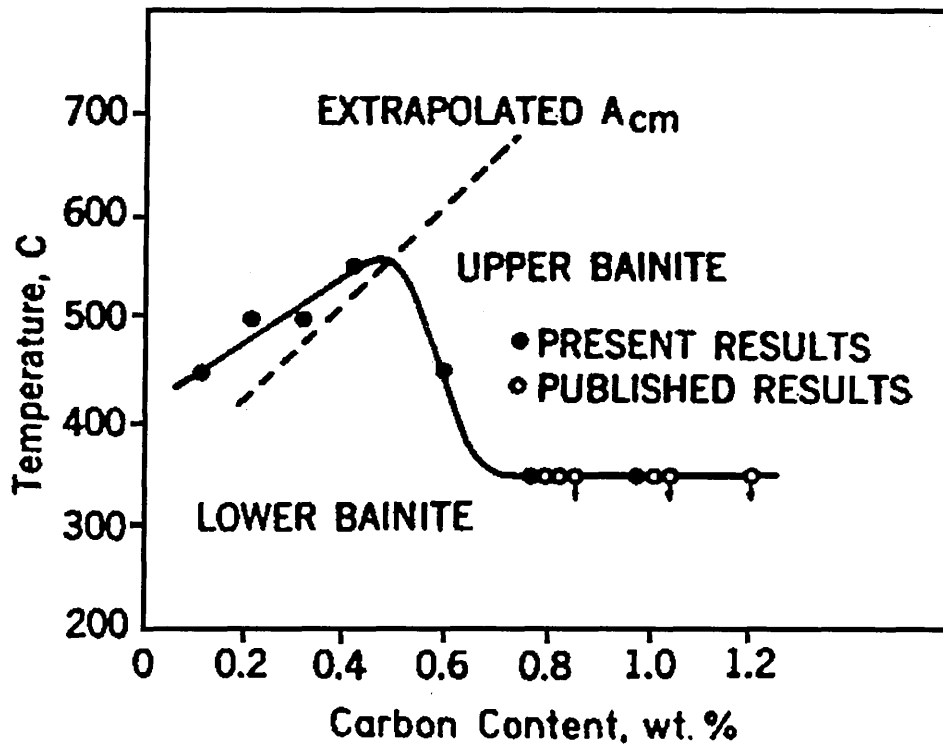
3.3 Transition temperature between upper and lower bainite

The division in the bainitic range into upper and lower bainite was first suggested by Mehl⁴⁶ based on microstructural differences, implying that in most steels there should be a fairly sharp change in morphology. The transition is usually found to occur at approximately 350°C and not to be very dependant on composition (Christian and Edmonds⁴¹), but Pickering⁴⁹ found appreciably higher transition temperatures in lower carbon steels (containing 0.5% molybdenum) rising to a maximum of ~550°C at ~0.5 wt.% carbon and then decreasing again as illustrated in figure 13.

As an example, consider a steel with carbon content of 0.8 mass%, if isothermally transformed at 400°C the resultant microstructure would consist of upper bainite, whereas a 0.4 mass % carbon steel transformed at the same temperature would possess a lower bainite microstructure.

Ohmori and Honeycombe²¹⁵ investigated a steel of similar composition except for molybdenum and found a constant transition temperature of 350°C down to 0.4% carbon with no lower bainite forming below this composition.

Figure 13: The temperature of the transition between upper and lower bainite versus carbon content. (Pickering^{23,49}).



Models for estimating the temperature at which upper bainite reaction gives way to the formation of lower bainite have been developed by Takahashi and Bhadeshia⁵⁰ based on an idea from Matas and Hehemann⁴⁸. The model involved a comparison between the times required to decarburise supersaturated ferrite plates with the time required to precipitate cementite within the plates. If the decarburisation process dominates, upper bainite is formed, whereas relatively rapid carbide precipitation within the ferrite leads to the formation of lower bainite.

3.4.1 Bain region definition

The Bain strain is the pure part of the lattice deformation which for displacive transformations in steels converts austenite into ferrite or martensite (Bain⁷⁸), see chapter 4 section 4.1.

During the Bain strain, no plane or direction is rotated by more than 11° so that any pair of corresponding planes or directions may be made parallel by utilising the lattice deformation with a rotation of no more than 11° (Crosky et al.⁷⁹).

This then defines the Bain region, where it is expected that the experimentally observed orientation relation will lie within this region, close to the Kurdjmov-Sachs / Nishiyama-Wasserman relationship.

Bhadeshia and Edmonds⁸⁰ along with many other investigators found that all the platelets / laths within a sheaf or packet have a common orientation. However Sarikaya et al.⁸¹ has claimed that although some groups of adjacent laths have a common orientation, others have different variants of the orientation relationship, or in lower bainite are twin related. One suggested reason for single orientation relationship is that the individual laths of a sheaf or packet are not separate crystals but continuously connected proportions of the growth front from one original nucleus. At relatively high temperatures during bainite formation, dislocation generation from plastic deformation brought about by the shape change prevents the forward growth of a lath after it has attained a certain size. Initiation and growth of a new platelet or lath only resumes by the breakaway of a part of the original interface in close proximity to the tip (Bhadeshia⁴⁴).

In bainite, growth would resume after the rejection of carbon from the ferrite into the austenite and would be most likely where pinning by dislocation debris is minimal. Alternatively it has been suggested that individual laths within the packet are completely separated from each other by thin layers of retained austenite, since some authors have claimed to observe retained austenite between individual laths (Srinivasan and Wayman⁸², Sandvik and Wayman⁸³).

3.5 Crystallography of carbide precipitation in bainite

Details of the crystal structure of the carbides found in bainite or tempered bainite are given in table 3 (Bhadeshia⁴⁴). Each individual reference is noted, alongside ratio of iron and other metal atoms to carbon designated Fe,M/C. Because long range diffusion of substitutional atoms is not permitted during typical heat treatment and cooling regimes when forming bainite, it is found that only ϵ -carbide, η -carbide or cementite precipitate within the bainitic ferrite. Also only κ -carbide or cementite precipitate from the carbon enriched austenite between the ferrite platelets. The other carbides listed in table 3 require long range diffusion, only obtainable during a tempering treatment or after prolonged holding at the isothermal transformation temperature.

Table 3:- Crystal structures of carbides. (Bhadeshia⁴⁴).

Carbide	System	Lattice parameters (Å)	Fe,M /C	Reference
K	Hexagonal	a=6.9 c=4.8	1.37	Deliry ⁷² Pomey ⁷³
ε	Hexagonal	a=2.735 c=4.339	2.4-3	Jack ⁸⁴ Hofer et al ⁸⁵
χ	Monoclinic	a=11.563 b=4.573 c=5.058 β=97.44°	2.2 or 2.5	Hägg ⁸⁶
η	Orthorhombic	a=4.704 b=4.318 c=2.830	2	Hirotsu and Nagakura ⁸⁷
Fe ₃ C	Orthorhombic	a=4.525 b=5.087 c=6.743	3	
M ₇ C ₃	Orthorhombic	a=4.526 b=7.010 c=12.142	7/3	Mornioli et al. ⁸⁸
(Fe,Si)C _x	Orthorhombic	a=8.8 b=9.0 c=14.4		Knoval et al. ⁸⁹
(Fe,Si)C ^X	Orthorhombic	a=6.5 b=7.7 c=10.4		Schissler et al. ⁹⁰
(Fe,Si,Mn)C _x	Orthorhombic	a=14.8 b=11.4 c=8.5		Schissler et al. ⁹⁰
M ₂₃ C ₆	Cubic	a=10.621	23/6	
M ₆ C	Cubic	a=11.082	6	
"C"	Triclinic	a=6.38 b=5.05 c=4.59 α= β=70.1 γ= 84.7		Sanvik ⁹⁶

3.5.1 The orientation relationship of Cementite

As in the case of martensite, the most frequently observed orientation relationship, called the tempering or Bagaryatski⁹¹ relationship is found to be:-

$$\{001\}_\theta \parallel \{211\}_\alpha$$

$$\langle 100 \rangle_\theta \parallel \langle 0\bar{1}1 \rangle_\alpha$$

The second most frequent observed α/θ orientation relationship which is also consistent with the tempering of martensite is:-

$$\{001\}_\theta \parallel \{\bar{2}\bar{1}5\}_\alpha$$

$$\langle 100 \rangle_\theta \text{ within } 2.6^\circ \text{ of } \langle 3\bar{1}1 \rangle_\alpha$$

$$\langle 010 \rangle_\theta \text{ within } 2.6^\circ \text{ of } \langle 131 \rangle_\alpha$$

For cementite that precipitates during the formation of upper bainite Shackleton and Kelly⁹² have showed that a large number of observed orientation relationships are all rationalised if it is assumed that the cementite precipitates from austenite with the Pitsch²¹⁶ γ/θ relationship:-

$$\{001\}_\theta \parallel \{\bar{2}25\}_\gamma$$

$$\langle 100 \rangle_\theta \text{ within } 2.6^\circ \text{ of } \langle \bar{5}54 \rangle_\gamma$$

$$\langle 010 \rangle_\theta \text{ within } 2.6^\circ \text{ of } \langle \bar{1}10 \rangle_\gamma$$

The α/θ relationship can then be found by considering the γ/θ relationship by allowing the ferrite to be a variant of the Kurdjumov Sachs α/γ orientation relationship.

The θ/α orientation relationship found by Isaichev⁹³ has also been reported for the cementite within lower bainitic ferrite (Ohmori⁹⁴, Huang and Thomas⁹⁵, which is quite close to the Bagaryatski relationship:-

$$\begin{aligned} \{103\}_{\theta} \parallel \{101\}_{\alpha} \\ \langle 010 \rangle_{\theta} \parallel \langle \bar{1}\bar{1}\bar{1} \rangle_{\alpha} \end{aligned}$$

3.5.2 The orientation relationship between epsilon (ϵ) carbide

Epsilon carbide is found to occur in the form of plates which are approximately 6-20 nm thick and 70-400 nm long (Huang and Thomas⁹⁵). The carbide ferrite interface tends to be ragged and forms the orientation relationship:-

$$\begin{aligned} (101)_{\alpha} \parallel (10\bar{1}\bar{1})_{\epsilon} \\ (2\bar{1}\bar{1})_{\alpha} \parallel (10\bar{1}\bar{0})_{\epsilon} \\ (011)_{\alpha} \parallel (0001)_{\epsilon} \\ (\bar{1}\bar{1}\bar{1})_{\alpha} \parallel (1\bar{2}\bar{1}\bar{1})_{\epsilon} \end{aligned}$$

This relationship was first deduced by Jack⁸⁴ in tempered martensite structures, Huang and Thomas⁹⁵ have since confirmed that the ϵ -carbide found in lower bainite obeys the same orientation relationship with bainitic ferrite as found during the tempering of martensite.

3.5.3 Orientation relationship of eta (η) carbide

This transition carbide, is usually associated with the tempering of martensite, (Hirotsu and Nagakura⁸⁷) where the martensite / carbide orientation relationship was found to be:-

$$\begin{aligned} (110)_{\eta} \parallel \{010\}_{\alpha} \\ [110]_{\eta} \parallel \langle 010 \rangle_{\alpha} \end{aligned}$$

Eta carbide has been recently found in a high silicon lower bainitic ferrite alloy (Franetovic et al.⁷⁵), where electron diffraction confirms that:-

$$[011]_{\theta} \parallel \langle 100 \rangle_{\alpha} \parallel \langle 011 \rangle_{\gamma}$$

3.5.4 Orientation relationship of chi (χ) carbide

Chi carbide is a transition carbide which is metastable with respect to cementite. It was first found in the tempered martensite structure, where the use of high magnification electron microscopy revealed interpenetrating layers of cementite and χ carbide. It was initially thought that this structure simply consisted of faulted cementite, further investigations however, revealed that these "faults" corresponded to regions of χ carbide, each only a few interplaner spacings thick. where the $\{200\}_{\chi}$ planes are found to be parallel to the $\{001\}_{\theta}$ planes of slightly different spacings (Bhadeshia⁴⁴).

3.6 Structure property relationships in the bainitic microstructure

The quantification of the mechanical properties of an upper or lower bainitic microstructure is by no means straightforward due to its complex nature comprising of many possible structures and strengthening mechanisms (Pickering²³), for example :-

- i) Packets of lath like ferrite grains of low misorientation between grains. (Pickering⁴⁹, Honeycombe and Pickering⁹⁶).
- ii) Variable dislocation density and dislocation arrays between ferrite laths.
- iii) large carbides at ferrite lath, prior austenite boundaries, and carbides within the ferrite laths in lower bainite.
- iv) Alloy enriched ferrite islands or high carbon bainite, martensite or even retained austenite between ferrite laths, i.e. the martensite-austenite (MA) constituent.
- v) Solid solutions of interstitial and substitutional solutes.

It can be concluded that some difficulties will arise in attempting to describe the individual effects of all these features quantitatively on the mechanical properties.

3.6.1 Hardness

For fully bainitic microstructures, the hardness is approximately linearly related to the carbon concentration, by 190 Hv per wt% (Irvine and Pickering⁹⁷). This contrasts with a change of about 950 Hv per wt.% of carbon for untempered martensite, where most of the carbon is in solid solution. The austenitising temperature does not influence the hardness unless it is not high enough to dissolve all the carbides (Irvine and Pickering⁹⁷). Also the hardness of bainite was found to be independent of the prior austenite grain size, even though this in turn influences the bainite sheaf thickness (Kamada et al.⁹⁸). This is not unexpected given that the bainite sub-unit (packet size) is hardly influenced by the prior austenite grain size and since the sub-units are much smaller they exert an overriding influence on strength (Bhadeshia⁴⁴).

NB:- In most cases microstructures obtained are often mixed, in which case the hardness will depend on the transformation temperature and composition.

3.6.2 Proof strength

Bainite steels do not possess a definite yield point, instead continuous yielding is observed hence the yield strength usually refers to the 0.2% proof strength. The major strengthening mechanisms are due to bainitic ferritic "grain size" (packets), dislocations, carbide dispersion and solid solution strengthening. It is well known (Irvine and Pickering⁹⁷; Pickering⁴⁹) that the tensile strength and proof strength increases linearly with decreasing transformation temperature. This is because the above mentioned strengthening mechanisms increases with decreasing transformation temperature.

One additional point to note however is that the transformation temperature is related to the steel composition (Steven and Haynes⁴⁵), hence equation 1 can be used to determine the approximate 0.2% proof strength value:

$$0.2\% \text{ PS} = 170 + 1300 (\text{wt.}\% \text{ C}) + 160 (\text{wt.}\% \text{ Mn}) + 160 (\text{wt.}\% \text{ Cr}) + 130 (\text{wt.}\% \text{ Mo}) + 88 (\text{wt.}\% \text{ Ni}) + 63 (\text{wt.}\% \text{ W}) + 45 (\text{wt.}\% \text{ Cu}) + 270 (\text{wt.}\% \text{ V}). \quad (3.2)$$

Pickering⁴⁷ showed that the proof strength increased linearly with the reciprocal of the square root of the mean linear intercept of the “bainitic ferrite” grain size and also increased with the increasing density of carbide particles.

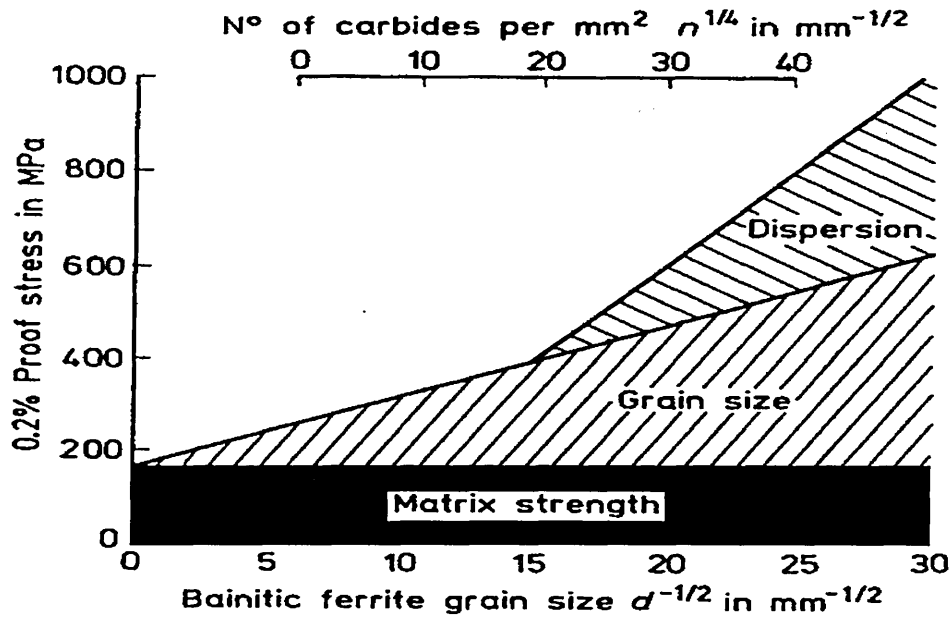
The contribution of “bainitic ferrite grain size” to proof strength was investigated by several workers, (Bush and Kelly⁹⁹, Gladman et al¹⁰⁰, Pickering⁴⁹). Conclusions drawn suggested that the bainitic ferrite grain size contributed less than 50% of the proof strength.

Equation 3.3 was developed (Pickering²³) to relate the proof strength to the individual effects of the bainite ferrite grain size, d , and the number of carbide particles per unit planar section of the structure, n .

$$\text{Proof strength } (\delta_y) = -191 + 17.2 d^{-1/2} + 14.9 n^{1/4} \quad (3.3)$$

From the negative constant in this equation it can be seen that a threshold carbide distribution exists, below which carbides do not contribute to strength. Thus in upper bainite the carbides at the bainitic ferrite lath boundaries do not add to the strengthening, as their spacing is equal to or greater than the bainitic ferrite lath size. In lower bainite however the carbides do contribute to the strength as they occur within the ferrite laths. The results from equation 3.3 are also illustrated in figure 15, and indicates that carbide strengthening only becomes significant at the finer bainitic ferrite lath sizes, i.e. at the lower transformation temperatures.

Figure 15:- Contributions of the bainitic ferrite grain size and carbide dispersion strengthening to the 0.2% proof stress of low carbon bainitic microstructures contain 0.05 - 0.15 wt. % carbon (Pickering²³).



It has also been suggested (Bush and Kelly⁹⁹), that strengthening from dislocations, which can be quite substantial due to the shear component of the bainite transformation, should be taken into consideration.

$$\delta_d = 1.2 \times 10^{-3} (\varphi)^{1/2} \quad (3.4)$$

Where φ is the dislocation density in lines cm^{-2}

An assessment has also been made on the effect of the MA (martensite-austenite) constituent which is usually found in bainite formed during continuous cooling. The contribution to the proof strength from the MA phase has been reported to be:-

$$\delta_{MA} = 360 + 900 (f MA) \quad (3.5)$$

Where f MA is the volume fraction of MA constituent.

3.6.3 Proof strength / UTS ratio

Many bainitic steels, particularly those with high strengths, have Proof / UTS (r_f) values much lower than 0.8 even though the UTS maybe very large (Irvine and Pickering⁹⁷). It is believed that the internal stresses caused by the displacive mode of transformation, and the existence of many mobile dislocations, has the effect of lowering the proof stress.

This was confirmed by the fact that a low temperature (400°C / 1 hour) tempering treatment, which has only a minor effect on the microstructure, reduces the internal stresses and raises r_f without any loss of strength.

Since relatively hard phases i.e. cementite exist in the microstructure, a gradual yielding behaviour is observed due to these particles acting as stress concentrators. In bainite there is also an irregular distribution of obstacles (solute atoms boundaries etc.) to the motion of dislocations, obstacles whose "strength" is variable. Also obstacle free areas will exist into which dislocations can penetrate at low stresses, thus giving rise to a gradual deviation from elastic behaviour (Kettunen and Kocks¹⁰¹, Kettunen and Lepistö¹⁰²).

An additional problem can arise when a large volume fraction of a phase harder or softer than bainite is included in the sample (Hehemann et al.¹⁰³). Much of the deformation is initially concentrated in the softer phase and this has the effect of reducing the yield stress of the softer phase (Tomota et al.¹⁰⁴). The hard phase commences to deform after the softer phase has strain hardened and is able to transfer some of the load.

3.6.4 Ductility

Low carbon bainitic or martensitic steels always show superior tensile ductility when compared to their high carbon, identical strength counterparts, (Irvine and Pickering⁹⁷). Subsequent research confirmed that the ductility can be improved by reducing the carbon content of a fully bainitic microstructure while maintaining its strength using substitutional solid solution strengthening.

The ductile fracture in good quality commercial steels which are free of metallic inclusions, propagates via a nucleation, growth and coalescence of voids mechanism, with fracture occurring on the coalescence of voids (Bhadeshia⁴⁴). Minimum deformation before fracture is obtained when the number density of voids is large, hence mean separation is small.

Increasing the carbon concentration of the bainitic steel (increase in number of carbide particle), facilitates an increase in the number of void nucleation sites, hence ductility decreases with increasing carbon content even if the strength remains constant (Pickering¹⁰⁵)

In steels which do not transform completely to bainite, voiding during deformation has also been observed at the hard regions of untempered martensite which form on the transformation of carbon enriched residual austenite (McCutcheon et al.¹⁰⁶).

The linking of voids during ductile deformation begins with internal necking between adjacent voids. Since this necking instability depends upon the ability of the material to work harden, ductility should decrease if the work hardening rate is small, however results to date do not show this. Deep and Williams¹⁰⁷ have shown that tempered upper bainite strain hardens more rapidly than tempered lower bainite. However, both microstructures were found to have identical ductility even though the structures possessed identical values of interparticle spacing and mean carbide size. Hence the effect of work hardening and yield stress on the ductile failure of bainitic steels is not yet understood.

The ductility (measures by elongation) of a fully bainitic, low carbon steel is found to be better than that of oil quenched and tempered martensitic steels of equal strength (Irvine and Pickering⁹⁷). This situation however, is reversed at higher carbon concentrations. The ductility as measured by reduction of area on the other hand, is always worse for bainitic steels, this phenomena is not fully understood (Bhadeshia⁴⁴).

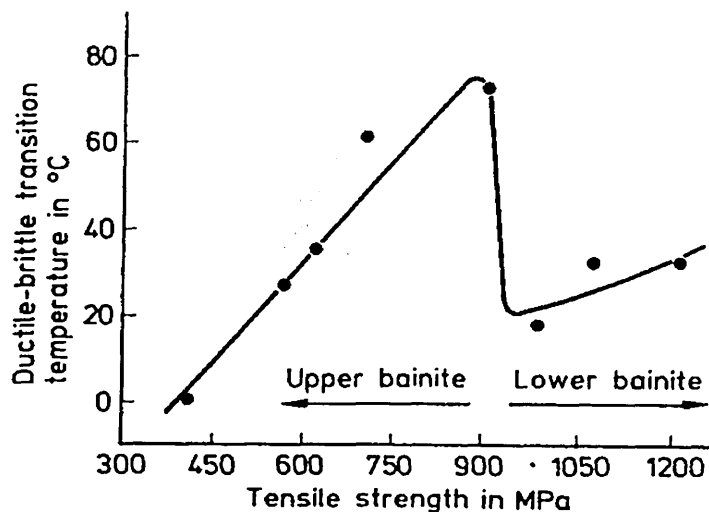
3.6.5 Toughness

Impact toughness is generally characterised by the Charpy test which essentially involves machining a notch in a standard sized test specimen, which is then fractured under certain conditions. The energy absorbed in the fracture process is then taken as a measure of the microstructural toughness. These tests can be carried out over a range of temperatures to determine the ductile brittle transition temperature (DBTT), i.e. the temperature at which the impact fracture surface of a material changes from ductile (high energy) to brittle cleavage (low energy).

It is known that the transition temperature increases with increasing strength for both upper and lower bainite, with upper bainite possessing a higher transition temperature than lower bainite as shown in figure 16 (Pickering⁴⁹). This latter conclusion is due to the following:-

- i) Unconstrained initiation of cleavage cracking in upper bainite due to the fracture of large inter-lath carbides, plus low angle bainitic ferrite lath boundaries are not effective in the prevention of cleavage crack propagation.
- ii) Finer carbides within the laths in lower bainite arrest cleavage crack propagation

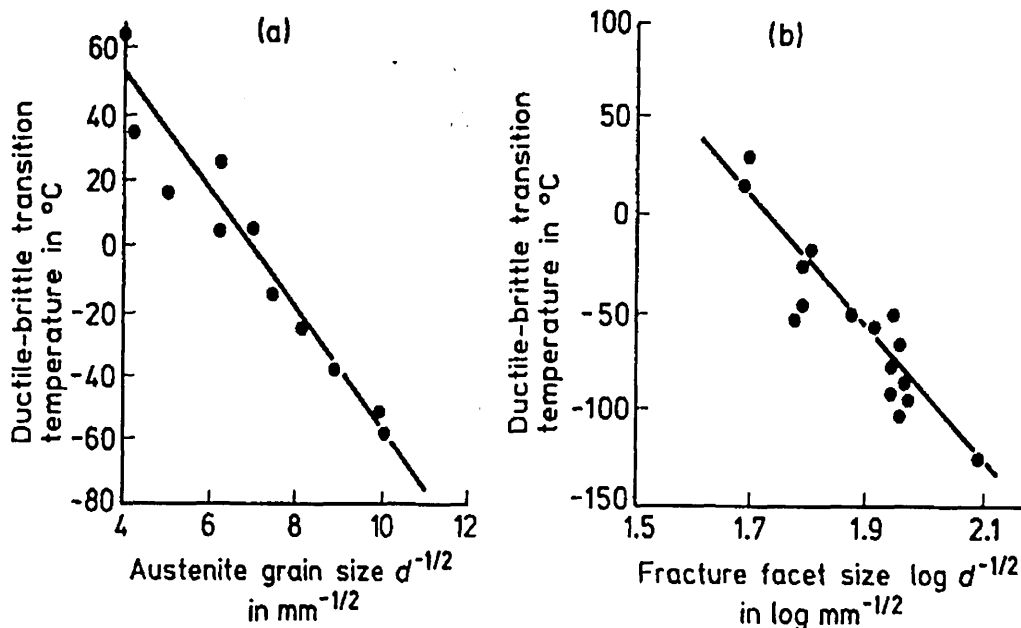
Figure 16:- Relationship between the ductile brittle transition temperature for low carbon bainitic microstructure containing 0.05-0.15 wt.% carbon (Pickering⁴⁹)



One additional barrier to the propagation of the cleavage crack is the high angle "packet" or prior austenite grain boundaries. Results clearly show that the ductile brittle transition temperature increases with prior austenite grain size (Irvine and Pickering¹⁰⁸). This data can be interpreted to show linear dependency of the transition temperature with $D^{-1/2}$ where D is the mean linear intercept of the austenite grain size Figure 17.

Other factors which increase the ductile brittle transition temperature include the presence of coarse carbides, dislocation "forests" and MA constituent (Pickering¹⁰⁹; Morrison¹¹⁰). These factors influence the transition temperature due to their embrittling effect. Low angle grain boundaries also increase the transition temperature, since they have no effect on impeding cleavage crack propagation.

Figure 17: The dependence of the ductile-brittle transition temperature on the prior austenite grain size or the fracture facet size in (a) bainitic microstructures, (b) martensitic microstructures (Irvine and Pickering¹⁰⁸).



3.7 Ideal chemistry and cooling procedure for bainite

In commercially important bainitic steels, a typical continuous cooling diagram features the ferrite nose pushed far to the right so that polygonal ferrite is formed only under exceptionally slow cooling rates. This exposes a broad flat bainite transformation region, hence bainite with an almost constant transformation start temperature is produced over a wide range of cooling regimes.

When developing a new alloy system, it is important to know the effect each element will have on transformation kinetics and hence final microstructure.

Apart from the widely used alloy additions such as chromium and molybdenum, elements such as boron, sulphur and the rare earths are also beneficial (Bhadeshia⁴⁴). Early commercial bainitic steels relied on the effect of boron on the transformation characteristics of low carbon steels, with boron retarding the nucleation of allotriomorphic ferrite permitting the formation of a fully bainitic microstructure under continuous cooling.

Umemoto et al.¹¹¹ found that quite small additions of sulphur (~0.005 wt.%) can in some circumstances lead to an enhancement in the nucleation rate of bainite. This was achieved by the nucleation of iron rich sulphides at austenite grain boundaries thereby promoting the nucleation of bainite, however this was found only when the austenitising temperature was sufficiently low. Umemoto et al.¹¹¹ also found that steels austenitised at elevated temperatures, and subsequently held at a lower temperature (still in the austenite phase field), precipitate a very small volume fraction of cementite particles at the austenite grain boundaries which also stimulate the nucleation of bainite.

The addition of rare earths (cerium, neodymium, lanthanum and yttrium) are also believed to suppress the formation of allotriomorphic ferrite to a greater extent than for bainite formation. The mechanism is believed to be similar to that of boron, involving segregation to the austenite grain boundary (Bhadeshia⁴⁴).

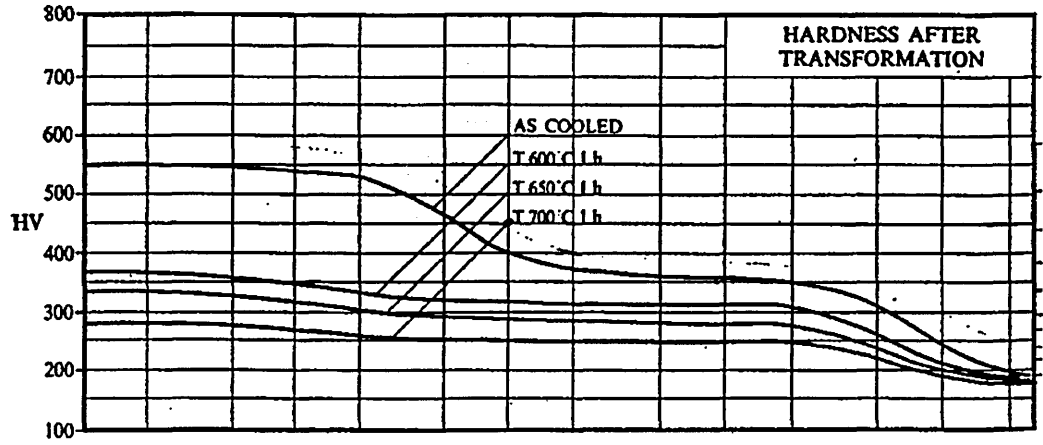
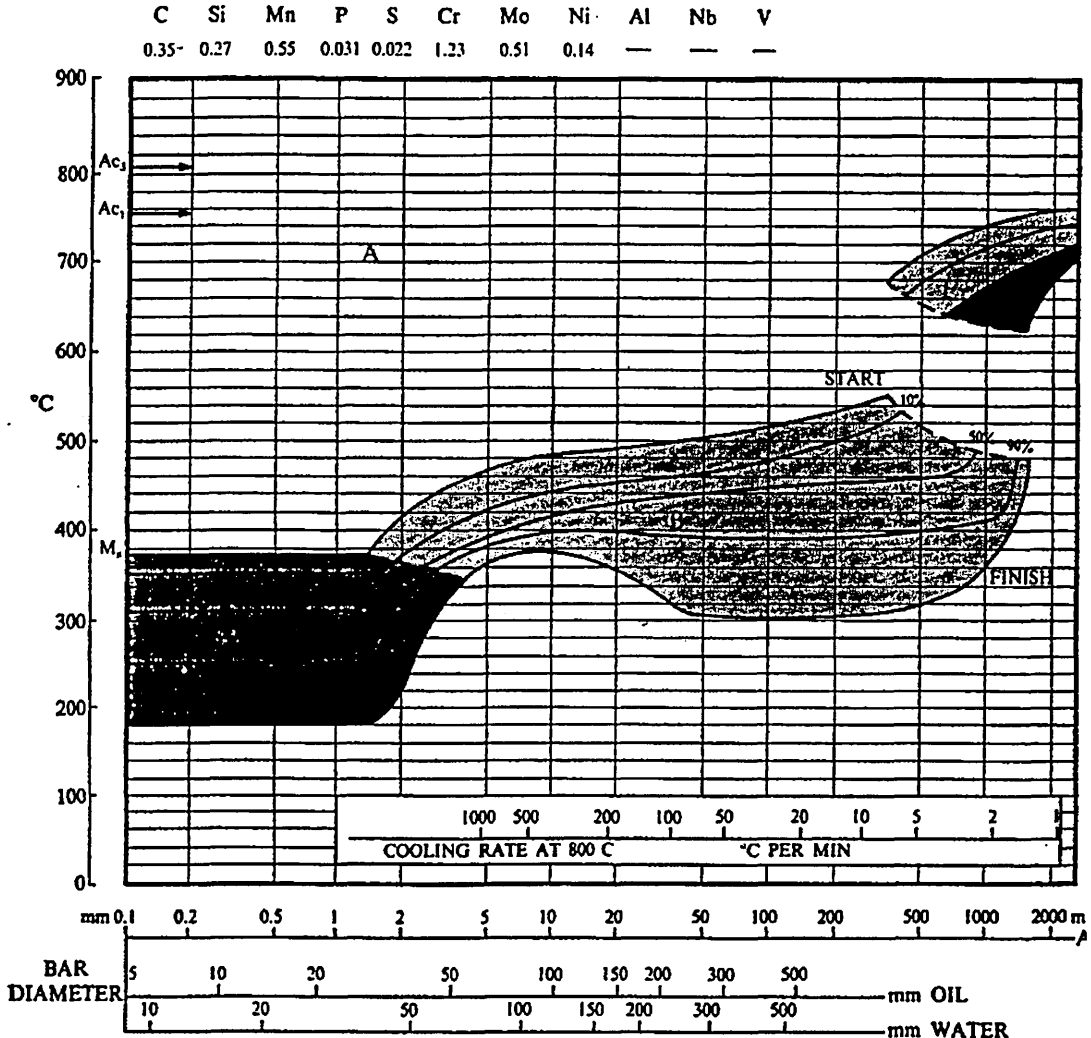
It is well known that 0.35 mass % carbon, 1.25 mass % chromium, 0.5 mass % molybdenum steel possesses a bainitic microstructure over a wide range of cooling regimes, and that this range can be extended further by increasing the carbon content to 0.48 mass %, since carbon suppresses ferrite formation. (Pickering²³). True transformation ranges during continuous cooling are then established by dilatometry or Jominy end quench methods.

Although many continuous cooling diagrams illustrate that a bainite microstructure is generated over a wide range of cooling regimes, the situation is complicated because of the wide variations in microstructure which are actually observed, from upper bainite to lower bainite as the cooling rate is increased. Thus it is apparent that the transformation in the bainite shelf does not produce a single constituent which can be uniquely termed bainite despite the uniformity in the transformation temperature range (Bhadeshia⁴⁴).

It is important to ascertain the transition from upper to lower bainite since the mechanical properties of these two morphologies differ quite significantly (Pickering²³). Of equal importance is the determination of the martensite and ferrite pearlite limit, that is the slowest cooling rate beyond which ferrite is formed and similarly the fastest cooling rate beyond which martensite is formed.

Figure 18 illustrates the continuous cooling transformation curve for a 1¼ chromium molybdenum steel with carbon content of 0.35 mass%. This figure clearly illustrates the wide range of cooling rates possible to produce various bainitic microstructure, hence the flat portion of the "bainite range."

Figure 18: Continuous cooling transformation diagram for 1¼ chromium molybdenum alloy. (Atkins¹¹²).



Chapter 4

Martensitic Microstructure literature review

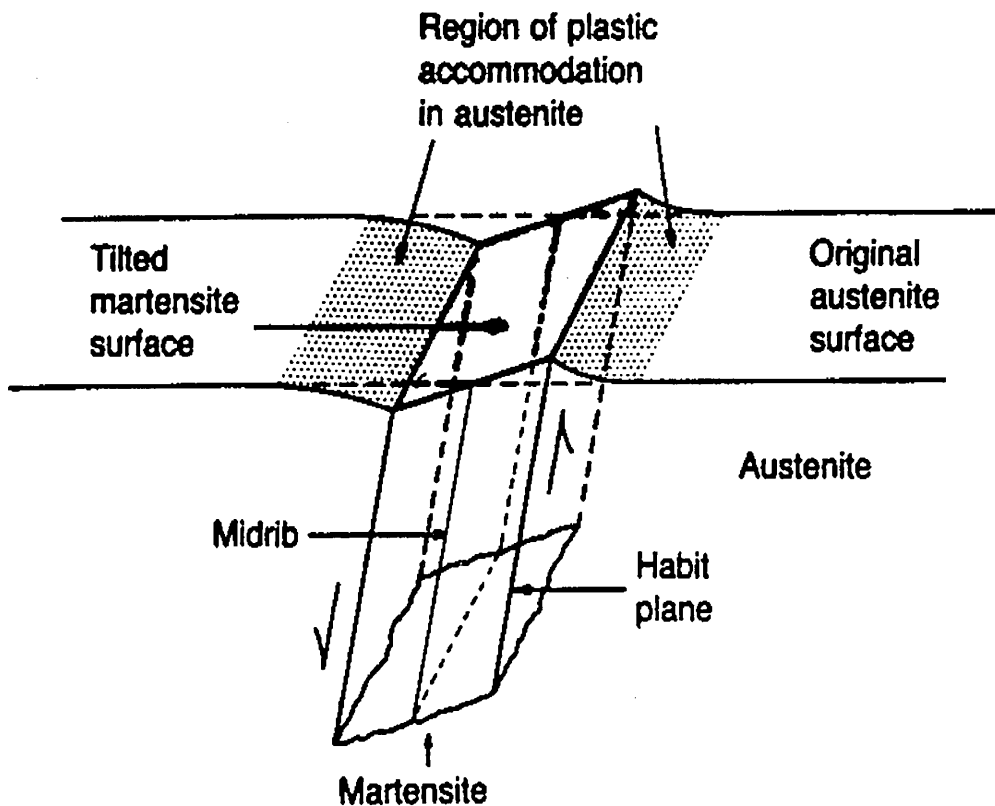
4.1 The martensite transformation

When austenite is cooled very rapidly and atom transfer is suppressed, there is insufficient time for diffusion and consequently austenite transforms to martensite (Krauss¹⁰). Similar effects are observed if the steel is highly alloyed, effectively pushing the nose of the transformation diagram to the right (Krauss¹⁰). Martensite is a phase which forms by a diffusionless displacive transformation mechanism where large numbers of atoms shear co-operatively to form the structure of martensite. This is in complete contrast to pearlite formation, where diffusion / transfer across interfaces are allowed. The martensite transformation produces a homogeneous displacement or shape change characterised by tilted surface relief. Martensite also forms on a specific crystal plane of the parent austenite (habit plane), which varies depending upon the steel composition and the temperature range at which the martensite forms. In order to accommodate this displacement associated with the formation of martensite, the parent austenite must also plastically deform, as illustrated in figure 19 (Krauss¹⁰).

Conventional martensite has a lath like structure with unique habit plane and an internal structure of parallel twins each about 1 μ m thick within the plates.

The martensite transformation can be described mathematically utilising a crystallographic theory which assumes that shape change is accomplished by a homogeneous plane strain maintaining an undistorted habit plane (Wechsler et al¹¹³, Bowles and MacKenzie¹¹⁴, Bilby and Christian¹¹⁵, Wayman¹¹⁶). In summary two deformations are required to accomplish the shape change as described in the following two sub-sections.

Figure 19:- Martensite transformation (Krauss¹⁰).



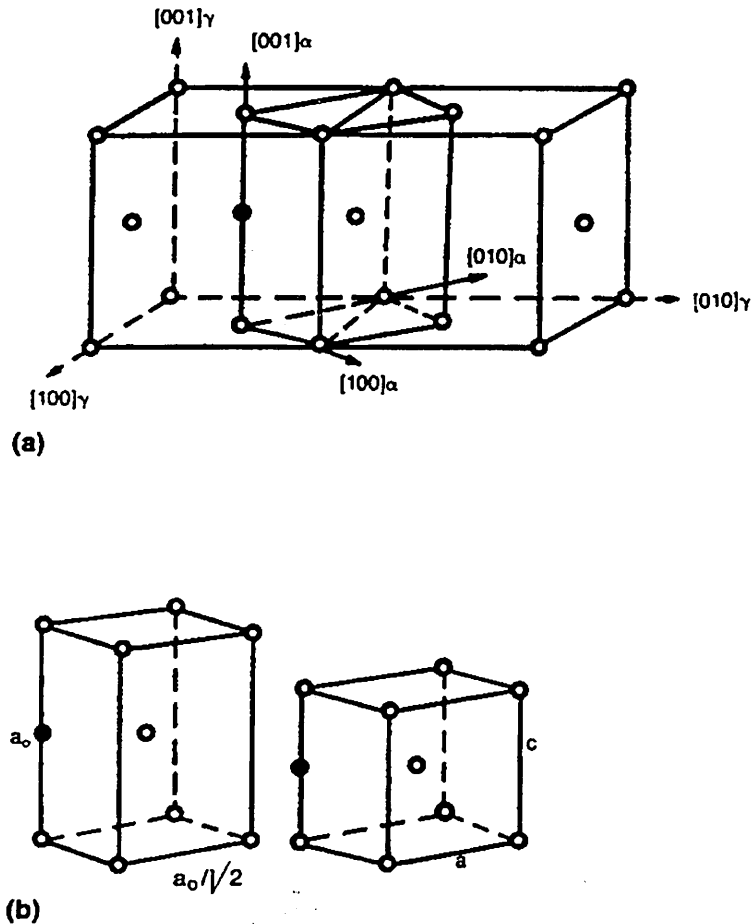
4.1.1 Lattice deformation or "bain" strain

Firstly there is the lattice deformation necessary to accomplish the crystal structure change from austenite to martensite.

In iron carbon alloys and steels the lattice deformation is referred to as the "Bain" strain after Bain⁷⁸, who first identified a set of atoms in f.c.c austenite which would correspond to a set of atoms with the body centred tetragonal (b.c.t) arrangement of martensite.

Figure 20a illustrates the bain correspondence, with figure 20b illustrating how the atoms must be displaced to produce a unit cell of martensite (Christian¹¹⁷).

Figure 20:- (a) Identification of a body centred tetragonal (b.c.t) cell in austenite by $\langle 100 \rangle_\alpha$ axes. (B) The b.c.t. cell before (left) and after (right) the lattice deformation or Bain strain (Christian¹¹⁷).

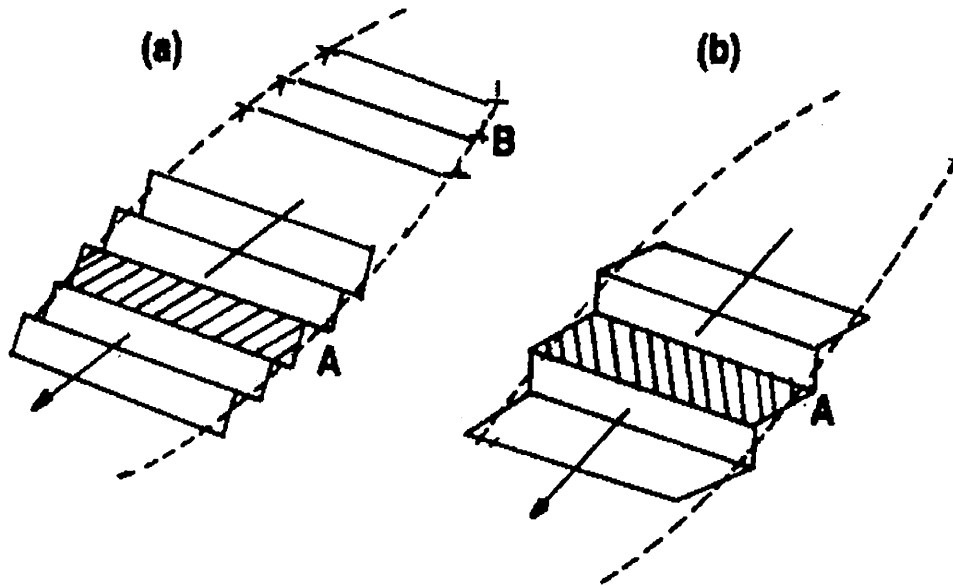


4.1.2 Lattice invariant deformation

The previously described lattice deformation however does not satisfy the requirements of plane strain deformation (Greniger and Troiano¹¹⁸)

Therefore a component known as the lattice invariant deformation is required to make martensite formation conform to plane strain conditions. Lattice invariant deformation is accompanied by extremely fine scale twinning or slip and leaves a characteristic twin or fine dislocation structure within martensite laths, as illustrated in figure 21.

Figure 21:- Schematic representations of the lattice invariant deformation by a) slip and b) twinning (Bilby and Christian¹¹⁵).



4.1.3 Martensite start / finish temperature determination

The temperature at which the martensite transformation begins is known as the M_s (martensite start) and is very specific for any given composition (Naylor and Cook¹¹⁹). Beyond this temperature, because diffusion is limited the austenitic structure rearranges itself via a diffusionless shear transformation to form martensite.

This transformation occurs over a temperature range M_s to M_f (martensite start to martensite finish) and proceeds as the temperature decreases. The range covers approximately 200°C but the transformation is not linear with decreasing temperature (Naylor and Cook¹¹⁹).

The relationship between composition and martensite start / finish has been thoroughly investigated (Grange and Stewart¹²⁰, Payson and Savage¹²¹, Steven and Haynes⁴⁵, Hornbogen¹²², Andrews¹²³). Steven and Haynes⁴⁵ reported the relationship:-

$$M_s (\text{°C}) = 561 - 474(\text{wt.\%C}) - 33(\text{wt.\%Mn}) - 17(\text{wt.\%Ni}) - 17(\text{wt.\%Cr}) - 21(\text{wt.\%Mo}) \quad (4.1)$$

Andrews¹²³ used a very large population of steels and obtained the relationship where 92% of the M_s values were predicted within +/- 25°C.

$$M_s (\text{°C}) = 539 - 423(\text{wt.\%C}) - 30.4(\text{wt.\%Mn}) - 17.7(\text{wt.\%Ni}) - 12.1(\text{wt.\%Cr}) - 7.5(\text{wt.\%Mo}) \quad (4.2)$$

Diggs¹²⁴ investigated the effect of carbon on the M_s temperature, for both plain carbon and alloy steels (see figure 22). The curve for alloy steels shows a higher M_s temperature for a given carbon content than a plain carbon steel because some of the carbon is present as alloy carbide and thus not dissolved in the austenite. Alloying elements dissolved in austenite also depress the M_s temperature, but to a much lesser extent than carbon (Rayson¹²).

In addition Petty¹²⁵ has shown that the M_f temperature (martensite completion) decreases more rapidly with increasing carbon content than the M_s and decreases from 400 C to 0°C as the carbon content is increased from 0 wt. % to 0.65 wt. %, (figure 23).

Figure 22:- M_s temperature as a function of carbon content in Fe-C alloys and steels (Diggs¹²⁴).

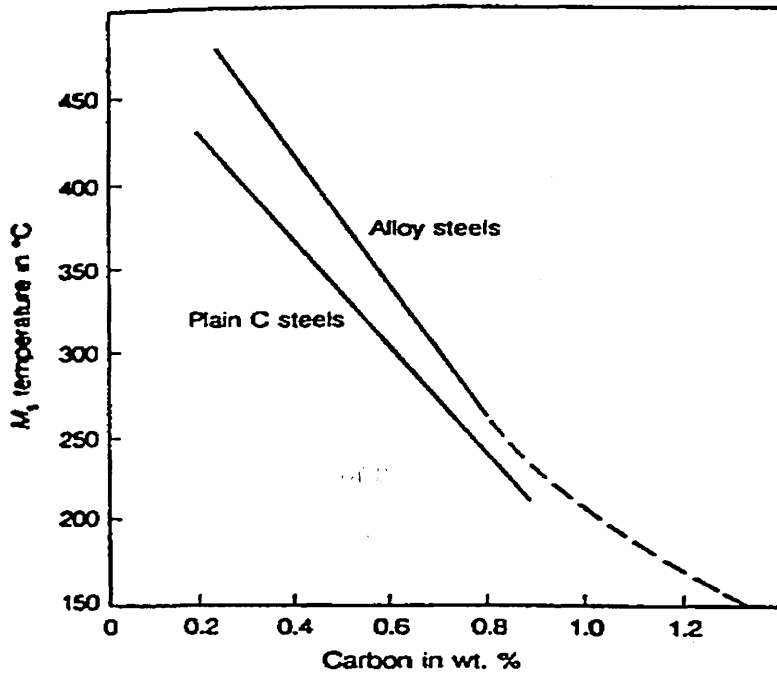
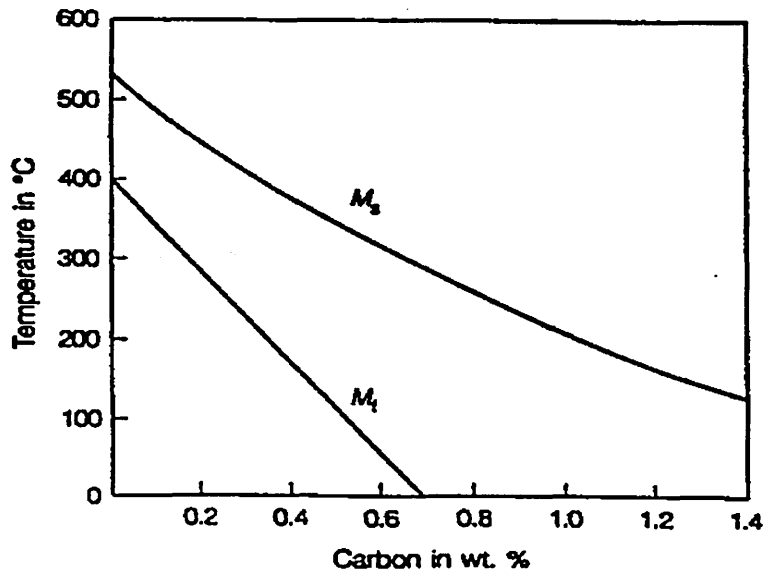


Figure 23 The effect of carbon content on the M_s and the M_f temperatures for the iron carbon alloys (Petty¹²⁵).



4.1.4 Auto tempered martensite formation.

The as quenched martensite microstructure possesses a relatively high strength but low toughness due to the highly stressed and hence brittle nature of the microstructure. It is well known that reducing the strength of a martensitic steel increases the toughness thereby making the alloy more suitable for engineering applications. Traditionally medium and high carbon steel are quenched into oil then tempered at various temperatures to allow the removal of internal strains and coalescence of carbides. This procedure gives satisfactory results, but requires complicated heat treatments. Also due to the rise in scrap recycling and the concomitant rise of tramp elements, problems with temper embrittlement are becoming more prevalent. The strength of the martensite structure arises mainly from the carbon content due to the distortion effects on the b.c.t structure. By reducing the carbon content to an optimum amount, and incorporating other elements for hardenability adequate strength and reasonable toughness are obtainable.

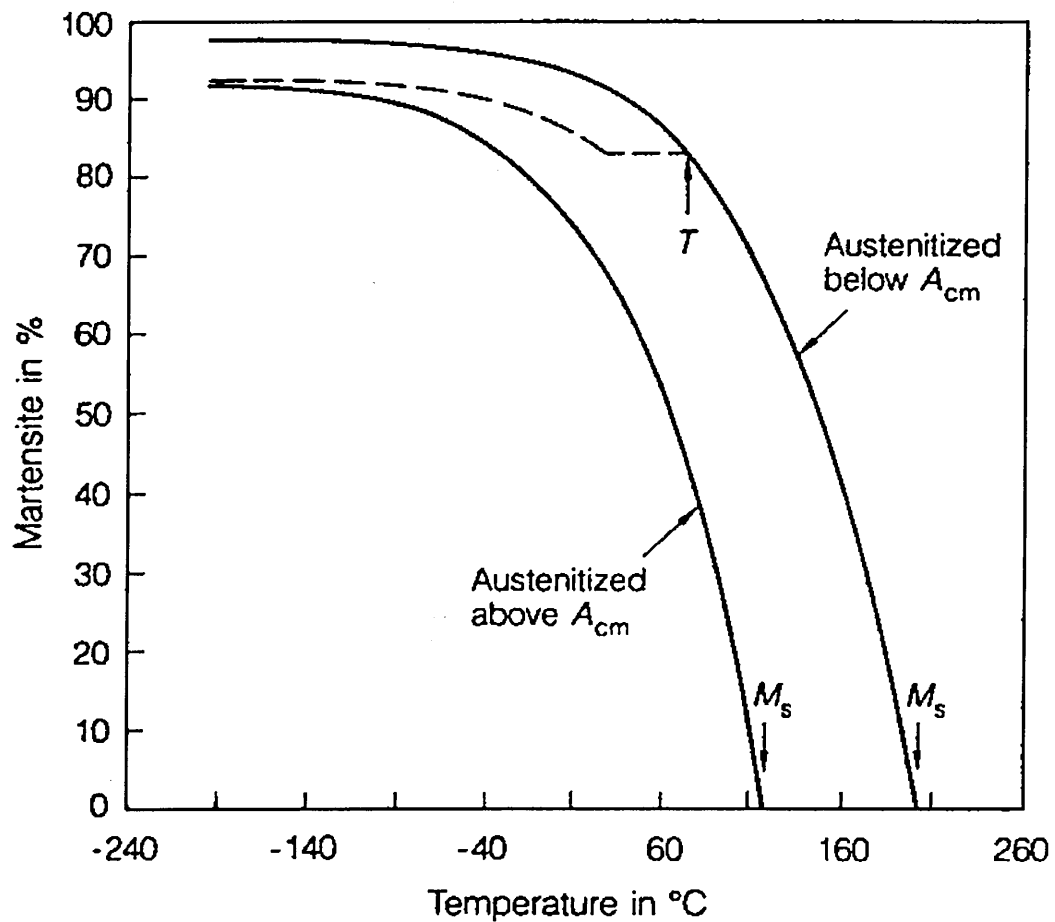
It has been shown that the carbon content of the alloy system is directly related to the martensite start temperature. This in turn affects the degree of auto tempering, which is facilitated when the martensite start temperature is sufficiently high. Therefore during the quench, as martensite forms, a significant removal of internal stress occurs by the annihilation of dislocations and the removal of some solid solution carbon in the form of carbides.

4.1.5 Retained austenite formation

Sections 2.3.1.1 detailed the effect of carbon / alloy content on the martensite start and finish temperatures. At critical carbon / alloy additions, excessive suppression of the M_s and M_f temperatures ensue, promoting the retention of unacceptable quantities of retained austenite on cooling to ambient temperature (Rayson¹²).

A similar effect is observed when raising the austenitising temperature, because the austenite is enriched in carbon and other alloying elements enhanced by carbide solution. Figure 24 illustrates this for a 1 wt.% carbon steel austenitised above and below A_{cm} (Rayson¹²).

Figure 24:- The effect of cooling below the M_s temperature on the amount of martensite formed as a function of the temperature during quenching for a hypereutectoid steel austenitised either below or above the A_{cm} . The broken line indicated the cessation of martensite formation over a restricted temperature range which is brought about by the stabilisation of the austenite caused by interrupting the cooling at temperature T in the 1 wt.% C steel (Rayson¹²).



Retained austenite is undesirable in a martensitic structure because it will transform to martensite if cold worked, tempered or aged even at room temperature (Rayson¹²). Such a transformation is accompanied by dimensional changes, brittleness and cracking. The only advantage of retained austenite is that it may improve fracture toughness (Gerberich et al.¹²⁶)

4.2 Hardenability assessment

4.2.1 Definition and test methods

Hardenability can be described as the capacity of a steel to transform from austenite to some given percentage of martensite under certain cooling conditions (Honeycombe⁹). The hardenability of an alloy system can be assessed using several standard test procedures, with the most widely used being the Jominy end quench method. This involves austenitising round bar which is then end quenched by a jet of water. After cooling opposite sides along the length of the specimen are ground and polished, then hardness measurements are made at increasing distances from the quenched end. When the cooling rate of a production component is known by experiment or calculation, the hardness of it can be estimated from that of the corresponding Jominy position. Various predictions of the parameters derived from Jominy curves have been made from the chemical composition of the steel, for example, the initial hardness at the quenched end (IH) can be estimated from the relationship between the maximum attainable martensitic hardness and the carbon content. (Burns et al.¹²⁷, Hodge and Orehoski¹²⁸, Nehrenberg et al.¹²⁹, Boyd and Field¹³⁰).

4.2.2 The ideal critical / critical diameter (D_i / D_c)

Grossman et al.¹³¹ established the concept of a critical diameter (D_c) and an ideal critical diameter (D_i) to allow the estimation of the hardenability of a steel given its chemical composition. The critical diameter (D_c) is defined as the diameter of a bar, the centre of which produces 50% martensite upon quenching with a known quenching severity, represented by the H value.

The ideal critical diameter (D_i), which is the diameter of the bar achieving a given percentage of martensite at its centre when quenched with an infinitely severe quench, can be calculated from the chemical composition utilising a procedure developed by Grossman et al.¹³¹

This method involves the multiplication of the different hardenability effects for various alloying elements as discussed in section 4.2.3.

4.2.3 Assessment of ideal critical diameter

There is a great amount of literature (Siebert, Doane and Breen¹³²) on the effect of alloy composition on hardenability, such data is usually provided in graph format giving a multiplication factor for a corresponding element concentration. For example, if the chemical composition is known, respective multiplication factors are noted and D_i is found corresponding to the maximum diameter where 100% martensitic structure is formed under an infinitely severe quench. Detailed literature (Siebert, Doane and Breen¹³²) also exists on the effects of hardenability from the interaction of elements with one another together with austenitising conditions (for example the effect of grain sizes from over heating). The effect of carbon content and grain size (figure 25) on the multiplication factor is based on the data of Kramer et al¹³³, who also presented data for the effect of manganese (figure 26).

Also included in figure 26 are comparisons with data from Crafts and Lamont¹³⁴. From this data it was evident that manganese contributes markedly to hardenability, especially in amounts greater than 0.8 mass %.

It was also recognised that a certain degree of alloy interaction also existed since addition of manganese increased hardenability to a greater or lesser extent in multi-alloy steels than in plain carbon steel.

The hardenability factors for silicon, nickel and chromium are given in a number of papers reviewed by Grossman¹³¹ Figures 27, 28 and 29 show typical multiplication factors.

Grossman also pointed out that in the case of strong carbide forming elements, two factors contribute to the variability in hardenability. One is the alloy interaction effect; the other is the degree of carbon in solution.

Figure 25 illustrating the effect of carbon content and grain size on multiplication factors

(Kramer et al.¹³³)

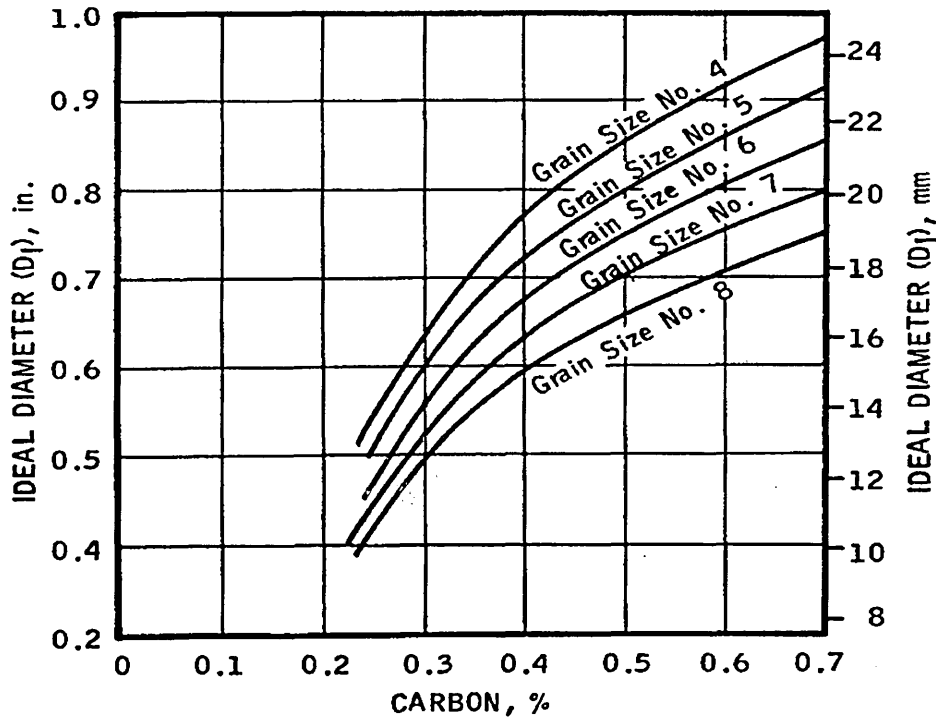


Figure 26 Illustrating the Multiplication factor for manganese

Kramer et al.¹³³ Crafts and Lamont¹³⁴

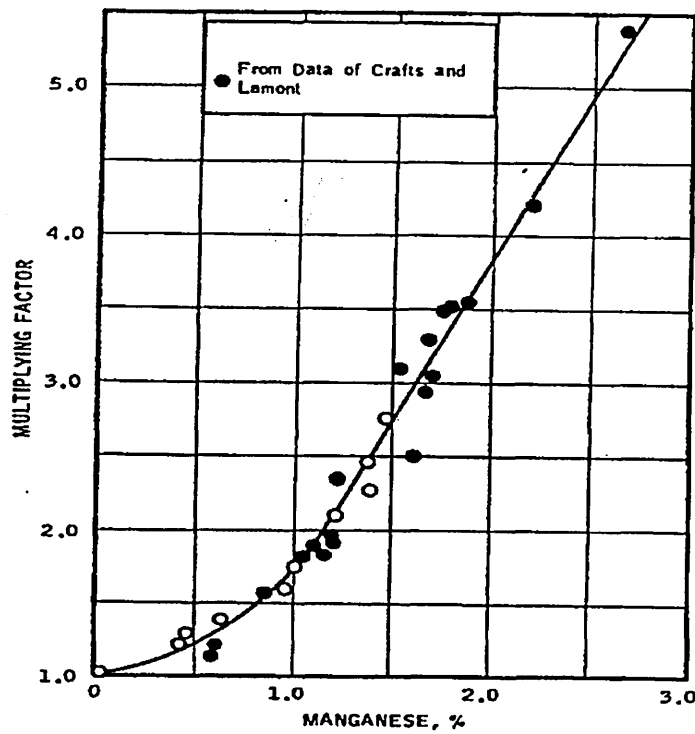


Figure 27:- Multiplication factors for silicon to assess hardenability
 (reviewed by Grossmann¹³¹)

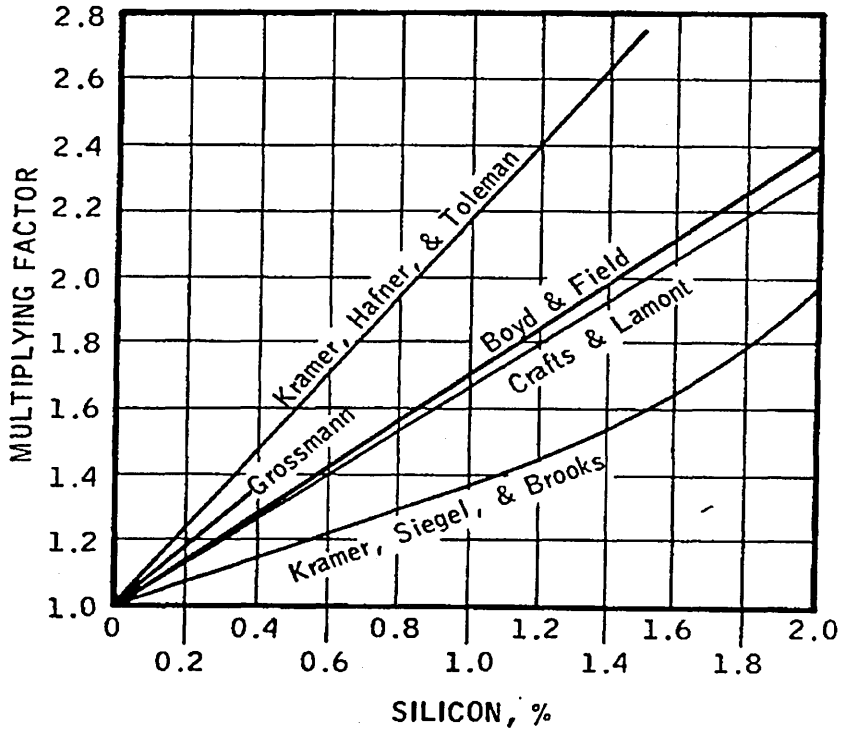


Figure 28:- Effect of nickel on hardenability multiplication factor
 (reviewed by Grossman¹³¹)

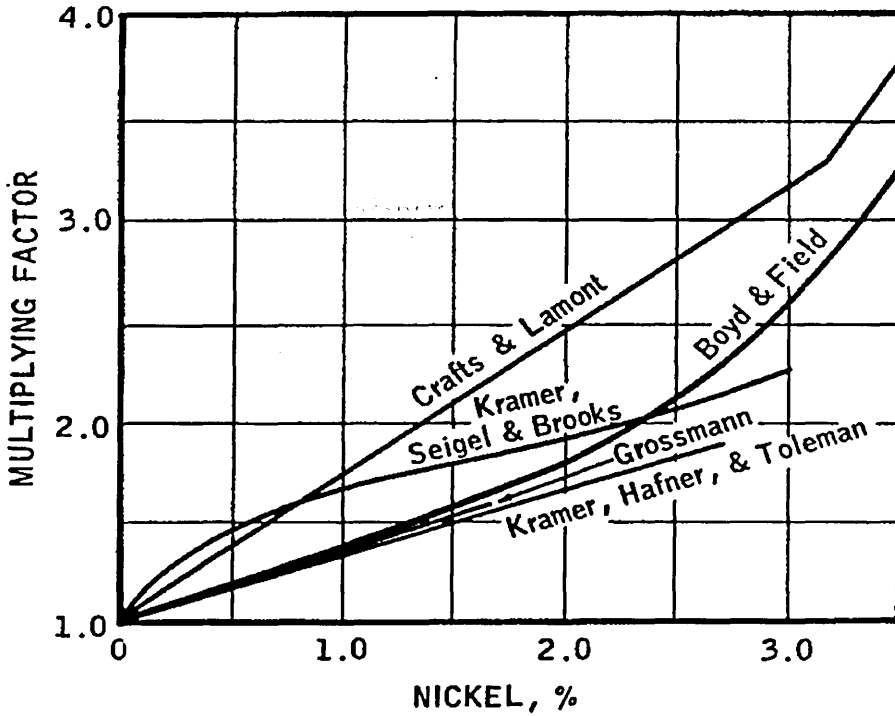
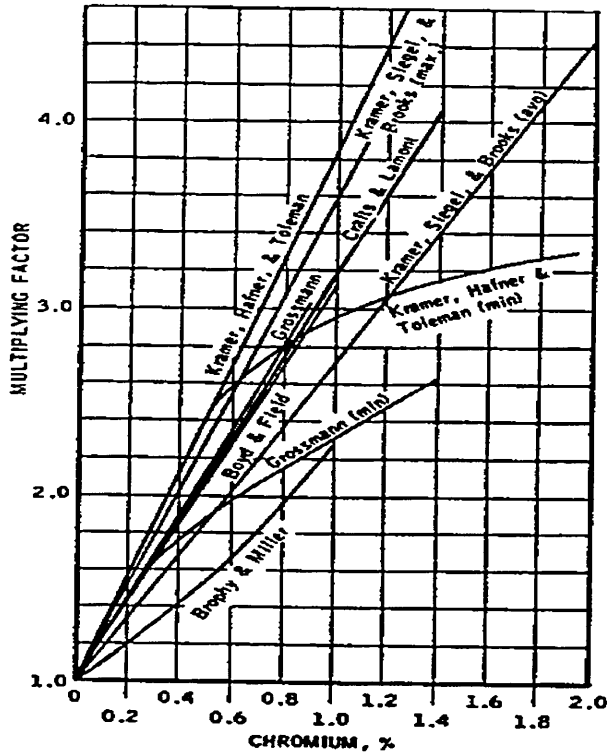


Figure 29:- Multiplication factors for calculating the effect of chromium on hardenability
(Grossman¹³¹)



4.2.4 Boron and Hardenability

In the 1930's boron treated steels were recognised for their unusual hardenability, with very small amounts required for powerful effects on hardenability. The early work of Grange and Garvey¹³⁵, defined the boron hardenability effect in terms of amount added, indicating that an addition of 0.0025 mass % boron or less will provide the maximum effect. This was confirmed by Crafts and Lamont¹³⁴ and many other authors. Kapadia et al¹³⁶., Lewellyn and Cook¹³⁷ and Melloy et al.¹³⁸, relating hardenability to an "effective" boron content, (β), deduced from the interaction of titanium and zirconium which was added with boron to control the nitrogen in steel. They found that the hardenability effect reached a maximum at about 0.001 mass% β in a steel containing 0.17 mass% carbon, 0.87 mass% manganese, 0.55 mass% chromium, 0.88 mass% nickel and 0.5 mass% molybdenum. Lewellyn and Cook¹³⁷ also found a maximum hardenability effect when the soluble boron was at or below 0.001 mass%.

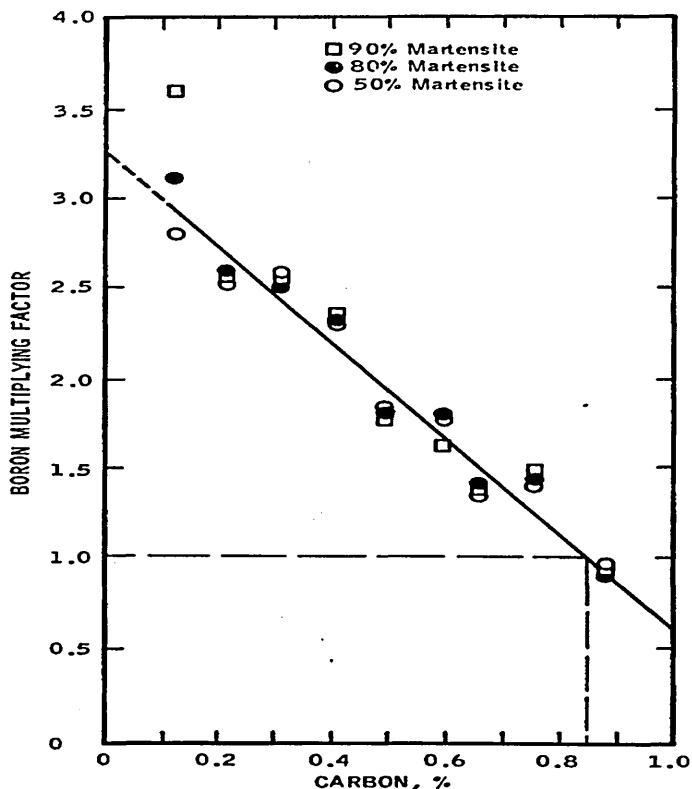
One further consideration is the influence of carbon on the effectiveness of boron, since it is well known that boron is most effective in low carbon steels and becomes less effective as the carbon content of the steel increases. Lewellyn and Cook¹³⁷ presented their data on the effect of boron in carbon steels containing 0.8 mass% manganese in terms of the boron multiplication factor, figure 30. They point out that the boron effect on hardenability reaches zero at the eutectoid carbon content, and that this carbon content is affected by alloy content. The data of Lewellyn and Cook¹³⁷ as shown in figure 30 for 0.8 mass% manganese steel can be expressed as the equation:-

$$\text{Boron multiplication factor} = 1 + 2.7 (0.85 - \%C) \quad (4.3)$$

A similar equation was developed by Breen and Walter¹³⁹

$$\text{Boron multiplication factor} = 1 + 1.76 (0.74 - \%C) \quad (4.4)$$

Figure 30 :- Multiplication factors for calculating the effect of carbon on boron multiplication factor in 0.8% Mn steels (Lewellyn and Cook¹³⁷).



4.3 Crystallography of martensite

Following the martensite transformation, certain crystallographic planes and directions in the austenite are parallel to specific planes and directions in the martensite. Two well known orientation relationships have been established in steels (Christian¹¹⁷). One determined by Kurdjumov and Sachs⁷⁶, is :

$$\{111\}_{\gamma} \parallel \{101\}_{\alpha} \quad \text{and} \quad \langle 110 \rangle_{\gamma} \parallel \langle 111 \rangle_{\alpha}$$

The other relationship determined by Greninger and Troiano¹¹⁸ and also by Nishiyama⁷⁷ is :-

$$\{111\}_{\gamma} \parallel \{011\}_{\alpha} \quad \text{and} \quad \langle 112 \rangle_{\gamma} \parallel \langle 011 \rangle_{\alpha}$$

4.4 Crystallography of carbides in martensite

The thermal history and chemistry of the martensitic alloy will obviously influence the amount and type of carbide present. For example, during water quenching of a low carbon "autotempered" martensite, the steel is not at a high temperature long enough to permit the long range diffusion of substitutional atoms, so that only ϵ -carbide, η -carbide or cementite precipitate (Bhadeshia⁴⁴). The other carbides which do require long range diffusion, allowed during a tempering or isothermal holding treatment are given in table 3, section 3.5 The orientation relationships between cementite, epsilon, eta and chi carbide are also discussed in section 3.5.1 to 3.5.4.

4.5 Strengthening of martensite

The strengthening mechanisms which occur in the martensite structure are broadly based on dislocation interactions with carbon in its various forms, for example :-

- Carbon and nitrogen in solid solution.
- Fine lath or plate size:- boundaries
- Restriction of dislocation movement by twin boundaries in high carbon lenticular martensite
- The precipitation of carbides, especially in tempered and auto tempered structures and clustering of carbon atoms.
- The high dislocation density in low carbon lath martensite.

It is not valid to consider these strengthening mechanisms singularly, since many of these features interact or are mutually influenced by each other (Pickering²³). These various mechanisms may also not be simply additive (Leslie¹⁴⁰). The major strengthening mechanisms for martensite structure are therefore due to solid solution carbon dislocations and packet / grain boundaries.

It is thought that prior austenite grain size affects the proof strength (Grange¹⁴¹, Porter and Dabrowski,¹⁴² Swarr and Krauss¹⁴³) as this influences the martensite packet size. However, Brownrigg¹⁴⁴ 1973, has demonstrated that strength is independent of austenite grain size in low carbon martensite. This therefore indicated that either packet size was insensitive to prior austenite grain size or that the packet boundary does not contribute to strength in low carbon martensite.

The strong influence of packet size on yield strength has also been attributed to carbon segregation at the packet boundaries but tempering reduces the dependency of proof strength on the packet size due to the formation of carbides (Swarr and Krauss¹⁴³).

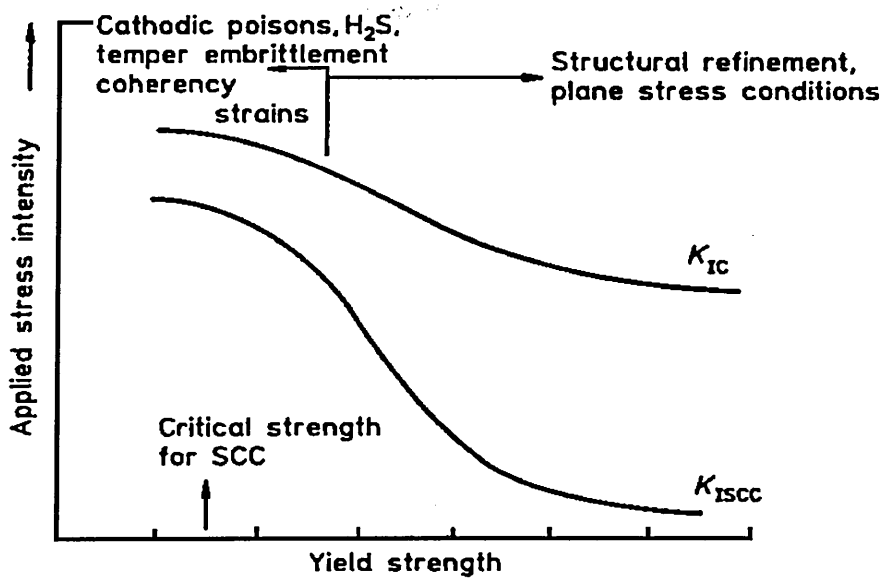
In section 4.6 reasons are given as to why it is necessary to keep the carbon level to an optimum amount, since although carbon provides strength, problems arise with for example, quench cracking, stress corrosion and retention of austenite in the untempered condition. Additional strengthening mechanisms, for example the restriction of dislocation movement are worthy of consideration for alloy applications where carbon levels have to be kept to a minimum. The restriction of dislocation movement can be achieved by cold working the alloy which causes interaction of moving dislocations in a slip plane with other sessile dislocations. The end result is an entanglement of dislocations which act as barriers to subsequent dislocation movement, hence extra force is required to continue deformation. Also if the carbon content in the alloy system is kept to a level to facilitate adequate auto tempering, precipitates formed on slip planes will also act as barriers to moving dislocations, hence dislocations will pile up at precipitates and become immobile. On increasing the carbon content less auto tempering takes place and strengthening mechanisms such as clustering of carbon atoms, dislocation atmospheres, solid solution strengthening and twin boundaries become important considerations.

4.6 Optimising mechanical properties

4.6.1 Strength and stress corrosion cracking

The strength of a martensite alloy is intimately related to the carbon content, increasing the carbon level gives rise to a significant increase in the ultimate tensile strength and hardness but decreases the toughness. The strength has a dominant effect in determining the susceptibility of an alloy to stress corrosion cracking, where the classical approach for reducing stress corrosion cracking problems is to lower the strength level, by tempering for example. The relationship between the yield strength and the stress intensity factor for fracture (K_{Ic}) and stress corrosion cracking (K_{Isc}) is shown in figure 31 (Naylor and Cook¹¹⁹).

Figure 31 Yield strength versus stress intensity factor illustrating that if the stress intensity factor is greater than K_{IC} and K_{ISCC} hence failure will occur (Naylor and Cook¹¹⁹).



4.6.2 Quench cracking

Hardenable alloy steels containing more than 0.25 mass% carbon may suffer from quench cracking due to the martensite transformation. Kunitake and Sugisawa¹⁴⁵ proposed the following carbon equivalent (C_{eq}) to estimate the quench cracking of steels.

$$C_{eq} = (\text{wt.\% C}) + (\text{wt.\% Mn} / 5) + (\text{wt.\% Mo} / 5) + (\text{wt.\% Cr} / 10) + (\text{wt.\% Ni} / 50) \quad (4.5)$$

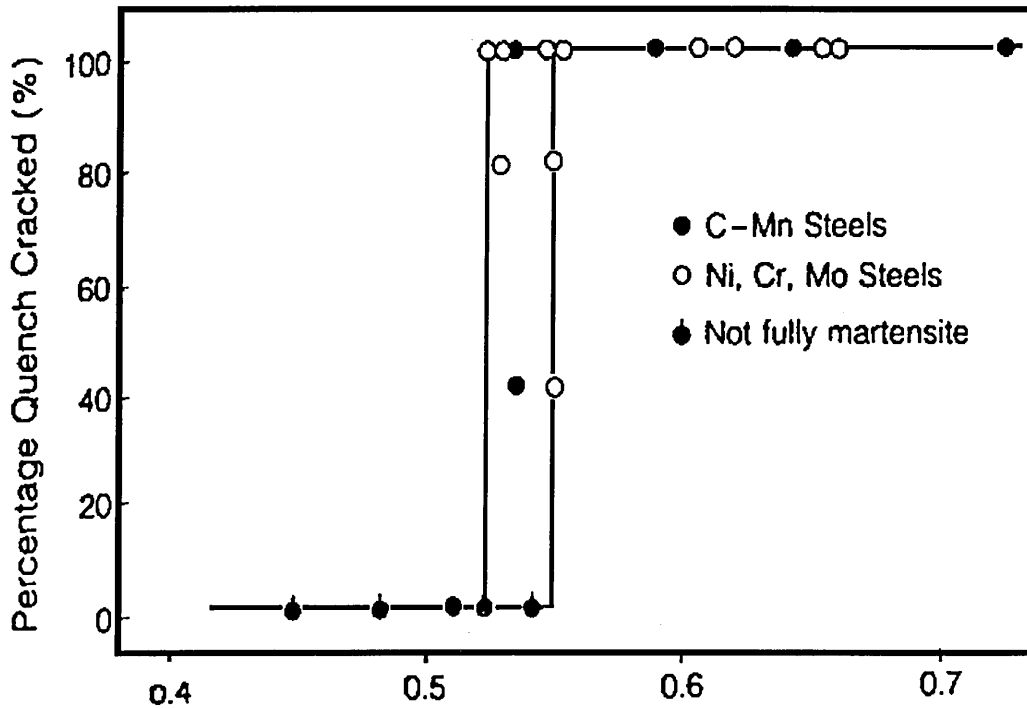
Hence for a 0.3 mass % carbon boron steel:-

$$C_{eq} = 0.30 + (1.02 / 5) + (0.24 / 10) = 0.528 \quad (4.6)$$

The higher the carbon equivalent value the more sensitive is the steel to quench cracking as shown in figure 32. Steels comprising of coarse austenite grains with low M_s temperatures are particularly susceptible to quench cracking. On increasing the carbon content to 0.35 mass% the carbon equivalent would increase to 0.578, figure 32 indicates that this steel would be extremely susceptible to quench cracking.

However since boron reduces the susceptibility of quench cracking it is possible that the 0.35 mass % carbon steel would not quench crack.

Figure 32 : Quench cracking versus carbon equivalent (Ohanti²¹⁴).

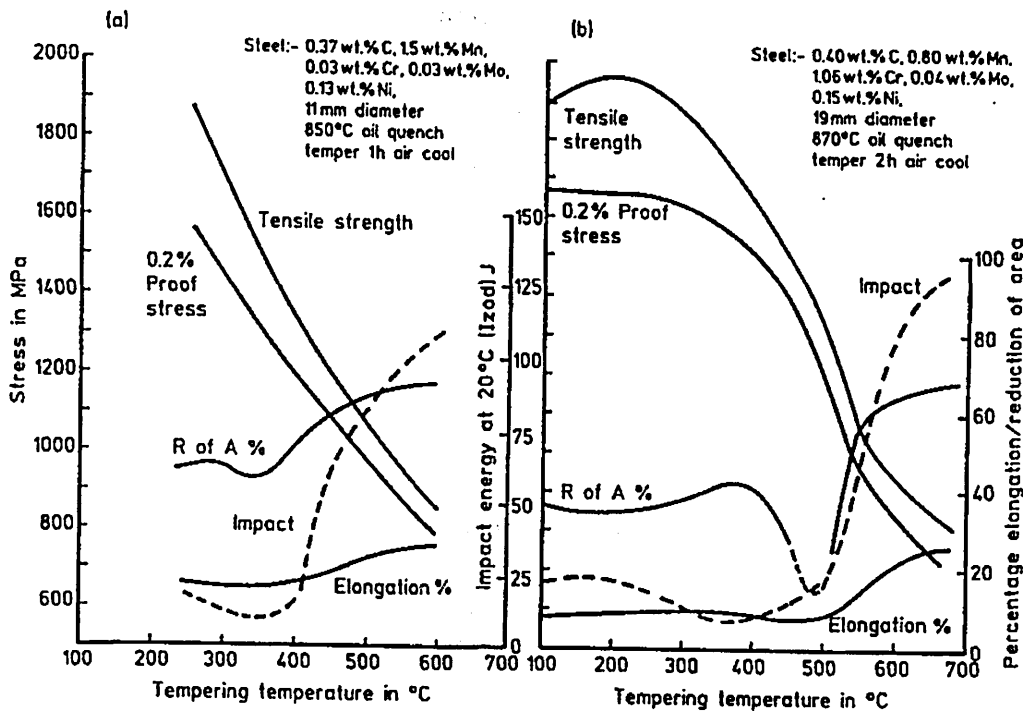


$$C_{eq.} = C + \frac{Mn}{5} + \frac{Mo}{5} + \frac{Cr}{10} + \frac{Ni}{50}$$

4.7 Tempering of martensite

Tempering is a heat treatment in which steels are heated to a temperature below the A_{c1} , to increase their ductility and toughness and to adjust the strength to the desired level, by removing carbon from solid solution in the form of carbides, and reducing the dislocation density. Typical effects of tempering on a low alloy steel are shown in figure 33 (Naylor and Cook¹¹⁹).

Figure 33:- Effect of tempering on the mechanical properties of a martensitic Ni-Cr-Mo steel (Naylor and Cook¹¹⁹).



4.7.1 Stages of tempering

The tempering of martensite has been summarised by Bhadeshia⁴⁴:-

- 1) Redistribution of carbon atoms at approximately 100°C (Speich⁶⁵, Kusunoki and Nagakura¹⁴⁶).
- 2) The precipitation of carbides at 100 t 300°C. In addition to ϵ -carbide (Hoffman¹⁴⁷, Ohmori⁹⁴) or η -carbide (Jack⁸⁴, Glenin and Flinn¹⁴⁸, Hirotsu and Nakazawa¹⁴⁹, Williamson et. al.¹⁵⁰) Cementite and cementite containing interpenetrating layers of χ -carbide are reported in high carbon steels (Jack⁸⁴, Hirotsu and Nakazawa¹⁴⁹).
- 3) The decomposition of retained austenite in medium carbon steels and high carbon unalloyed steels at 200°C.
- 4) The growth and spheroidisation of cementite, accompanied by the recovery and recrystallisation of the matrix and a decrease in strength above 300°C

5) Secondary hardening at 500°C to 650°C, due to the precipitation of alloy carbides causing an increase in strength which compensates for the strength decrease which normally accompanies the tempering process.

4.7.2 Temper embrittlement

Two types of temper embrittlement have been defined by several authors (Hollomon¹⁵¹, Woodfine¹⁵², Low¹⁵³, McMahon¹⁵⁴). The first type is observed in martensite tempered in the range 200°C - 400°C, and results in a loss of impact strength, toughness and ductility. This is known as temper embrittlement, tempered martensite embrittlement or 350°C embrittlement. The following characteristics are pertinent to this type of embrittlement:-

- High phosphorus and sulphur steels are susceptible to this type of embrittlement .
- Is associated with martensite but not bainite (Ohmori et al.¹⁵⁵ suggesting that carbide precipitation along grain boundaries in conjunction with the redistribution of impurities may play a dominant role in the embrittlement.
- It occurs in both low alloy and plain carbon steels.
- The embrittlement is not reversible.
- The mode of fracture is intergranular along the prior austenite grain boundaries.

The second type of embrittlement is observed when steels are heated in the temperature range 400°C to 600°C or when slow cooled through this range. This is generally known as temper embrittlement or reversible temper embrittlement, exhibiting the following features:-

- Susceptibility is greatest in martensite and smallest in ferrite-pearlite microstructures.
- The fracture is often observed to be along the prior austenite grain boundary.

- The reaction is reversible, i.e. the embrittlement can be removed if the steel is heated above 600°C.
- Steels containing P,Sb,As and Sn are highly susceptible.
- The addition of major alloying elements such as Si,Mn, Ni and Cr accelerates the embrittlement .

Chapter 5

Dislocation theory, strengthening mechanisms and stress strain modelling

5.1 Introduction: dislocations and strength

The fundamental strength of any metal is determined by the basic crystal structure which in turn characterises the type of slip system, fixes the Burgers vector and determines the lattice friction stress (Dieter¹⁵⁶). Additionally in close packed structures, the stacking fault energy determines the extent of dislocation dissociation, which influences the ease of cross slip and the subsequent strain hardening rate. The majority of commercial metal products however, consist of complex microstructure with further strengthening from grain size control, solid solution atom addition and fine dispersion of precipitates (Dieter¹⁵⁷).

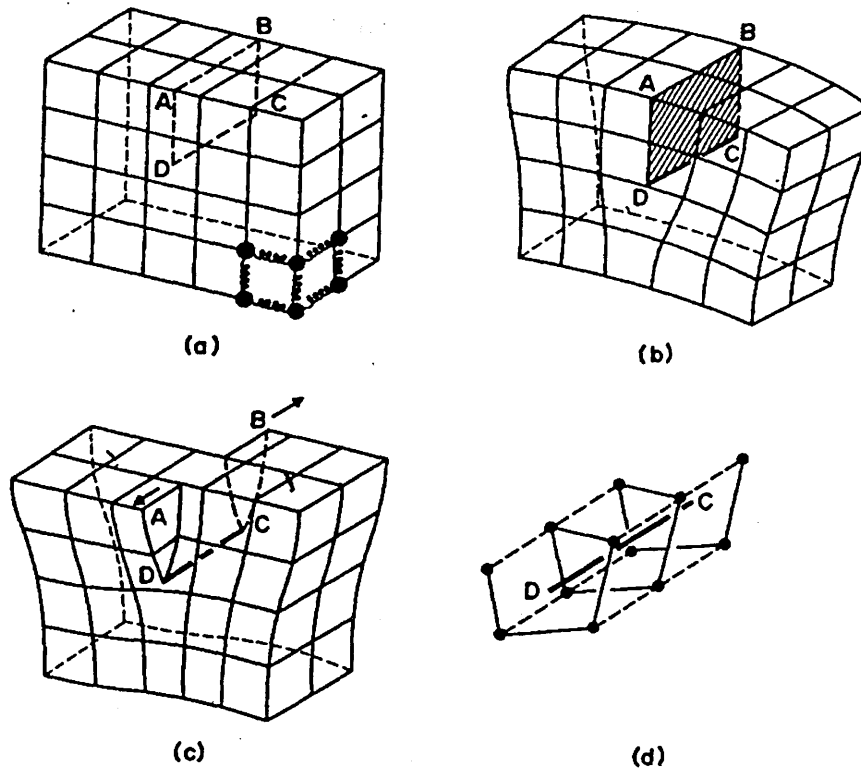
Nevertheless, whether the strengthening arises from inherent crystallographic features or is incorporated during microstructural fabrication, the fundamental objective is exactly the same, which is to impede dislocation movement. Hence the strength of a microstructure is inversely related to dislocation mobility which in turn is related to the number and nature of barriers to the glissile dislocation (Cottrell¹⁵⁸).

5.1.1 The dislocation

The existence of dislocations (essentially a line defect), was first suggested because of the vast difference between theoretical and experimental values of the applied shear stress required to plastically deform a single crystal. (Orowan¹⁵⁹, Polanyi¹⁶⁰ and Taylor¹⁶¹). There are two basic geometrical types of dislocation, namely the edge and screw.

Figure 34 represents a simple descriptive model of the atomic arrangement and bonding in a simple cubic structure.

Figure 34:- a) model of a simple cubic lattice, b) positive edge dislocation
 c) left hand screw dislocation, d) spiral of atoms adjacent to the line DC in (c)
 (Hull and Bacon¹⁶²)



5.1.2 Burgers Vector and Burgers circuit

A useful definition of a dislocation is given in terms of the Burgers circuit, which is an atom to atom path taken in a crystal containing dislocation which form a closed loop (Hull and Bacon¹⁶²). Such a path is illustrated in figure 35 (i.e. MNOPQ). When the same atom to atom sequence is made in a dislocation free crystal and the circuit does not close, then the first circuit must enclose one or more dislocations (Hull and Bacon¹⁶²). The vector required to complete the circuit is called the Burgers vector, and for an edge dislocation is normal to the line of the defect whilst in a screw dislocation runs parallel to the line of the dislocation. Figure 36 illustrates a burgers vector around a screw dislocation with the same circuit in a perfect crystal thus illustrating the Burgers vector.

Figure 35:- a) Burgers circuit around an edge dislocation and b) the same circuit in a perfect crystal with the closure failure being the Burgers vector.

(Hull and Bacon¹⁶²)

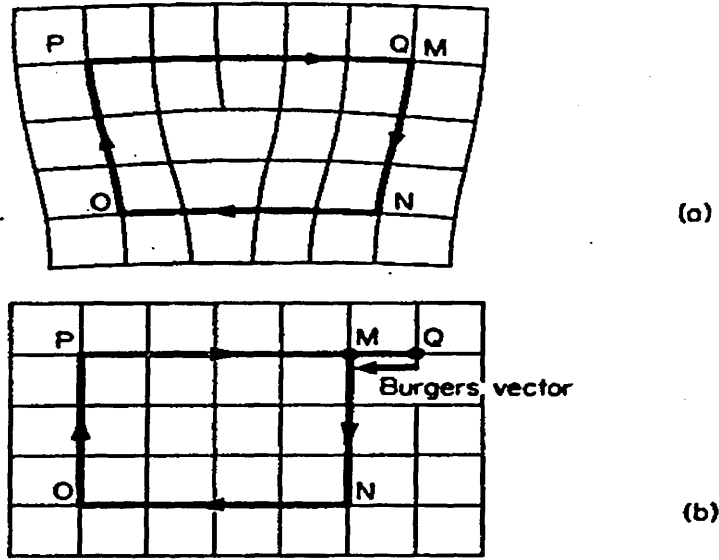
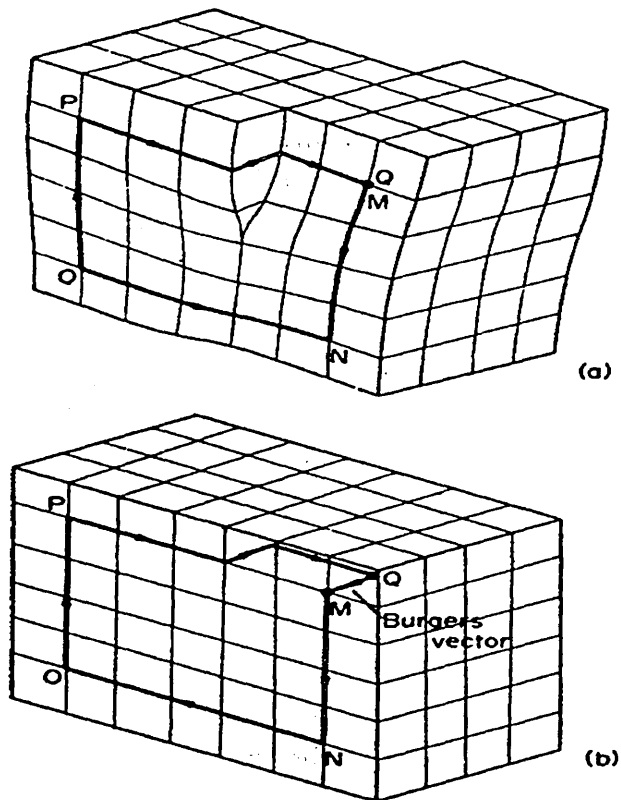


Figure 36:- a) Burgers circuit around a screw dislocation b) same circuit in a perfect crystal with the closure failure being the Burgers vector.

(Hull and Bacon¹⁶²)

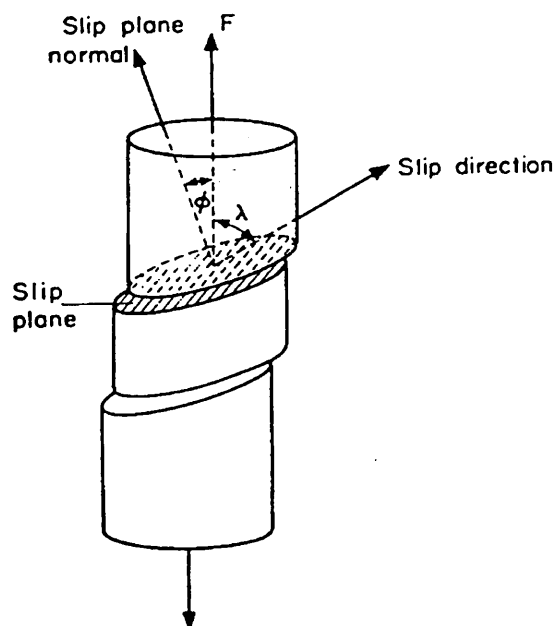


5.2 Movement of dislocations via slip

The two basic types of dislocation movement are glide (conservative motion) in which the dislocation moves to the surface which contains both its line and Burgers vector, and climb (non conservative motion) in which the dislocation moves out of the glide surface normal to the Burgers vector. (Hull and Bacon¹⁶⁴, Groves and Kelly¹⁶³). Climb is associated with high temperature edge dislocation motion where the diffusion of atoms are allowed (Hull and Bacon¹⁶⁴, Reed-Hill¹⁶⁵). Glide, in contrast takes place at low temperatures where diffusion is difficult and there is an absence of non equilibrium concentration point defects.

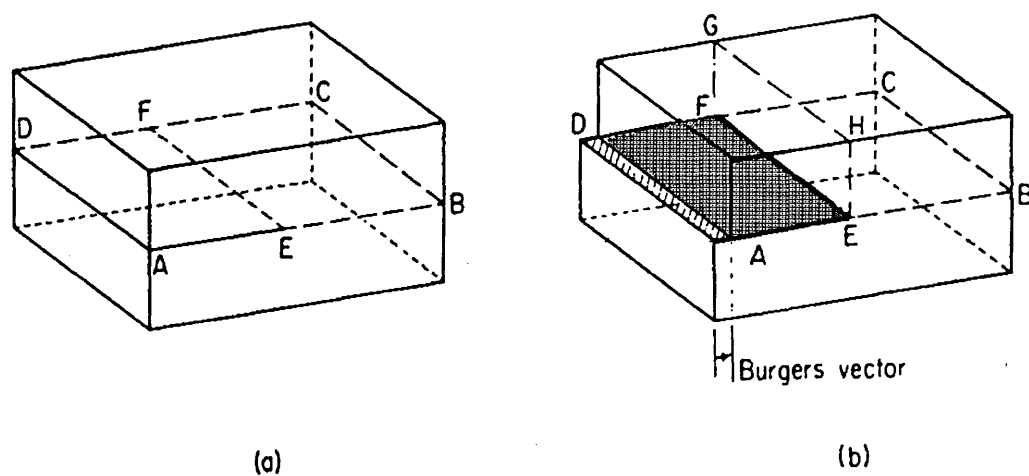
Glide of many dislocations results in slip, which is the most common phenomenon of plastic deformation in crystalline solids (Dieter¹⁵⁷). Figure 37 illustrates slip as successive displacement of one plane of atoms over another on a defined slip plane. Discrete blocks of crystal between two slip planes remain undistorted and further deformation occurs either by more movement on existing slip planes or by the formation of new slip planes (Hull and Bacon¹⁶⁴).

Figure 37:- Illustration of the geometry of slip in crystalline materials (Hull and Bacon¹⁶⁴).



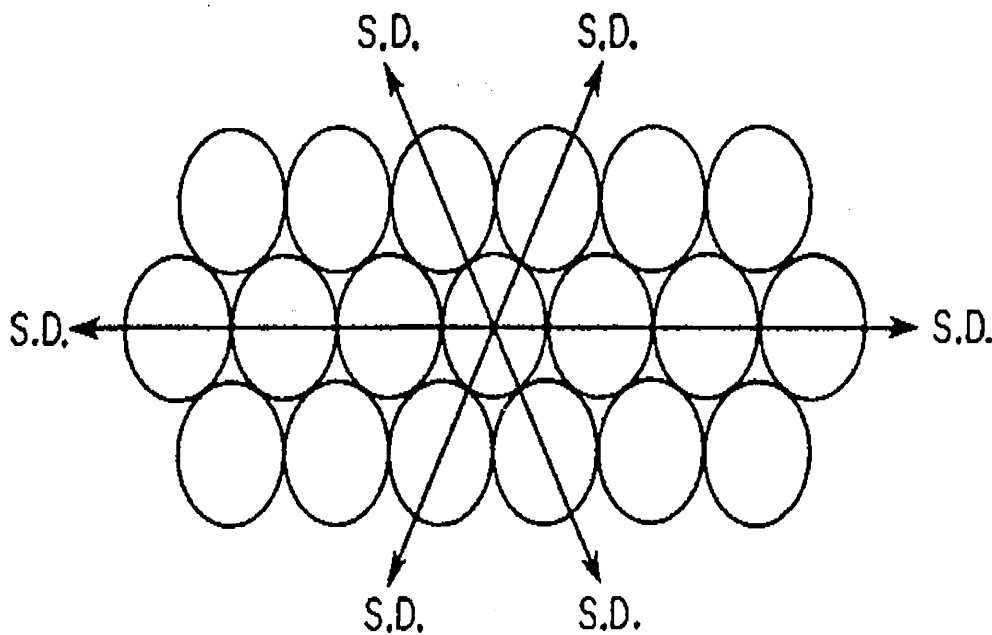
Dislocations move on specific planes (section 5.2.1), figure 38 illustrates an edge dislocation which has moved in the plane ABCD (the slip plane). This is uniquely defined as the plane which contains both the line and the Burgers vector of the dislocation (Hull and Bacon¹⁶⁴). The glide of an edge dislocation is therefore limited to a specific plane. In contrast, the glide of a screw dislocation (AA' to BB' figure 39) can be imagined to take place in the LMNO slip plane with formation of a slip step. The line of the screw dislocation and the Burgers vector, however, do not define a unique plane and the glide of the dislocation is not restricted to a specific plane (Hull and Bacon¹⁶⁴, Dieter¹⁵⁷). The process in which screw dislocations move from one crystallographic plane to another is known as cross slip and in f.c.c metals screw dislocations move on the {111} planes. In contrast because of ill defined slip planes in b.c.c metals, the screw dislocation tends to wander from one plane to another producing wavy slip lines on prepolished surfaces (Hull and Bacon¹⁶⁴).

Figure 38:- Formation of a pure edge dislocation (Hull and Bacon¹⁶⁴)



The slip direction and slip plane in crystals are denoted by direction and miller indices such as $[111]$ and (101) respectively. The combination of a slip plane and one of its close packed directions defines a possible slip mode or slip system (Abe¹⁶⁶, Hull and Bacon¹⁶⁴). For example in figure 40, if the plane of the paper is considered to define the slip plane, then there will be three slip systems associated with the indicated close packed plane, one mode corresponding to each of the three slip directions. The close packed directions in the f.c.c lattice are the $\langle 111 \rangle$ directions and run diagonally across the faces of the unit cell. There are also four octahedral planes of closest packing i.e. (111) , $(\bar{1}11)$, $(1\bar{1}1)$ and $(11\bar{1})$ each one containing three close packed directions, hence a total of 12 octahedral slip systems.

Figure 40:- The three slip directions in a plane of closest packing. (Reed-Hill¹⁶⁵)

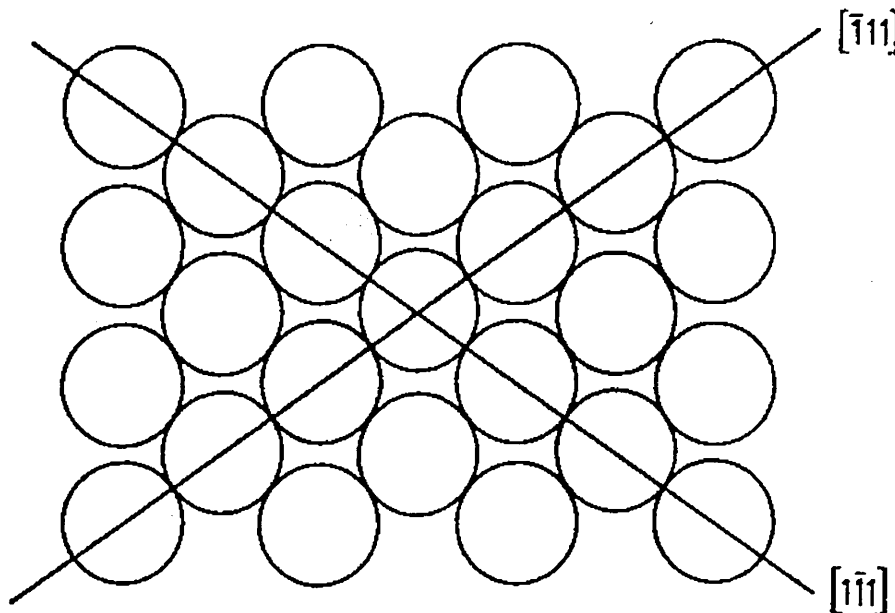


Hence the important slip systems in a face centred cubic structure are those associated with slip on the octahedral plane, with the critical resolved shear stress much lower than for other forms. Also since there are twelve slips systems uniformly distributed in space, it is almost impossible to strain a f.c.c lattice and not have at least one $\{111\}$ plane in a favourable position for slip.

The b.c.c crystal is characterised by four close packed directions, $[111]$, but lacks a truly close packed plane such as the octahedral plane of the f.c.c lattice or the basal plane of the hexagonal lattice. Figure 41 models the b.c.c (110) configuration, (closest packed plane). The slip phenomena observed within body centred cubic crystals corresponds to that expected in crystals with close packed directions and no truly close packed planes (Reed-Hill¹⁶⁵).

The slip direction in the b.c.c crystal is the close packed direction $\langle 111 \rangle$, the slip plane however, is not well defined. Body centred cubic slip lines are wavy and irregular, often making the identification of a slip plane difficult (Reed-Hill¹⁶⁵).

Figure 41:- The (110) plane of the body centred cubic lattice (Reed-Hill¹⁶⁵).



The {110}, {112} and {123} planes have all been identified as slip planes in b.c.c crystals, additionally work on iron single crystals has indicated that any plane that contains a close packed $\langle 111 \rangle$ direction can act as a slip plane (Reed-Hill¹⁶⁵). This lack of true close packed plane explains why the critical resolved shear stress for slip in b.c.c metals is particularly high.

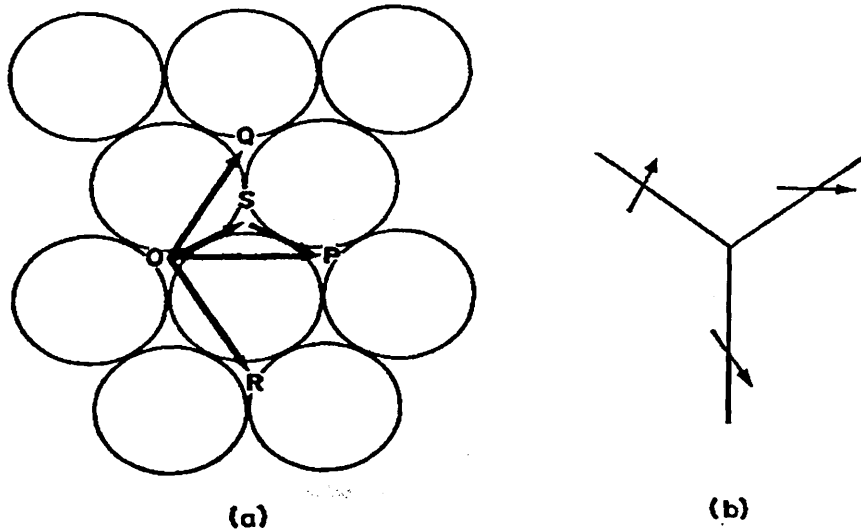
5.2.2 Perfect dislocation in the fcc lattice

The shortest lattice vectors and therefore the most likely Burgers vectors for dislocations in the face centred cubic structure are of the type $\frac{1}{2}\langle 110 \rangle$ and $\langle 001 \rangle$. The latter dislocation is much less favoured energetically and in fact has not been observed (Hull and Bacon¹⁶⁷). This is because the energy of a dislocation is proportional to the square of the magnitude of its Burgers vector hence the energy of $\frac{1}{2}\langle 110 \rangle$ dislocation is half that of $\langle 001 \rangle$ and therefore more likely to occur. Also since $\frac{1}{2}\langle 110 \rangle$ is a translation vector for the face centred cubic lattice, glide of a dislocation with this Burgers vector leaves behind a perfect crystal hence the dislocation is known as a perfect dislocation.

5.2.3 Shockley partial dislocation in the fcc lattice

The motion of a dislocation whose Burgers vector is not equivalent to the lattice vector will leave behind an imperfect crystal containing a stacking fault. where the stacking fault ends inside a crystal, the boundary in the plane of the fault separating the faulted region from the perfect region of the crystal is known as a partial dislocation (Hull and Bacon¹⁶⁷, Reed-Hill¹⁶⁵). Two of the important partial dislocations recognised in face centred cubic crystals are the Shockley partial, which is associated with slip and the Frank partial (Cottrell¹⁵⁸). The partial dislocations associated with slip are of the Shockley configuration which readily forms during movement of layers of atoms on the {111} slip plane via the energetically favoured "zig zag" motion as illustrated in figure 42.

Figure 42:- Slip of {111} planes in face centred cubic crystals Cottrell¹⁵⁸

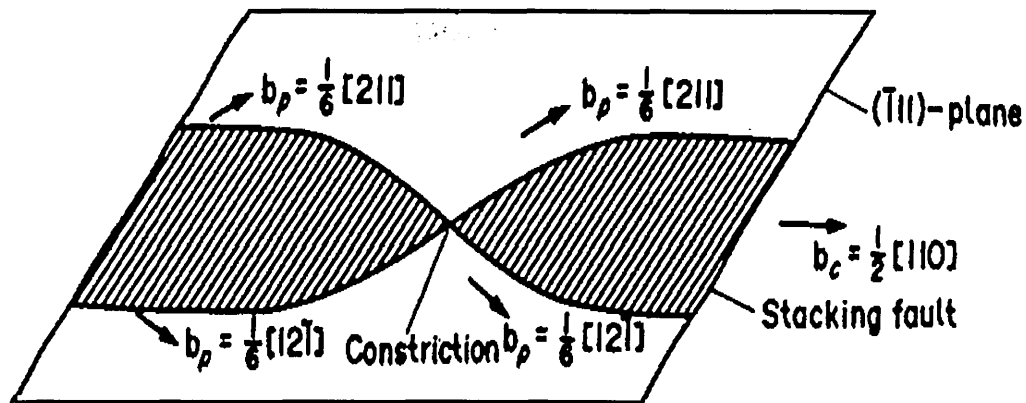


Hence the perfect dislocation with Burgers vector b_1 splits up or dissociates into two partials b_2 and b_3 . The dissociation of this total dislocation into a pair of separated partials is known as an extended dislocation. (Cottrell¹⁵⁸).

Since b_2 and b_3 are the burgers vector of the Shockley partial dislocations, it follows that if they separate there will be a discontinuity in the stacking sequence, (stacking fault) between them. This region therefore has an increased energy known as the stacking fault energy (SFE) which attempts to bring the partial dislocations back together again. An equilibrium separation is established when the repulsive and attractive forces balance, with the width of this separation depending upon the stacking fault energy (Cottrell¹⁵⁸). The stacking fault energy, hence the separation between the two partial dislocations is important when considering plastic deformation and work hardening characteristics of f.c.c metals. This is because before cross slip of a screw dislocation can take place the extended dislocation must first constrict, and only then is the unit dislocation at the point of constriction, able to move onto other planes as illustrated in figure 43 (Seeger¹⁶⁸).

A certain amount of energy is associated with the formation of the constriction and it will form more readily in metals with high stacking fault energy (smaller separation between partial dislocations).

Figure 43:- Constriction in an extended dislocation. The drawing corresponds to a screw dislocation in a f.c.c lattice (Seeger¹⁶⁸).



Hence metals with high stacking fault energy (aluminium for example) are expected to work harden less rapidly because partial dislocations readily constrict thus allowing cross slip to take place. In contrast, slip in low stacking fault metal is restricted to the $\{111\}$ plane with no allowance for constriction hence no cross slip resulting in significant differences in the deformation behaviour (Hull and Bacon¹⁶⁷).

5.2.4 Dislocations in the b.c.c lattice

As discussed previously, slip occurs in the close packed $\langle 111 \rangle$ directions, with the shortest lattice vector, i.e. the Burgers vector of the perfect slip dislocation, is of the type $\frac{1}{2} \langle 111 \rangle$ (Hull and Bacon¹⁶⁴). The crystallographic slip planes are also given as $\{110\}$, $\{123\}$ and $\{112\}$, thus if cross slip is easy, it is possible for screw dislocations to move in a random way onto different closest packed planes. It has also been found that the apparent slip plane varies with composition, temperature and strain rate. For example when pure iron is deformed at room temperature the slip plane appears to be close to the maximum resolved shear stress irrespective of crystal orientation.

However, when iron is deformed at low temperatures or if it is alloyed with silicon, slip appears to be restricted to a specific $\{110\}$ plane (Hull and Bacon¹⁶⁹). Stacking faults have not been observed in bcc metals, and since cross slip is generally allowed with some degree of ease, this must suggest that faults are at best of exceptionally high energy (Hull and Bacon¹⁶⁹).

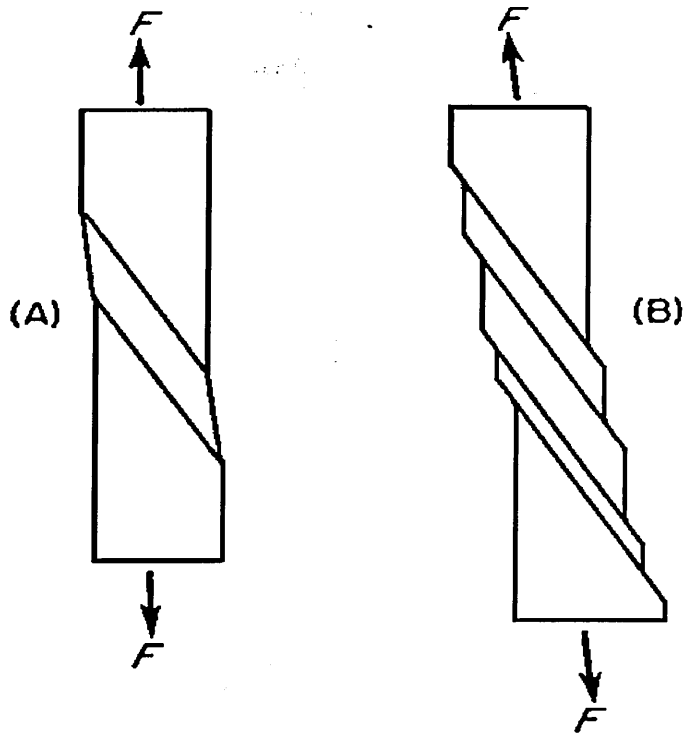
5.3 Movement of dislocations via twinning

The second important mechanism by which metals deform is the process known as twinning and is common in h.c.p metals where the possible slip systems are severely limited to the unique basal system(Dieter¹⁵⁷, Hertzberg¹⁷⁰). Deformation twinning is also observed in b.c.c metals under conditions of rapid rate of loading (shock loading) or decreased temperatures (Dieter¹⁵⁷).

The major difference between twinning and slip arises from the scale at which the lattice is sheared (Reed-Hill¹⁷¹) and is illustrated in figure 44. In slip, it has been noted that deformation occurs on individual lattice planes, also the shear on a single slip plane may be many times larger than the lattice spacing and depends upon the number of dislocations emitted by the dislocation source. In contrast the shear associated with deformation twinning is uniformly distributed over a volume rather than focused on a discrete number of slip planes. Additionally atoms move only a fraction of interatomic spacing relative to each other (Reed-Hill¹⁷¹) . The total shear deformation due to twinning is also small, so that slip is a much more important primary mode of plastic deformation.

The twinned part of the crystal is a mirror image of the parent crystal with the plane of symmetry between the two portions known as the twinning plane. Crystallography is identical in all of the body centred cubic transition metals occurring on $\{112\}$ $\langle 111 \rangle$ systems and is explained in terms of surface energy associated with the interface between twins and the parent crystal (Reed-Hill¹⁷¹).

Figure 44:- The difference between the shears associated with (a) twinning and (b) slip (Reed Hill¹⁷¹)



5.4 Nucleation of twins during deformation

Twins form as a result of the shear stress component of an applied stress which is parallel to the twinning plane and lies in the twinning direction. While twinning usually requires a higher shear stress to initiate than it does for slip, these stresses are well below the theoretical strength suggesting that twins nucleate heterogeneously as a result of dislocation interactions (Dieter¹⁵⁷). Literature suggests that the nucleation centres for twinning are positions of highly localised strain in the lattice and this is confirmed by the fact that twins appear to form in metals that have previously suffered deformation by slip (Bell and Cahn¹⁷²). Additionally it is thought that the slip process becomes impeded by barriers (grain boundaries, sessile dislocations, precipitates etc.) preventing the motion of dislocations.

Hence as a dislocation tries to move under an applied stress, dislocation pile up ensues and since a stress field exists around each dislocation, an intensification of stress in the pile up region is formed (Reed-Hill¹⁷¹).

It has been proposed that the stress associated with local concentrations of dislocations can lower the magnitude of the external stress needed to nucleate the deformation twins. It is recognised that these localised stress fields (of twin nucleation centres) can be formed in various ways, therefore it is probable that there can be no universal critical resolved shear stress for twinning as there is for slip and explains the observed wide range of shear stresses required (Reed-Hill¹⁷¹). The morphology of the twin suggests that the boundary with the parent lattice is not strictly coherent, since they appear as small lens shaped structures. Hence it is generally accepted that a dislocation array is necessary in order to adjust the mismatch between lattices of parent and twin and represents a surface of considerably higher energy than a corresponding coherent boundary (Reed-Hill¹⁷¹).

5.5 Strain (work) hardening

One of the most important characteristics of the plastic deformation of metals is the fact that the shear stress required to produce slip continuously increases with increasing shear strain (Dieter¹⁵⁷). The increase in the stress required to cause slip because of previous plastic deformation is known as work or strain hardening. The strain hardening of a metal occurs as a result of dislocation interaction with a) specific microstructural barriers (e.g. precipitates, solid solution atoms, grain boundaries) and b) other dislocations (Dieter¹⁵⁷).

One of the first dislocation models to explain strain hardening was based on the belief that dislocations pile up on slip planes at specific barriers producing a back stress which opposes the applied stress on the slip plane.

This leads to a high concentration of stress on the leading dislocation in the pile up which could initiate either yielding on the other side of the barrier or under certain conditions initiate twinning. The number of dislocations which can be supported by an obstacle depends upon the type of barrier, the orientation relationship between the slip plane and the structural features of the barrier, the material and the temperature. (Dieter¹⁵⁷).

Breakdown of a barrier can occur by slip on a new plane, by climb of dislocations around the barrier, or by generation of high enough tensile stresses to produce a crack.

In the early stages of deformation dislocation movement tends to be confined to a single set of parallel slip planes. However, as deformation proceeds, slip occurs on other slip systems and dislocations moving on other systems intersect and react. This process encourages formation of sessile dislocations, dislocation forests and jogs which either lock glissile dislocations or in the case of jog formation, encourage multiplication of further dislocations (Dieter¹⁵⁷).

A comprehensive summary of microstructural barriers and dislocation reactions is provided in the following subsections.

5.5.1 Interstitial / substitution atom - dislocation interaction

The addition of a solute atom to the crystal lattice usually raises the yield stress and the level of the stress strain curve as a whole. This suggests that solute atoms have more influence on the frictional resistance to dislocation motion than on the static locking of dislocations (Dieter¹⁵⁶).

Solute atoms fall into two broad categories (Fleischer¹⁷³) with respect to their relative strengthening effect. First, there are atoms which produce non spherical distortions (i.e. most substitution atoms) having a relative strengthening effect per unit concentration of about three times their shear modulus. The second type (mainly interstitial atoms) produce spherical distortions and possess a relative strengthening effect of about one tenth of the shear modulus. The interaction of dislocations with solute atoms has been summarised by Dieter¹⁵⁶ and is given as follows:-

- Elastic interaction
- Modulus interaction
- Stacking fault interaction
- Electrical interaction
- Short range interaction
- Long range order interaction

Elastic interaction arises from the mutual interaction of elastic stress fields which surround the misfitting solute atom and the core of edge dislocations. The amount of strengthening is thought to be proportional to the misfit of the solute, with interstitial being more effective than substitution solutes since the former has a dilation and shear component therefore impeding the motion of both types of dislocation (Dieter¹⁵⁶, Reed-Hill¹⁷⁴).

A modulus interaction occurs if the solute atom locally alters the modulus of the crystal, i.e. if the solute atom has a smaller shear modulus than the matrix, then the strain field energy of the dislocation will be reduced and there will be an attraction between solute and matrix. Edge and screw dislocations are subject to this interaction because a change in the shear modulus will effectively also alter the bulk modulus (Dieter¹⁵⁶).

Stacking fault interactions are due to the fact that solute atoms preferentially segregate to stacking faults contained in extended dislocations. As the concentration of the solute atom within the stacking fault increases, it effectively lowers the stacking fault energy and therefore makes constriction of the partial dislocations more difficult (Dieter¹⁵⁶). The end effect is to minimise the amount of cross slip, (since constriction of partial dislocations is required prior to cross slip) and therefore the partial dislocations become restricted to glide on one specific plane.

Electrical interactions occur in solute atoms with dissimilar valence to the matrix atom, where residual charge remains localised around the solute atom which can interact with dislocations that have electrical dipoles (Cottrell et. al¹⁷⁵). Such an interaction only becomes significant where there is a large valence difference between the solute and the matrix and the elastic misfit is small.

Some solute atoms tend to arrange themselves so that they have more than the equilibrium number of dissimilar neighbours giving rise to short range ordering. In contrast some solute atoms group together in regions of the lattice (i.e. clustering). Strengthening arises from short range ordering or clustering because the movement of a dislocation through this region reduces the degree of local order (Dieter¹⁵⁶).

This process of disordering will therefore cause an increase in the energy of the alloy, hence to sustain dislocation motion, extra work must be provided.

The resistance to dislocation motion that constitutes solid solution strengthening can come from one or more of these factors depending upon chemistry, crystal structure and method of fabrication. However, common to all types of solid solution strengthening is the way in which dislocation motion is impeded. An essential key to this theory was provided by Mott and Nabarro¹⁷⁶ after noting that dislocation lines are generally not straight but quite flexible therefore the entire line does not have to move simultaneously. The dislocation can therefore take up lower energy positions by bending around regions of high interaction energy. However, the smallest radius of curvature that a dislocation line can accommodate under a local stress is generally much greater than the average spacing of the barrier solute atom, thus the dislocation can only move in lengths much greater than the barrier spacing. Labusch¹⁷⁷ has presented a statistical treatment of the interaction of dislocations and solute atoms which lie at various distances from the dislocation line.

5.5.2 Precipitate - dislocation interactions

Precipitation hardening is accomplished by solution treating and quenching an alloy, in which the second phase is in solid solution at the elevated temperature, but then precipitates upon quenching and ageing to lower temperature (Martin¹⁷⁸).

For certain alloy systems, an ageing treatment is also required to promote precipitation, however low carbon martensitic steel for example, auto tempering during the quench ensues allowing the formation of fine carbides without the need for a temper (ageing) treatment (Naylor and Cook¹¹⁹). For precipitation hardening to occur, the second phase must be soluble at elevated temperatures and exhibit decreasing solubility with decreasing temperature.

The amount of strengthening resulting from precipitates depends upon the size, shape and distribution in the ductile matrix, with the strongest alloys produced by combining the effect of precipitation and strain hardening (Dieter¹⁵⁶). Fine particles can prevent the motion of dislocation in several ways, for example they can act as strong impenetrable barriers through which the dislocation can only pass by sharp changes in curvature. Alternatively, they can act as coherent particles through which the dislocation can pass, but only at a stress level much higher than that required for normal dislocation glide (Dieter¹⁵⁶). Hence the particle may either cause dislocation bypass, or as in the later case, the dislocation has to cut through the particle before further glide can commence.

The ease at which a particle is sheared by a dislocation is dependent on a number of factors. Mott and Nabarro¹⁷⁶ established that the strain field resulting from the mismatch between a particle and the matrix would be a source of strengthening. Additionally precipitates which have stacking fault energies significantly different from the matrix must be considered. Hirsch and Kelly¹⁷⁹ have shown that the increase in flow stress is proportional to the difference in stacking fault energy between the particle and the matrix.

The energy of a dislocation is related to the local modulus, hence particles which possess a modulus which differs significantly from the matrix will alter the energy of the dislocation as it cuts through them (Dieter¹⁵⁶). In the majority of alloys the modulus difference between matrix and particle is small, however a large difference in modulus is obtained if a void is present around the precipitate and this can contribute to the strengthening.

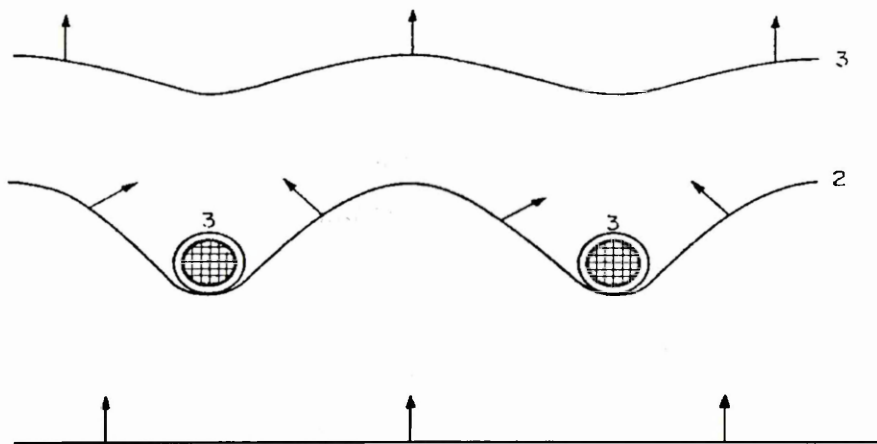
On the shearing of a particle, an increase in surface area is obtained and associated with this is an increase in surface energy which must be supplied by the external stress (Kelly and Nicholson¹⁸⁰). It follows then that the greatest strengthening due to surface effects arises from thin plate shaped particles which produce large increases in surface area on shearing (Dieter¹⁵⁶).

Finally, there is a strengthening component due to the Peierls stress in the particle and the matrix as deduced by Glieter and Hornbogen¹⁸¹.

If particle morphology is designed so that dislocation motion via cutting through the precipitate is difficult, then the dislocation will attempt to move around the precipitate. In this case the precipitate spacing is the essential strengthening feature (Corti et. al.¹⁸²).

If the precipitates are non coherent spaced apart at a distance greater than the minimum allowable dislocation bowing distance then the yield stress is determined by the shear stress required to bow a dislocation line between two particles. This mechanism was first proposed by Orowan¹⁸³ and is illustrated in figure 45.

Figure 45:- Schematic drawing of stages in passage of a dislocation between widely spaced obstacles based on Orowan's mechanism of dispersion hardening.



As a dislocation approaches two particles, the dislocation line begins to bend until critical curvature is reached. The segments of the dislocation that meet on the other side of the particle are of opposite sign and therefore partly annihilate each other leaving a dislocation loop around each particle (Dieter¹⁵⁶ Hull and Bacon¹⁸⁴).

The dislocation is then allowed to glide freely as shown in stage 5, figure 45. Every time a dislocation glides up to and past these particles, a loop is added, and since these loops exert a back stress, it follows that additional work must be incorporated for additional slip to take place.

5.5.3 Grain boundary - dislocation interaction

There is much evidence to suggest an inverse relationship between grain size and the yield stress of a material. A general relationship between these two parameters was proposed by Hall¹⁸⁵ and refined by Petch¹⁸⁶.

$$\sigma_0 = \sigma_i + K D^{-1/2} \quad (5.1)$$

where σ_0 = yield stress
 σ_i = frictional stress
K = Locking parameter
D = grain diameter

This equation is useful because it has been found to be applicable to ferrite-cementite boundaries, mechanical twins and martensite plates as well as grain size (Dieter¹⁵⁶).

The original dislocation model for the Hall-Petch equation was based on the concept that grain boundaries act as barriers to dislocation motion, and that pile up at grain boundaries eventually producing a back stress which must be overcome to continue slip past this barrier. This in fact may be the case, however there is a growing realisation that the grain boundary acting as a source of dislocations is more important as discussed in section 5.5.6.3 (Dieter¹⁵⁶).

A more general model (Li¹⁸⁷) considered grain size and dislocation density due to grain boundaries acting as dislocation sources, as opposed to the influence of stresses at the grain boundary. The flow stress is given in terms of dislocation density as:-

$$\sigma_0 = \sigma_i + \alpha G b \rho^{1/2} \quad (5.2)$$

Where α is a numerical constant (0.3 - 0.6)
 ρ is dislocation density.
 σ_i = frictional stress.
G = Line Energy

The relationship to grain size is based on experimental observation that dislocation density (ρ) is an inverse function of the grain size (D) and $\rho = 1/D$, therefore:-

$$\sigma_0 = \sigma_i + \alpha G b D^{-1/2} \quad (5.3)$$

5.5.4 Dislocation intersections and forests

In the advanced stages of plastic deformation dislocations from different systems cut across one another with predictable changes in geometry. This intersection of dislocations is often referred to as a forest of dislocations, and as plastic deformation proceeds, slip takes place on other systems thereby increasing the number of intersections and number of forest dislocations (Dieter¹⁵⁶).

When dislocations intersect, jogs form on one or both dislocations, with a dimension equivalent to the Burgers vector. Hence the dislocation line is extended with a respective increase in dislocation energy (Dieter¹⁵⁶).

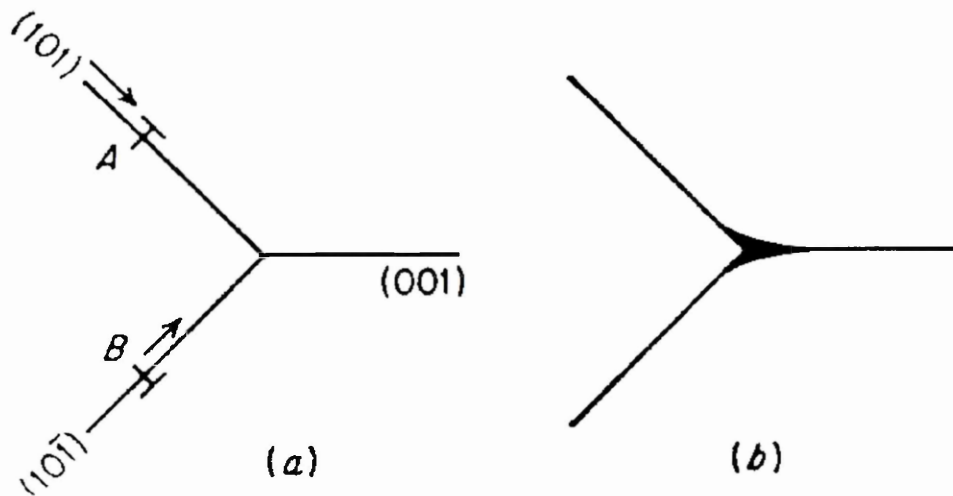
Additionally, in the case of the intersection of two pure screw dislocations, the jogged section is also restricted in movement and can only move non-conservatively (Climb) to keep up with the moving dislocation (Hull and Bacon¹⁸⁸, Dieter¹⁵⁶). Since climb is energetically not favoured at lower temperatures, the screw-screw dislocation jog is considered sessile and therefore able to provide resistance to other glissile dislocations (Hull and Bacon¹⁸⁸). This is consistent with the experimental observation (Chen and Pond) that screw dislocations move more slowly through a crystal than edge dislocations.

5.5.5 Dislocation reactions to form sessiles - bcc structures

Cottrell¹⁸⁹ has suggested a dislocation reaction which appears to lead to the formation of immobile dislocation in the bcc lattice. The reaction has been shown to be one of the mechanisms for producing crack nucleus for brittle fracture and is also thought responsible for producing $a_0[001]$ dislocation networks observed in iron (Hull and Bacon¹⁶⁹).

Figure 46 shows dislocation A with burgers vector $(a_0 / 2)[111]$ gliding on the (101) plane. Dislocation B with Burgers vector $(a_0 / 2)[\bar{1}\bar{1}1]$ is also gliding on the intersecting (101) slip plane.

Figure 46:- Formation of sessile dislocation in b.c.c iron (Cottrell¹⁸⁹).



The two dislocations come together and react to lower their strain energy to form a pure edge dislocation which lies on the (001) plane, i.e.:-

$$\frac{a_0}{2}[\bar{1}\bar{1}1] + \frac{a_0}{2}[111] = \frac{a_0}{2}[001] \quad (5.4)$$

Because the (001) is not a close packed slip plane in the b.c.c lattice, the dislocation is immobile. Perhaps more significant is the fact that the (001) plane is the cleavage plane along which brittle fracture occurs (Dieter¹⁵⁷).

5.5.6 Dislocation multiplication

One of the original problems in the development of the dislocation theory was the creation of a tangible mechanism by which sources already present in the metal could emit new dislocations by slip (Dieter¹⁵⁷). To date, several mechanisms for dislocation multiplication have been proposed and identified. Examples include Frank-Reed, multiple cross glide and dislocation generation by climb at elevated temperature via a mechanism similar to Frank-Reed known as the Bardeen-Herring source (Hull and Bacon¹⁹¹).

Microstructural sources of dislocation multiplication include grain boundaries and phase interfaces, for example, it has also been suggested by several authors that the ferrite cementite interface in pearlite acts as a source of dislocations, (Gladman, Holmes and McIvor¹⁰⁰)

5.5.6.1 Frank Read source

The Frank-Read source essentially involves generation of dislocations from existing dislocations within the microstructure (Dieter¹⁵⁷, Hull and Bacon¹⁹¹).

A schematic representation of the operation of a Frank-Read source is illustrated in figure 47, where line DD' is a dislocation of screw orientation and the plane of the figure is the slip plane. If a shear stress is applied on this slip plane and the dislocation is immobilised at point D and D' the dislocation line would bulge out and produce slip as shown in figure 47 (b). For a given stress the dislocation line will assume a certain radius of curvature, with the maximum value of shear stress required when the dislocation bulge becomes a semicircle. Beyond this point, the dislocation loop continues to expand under decreasing stress and when the loop reaches figure 47 (d), the segments at *m* and *n* meet and annihilate each other (Hull and Bacon¹⁹¹).

Annihilation is possible at this point because the segments are in edge orientation but of opposite sign, hence the end product is a large loop and new dislocation as shown in figure 47 (e).

This process can be repeated over and over again at a single source, each time producing a dislocation loop which produces slip of one Burgers vector along the slip plane. However, once the source is initiated it does not continue indefinitely. The back stress produced by the dislocations piling up along the slip plane opposes the applied stress and when this equals a critical stress, the source ceases to operate (Dieter¹⁵⁷).

Figure 47:- Multiplication of dislocations by frank reed source (Hull and Bacon¹⁹¹)

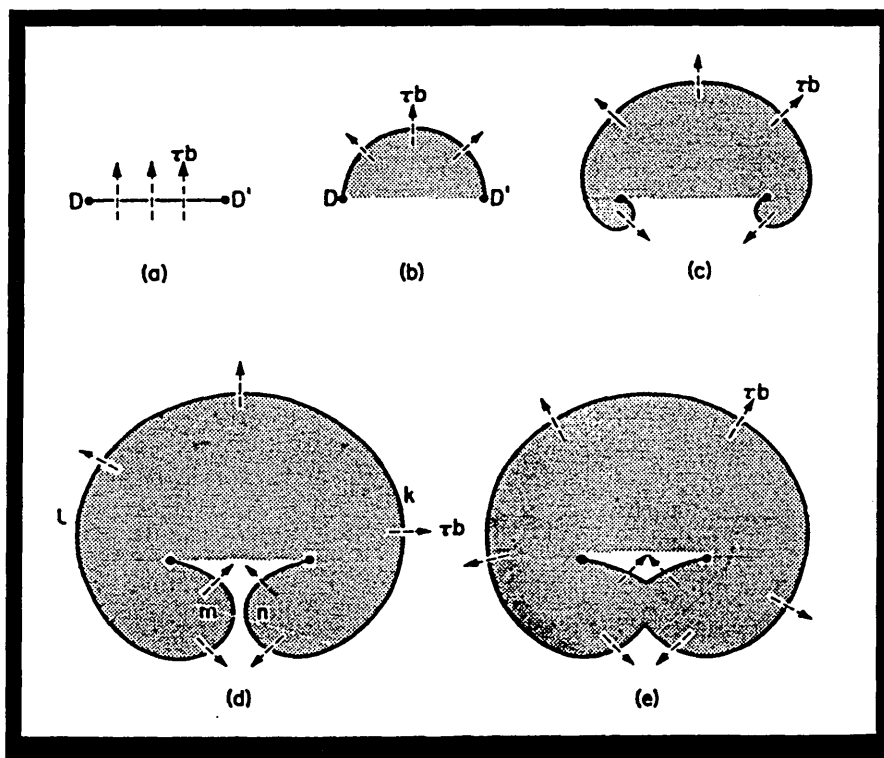


Figure 47 illustrates double ended Frank-Read sources which, although observed, their occurrence is not particularly frequent (Dieter¹⁵⁷).

Where only part of the dislocation is mobile, for example the formation of a superjog on a screw dislocation, an increase in the dislocation length occurs from rotation around the immobilised segment resulting in a spiral slip step (Hull and Bacon¹⁹¹).

This step on the dislocation line is known as a jog, and when this step or jog is more than one atomic spacing high it is referred to as a super or long jog. If the stress is greater on the primary slip planes, then these long jogs AC and BD in figure 45 are relatively immobile. However the segments lying in the primary slip plane will be free to expand and can operate as a Frank-Read source (Hull and Bacon¹⁹¹). It is therefore possible for a single dislocation loop to expand and multiply in a manner so that slip spreads from one plane to another. Such a mechanism is more effective than simple the Frank-Reed source as it results in more rapid multiplication (Dieter¹⁵⁷).

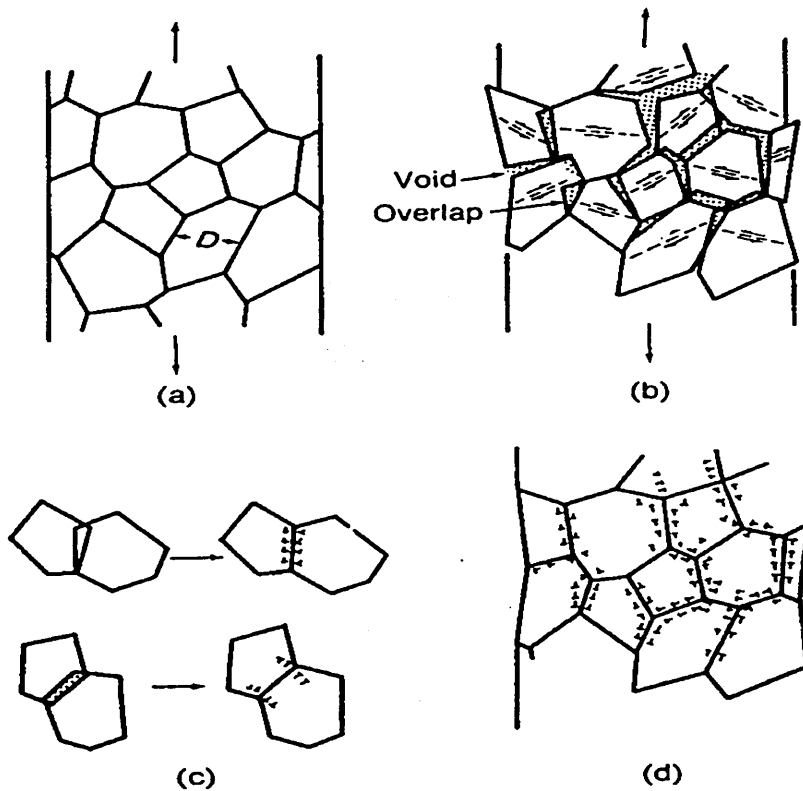
5.5.6.3 Grain boundary sources

Two types of grain boundary exist in a polycrystalline aggregate, the first are high angle grain boundaries representing a region of random misfit between the adjoining crystal lattices (Hu¹⁹³). Secondly a definite substructure exists within the grains with very small orientation differences which are commonly referred to as low angle grain boundaries. In both cases the grain boundary structure contains grain boundary dislocations, which are sessile and therefore their primary role is to group together within the boundary to form a step or grain boundary ledge (Dieter¹⁵⁶). As the misorientation angle of the grain boundary increases, the density of the ledge increase, hence grain boundary ledges are effective sources of dislocations.

When a polycrystalline specimen is subject to deformation, continuity must be maintained, so that the boundaries between the deforming crystals remain intact. The necessity for continuity led Ashby¹⁹⁴ to suggest a dislocation model for polycrystalline deformation where the polycrystal is deformed by disassembling it into constituent grains and allowing each to slip generating static dislocations as shown in figure 49 (b). This process also generates overlaps and voids in the grains which are corrected by the introduction of appropriate geometrically necessary dislocations (figure 49 (c)) until the grains again fit together.

It is then probable that subsequent multiplication of dislocations within the grains takes place via the multiple cross slip process as described in section 5.5.6.2.

Figure 49:- Ashby¹⁹⁴ model of deformation of a polycrystal. (a) polycrystal deforms in macroscopic uniform manner producing overlap and voids at boundary (b). These are corrected by the introduction of dislocation at (c) and (d).



5.6 Strain hardening rate and exponent

If an alloy system has a high rate of strain hardening (rapidly hardens after minor deformation) this suggests mutual obstruction of dislocations gliding through intersecting systems (McLean¹⁹⁵, Meyers and Chawla¹⁹⁶) as described in section 5.5. It is also interesting to note that for alloys strengthened by solid solution additions, the rate of strain hardening may be either increased or decreased compared to the behaviour of the pure metal.

However, the final strength of the cold worked solid solution alloy is almost always greater than that of the pure metal (Dieter¹⁵⁶)

The rate of strain hardening can be gauged from the gradient of a stress strain curve. However, It is important that a true stress strain curve is obtained since the normal or engineering curve is no more than a load-elongation curve, and is unsuitable for describing work hardening characteristics (Dieter¹⁹⁷). Additionally, the flow curve of many metals in the plastic region of uniform plastic deformation can be expressed by the simple power curve relation:-

$$\sigma = k \varepsilon^n \quad (5.5)$$

where n is the strain hardening exponent and K is the strength coefficient. A log log plot of true stress versus true strain up to maximum load will result in a straight line if equation 5.5 is satisfied where the linear slope of this line is n and K is the true stress at $\varepsilon = 1.0$. (Dieter¹⁹⁷).

There are many other techniques available for measuring the work hardening exponent and have been extensively reviewed by Duncan¹⁹⁸. occasionally data which does not plot according to equation 5.5 will yield a straight line according to the relationship:-

$$\sigma = k (\varepsilon_0 + \varepsilon)^n \quad (5.6)$$

Datsko¹⁹⁹ has indicated that ε_0 can be considered to be the amount of strain hardening that a material received prior to the tensile test.

Another common variation of equation 5.5 is the Ludwik²⁰⁰ equation given as:-

$$\sigma = \sigma_0 + K \varepsilon^n \quad (5.7)$$

where σ_0 is the yield stress and K is the material constant.

Equation 5.7 is perhaps superior compared to equation 5.5 since the latter implies that at zero true strain the stress is zero.

It is important to note that the strain hardening exponent (n) is not the same as the strain hardening rate ($d\sigma/d\varepsilon$) which can be determined from the strain hardening exponent utilising the following relationship:-

From Dieter¹⁹⁷
$$\sigma = k \varepsilon^n \quad (5.5)$$

Hence
$$\ln \sigma = \ln k + n \cdot \ln \varepsilon \quad (5.8)$$

and
$$n = \frac{d(\ln \sigma)}{d(\ln \varepsilon)} = \frac{\varepsilon}{\sigma} \cdot \frac{d\sigma}{d\varepsilon} \quad (5.9)$$

hence
$$\frac{d\sigma}{d\varepsilon} = n \frac{\sigma}{\varepsilon} \quad (5.10)$$

For a given value of stress / strain the work hardening rate is therefore simply the work hardening exponent multiplied by the stress strain ratio.

5.6.1 Determination of strain hardening rate from hardness

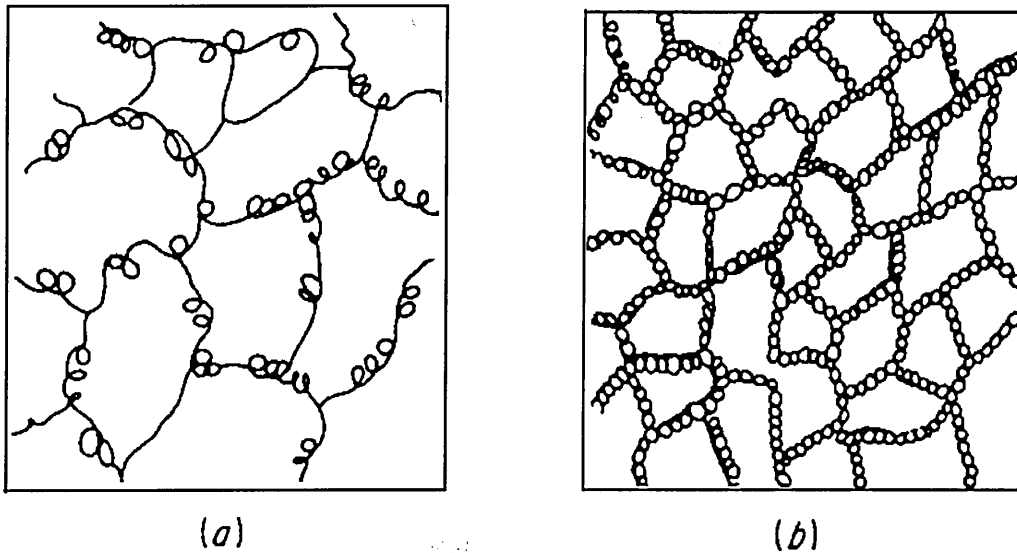
The simplest way to measure a metal's work hardening characteristics is to hit a sample with a known force a number of times and to measure the hardness between each blow (Peterson²⁰¹).

This procedure is continued until the hardness remains fairly constant. Similarly, it is also possible to ascertain the strain hardening rate of a cold rolled metal on examining its hardness for a given percentage deformation. Hence the gradient or slope of the curve corresponds to the strain hardening rate at a particular amount of deformation.

5.7 The deformed microstructure

Considerable detailed knowledge on the structure of the cold worked state has been obtained by thin foil electron microscopy (Dieter²⁰²). In the early stages of deformation slip is on primary glide planes and the dislocations form coplanar arrays. As deformation continues cross slip takes place with the possible formation of sessile jogs, dislocations tangle with other dislocations and microstructural barriers and dislocation multiplication takes place (Hansen et al²⁰³, Martin and Argon²⁰⁴). Hence the characteristic structure of the cold worked state is a cellular substructure in which high density dislocations form the cell walls as illustrated in figure 50 (Dieter¹⁵⁶). This cell structure can develop at strains of about 10 percent and its unit size is found to be inversely related to the amount of strain at low deformations. However at larger deformations the unit size of the cell structure remains constant indicating that as strain proceeds the dislocations sweep across the cells and join the tangle in the cell wall (Dieter¹⁵⁶).

Figure 50:- Typical cellular substructure formed as a result of cold work (Dieter¹⁵⁶)



The formation of microbanded dislocation subgrains has also been observed (Barlow et al.²⁰⁵, Yan and Men²⁰⁶) after large amounts of strain. This has been described as the rearrangement and annihilation of dislocations in cell walls (Sevillano et al.²⁰⁷) and is thought to be responsible for the reduction in the strain hardening rate. The precise morphology of the cold worked substructure depends upon the material, the strain rate, strain amount and the temperature of deformation (Dieter¹⁵⁶). Additionally the formation of distinct dislocation substructures at every different deformation stage will result in different mechanisms of strain hardening (Yan and Men²⁰⁶).

The applied stress (σ) is related to dislocation density (ρ) as given in equation x (Taylor²⁰⁸).

$$\sigma = \sigma_0 + \alpha G b \rho^{1/2} \quad (5.11)$$

where σ_0 is the frictional stress opposing dislocation movement, G is the shear modulus and b is the Burgers vector.

The relationship between dislocation cell size (d) and dislocation density (Holt²⁰⁹) is given by:-

$$d = K \rho^{-1/2} \quad (5.12)$$

where K is a constant which depends upon the character of material. Combining equations (5.11) and (5.12) results in equation (5.13) which is analogous to the Hall -Petch equation for grain boundary strengthening (Yan and Men²⁰⁶).

$$\sigma = \alpha_0 + k G b d^{-1} \quad (5.13)$$

5.7.1 Stored energy in the deformed microstructure

Most of the energy utilised to deform a metal by cold work is converted into heat with only 10% of the expended energy stored in the lattice noted as an increase in internal energy (Dieter¹⁵⁶). Typical values of stored energy range from about 0.04 to 4 KJ Kg⁻¹ of metal (Bever et. al²¹⁰), with the highest amounts of lattice stored energy found in high melting point solid solution hardened metals.

The major part of stored energy is due to the generation and interaction of dislocations during cold work. Vacancies also account for part of the stored energy for metals deformed at very low temperature. Other contributors include stacking faults, twin faults, and a reduction in short range ordering for solid solutions (Dieter¹⁵⁶).

Chapter 6

Experimental Procedure

Project material was selected based on a knowledge of hardenability, strengthening effects and phase transformations. Samples were then heat treated and control cooled to produce an optimum microstructure, with the addition of cold rolling for certain alloys to increase strengths further. Property assessment included tensile, hardness and impact evaluation. Optical, scanning and transmission electron microscopy were utilised to examine microstructural and fracture surface features. Unless stated otherwise, project alloy was supplied in 20 mm diameter round bar. Where necessary, material was also hot rolled from 20 mm diameter round bar to 4 mm thick strip.

6.1 Alloy selection procedure

6.1.1 Precipitation strengthened eutectoid pearlite

By strengthening a eutectoid 0.8 mass % carbon steel by the introduction of vanadium in the presence of nitrogen it is possible to obtain a steel with tensile properties similar to oil quenched and tempered steels (Pickering²³). Experimental casts were made (aluminium killed) and ultra grain refined by titanium additions with vanadium and nitrogen for precipitation strengthening at three carbon levels of 0.75, 0.80 and 0.85 mass %. The full actual cast analysis is given in Table 4.

Table 4 cast analysis of three eutectoid alloys under investigation (mass%)

Alloy number	C	Mn	Si	V	Ti	N
1	.77	1.31	0.38	0.2	0.018	0.017
2	.81	1.30	0.38	0.2	0.017	0.017
3	.86	1.29	0.38	0.2	0.017	0.015

6.1.2 Air cooled bainitic microstructure

An extensive literature review, examining continuous cooling transformation and time temperature transformation curves was carried out to find a commercially available steel which would provide a fully bainitic microstructure on air cooling. The pre-requisite as before was favourable resultant mechanical properties, however because of commercial implications the microstructure must be attainable over a relatively wide range of cooling rates. A suitable alloy was found which was also commercially available containing 1.25 mass % chromium, 0.25 mass % molybdenum and 0.40 mass % carbon.

This alloy was deemed suitable since a bainitic microstructure with adequate hardness was obtainable over a wide range of cooling regimes (see figure 18). A second alloy was developed at British steel plc (Swinden technology laboratories) based on the former composition, but with increased amounts of carbon added to increase the critical "bainite shelf" thereby allowing bainite to form over a wider range of cooling rates. The full cast analysis of both alloys are given in Table 5 .

Table 5 Chemical composition of two bainite alloys under investigation (Mass%)

Alloy identification	C	Si	Mn	P	S	Cr	Ni	Al	Mo
Lower Carbon bainite	0.40	0.23	0.64	0.006	0.032	1.39	0.25	0.005	0.51
Higher carbon bainite	0.48	0.25	0.59	0.005	0.005	1.21	0.18	0.005	0.52

6.1.3 Martensitic and martensite-bainite microstructure

A series of alloys were developed containing chromium, nickel or boron for hardenability, with reduced carbon contents to facilitate auto tempering. The amounts of alloying additions made were decided after careful consideration of hardenability data and literature (Siebert, Doane and Breen¹³²). The chemical composition of the martensite alloys are given in Table 6.

Table 6 Chemical composition of martensite alloys under investigation (mass%)

Alloy type	C	Si	Mn	Cr	Ni	Mo	Ti	N	B
Low carbon boron	0.22	0.22	1.07	0.27	0.06	0.01	-	-	0.0023
High carbon boron	0.30	0.23	1.02	0.24	0.021	0.011	0.02	-	0.0029
Low carbon chromium	0.21	0.2	1.5	0.51	-	-	0.02	0.011	-
High carbon chromium	0.25	0.2	1.5	0.5	-	-	0.02	0.011	-
Low carbon nickel	0.19	0.2	1.5	-	0.75	-	0.02	0.016	-
High carbon nickel	0.24	0.2	1.5	-	0.75	-	0.02	0.013	-

6.2 Thermal treatment

All alloy types were austenitised at 950°C for approximately 15 minutes. Cooling regime / isothermal treatment depended upon the alloy, i.e.:-

- (i) Eutectoid :- (A) Austenitise at 950°C for 15 minutes followed by air cool (normalised).
- (B) Austenitise at 950°C followed by submersion into a salt bath at 550, 600 and 650°C, samples were held in the bath for 15 minutes to allow complete pearlite transformation.

- (ii) Bainitic :-
- (A) Austenitise at 950°C, still air cool.
 - (B) Austenitise at 950°C, accelerated air cool at various air flow rates in a controlled air tunnel.
 - (C) Austenitise at 950°C, quench into salt bath at 320°C. Hold for 10 minutes.
- (iii) Martensitic:-
- (A) Heat to 950°C quench into water at various temperatures to facilitate full martensite transformation.
- (iv) Mixed :-
- (A) Heat to 950°C quench into water with martensite-bainite microstructure forming due to inadequate hardenability.

6.2.1 Clip thermal treatment

Type 2009 clips were manufactured in the development laboratory using both 0.2 mass% and 0.3 mass% carbon boron alloy. Standard production methods were used where bar was austenitising at 950 - 1000°C, formed using a two press operation then quenched into agitated water. The press operation took approximately 8 seconds and is illustrated in Figure 51 . Batches of 10 clips were then placed in a large water tank (15°- 20°C) and quenched down to ambient temperature.

The quench time versus water temperature was investigated and the maximum allowable water temperature was determined from microstructural and hardness analysis. Table 7 summarises the type of quenching routines employed to determine maximum water temperatures allowed.

Figure 51:- Clip press operation at Pandrol Laboratory

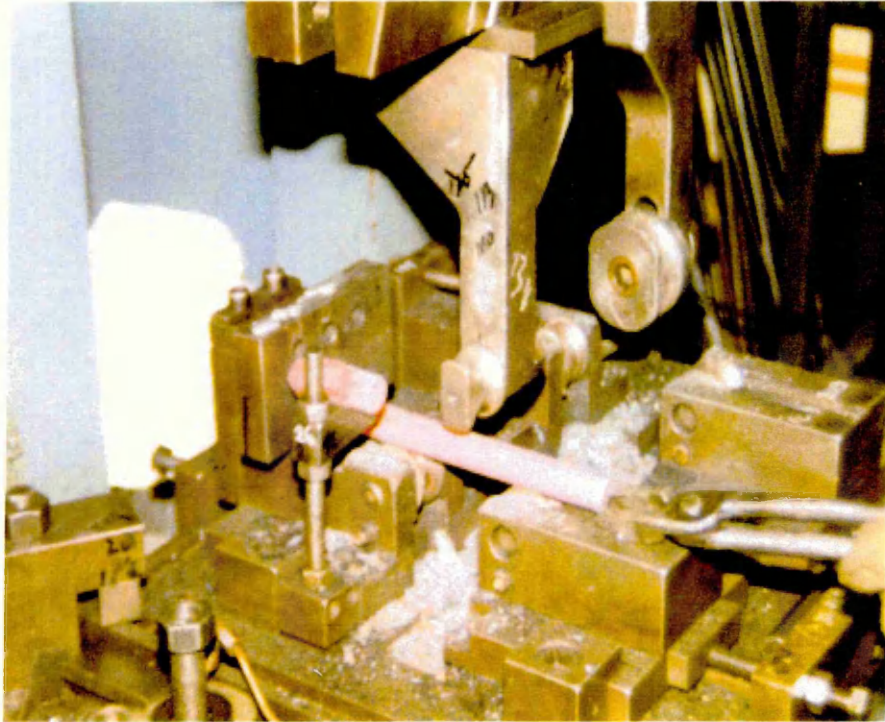


Table 7:- Quench routines employed on Pandrol clips

Temperature range	Comments	Property evaluation
10 - 20°C	Clips allowed to cool to room temperature, time taken to cool to 150°C noted.	Hardness, charpy impact, tensile strength and microstructure
10 - 20°C	Clips removed after 4 seconds.	Hardness and microstructure
30 - 40°C	Clips removed after 4 seconds.	Hardness and microstructure
50 - 70°C	Clips removed after 4 seconds.	Hardness and microstructure
100°C	Clips allowed to cool to water temperature, removed after 10 minutes	Hardness and microstructure

6.3 Mechanical treatments

Various types of mechanical treatments were carried out on a selection of alloy systems from the original matrix. Initially a standard engineering tensile test was used as a method of work hardening on the boron grade martensitic steel, this was then extended to incorporate the Pandrol clip. Advanced mechanical treatments included the cold rolling of martensitic, bainitic and mixed structures of martensite and bainite.

6.3.1 Strain hardening under the tensile test

To investigate the work hardening characteristics of the water quenched martensitic alloy standard tensile samples were plastically deformed to a specified stress / strain level, deloaded to zero then retested alongside "virgin" alloy for comparison. The specified initial stress levels to incorporate the various amounts of work hardening corresponded to the 0.1, 0.2, 0.3, 0.4 and 0.5% proof strength value on the engineering stress / strain curve.

6.3.2 Strain hardening of the Pandrol clip

Work hardening (scragging) of Pandrol clips formed from the water quenched boron alloy was facilitated mechanically during the load deflection test, or manually on driving a deliberately underpressed* clip into the rail assembly, as described in the following two sub-sections.

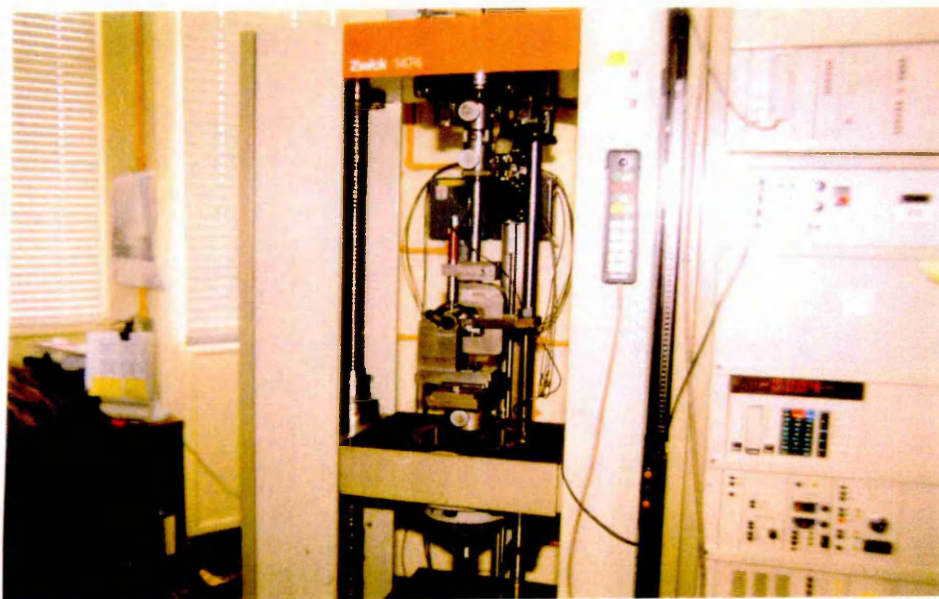
It was noted that the work hardening of Pandrol clips using either process was limited to the toe region only.

6.3.2.1 Load deflection of the Pandrol clip

Figure 52 shows the Zwick load deflection rig based within Pandrol development laboratory. Clips were placed in the assembly shown in figure 53 then loaded until a specified clip deflection was reached.

These clips were then deloaded to zero, their shape virtually unchanged, but with a degree of cold work from the load deflection cycle. The amount of cold work incorporated in this procedure was dependant on the amount of deflection imposed on the clip.

Figure 52:- Zwick Load deflection rig - Pandrol International Laboratory



6.3.2.2 Underpressing of the Pandrol clip

When a Pandrol clip is driven into the rail assembly a certain degree of cold work will take place (i.e. the clip plastically deforms) Working on this assumption, clip toes were underpressed by 4 mm., driven into the rail assembly using a "Pandrol Panpuller", then removed with a hammer. This operation produced a clip with a nominal toe height, with a small amount of cold work.

6.3.3 Plain strain cold rolling of strip

To incorporate known amounts of plastic deformation under plain strain conditions, strips of selected alloys were machined to a predetermined thickness then cold rolled at Swinden Technology Laboratories to a finishing thickness of 1 mm. For example, an initial strip thickness of 2.0 mm. finishing at 1 mm. was used to incorporate 50% plastic deformation.

The reduction in strip thickness per pass was carefully monitored to ensure deformation occurred through to the centre of the strip. Minimum allowed reduction per pass was calculated based on a knowledge of roll diameter and initial stock thickness.

Table 8 shows alloy systems investigated plus the amounts of cold deformation imposed.

Table 8:- The alloy systems used for cold rolling at Swinden Technology laboratories

Alloy Type	Thermal treatment	Mechanical treatments
1¼CrMo bainite	Austenitised at 950°C quenched into salt bath at 320°C	cold rolled 10, 25 and 50% based on reduction in thickness
0.5%Cr /0.25%C Martensite bainite	Austenitised at 950°C quenched into water at 15°C	cold rolled 10, 25 and 50% based on reduction in thickness
0.3%C / B alloy martensite	Austenitised at 950°C quenched into water at 15°C	cold rolled 10, 25 and 50% based on reduction in thickness
0.3% C / B alloy tempered martensite	Austenitised at 950°C quenched into water at 15°C, tempered at 400°C	cold rolled 10, 25 and 50% based on reduction in thickness
0.3% C / B alloy tempered martensite	Austenitised at 950°C quenched into water at 15°C, tempered at 250°C	cold rolled 10, 25 and 50% based on reduction in thickness

6.3.3.1 Determination of minimum reduction per pass

For plastic deformation into the centre of strip material generally, the pass factor must equal 1.8 or less (Ryalls²¹¹), for example:-.

$$\text{Pass Factor} = H_m / L = 1.8 \text{ or less} \quad (6.1)$$

Where:-

$$H_m \text{ (mean stock thickness) } = (H_f + H_i) / 2 \quad (6.2)$$

$$L \text{ (arc contact) } = (\Delta h \cdot R)^{1/2} \quad (6.3)$$

H_f = Final stock thickness

H_i = Initial stock thickness

R = Roll radius

Δh = Change in stock thickness

Example

The roll radius used in cold deformation was 50 mm.

During one pass stock thickness changed from 4.059 mm to 3.903 mm, a reduction of 0.156 mm, hence mean stock thickness (H_m) of 3.981 mm.

$$\begin{aligned} L (\text{arc contact}) &= (\Delta h \cdot R)^{\frac{1}{2}} &= (0.156 \text{ mm} \cdot 50 \text{ mm})^{\frac{1}{2}} && (6.4) \\ & &= 2.792 \end{aligned}$$

$$\begin{aligned} \text{Pass factor} &= H_m / L &= 3.981 / 2.793 && (6.5) \\ & &= \underline{1.42} \end{aligned}$$

Hence deformation to the centre of the strip was achieved. Similar reductions per pass were achieved for all alloy systems, ensuring complete deformation of the microstructure.

6.4 Hardness measurements

Approximately 3mm of material was machined off to ensure no decarburised microstructure existed. Samples were then ground to a surface finish of 1200 grit prior to hardness measurement. Vickers hardness determination was made using a calibrated* pyramidal diamond indentation with 30 Kg load to suit the hardness and thickness of the material. The diagonals were measured using a micrometer ocular giving a value which was then translated to Vickers hardness using conversion tables. A total of ten readings were taken from each sample, noting minimum, maximum and average result as well as the standard deviation. The accuracy of the machine was also evaluated using a standard test block prior to the testing of every microstructure.

* Vickers hardness machine calibrated to BS 427 (1990)

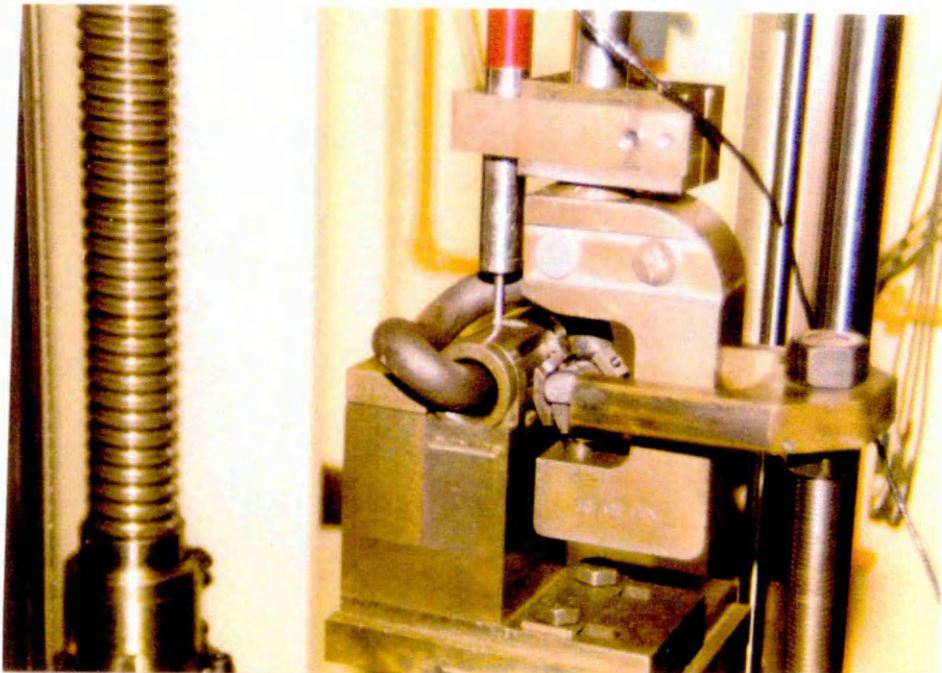
6.5 Tensile testing

Several types of tensile tests were employed. To investigate the tensile behaviour of the formed clip the Zwick load deflection rig based at Pandrol International laboratory was used. The testing of strip and round bar was carried out at Sheffield Testing Laboratories, where a laser extensometer facility allowed the determination of true stress strain behaviour up to fracture.

6.5.1 Tensile testing of formed clip

The tensile testing of Pandrol clips (type 2009) on the Zwick load deflection rig (figure 52) was carried out by placing the clip in the assembly shown in figure 53. The machine allowed the operator to specify the test parameter, i.e. whether to deflect the clip to a nominated deflection or load.

Figure 53:- Zwick Load deflection rig with clip in assembly ready for tensile testing.



Generally 2009 type Pandrol clips were tested to a design deflection of 12.6 mm noting the achieved load and permanent set (Specification 1250 Kg +/- 150 kg, 1 mm maximum set). However, on the tensile testing of boron clips, it was thought more appropriate to deflect to 15 mm, which would normally procure 0.6 to 0.8 mm permanent set in the silicon manganese clip. Permanent set values were determined by measuring toe position on a calibrated toe height and angle gauge. Toe load was determined from the load extension graph which also illustrated the elastic plastic characteristics of the clip.

6.5.2 Tensile testing of bar and strip material

The tensile testing of the actual material as opposed to the formed clip carried out at Sheffield Testing Laboratories, included engineering and true stress strain analysis. In the former 20 mm. diameter round bar was machined into standard test piece samples, and tested to failure using an Avery Dennison universal testing machine with 250 KN capacity. The later process was used to determine the mechanical properties of the cold rolled strip samples, where smaller non standard test pieces were used because the proof and ultimate tensile strengths were known to be particularly high. 1mm thickness by 7 mm width cold rolled strip samples were tested on a Nene universal testing machine with 50 KN capacity with laser extensometer to allow the determination of true stress / strain values up to failure. Cross sectional area measurements were taken at 0.5 KN intervals with a calibrated digital micrometer.

Both testing machines were calibrated to grade 1 requirements of BS 1610 part 1 (1985). Tensile testing was carried out in accordance with British Standard BS EN 10,002-1 with the 0.2% proof strength, ultimate tensile strength, elongation and reduction of area calculated for each sample.

6.6 Toe load testing of formed clip

Toe load evaluation involved driving the clip into the rail assembly as shown in figure 54, the toe load was then measured by following a standard Pandrol test procedure detailed as follows:-

- i) Clip toe lifted with claw attached to a calibrated strain gauge.
- ii) A thin metal strip was placed under the toe, clip toe was then dropped down onto strip.
- iii) Strain value was noted when strip could be removed on lifting the clip toe.
- iv) Strain value was converted to toe load using table.
- v) On removing the clip, the amount of permanent set (plastic deformation) was measured using toe height and angle gauge.

Figure 54:- Toe load testing at Pandrol International Development Laboratory

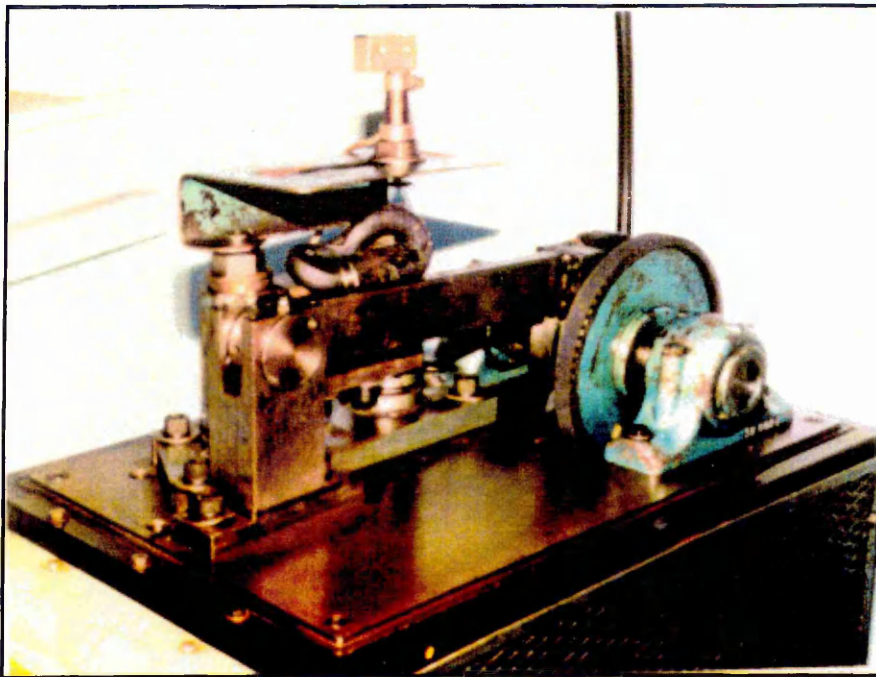


6.7 Fatigue testing of formed clip

The fatigue endurance limit of clips manufactured from the low and high carbon boron alloy were evaluated utilising a specialised rig at Pandrol metallurgy laboratory (figure 55). Clips were fatigue tested for 5 million cycles (65 hours), to various dynamic deflections, with toe load and height noted before and after testing.

The amount of permanent set and loss of toe load were determined as well as the “deflection” endurance limit (the maximum deflection to initiate the fatigue clip failure). For the Pandrol silicon manganese clip manufactured from 20 mm diameter bar, the endurance limit is typically 1.4 mm dynamic deflection.

Figure 55:- Fatigue testing rig at Pandrol International Metallurgy Laboratory



6.8 Charpy “V” notch Impact testing

To assess toughness characteristics of certain alloy systems, 10mm square samples were machined with “V” shaped notch then impact tested in accordance with BS 131 at Pandrol International Metallurgy Laboratory.

This test provided useful information in terms of alloy impact strength and fracture appearance with a comparison made with fracture toughness properties of existing Pandrol alloy systems. The fracture surface of the broken test pieces were also examined using scanning electron microscopy.

6.9 Optical microscopy

Prior to mounting samples in conductive bakelite, approximately 300 μ m of material was removed using a horizontal lathe to ensure no decarburised microstructure remained. samples were then carefully ground using a series of silicon carbide grit papers finishing with a polishing procedure using 6 then 1 μ m diamond lapping pad.

Polished samples were then submerged in a 2% by volume Nital solution for approximately 5 seconds, washed in water and dried under hot air to prevent staining. The microstructure was examined utilising a Vanox Optical microscope at magnifications up to approximately 1000x.

6.10 Scanning electron microscopy

Scanning electron microscopy was carried out on a Philips XL40 microscope to examine and characterise fracture surfaces of charpy impact and fatigue samples.

The energy dispersive spectrometry (EDS) facility was used to determine elemental segregation in the higher carbon bainite alloy using the sample previously prepared for optical microscopy.

It was important to ensure that the fracture surfaces from impact and fatigue testing were kept as dry as possible to prevent oxidation which would render the sample unfit for examination, hence samples were stored in a desiccator. Occasionally sample surfaces were protected with acetate sheeting which was then dissolved away from the fracture face using acetone.

Note Conductive bakelite was used where necessary for electron microscopy.

6.10.1 EDS digital line scanning

The amount and type of elemental segregation in the high carbon bainite alloy was initially assessed by placing a fine electron probe on the “depleted” area, obtaining spectra, then repeating the process on the “rich” region. On comparing each spectrum, the segregated elements were determined, with an approximate level of segregation noted on comparing the peak heights.

The location of segregated species with respect to the microstructure was displayed utilising digital line scanning. This technique involved isolating peak energies from spectra that corresponded to the peak width of segregated elements. Hence as the fine electron probe scanned a designated path, only x-rays with the predetermined energies were noted.

The dwell time, pixel and line scan number were optimised to give reasonable statistical accuracy. Typically data acquirement time was 2 hours, with dwell time of 2 μ s plus 5000 line scans

Results were displayed as a statistical line plot for each element of interest. The location of the segregation was then determined by superimposing each line plot onto the scan line.

6.11 Transmission electron microscopy

Transmission electron microscopy (TEM) was performed using a Philips CM20 instrument equipped with scanning transmission (STEM) facility and energy dispersive X-ray (EDS) microanalysis system.

6.11.1 Sample preparation

The microstructure was identified using thin foil samples which were obtained from bulk material using the following procedure.

i) 3 mm discs were spark eroded from strip material using a Sparcatron machine. The conditions used are given in table 9, and were maintained to ensure steady erosion without localised sample heating. (Full procedure is provided in appendix 3).

Table 9:- Conditions for Spark erosion on Sparcatron machine

Parameter	Setting
Micropower	1
Transistors	4
Pulse	8 μ m
Middle	x10
Pause	2 μ s
Suppresser	switched to ON
Dither	Switched to OFF

ii) Discs were manually ground on a series of silicon carbide papers, finishing on 1200 grade, taking the thickness from 1 mm to approximately 100 μm .

iii) A Tenupol-3 twin jet polishing unit was then used to polish and thin discs down to a thickness of electron translucency. The solution used for this operation consisted of analar methanol with 5% by volume perchloric acid addition, chilled with liquid nitrogen to a temperature between -40 and -50°C . The flow rate was set between 2 and 3, with a 90% sensitivity setting ensuring a reasonable sized hole on completion. A current setting of 0.15 mA was used which gave a voltage reading of 30 - 40 volts depending on the temperature of the electrolyte.

iv) After thinning, foils were washed in chilled analar methanol then stored in anhydrous ethyl alcohol prior to transmission electron microscopy.

6.11.2 Calculation correct magnification and the TEM camera constant

The magnification of each TEM micrograph was adjusted accordingly using tables generated from silicon monoxide cross grating specimens of known line spacing (see appendix 4).

In addition, settings of the various magnetic lenses within the column of a transmission electron microscope affect the magnification of diffraction patterns. Usually the microscope was operated at 200 Kv accelerating voltage ($\lambda = 0.0251 \text{ \AA}$) and with the lenses at fixed settings so that the magnification of the diffraction pattern was constant. This magnification factor was expressed in terms of an equivalent camera length (see figure 56).

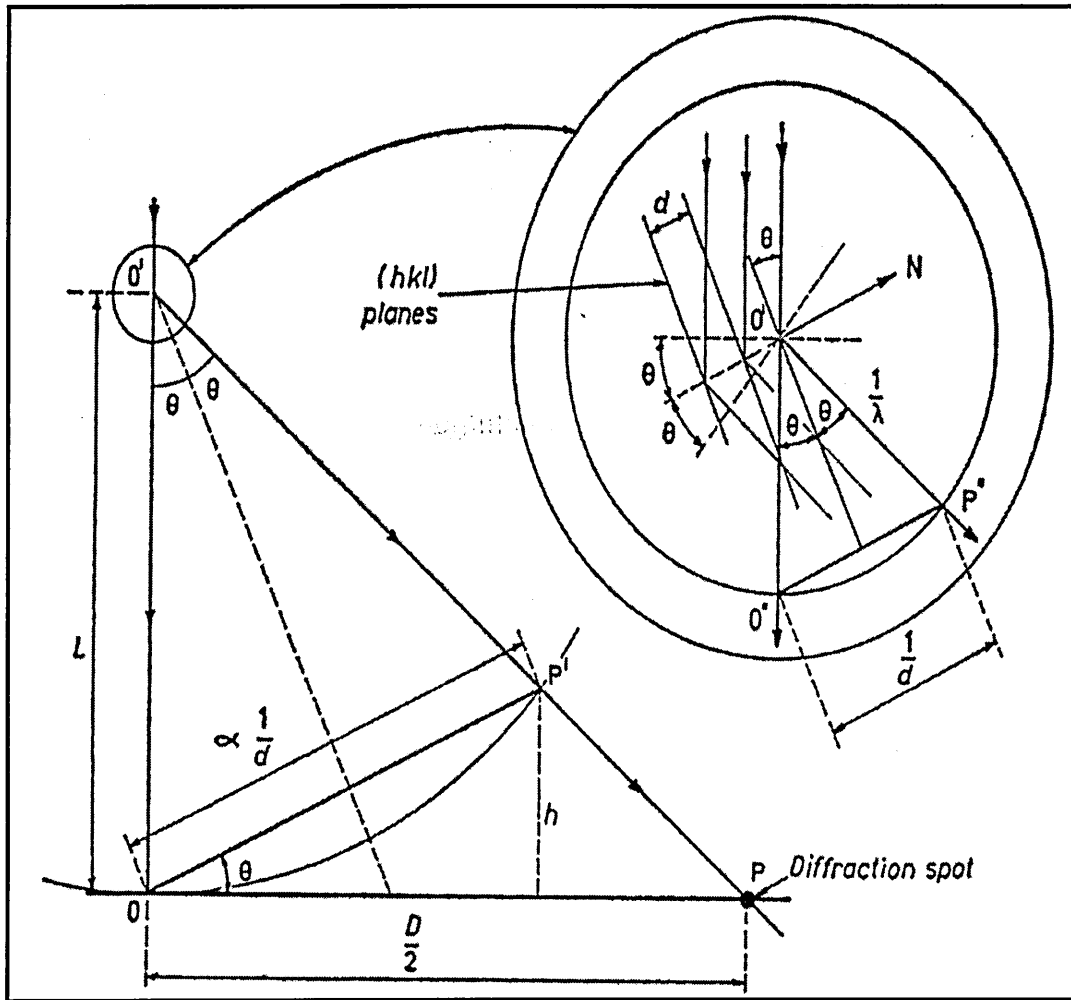
Braggs law states that:- $\lambda = 2d_{\{hkl\}} \sin\theta$ (6.6)

From geometry in figure 56:- $\tan 2\theta = R / L$ (6.7)

Now because 2θ is only small $\tan 2\theta \approx 2\sin\theta \approx 2\theta(\text{rad})$ (6.8)

From equations (1) and (2): $Rd = L\lambda = \text{Camera constant.}$ (6.9)

Figure 56 :- Schematic illustration of the magnification of a diffraction pattern



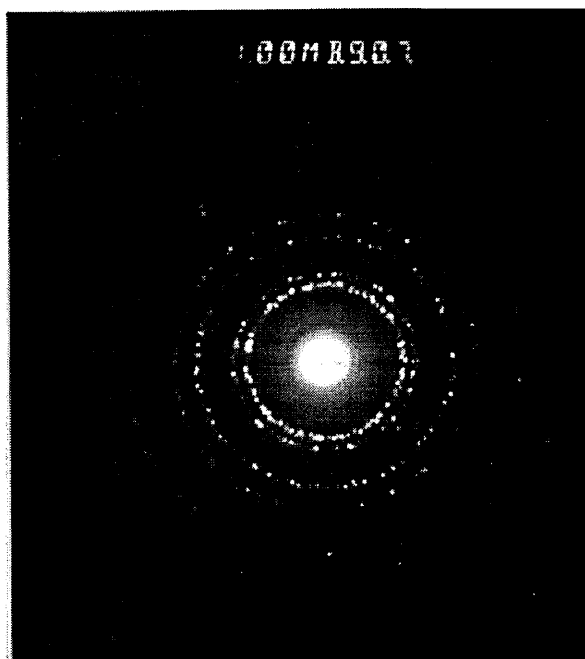
In order to correctly identify the crystallographic nature of phases present in the microstructure, it was essential to obtain an accurate camera constant for the CM20 microscope. This was achieved by the examination of a ring diffraction pattern from a standard polycrystallised pure aluminium sample (Andrews, Dyson and Keown²¹²). From this information, together with a knowledge of allowed reflections considering structure factors, the interplanar spacings $d_{\{hkl\}}$ were calculated and are illustrated in table 10, with ring pattern illustrated in figure 57 (measurements taken from original negative)

Table 10:- Determination of camera constant using pure aluminium sample.

Ring number	Associated (hkl)	$d_{(hkl)}$ Å	Measured D (ring diameter in mm)	Dd (Camera constant) $2\lambda L$
1	111	2.338	21.47	50.2
2	002	2.025	24.85	50.2
3	022	1.432	35.14	50.3
4	113	1.221	41.60	50.8
5	222	1.169	43.46	50.8

The average camera constant from the first to ring patterns were used (i.e Camera constant = 50.25 Å mm).

Figure 57:- Ring pattern of aluminium standard



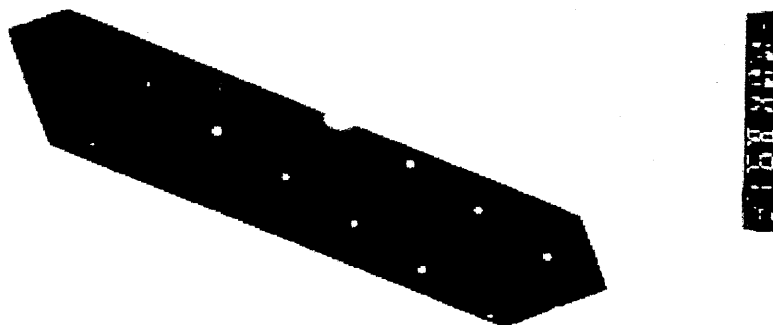
When collecting diffraction pattern data from the CM20 electron microscope, it was important that the sample height was corrected for eucentricity, otherwise a camera constant correction factor was required. At the correct eucentric height, the objective lens current reading was 5451 mA, and was set to this value prior to imaging and diffraction work.

6.11.3 Determination of image / diffraction pattern rotation.

When interpreting diffraction data, for example, determining the growth direction or habit plane of a precipitate, it was important to take proper account of the fact that the image was rotated with relation to the diffraction pattern. This angle was determined by examining a crystal of molybdenum trioxide with known structure and geometry.

A series of double exposure plates at different magnifications were produced containing both image and diffraction pattern of the molybdenum trioxide. The angle was then measured between the molybdenum trioxide crystal interface and 110 direction as shown in figure 58.

Figure 58:- Molybdenum trioxide crystal with diffraction pattern superimposed.



When collecting diffraction pattern data from the CM20 electron microscope, it was important that the sample height was corrected for eucentricity, otherwise a camera constant correction factor was required. At the correct eucentric height, the objective lens current reading was 5451 mA, and was set to this value prior to imaging and diffraction work.

6.11.3 Determination of image / diffraction pattern rotation.

When interpreting diffraction data, for example, determining the growth direction or habit plane of a precipitate, it was important to take proper account of the fact that the image was rotated with relation to the diffraction pattern. This angle was determined by examining a crystal of molybdenum trioxide with known structure and geometry.

A series of double exposure plates at different magnifications were produced containing both image and diffraction pattern of the molybdenum trioxide. The angle was then measured between the molybdenum trioxide crystal interface and 110 direction as shown in figure 58.

Figure 58:- Molybdenum trioxide crystal with diffraction pattern superimposed.

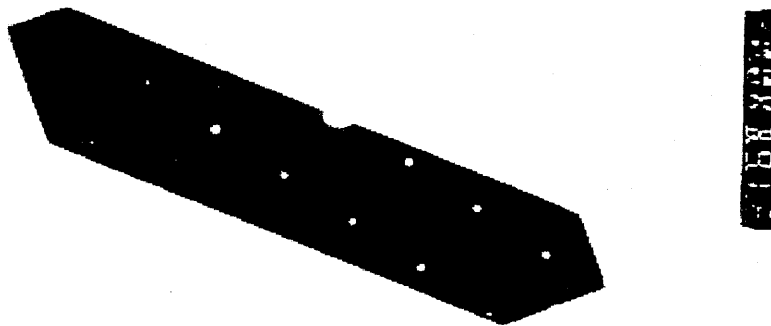
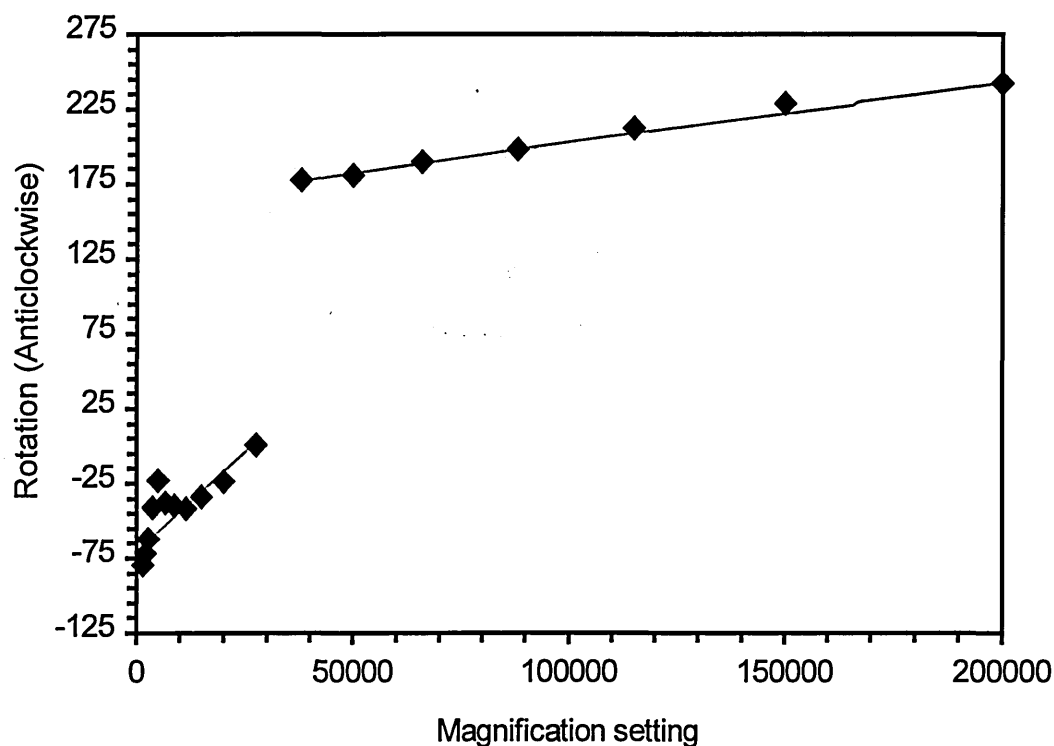


Figure 59 shows the relationship between angle of rotation and magnification. Hence before interpreting diffraction data in terms of growth direction and habit plane, it is necessary to rotate the structural image until it orientates exactly with the diffraction pattern for a given magnification.

Figure 59:- Relationship between angle of rotation and magnification



ii) On solving each pattern the zone axis was also determined by taking two diffraction spots and cross multiplying:-

$$\text{Zone axis (uvw) = } \quad u = k_1 l_2 - k_2 l_1 \quad (6.10)$$

$$v = l_1 h_2 - l_2 h_1$$

$$w = h_1 k_2 - h_2 k_1$$

All indices should satisfy the condition:-

$$hu + kv + lw = 0 \quad (\text{Weiss zone law}) \quad (6.11)$$

iii) Stereographic projections were then constructed for the two phases as orientated about these zone axis.

iv) Where necessary, planes of interest were located on the stereogram to examine their proximity to similar planes in the second phase, allowing 1 to 2° for inaccuracies.

6.12 X-ray diffraction technique for the assessment of retained austenite

6.12.1 Sample preparation

Prior to X-ray diffraction (XRD), samples were ground to a roughness of 6µm followed by an electropolish (conditions given in table 11).

Notes:-

If any staining was present on the sample, then a regrind and electropolish was necessary.

Samples were useful for XRD up to 3 weeks after electropolish, providing they were stored in a desiccator.

Table 11:- Setting used for electropolishing prior to XRD

Electrolyte used	Type "A2"
Voltage step	3/4
Current setting	50 μ A
Flow rate	set to high
Time to polish	20 s

6.12.2 XRD- Calculation of retained austenite

A peak profile was obtained corresponding to (111), (110), (200) etc. after full scan of $\theta = 0$ to 180° . Essentially the amount of retained austenite was calculated by comparing f.c.c peak height to b.c.c peak heights (after taking background counts into consideration).

The $(111)_\gamma$ and $(110)_\alpha$ peak overlap somewhat on the peak spectrum, hence are not used in the analysis. Instead the peak heights of the $(200)_\gamma$ and $(311)_\gamma$ are compared to the peak heights of $(200)_\alpha$, $(211)_\alpha$ and $(220)_\alpha$.

The calculation of retained austenite requires knowledge of the peak intensity (P_i) which is peak height minus background and the R value which is defined in equation 6.12. It can be seen that there are several parameters to equation 6.12, a full definition is provided in appendix 1.

$$\text{Concentration (Cx)} = \frac{P_i}{R} \quad (6.12)$$

where C_x is the concentration of phase x.

P_i is the peak intensity.

$$R = \frac{1}{v} \times F^2 \times LP \times M \times e^{-2m} \quad (6.13)$$

where v = volume of a unit cell (a^3)

F = Structure factor

LP = Lorentz Polarisation factor

M = multiplicity factor

e^{-2m} = Temperature factor

$$\text{Retained austenite (\%)} = \frac{1}{1 + (C_a / C_b)} \times 100 \quad (6.14)$$

where C_a and C_b are concentrations of phase a and b . (i.e. austenite and martensite).

Chapter 7

Optimisation of alloy system

7.1 Introduction

This chapter discusses initial mechanical and microstructural results for all alloy systems. From this preliminary assessment promising alloy systems for further research were chosen.

7.2 Eutectoid alloy system results

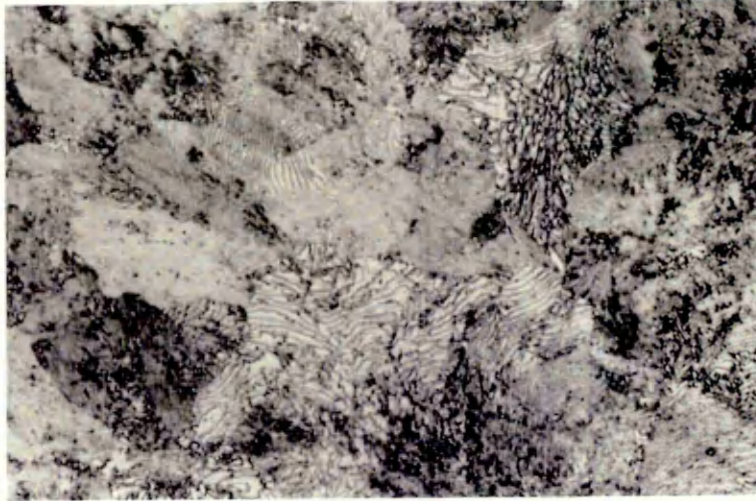
7.2.1 Normalised (continuous air cooled) pearlite results

A summary of the mechanical properties for each alloy are given in Table 12. Optical microscopy confirmed that each alloy systems composed of a predominantly pearlitic microstructure with fine interlamellae spacing, however the pearlite colony size was difficult to establish. These results are illustrated in figure 60.

Table 12 : Mechanical results Pearlite alloy systems (continuously air cooled)

C%	0.2% Proof strength (MPa)	Ultimate Tensile Strength (MPa)	Proof / UTS (%)	Elongation (%)	Reduction in Area (%)	Hardness (VPN)	Charpy Impact (J)
0.75	627	1064	59	16.5	36.7	343	7
0.80	647	1095	59	15.7	37.9	338	8
0.85	616	1090	56	13.5	31.5	343	6

Figure 60:- Microstructure for normalised (air cooled) pearlitic alloy
0.75, 0.8 and 0.85% carbon contents respectively. (Magnification 700X)



7.2.2 Isothermally treated pearlite results

A summary of the mechanical properties of the 0.8 mass% alloy system isothermally transformed at 550, 600 and 650 °C are shown in Table 13.

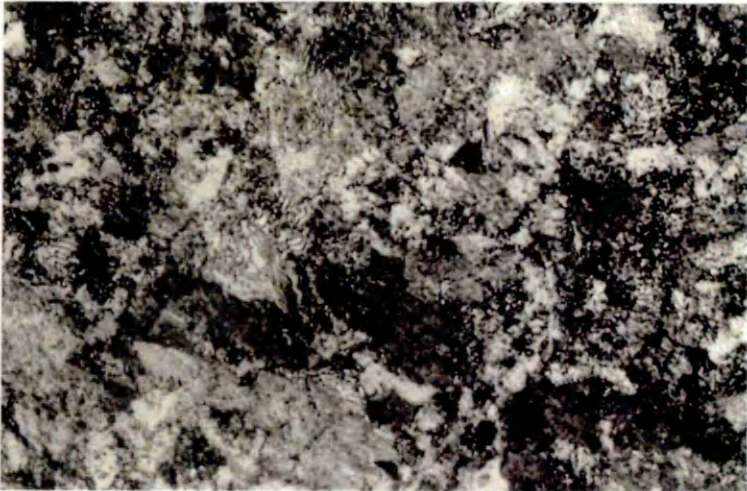
Optical microscopy was used to assess microstructural features, especially interlamellae spacing which is known to affect strength quite dramatically. Figure 61 illustrates the microstructure obtained for each transition temperature.

Table 13: Mechanical results of 0.8% carbon pearlite alloy isothermally transformed at 550, 600 and 650 °C

Salt bath temp (°C)	0.2% Proof strength (MPa)	Ultimate Tensile Strength (MPa)	Proof / UTS (%)	Elongn. (%)	Reduction in Area (%)	Hardness (VPN)	Charpy impact (J)
550	499	968	52	15	31.5	284	6
600	499	988	51	13.5	31.5	288	6
650	497	1007	49	14.3	26.8	287	7

Figure 61:- 0.8% carbon pearlite alloy austenitised at 950°C, quenched into salt bath at 550, 600 and 650°C respectively.

(Magnification 650X)



7.3 Bainitic alloy system results

7.3.1 0.40% carbon bainite results

Mechanical properties for various cooling regimes are given in Table 14. From optical microscopy it was found that the slowest cooling regimes produced a predominantly upper bainite microstructure. At a moderate cooling rate (130°C/min.), the microstructure consisted of lower bainite with the fastest cooling rate producing a martensitic microstructure. This explains the dramatic increase in hardness accompanied by a loss in impact strength observed in the fastest cooled samples. Examples of microstructure are shown in figures 62-65.

Table 14 Mechanical properties of 0.40% carbon bainite alloy (1¼ Cr Mo) air cooled at various rates

Cool rate	Transformation temperature	.2%PS (MPa)	UTS (MPa)	roof / UTS (%)	Elongn (%)	Redn. of Area (%)	ardness (VPN)	Impact (J)
88°C/ min	370 - 390	917	1327	69	13.5	46.4	415	11
105°C/min	345 - 365	1005	1423	70	13.5	46.7	424	11
130°C/min	300 - 310	1093	1642	67	10	46.4	520	13
142°C/min	280 - 285	-	-	-	-	-	590	6

Notes

Cool rate was calculated between 700 and 450°C

0.2% PS = 0.2% proof strength

UTS = Ultimate tensile strength

Figure 62- 1¼ Cr Mo, 0.4% carbon bainite, cool rate (700 - 450°C) = 88°C / minute.
Transformation temperature = 370 -390°C Hardness = 415 VPN. Magnification = X500

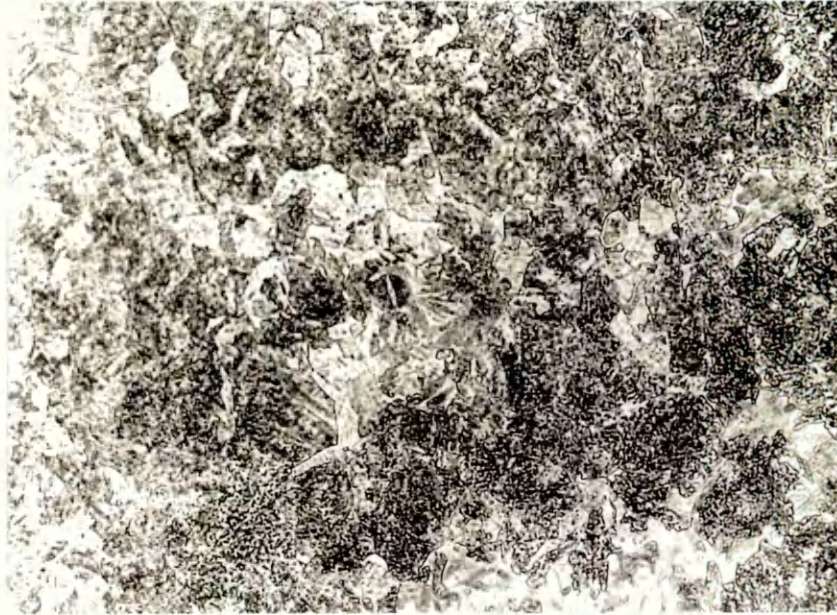


Figure 63:- 1¼ Cr Mo, 0.4% carbon bainite, Cool rate (700 - 450°C) = 105°C / minute
Transformation temperature = 345 -365°C Hardness = 424 VPN. Magnification = X600

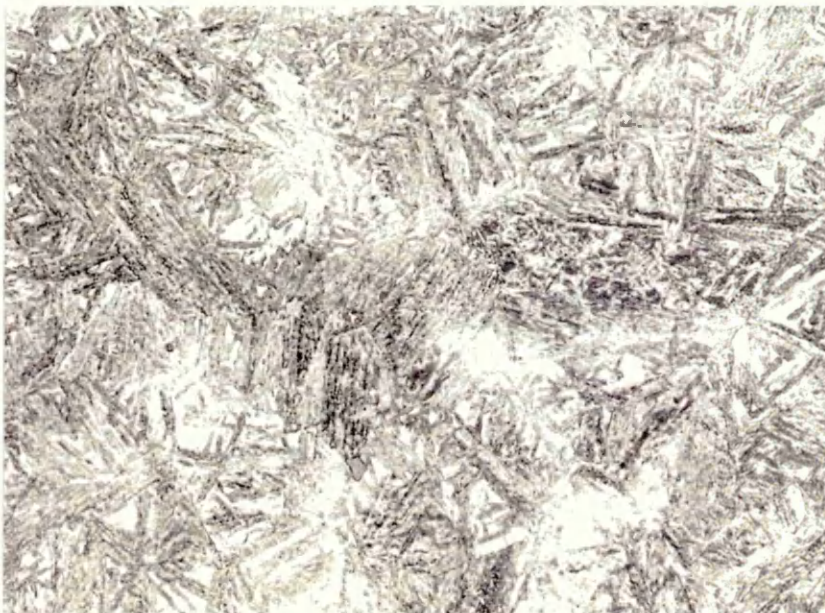


Figure 64:- 1¼ Cr Mo, 0.4% carbon bainite, Cool rate (700 - 450°C) = 130°C / minute
Transformation temperature = 300 -310°C Hardness = 520 VPN. Magnification = X500



Figure 65:- 1¼ Cr Mo 0.4% carbon bainite. Cool rate (700 - 450°C) = 142°C / minute
Transformation temperature = 280 -285°C Hardness = 590 VPN. Magnification = X600



7.3.2 0.48% carbon 1 ¼ Cr Mo bainite alloy results

Mechanical properties for various cooling regimes are given in Table 15 with some example microstructure illustrated in figures 66 to 69.

As with the lower carbon bainite, the microstructures obtained ranged from a mixed upper lower bainite though to lower bainite with increasing amounts of martensite at the fastest cooling rate. Thus as expected, hardness and ultimate tensile strength increased gradually, with the proof to ultimate tensile strength ratio maximised at a cooling rate of approximately 125°C / min corresponding to a predominantly lower bainitic microstructure.

Table 15 Mechanical properties of high carbon bainite alloy (1¼ Cr Mo) air cooled at various rates

Cool Rate	Transformation temperature (°C)	0.2% PS (MPa)	UTS (MPa)	Proof / UTS (%)	Elongn. (%)	edn. in Area (%)	Hardness (VPN)	Charpy Impact (J)
88°C/min	400 -430	970	1498	65	8	24.7	412	10
100°C/min	365 - 380	995	1510	66	9.2	26.2	437	11
110°C/min	355 - 370	1005	1545	65	9.3	24.9	456	10
115°C/min	330 - 345	1073	1568	68	9.5	26.1	472	14
115°C/min	355 - 370	1090	1578	69	9.5	26.6	473	13
125°C/min	330 - 345	1112	1592	70	9	26.1	489	13
125°C/min	335 - 340	1069	1555	69	8.9	26.3	489	12
136°C/min	310 - 325	1125	1598	70	9	25.8	482	14
136°C/min	315 - 325	1112	1604	69	-	-	506	14
150°C/min	310 - 315	1100	1650	66	-	-	523	10

Figure 66: 1¼ Cr Mo, 0.48% carbon bainite. Cool rate (700 - 450°C) = 100°C / minute
Transformation temperature = 365 - 380°C. Hardness = 437 VP. Magnification X550



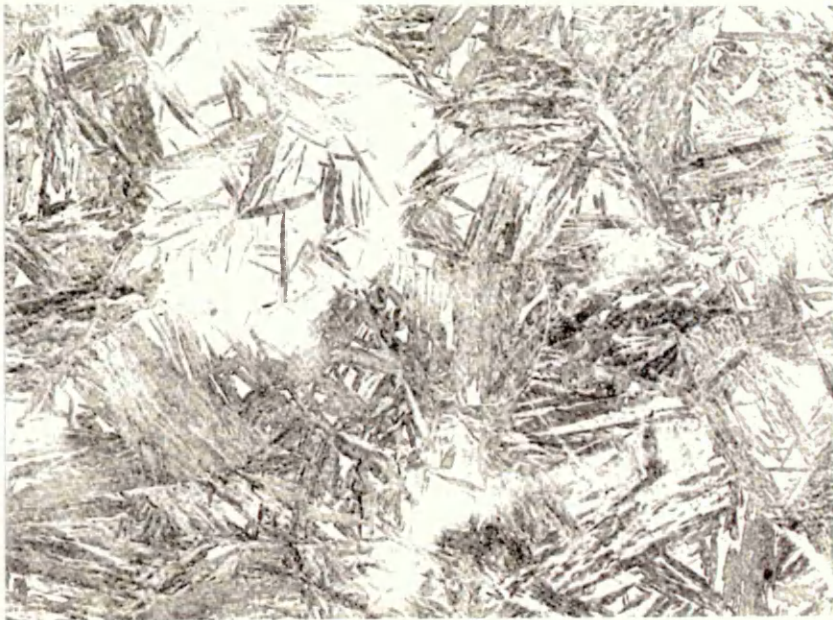
Figure 67: 1¼ Cr Mo, 0.48% carbon bainite. Cool rate (700 - 450°C) = 115°C / minute
Transformation temperature = 330 - 345°C. Hardness = 472 VP. Magnification X550



Figure 68: 1¼ Cr Mo, 0.48% carbon bainite. Cool rate (700 - 450°C) = 136°C / minute
Transformation temperature = 315 - 325°C. Hardness = 506 VPN. Magnification X550



Figure 69: 1¼ Cr Mo, 0.48% carbon bainite. Cool rate (700 - 450°C) = 150°C / minute
Transformation temperature = 310 - 315°C. Hardness = 523 VPN. Magnification X550



7.4 Martensitic alloy system results

7.4.1 Chromium / nickel alloy system results

The mechanical properties of the water quenched chromium / nickel alloy systems are given in Table 16, optical microscopy was used to clarify each microstructure, results are illustrated in figures 70 to 73.

Each microstructure consisted of martensite with quite a high proportion of bainite appearing as the darker phase often located near grain boundaries. Microhardness measurements confirmed optical results with an average 100 VPN decrease in hardness from the martensitic region to the darker etched bainitic region.

Table 16 Mechanical properties of nickel chromium alloy systems

Alloy Type	Proof strength (MPa)	Tensile strength (MPa)	Elongation (%)	Reduction in area (%)	Hardness (VPN)	Charpy Impact (J)
0.2% carbon with Cr (number 1)	930	1431	11.5	31.5	451	16.5
0.25% carbon with Cr (number 2)	1045	1658	7.5	18.9	501	9
0.2% carbon with Ni (number 3)	817	1310	11.1	30.6	423	19.5
0.25% carbon with Ni (number 4)	897	1591	4	8.8	500	10

Figure 70:- 0.2% carbon / 0.5% chromium alloy water quenched from 950°C.
Magnification X450.

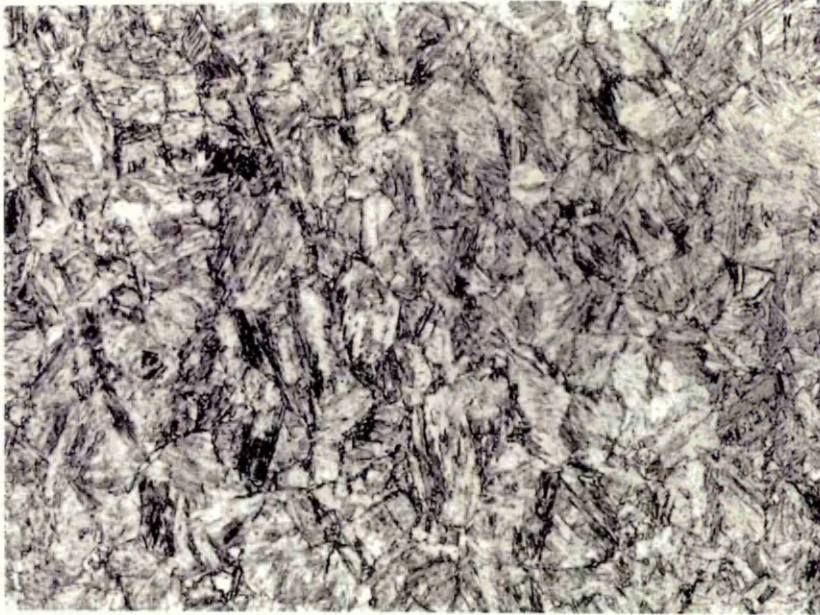


Figure 71:- 0.25% carbon / 0.5% chromium alloy water quenched from 950°C.
Magnification X450.



Figure 72:- 0.2% carbon / 0.75% nickel alloy water quenched from 950°C.
Magnification X450.



Figure 73:- 0.25% carbon / 0.75% nickel alloy water quenched from 950°C.
Magnification X450.



7.4.2 Boron martensite alloy system results

The surface condition of bar before and after the water quench was examined using a magnetic particle detector and was found to be satisfactory with no evidence of quench cracking observed.

The mechanical properties of both variants in the water quenched condition are given in Table 17. Optical microscopy confirmed that the microstructure consisted of martensite with perhaps minute quantities of bainite in the lower carbon variant (figures 74-75).

X-ray diffraction was also performed on the 0.3% carbon variant to assess the amount of retained austenite, which was found to be below 1.5% and therefore considered minimal.

Table 17 Mechanical Properties of 0.2 and 0.3% carbon boron steel

Carbon content	Proof Strength (MPa)	Ultimate tensile Strength (MPa)	Proof / UTS (%)	Elongation (%)	Reduction in Area (%)	Hardness VPN	Charpy Impact (J)
0.2% variant	1080	1506	72	9.2	43.9	459	44
0.3% variant	1205	1758	69	10	41.6	526	23

Figure 74:- 0.2% carbon boron microstructure. Austenitised at 950°C
quenched into water at 20°C (magnification X500)

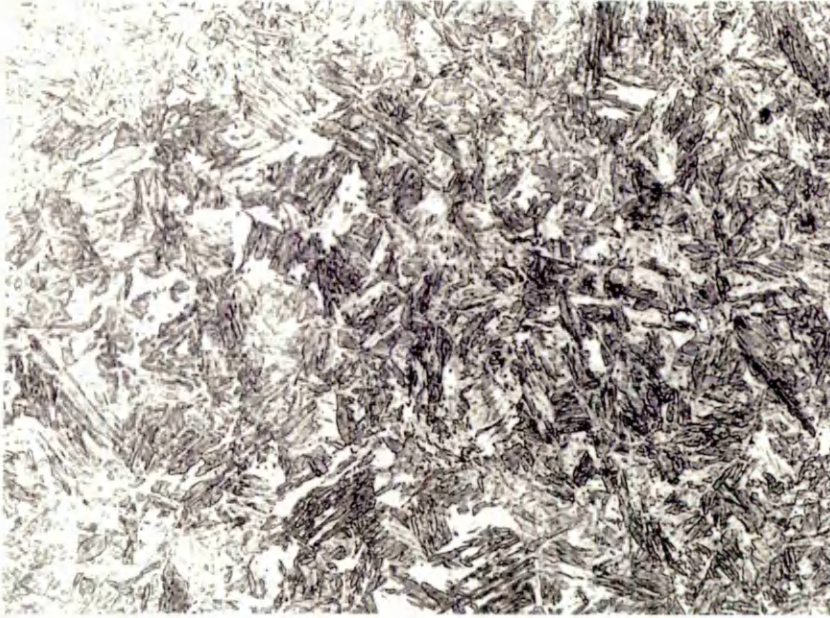


Figure 75:- 0.3% carbon boron microstructure. Austenitised at 950°C
quenched into water at 20°C (magnification X700)



7.5 Preliminary discussion:- Which alloy?

After close examination of microstructure and mechanical properties of all alloy systems, a select few were chosen for further investigations. The decision to eliminate certain alloy grades from the project was taken after the following considerations:-

- Mechanical properties must be comparable to current used material.
- Optimum structure production easily reproduced at mass production level.
- Additional strengthening where required easily accomplished during mass production .

7.5.1 Unsuitable alloy systems

The mechanical strengths obtained in the continuously cooled and isothermally treated eutectoid microstructure fell quite short of the desired Pandrol requirement even though a pearlitic microstructure of reasonable fineness with some degree of strengthening was obtained.

Interestingly, it was found that the 550, 600 and 650°C isothermally transformed 0.80 mass% carbon pearlite alloy possessed a lower hardness and ultimate tensile strength compared to the air cooled pearlite alloy. This loss in mechanical properties could be attributed to the coarsening of vanadium carbide particles and interlamellae spacing, both of which could only be correctly assessed under electron microscopy.

It is thought that even if all possible strengthening mechanisms were maximised, a significant short fall would still exist, leaving the application of cold work as the only option for further strengthening. The implementation of strict cooling regimes followed by exceptional amounts of cold work is not realistic for this type of product, hence it was decided that the eutectoid microstructure should be eliminated from the programme of research.

7.5.2 Promising alloy systems

7.5.2.1 1¼Cr Mo bainitic alloy system

This microstructure was a “borderline candidate” for further research because comparable mechanical properties were only achieved over a relatively narrow cooling regime. This was perhaps as expected, because although the continuous cooling transformation diagram of this particular alloy system indicated that a bainitic microstructure could be obtained over a relatively wide range of cooling rates, the morphology and hence mechanical properties were expected to differ significantly depending upon the proportion of upper or lower bainite obtained.

Optimum mechanical properties were obtained in the 0.4% carbon bainite alloy on application of a 110-130°C / min cooling regime from austenitisation, producing a lower bainitic microstructure. Faster cooling rates produced a mixed bainite martensite microstructure, the amount of the latter phase increased proportionally with increasing cooling rate. The fastest cooling rate employed (150°C/min.) produced a predominantly martensite structure possessing exceptionally high hardness with reduced toughness.

Decreasing the cooling rate below 110°C/min. affected the hardness quite significantly and was due to the increasing amounts of upper bainite within the microstructure.

The 0.48% carbon bainite alloy results confirmed that a lower bainite microstructure with reasonable mechanical properties was obtainable over a wider range of cooling rates compared to the previous 0.4% carbon variant.

However the optimum cooling regime required to produce a predominantly lower bainite microstructure was still quite narrow at 110-150°C/ min, and certainly not wide enough for this particular industrial application.

This was because on continuously cooling the “e” clip by forced air for example, it would be very difficult to maintain uniform optimum cooling through the clip, with notable heat transfer differences between the rear arch to the clip toe. This argument would obviously be different if the product was a simple leaf spring.

This situation is alleviated somewhat if alternatively an isothermal heat treatment is performed where after austenitisation, the alloy is quenched into a salt bath at the optimum transformation temperature.

On considering the 0.48% carbon alloy results, isothermal treatment after austenitisation should be carried out between 310 and 345°C, to produce a predominantly lower bainitic microstructure. There are however several disadvantages when quenching into salt, for example:-

- Salt bath quenching has to be carefully monitored in terms of operator safety, especially in terms of fire risk.
- Maintaining operating temperature may be difficult due to slow heat transfer.
- Product requires a cleaning operation after quench.
- Disposal / renewal of cleaning solution required at frequent intervals.

Despite these problems, it was still thought that the lower bainitic microstructure was worthy of further research, because of its promising mechanical properties, and where improvements in strength were possible after relatively small amounts of cold work.

On the development of quenching media which would procure a rapid quench to 310-350°C, but without the problems mentioned previously, this alloy system would then become a realistic alternative to current oil quenched and tempered Pandrol alloy.

7.5.2.2 Chromium and nickel martensite alloy systems

The mechanical properties of both chromium martensite variants were found to be slightly better than the nickel martensite, with approximately 15% increase in the 0.2% proof strength value. The increase in carbon content in both alloy systems also increased the proof strength and hardness but at the cost of toughness which was reduced by as much as 50%.

From the four alloy systems, the 0.25% carbon 0.5% chromium alloy possessed the best mechanical properties, with a 0.2% proof strength value only 200 MPa below the current Pandrol specification. However, the mechanical properties were perhaps not quite as expected and this was due to the fact that an appreciable amount of bainite was present in all microstructures.

The reason why a fully martensitic microstructure was not obtained appears to be due to elemental segregation since some of the optical results indicate the presence of bainite at near proximity to grain boundaries. Obviously the segregation of chromium and nickel would then create regions with inadequate hardenability allowing the formation of bainite.

Despite the mixed nature of this microstructure, the 0.25% carbon, 0.5% chromium alloy was considered as a possible replacement to the current used oil quenched and tempered Pandrol alloys, since it was realised that the mechanical properties could be improved upon by the application of cold work.

7.5.2.3 Boron martensite alloy systems

Initial alloy assessment included the examination of microstructure and mechanical properties in the straight bar form. The results obtained were very encouraging, hence the boron martensite alloy system became the most favoured, for example:-

- 0.2% proof strength close to specification, especially in the 0.3% carbon variant.

- Impact strength exceptionally superior to currently used oil quenched and tempered alloy.
- Uniform martensite microstructure with optimum hardness.
- Easy production route requiring a simple water quench from austenitisation.
- Carbon content optimised allowing for some degree of auto tempering.

Table 18 compares the results of the 0.3% carbon boron alloy to the required mechanical properties of the oil quenched and tempered silicon manganese alloy. It was noted that although proof strengths were more or less identical, the ratio of the proof strength to ultimate tensile strength was considerably less for the boron alloy. This indicated that the elastic plastic behaviour of the two alloy systems differed quite considerably, and as was later discovered (chapter 8), affected the performance of the formed clip. However, it was envisaged that additional strengthening via small amounts of cold work would dramatically improve the proof / ultimate tensile strength ratio to give an alloy system comparable, perhaps superior to the currently used SiMn Pandrol alloy.

Table 18 comparison of mechanical properties for 0.3% boron carbon alloy and Pandrol Si Mn alloy.

Alloy type	.2% Proof Strength (MPa)	Ultimate tensile strength (MPa)	PS / TS ratio (%)	Elongn. (%)	Redn. In area (%)	Hardness VPN	Charpy impact (J)
0.3% carbon Boron	1200	1750	69	9-11	40-42	~520	20-25
androl OQ & T SiMn	1200	1500	83	10-15	30-40	~480	10-12

Chapter 8

Clip results and additional mechanical results of boron alloy

8.1 Tensile results of plain bar

The tensile properties of work hardened 0.2 and 0.3% carbon boron alloy are given in table 19 and 20 respectively.

Various amounts of cold work were incorporated by initially loading each specimen to a designated value (corresponding to the 0.1, 0.2% proof strength etc.), deloading back to zero, followed by complete tensile test to failure.

Table 19:- Mechanical properties of 0.2% carbon boron steel cold worked by pre-loading the tensile specimen to a load corresponding to the 0.1 - 0.5 % proof strength

Alloy type	Amount of work hardening (Take to x% proof strength)	0.2% Proof strength MPa	Ultimate Tensile strength MPa	Proof / UTS (%)
0.2% carbon boron	0.1%	1209	1521	79
0.2% carbon boron	0.2%	1267	1534	83
0.2% carbon boron	0.3%	1324	1535	86
0.2% carbon boron	0.4%	1346	1518	89
0.2% carbon boron	0.5%	1381	1530	90

Table 20:- Mechanical properties of 0.3% carbon boron steel cold worked by pre-loading the tensile specimen to a load corresponding to the 0.1 - 0.5 % proof strength

Alloy type	Amount of cold work (Take to x% proof strength)	0.2% Proof strength MPa	Ultimate Tensile strength MPa	Proof / UTS (%)
0.3% carbon boron	0.1%	1323	1724	77
0.3% carbon boron	0.2%	1412	1763	80
0.3% carbon boron	0.3%	1467	1724	85
0.3% carbon boron	0.4%	1529	1724	89
0.3% carbon boron	0.5%	1565	1774	89

A relationship between the 0.2% proof strength and amount of cold work incorporated is illustrated in figure 76.

The stress strain curve for virgin and work hardened boron martensite alloy is also shown in figure 77, and clearly illustrates the straightening of the elastic portion of the cold worked alloy. Included on this graph is current Pandrol material in the unworked oil quenched and tempered condition for comparison.

On comparing the results in tables 19 and 20, a clear relationship between carbon content and the amount of cold work required to obtain the desired mechanical properties was evident. Figure 78 illustrates this, showing that from a knowledge of carbon content it was possible to calculate the amount of cold work required to achieve the desired mechanical properties, i.e. a 0.2% proof strength value of 1350 MPa.

Figure 76 :- Graph showing the relationship between the amount of cold work and the 0.2% proof strength obtained, for the 0.2 and 0.3% carbon boron alloy

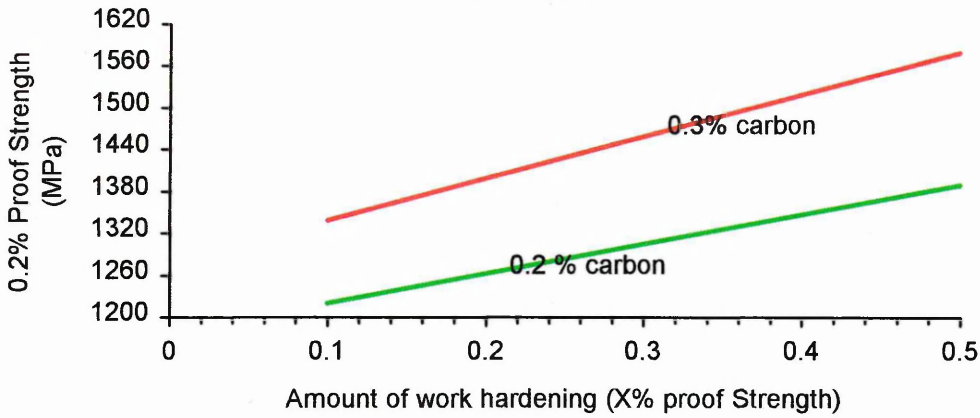
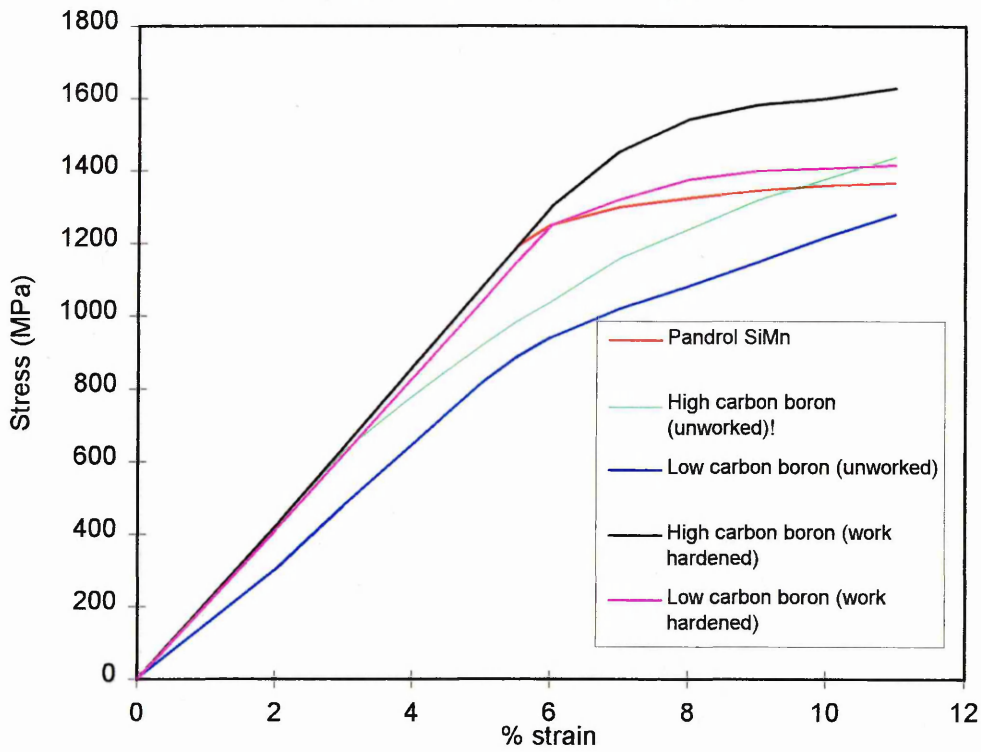
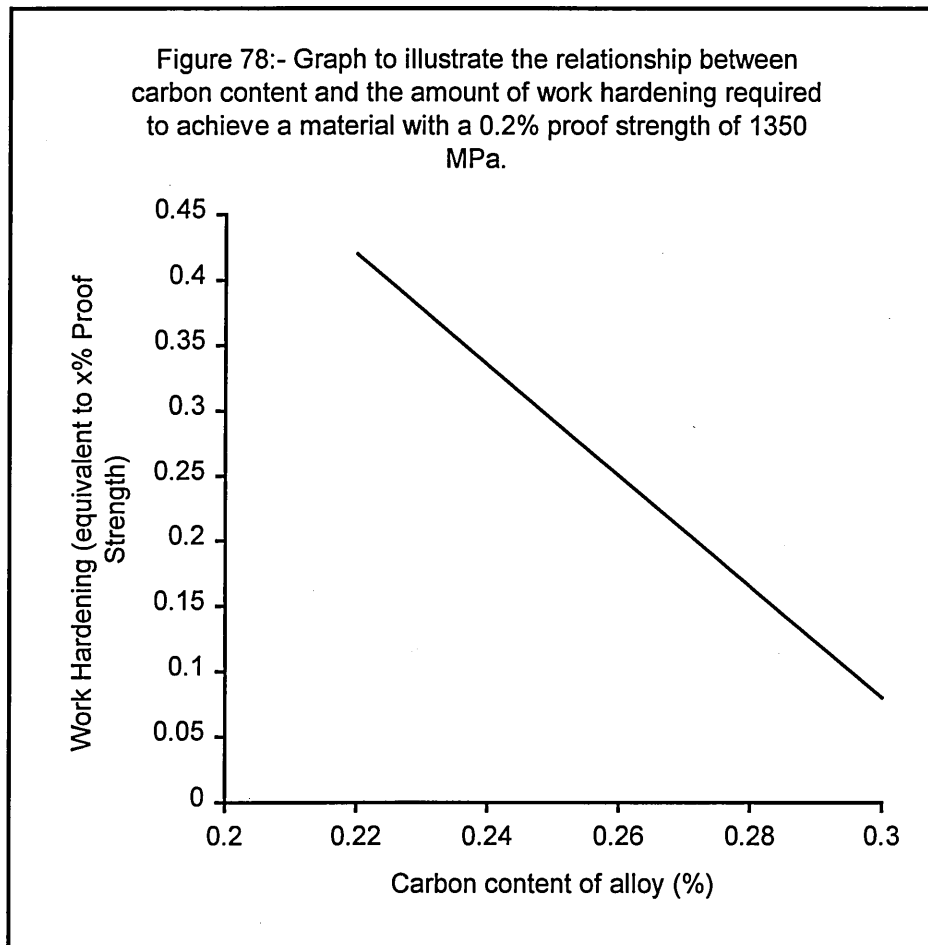


Figure 77:- Stress strain curve for work hardened boron alloy (previously loaded to the 0.2% proof strength limit, then deloaded to zero) with unworked boron alloy and tempered silicon manganese Pandrol alloy for comparison.





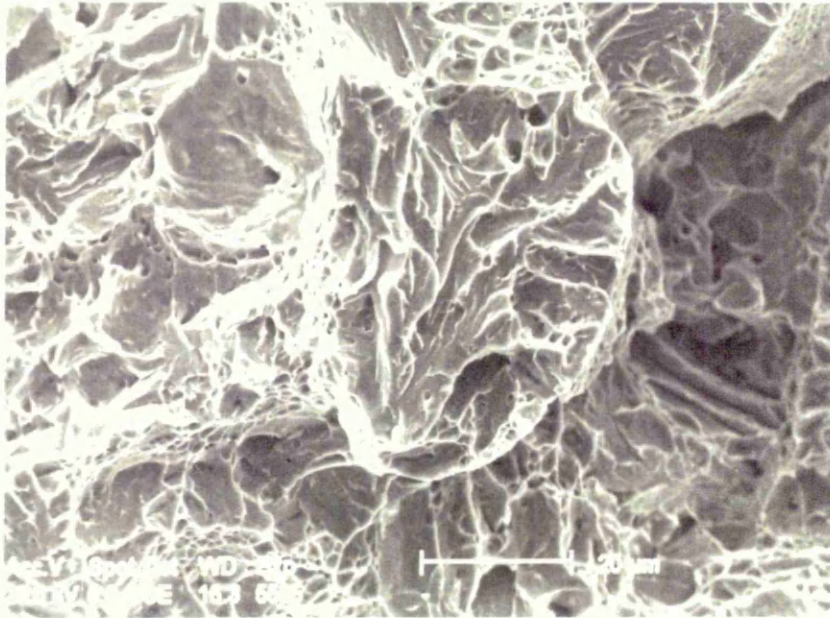
8.2 Tensile and Impact properties of specimens from formed clip

Table 21 provides tensile results for the 0.2 and 0.3% carbon boron alloy. The results obtained were consistent with tensile results of the straight bar which was as expected since the quenching rates were similar.

The fracture surface of Charpy impact specimens were examined utilising scanning electron microscopy. The results are illustrated in figure 79 and 80, for the 0.2 and 0.3% carbon boron alloy systems respectively.

The 0.2% carbon alloy impact surface exhibited a typical ductile fracture surface, whilst in the higher carbon variant regions of quasi-cleavage were observed. This explains the quite dramatic decrease in impact energy which was also observed in impact specimens taken from straight bar (chapter 7).

Figure 80:- Impact fracture surface of 0.3% carbon boron alloy system



8.3 Toe load results from “virgin” clips

Table 22 provides toe load results of the 0.2 and 0.3% carbon boron alloy clips with Pandrol oil quenched and tempered silicon manganese clip for comparison.

The results indicate that the boron clips were capable of attaining the specified toe load of 1250 Kg (+/- 100 Kg). However these clips were inadvertently overpressed during production thus placing the toe out “of position” relative to the clip body. The effect of this was detected when the clip was driven into the test assembly with an unusually high toe load achieved in both boron and Silicon manganese alloy systems.

In the case of the silicon manganese Pandrol clip, the toe load achieved was almost 350Kg above specification, and if all these clips had been manufactured with correct toe heights, the boron alloy clips would have fallen quite short of Pandrol specification.

On comparing silicon manganese Pandrol alloy to both boron grades in terms of permanent set, up to a four fold increase was observed in the later alloy, and was due to a lower proof strength ultimate tensile strength ratio in the boron alloy .

Table 22: Toe load and Permanent set results:

0.2, 0.3% carbon boron and Silicon manganese alloy (clip type 2099)
water quenched from forming at 950°C

Alloy Type	Permanent set (mm)	Toe load (Kg)
Si Mn clip	1.22	1595
Si Mn clip	0.94	1560
Si Mn clip	1.24	1432
0.2% carbon boron clip M4	3.73	1226
0.2% carbon boron clip M46	3.96	1262
0.2% carbon boron clip M17	4.14	1240
0.3% Carbon boron clip N2	3.98	1397
0.3% Carbon boron clip N44	3.37	1475
0.3% Carbon boron clip N5	3.68	1383

M and N identifies particular clip.

8.3.1 Toe load results of work hardened clip

To recap, clips that had been previously toe load tested were once again driven into the test assembly where it was assumed that some degree of cold work had been incorporated from the previous test (detailed in section 8.3)

The results of strain hardened 0.2% boron carbon alloy are given in table 23, and clearly indicate that a sufficient amount of work hardening had taken place since the permanent set values were well within specification with adequate toe load also maintained.

Note:- Once again these clips were also inadvertently overpressed during manufacture, hence possess an artificially high toe load.

**Table 23: Toe load results of 0.2% boron carbon alloy clips
(Virgin and scragged)**

Clip identification	Virgin clip toe load(Kg)	cold worked clip toe load (Kg)	Permanent set after first test (mm)	Permanent set after second test (mm)
Clip 274	1250	1220	5.08	0.3
Clip 278	1320	1250	5.10	0.27
Clip 285	1290	1250	5.43	0.27
Clip 291	1280	1240	5.36	0.25
Clip 296	1240	1220	5.21	0.26

8.4 Load deflection results of “virgin” clips

The load deflection results of “virgin” 0.2 and 0.3% carbon boron clips determined on the Zwick tensile machine at Pandrol Laboratory are shown in table 24. These clips were load deflected to 15 mm, with permanent set calculated from a toe height and angle gauge. Achieved loads were noted from load extension graphs as shown in figure 81 and 82.

Note:- Toe height of clip did not effect load deflection testing as with toe load evaluation.

Table 24:- Load deflection results of "virgin" 0.2 and 0.3% boron clips deflected to 15 mm. on Zwick tensile testing machine.

Clip identification	Achieved load at 15 mm deflection (Kg)	Permanent set mm
0.2% carbon boron clip M3	1167	2.94
0.2% carbon boron clip M9	1157	2.99
0.2% carbon boron clip M13	1160	2.89
0.3% carbon boron clip N3	1248	2.54
0.3% carbon boron clip N43	1307	2.23
0.3% carbon boron clip N39	1277	2.26

This table clearly illustrates the effect of carbon content on the achieved clip load and permanent set characteristics, with an average load increase of 116 Kg. and 0.6 mm reduction in set for the higher carbon variant.

Figure 81:- Load deflection curve for "virgin" 0.2% carbon boron clips deflected to 15 mm on Zwick tensile testing machine at Pandrol Laboratory.

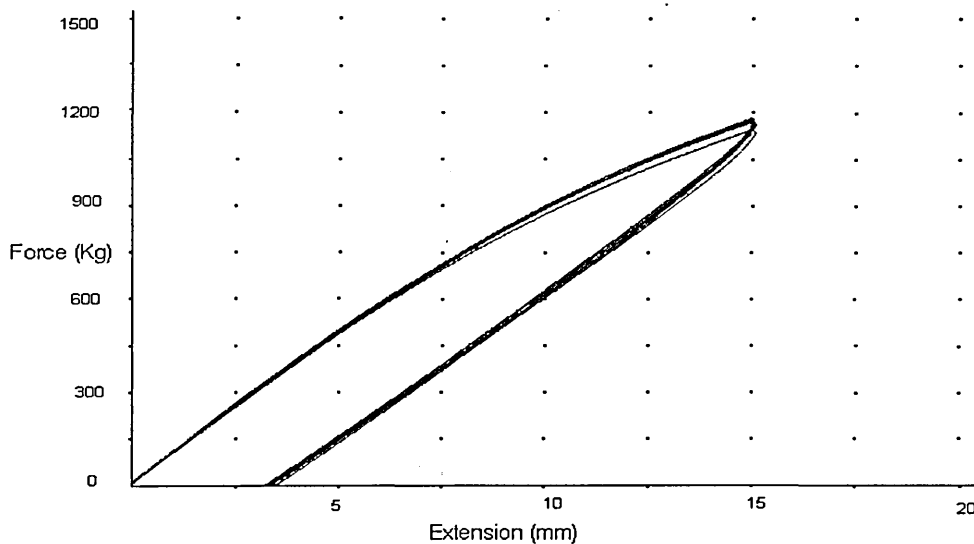
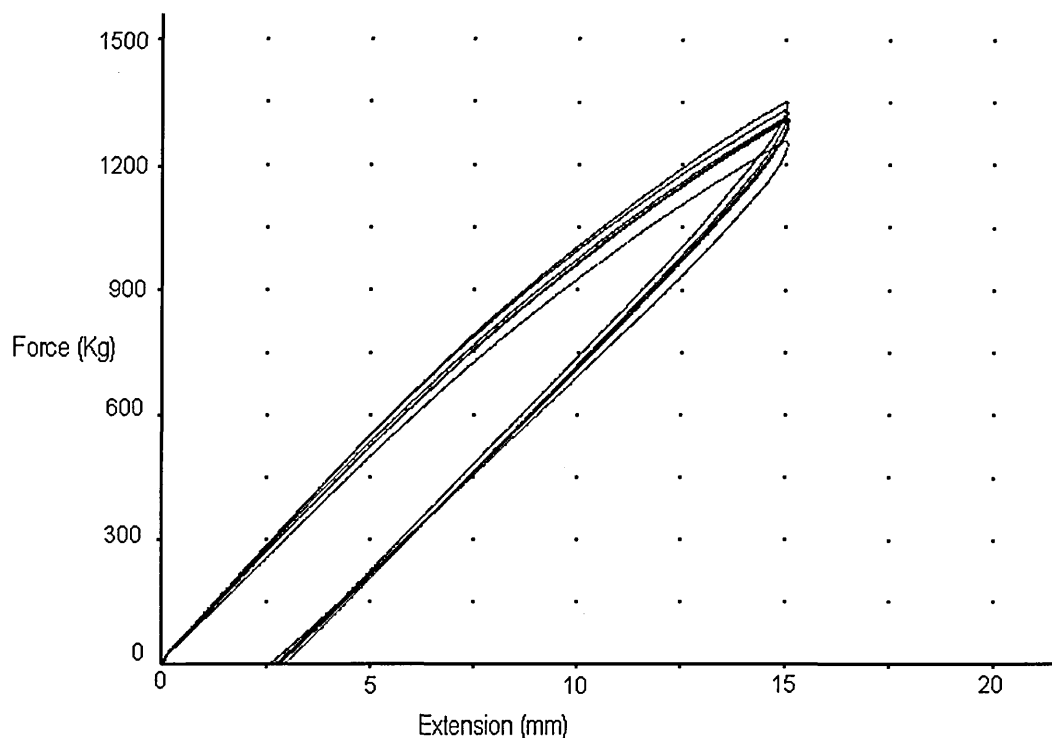


Figure 82:- Load deflection curve for "virgin" 0.3% carbon boron alloy deflected to 15 mm on Zwick tensile testing machine at Pandrol Laboratory.



Figures 81 and 82 clearly showed that both the 0.2 and 0.3% carbon boron clips began to plastically deform at quite low loads (hence the high values of permanent set). These results mirror findings in section 8.3 from toe load testing in the clip assembly.

8.4.1 Load deflection results of work hardened clips

The work hardening of clips using the load deflection rig in the Pandrol laboratory was achieved by loading clips to a deflection of 15 mm. (2.4 mm beyond the design deflection), this load was then removed gradually.

These clips were then tested to the design deflection noting load obtained and permanent set as given in table 25.

Table 25 Mechanical properties of work hardened low and high carbon boron alloy clips (previously taken to 15 mm deflection)

Clip identification	Measured permanent set (mm)	Load (Kg)
M3 / 0.2%carbon	0.304	1185
M9 / 0.2%carbon	0.254	1183
M13 / 0.2%carbon	0.305	1207
N7 / 0.3% carbon	0.178	1380
N1 / 0.3% carbon	0.127	1299
N6 / 0.3% carbon	0.203	1322
N36 / 0.3% carbon	0.152	1348
N12 / 0.3% carbon	0.152	1330
N28 / 0.3% carbon	0.007	1331

Figure 83 and 84 illustrates typical load deflection curves for the work hardened 0.2, 0.3% carbon boron alloy. On comparing these curves to the previous load deflection curves obtained from the “virgin” boron clips (figure 81 and 82), a definite straightening of the elastic portion was observed.

Figure 83:- Load deflection curve for work hardened 0.2% boron carbon alloy (previously loaded to 15mm)

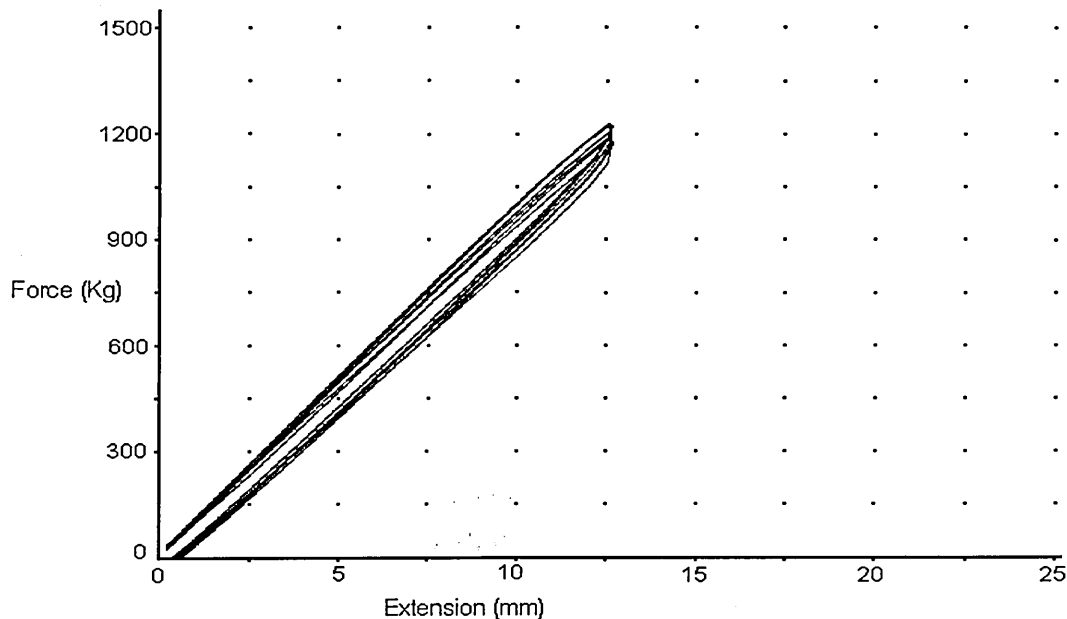
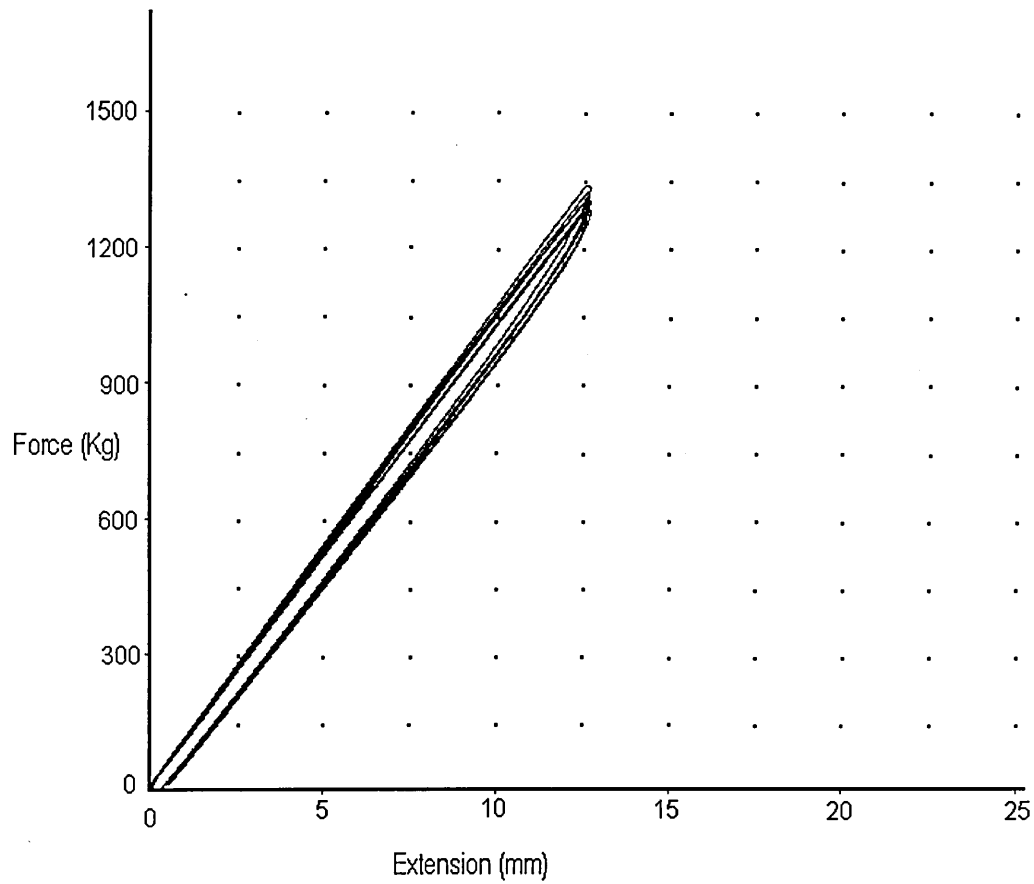


Figure 84:- Load deflection curve for work hardened 0.3% boron carbon alloy (previously loaded to 15mm)



8.5 Microstructural results

Samples taken from the centre leg region were examined using optical microscopy, figures 85 and 86 illustrate typical microstructures obtained for both boron grades.

As with samples taken from the water quenched straight bar, the microstructure consisted of predominantly martensite with perhaps small amounts of bainite. Clarification of the presence of bainite plus auto tempered martensite required transmission electron microscopy as discussed in chapter 9.

Figure 85:- Optical microstructure of 0.2% boron carbon alloy.

Sample taken from clip centre leg

(water quenched from forming at 950°C) Magnification 500X

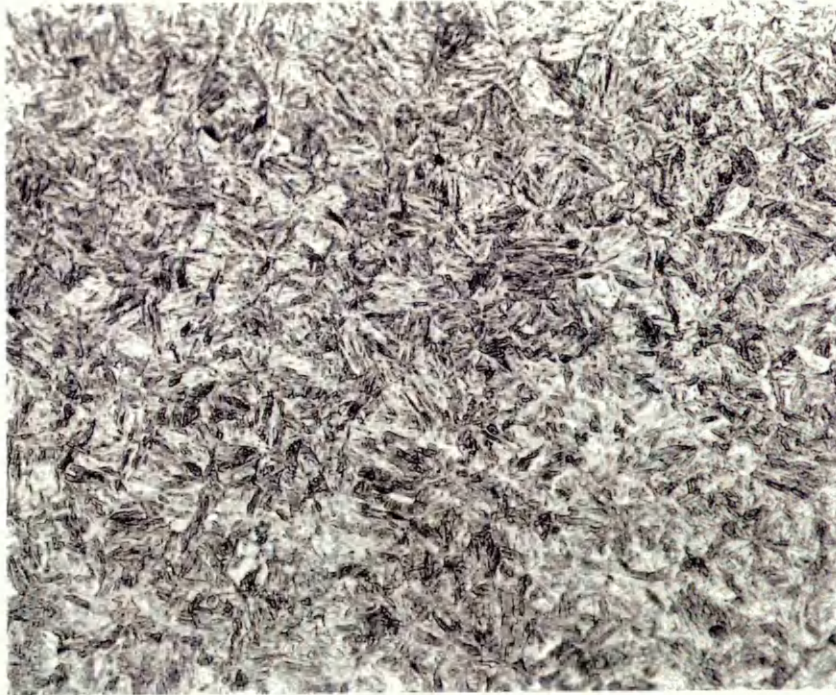
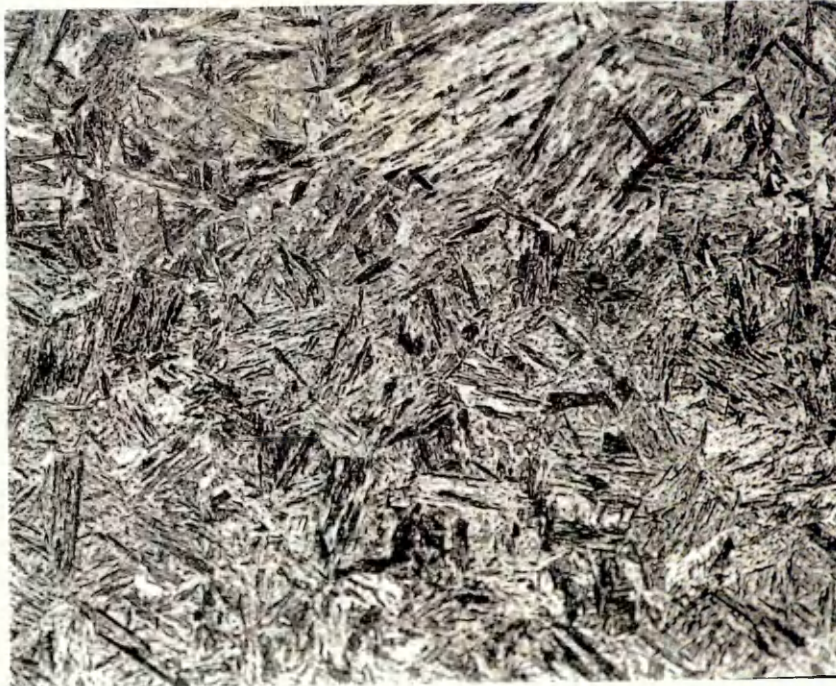


Figure 86:- Optical microstructure of 0.3% boron carbon alloy.

Sample taken from clip centre leg

(water quenched from forming at 950°C) Magnification 500X



8.6 Fatigue results

The fatigue results of water quenched 0.2% boron carbon and oil quenched and tempered silicon manganese clips are surmised in table 26.

The endurance limits for both alloys were determined by noting the dynamic deflection when 6 or more clips survived after 3×10^6 cycles (65 hours). The specification endurance limit for oil quenched and tempered silicon manganese Pandrol alloy was given as ± 6.5 mm dynamic deflection, with clips often easily surpassing this. Table 26 shows that the endurance limit for both boron and silicon manganese alloy was well within the specified dynamic deflection, however as anticipated the measured toe load and permanent set for the boron grade was much lower which probably accounted for the improved fatigue performance. Figure 87 shows the fracture surface of a clip which had failed under ± 0.8 mm dynamic deflection. This was attributed to the fact that crack initiation had taken place at a tool mark and was not due to any microstructural defect.

Figure 87:- Fatigue fracture surface of clip failed due to tool mark.

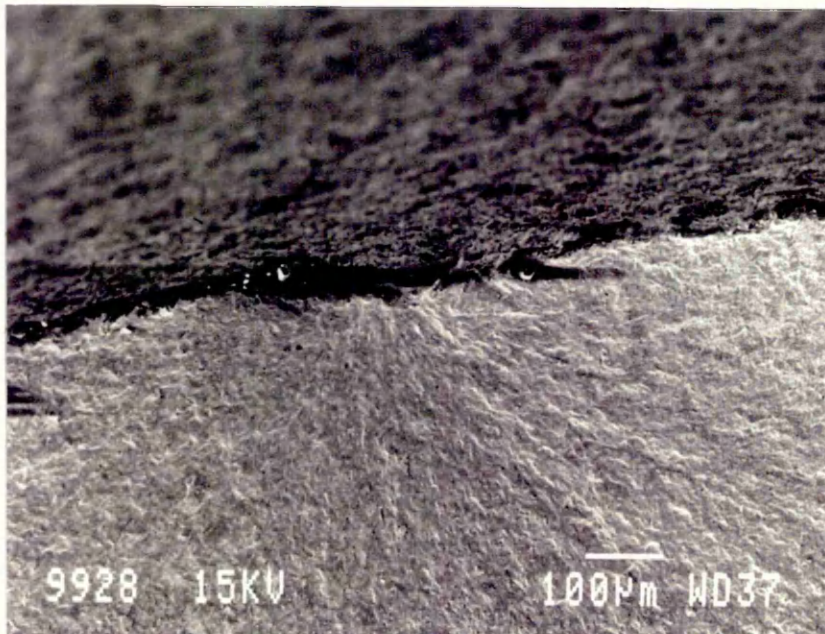


**Table 26:- Fatigue results of 0.2% carbon boron
and silicon manganese alloy clips**

Alloy type	Dynamic deflection	Average load before test (Kg)	Average load after test (Kg)	Average loss of toe load (Kg)	Perm. set (mm)	percentage pass (Pass/ tested)
Si Mn	+/- 0.7mm	1137	1061	79	0.56	100%(6/6)
0.2% Boron carbon	+/- 0.7mm	1025	875	150	2.9	100%(6/6)
SiMn	+/- 0.8 mm	1146	1069	77	0.56	83%(10/12)
0.2% Boron carbon	+/- 0.8 mm	990	829	161	2.43	90%*(9/10)
SiMn	+/- 0.85 mm	1135	1021	114	0.70	33%(2/6)
0.2% Boron carbon	+/- 0.85 mm	980	840	140	2.67	90%*(9/10)
SiMn	+/- 0.9 mm	1217	1102	115	0.72	28%(2/7)
0.2% Boron carbon	+/- 0.9 mm	1038	890	148	3.9	100%(6/6)
Si Mn	+/- 0.95 mm	1160	-	-	-	0%(0/6)
0.2% Boron carbon	+/- 0.95 mm	1015	847	168	4.1	33%(2/6)
0.2% Boron carbon	+/- 1.0 mm	1090	935	155	4.15	20%(1/5)

Notes :- * These clips failed due to excessive tool marks / surface defect.

Chapter 9

Microstructural evaluation of optimum alloy systems

9.1 Morphological studies 1.25% chromium molybdenum alloy system

9.1.1 Optical microscopy

Optical microscopy revealed a lath like structure with well defined bands of a lighter etched featureless phase (figure 88 and 89). Because of the isothermal history and chemistry of this alloy system (quenched into salt bath at 320°C), a predominantly lower bainitic microstructure was anticipated and indeed found. The light etched phase was thought to consist of martensite with a microhardness of 590 VPN, some 100 VPN higher than the bulk microstructure. This phase was thought to have formed as a result of elemental segregation which was confirmed by EDS digital line scanning detailed in section 9.1.2.

Figure 88 shows the 25% deformed sample with only a few lath packets orientated with respect to the deformation direction. However, it was noted that a significant number of lath packets were orientated at an angle close to the deformation direction. In contrast the 10% deformed sample (figure 89) appeared no different to undeformed sample (figure 90) with lath packets aligned in a random manner.

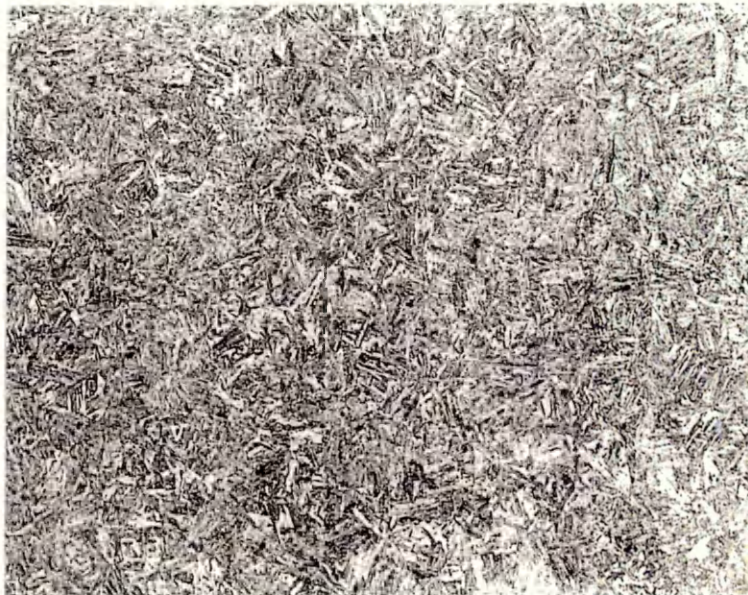
In the 50% deformed sample, a relatively significant amount of the laths were orientated close to and in the direction of rolling (figure 92). Additionally some laths appeared almost banded in nature (broken up) as shown in figure 92.

Figure 88:- 1.25 Cr Mo sample, isothermally treated at 320°C, deformed 25% showing some lath packets aligned close to and in roll direction Magnification ~200X.



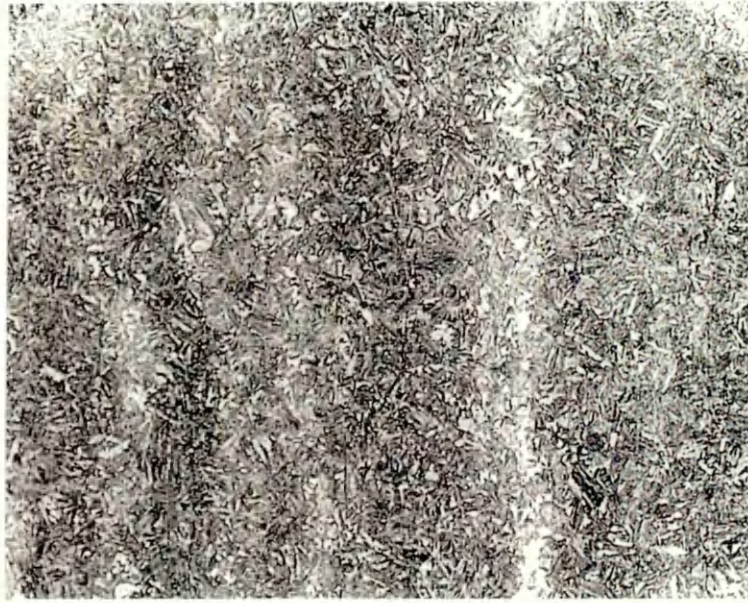
Laths orientated close to and in roll direction

Figure 89:- 1.25 Cr Mo sample, isothermally treated at 320°C, deformed 10% showing lath packets orientated in a random manner. Magnification ~200X.



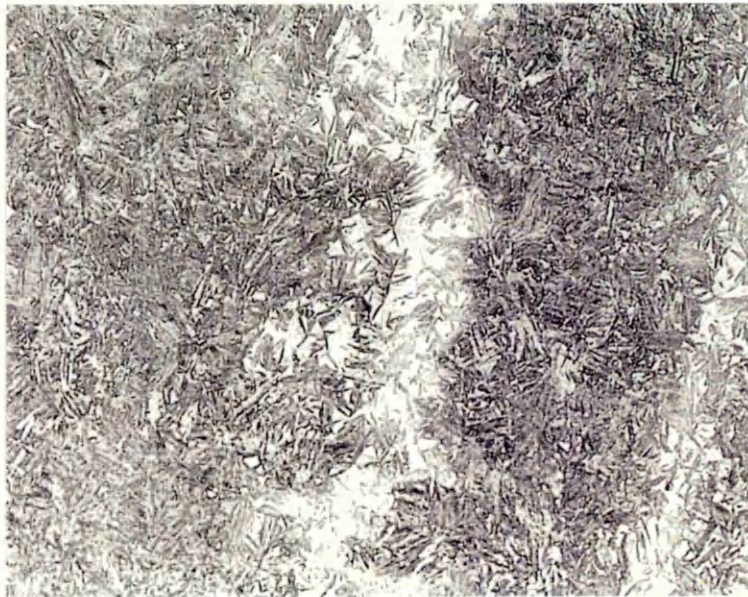
↓ roll direction

Figure 90:- 1.25 Cr Mo sample, isothermally treated at 320°C, undeformed.
Lower bainitic microstructure with light etched banded regions of martensite.
Magnification ~200X.



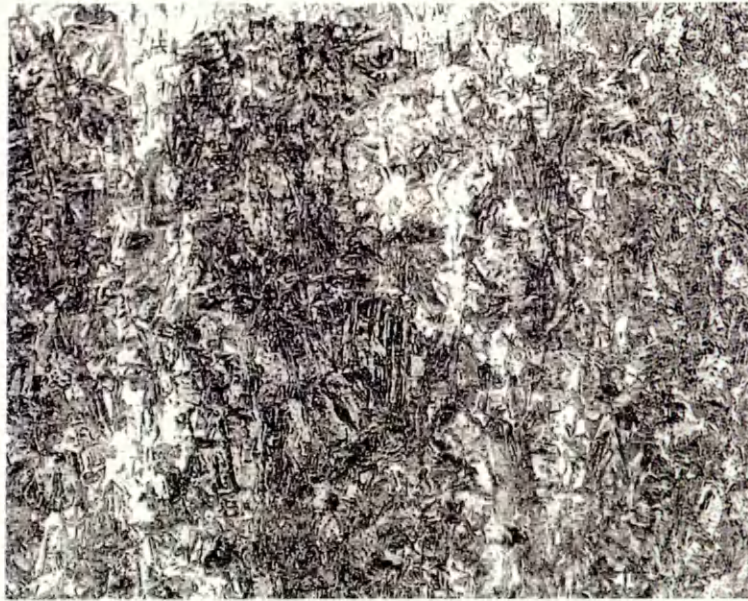
↓ Roll direction

Figure 91:- 1.25 Cr Mo sample, isothermally treated at 320°C, deformed 25%.
Lower bainitic microstructure with light etched banded regions of martensite.
Magnification ~350X.



↓ roll direction

Figure 92:- 1.25 Cr Mo sample, isothermally treated at 320°C, deformed 50% showing laths aligned close to and in the roll direction Magnification ~200X.



↓ roll direction

Laths orientated in roll direction

9.1.2 Segregation analysis results using scanning electron microscopy

The segregation of chromium, molybdenum silicon and iron was investigated utilising the EDS digital line scanning facility on the Philips XL40 scanning electron microscope. Figure 93 illustrates the region examined with the concentration of each element determined along the line shown. The analysis line traversed along a fully bainitic region, through to a mixed bainite martensite area, onto a fully martensitic band then abruptly back into the bainite region. Figure 94 shows the line scan result for chromium, molybdenum silicon and nickel. A significant increase in chromium and molybdenum was observed with perhaps a subtle increase in silicon also. Additionally a magnified version of the iron line scan shown in figure 95 indicated a minute amount of iron depletion within the chromium / molybdenum rich region.

The profile shape of the chromium and molybdenum line indicated a gradual increase in segregation to a maximum followed by a sharp decrease. Figure 96 shows the chromium molybdenum line scan superimposed onto the analysed region of microstructure. The scan line first passes through a mixed region of martensite bainite before entering the martensite band hence the gradual increase in chromium and molybdenum segregation. In contrast, to the right of the martensite band, the microstructure changes abruptly to bainite and this is reflected in the line scan with a rapid decrease observed in chromium and molybdenum concentration (point x).

Figure 93:- Microstructure examined for segregation analysis utilising XL40 SEM EDS facility
Magnification approx.

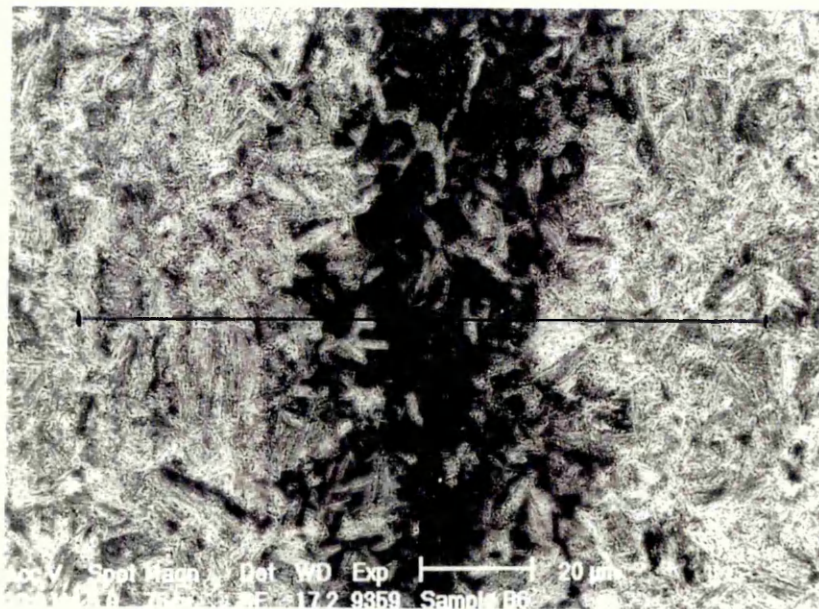


Figure 94:- Line scan for chromium, molybdenum and silicon
taken from region shown in figure 93

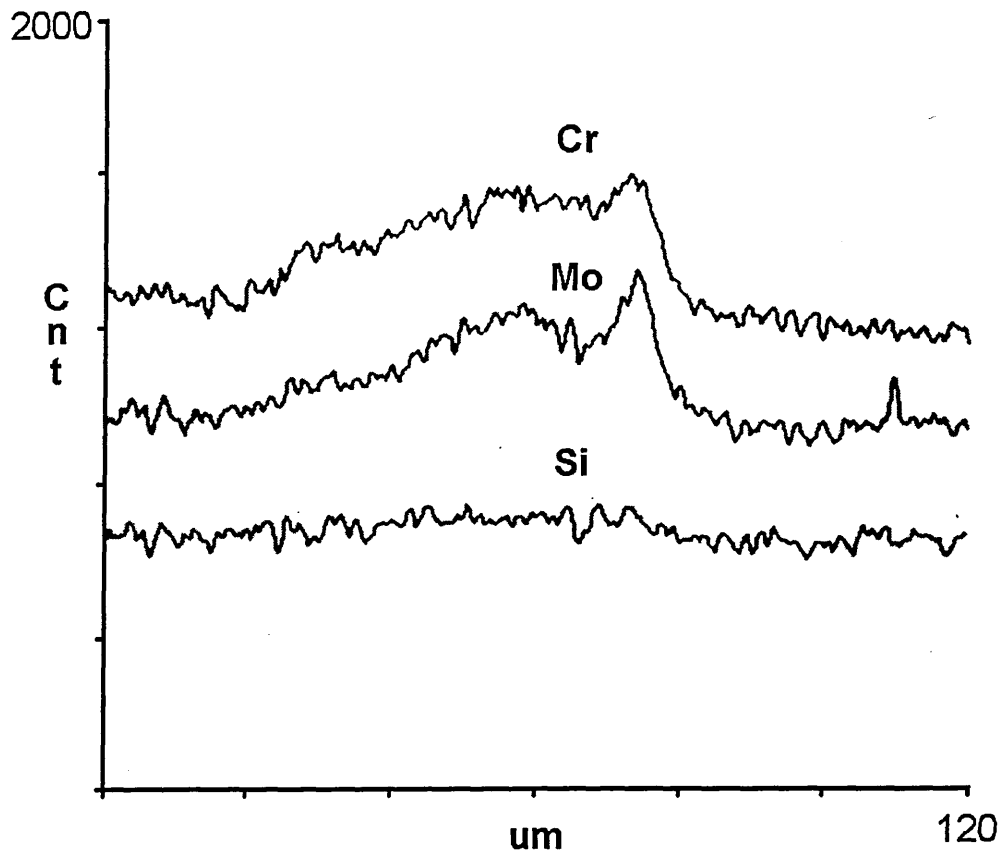


Figure 95:- Line scan for iron magnified to show subtle depletion in chromium / molybdenum
rich region (taken from region shown in figure 93).

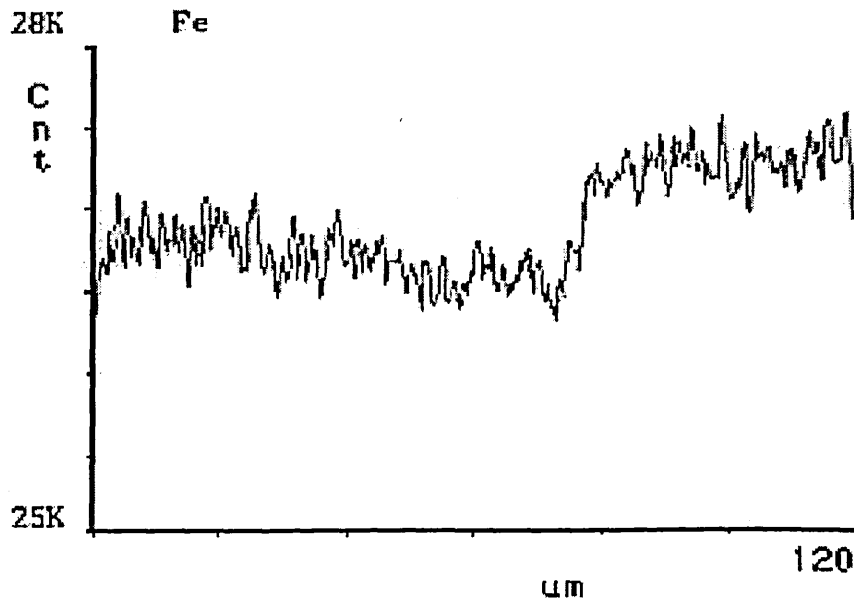
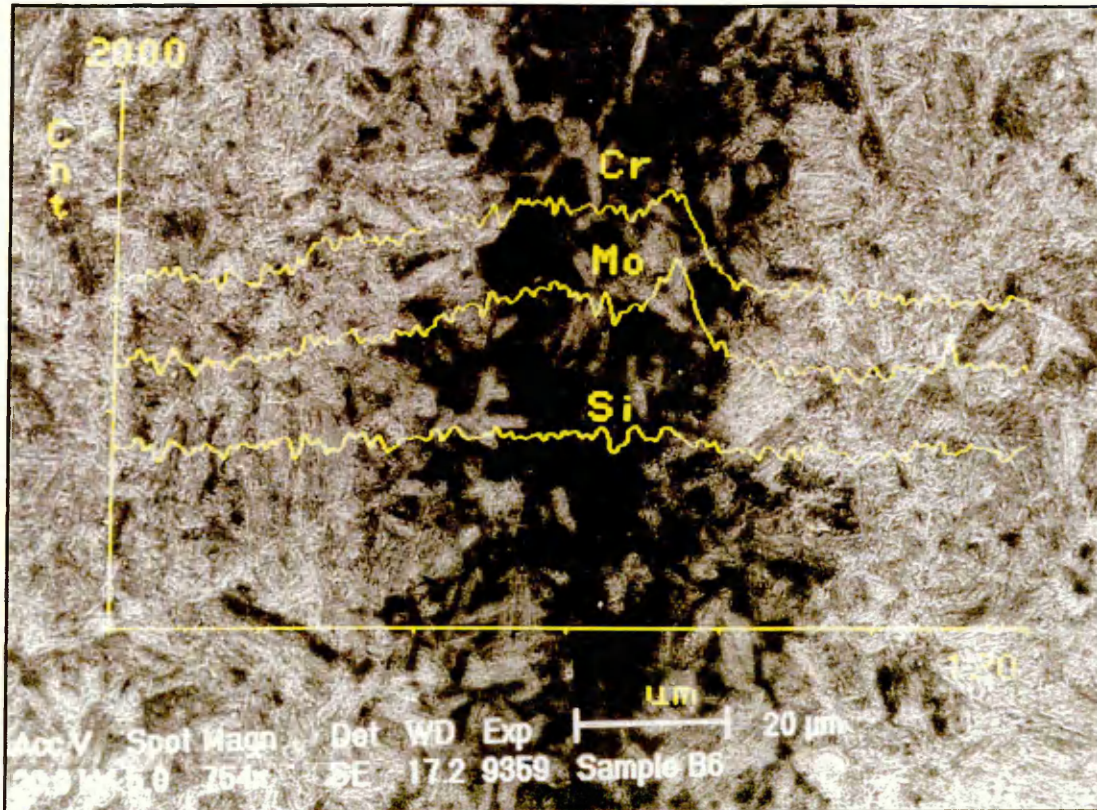


Figure 96:- Chromium, molybdenum line scan superimposed onto microstructure examined (magnification approx.)



9.1.3 Transmission electron microscopy

Transmission electron microscopy on all 1.25 mass% chromium molybdenum alloy systems revealed a predominantly lath like structure with a fine dispersion of elongated disc shaped carbides. Lath thickness varied considerably, as did the carbide population within, ranging from virtually nil to prolific. The majority of carbide precipitates were found actually within the lath, occasionally carbides were also found at the lath boundary. (Carbide identification given in section 9.6)

Figure 97 illustrates a lath packet which appeared free of carbides. A high localised dislocation density was also noted and an approximate lath width of $0.2 \mu\text{m}$ suggests that these laths are martensitic. Figure 98 also shows a typical highly dislocated martensitic lath of $0.2 \mu\text{m}$ in thickness within a lath packet.

Figure 97- Transmission Electron Micrograph of 1.25% Cr Mo alloy (10% deformed)
illustrating packets of martensite laths.
(Magnification 52K)

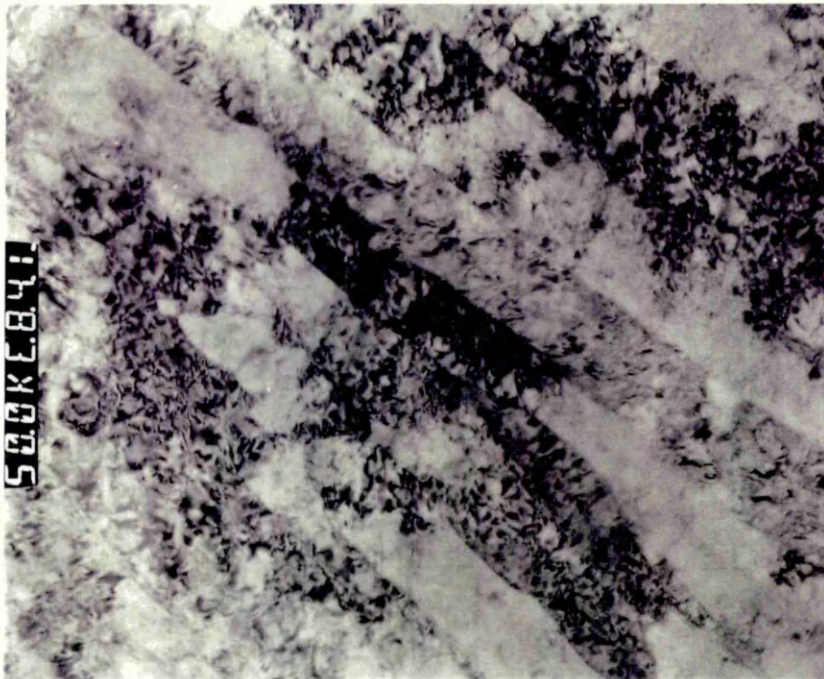
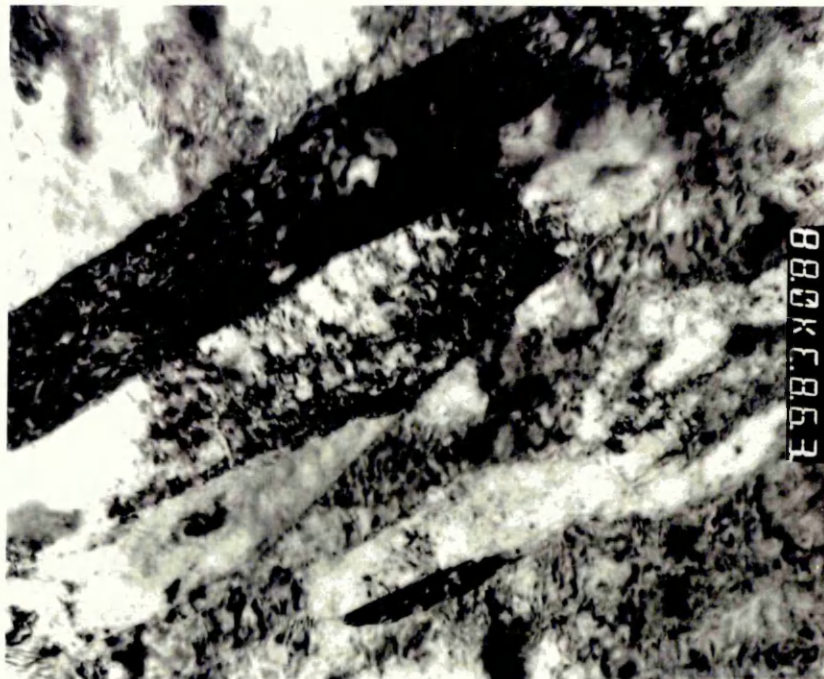


Figure 98- Transmission Electron Micrograph of 1.25% Cr Mo alloy (10% deformed)
illustrating highly dislocated martensite lath .
(Magnification 90K)



In contrast figure 99 shows a packet of laths containing carbides typically oriented at 60° to the long axis of the plates. The average lath thickness was also found to be greater than the former ranging from 0.7 to $1.0\mu\text{m}$. In addition, subtle banding within the bainitic laths was occasionally observed, often with carbides extending beyond these boundaries (figure 99).

The frequency of relatively wide laths coupled with interlath carbide indicated that this microstructure consisted predominantly of lower bainite. Packets of thinner carbide free laths identified as martensite were possibly associated with the chromium molybdenum rich regions.

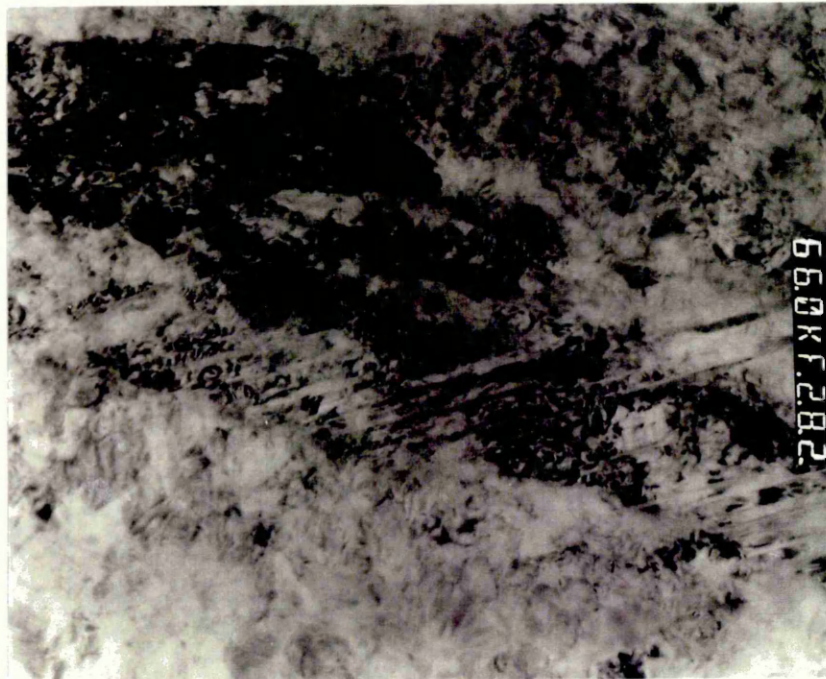
Figure 99- Transmission Electron Micrograph of 1.25% Cr Mo alloy (undeformed) illustrating packets of lower bainitic laths. (Magnification 29.5K)



At high magnification (50K and above) pockets of exceptionally fine laths were also observed. These differed from the previously mentioned martensitic laths on a degree of fineness being approximately 0.01 to 0.025 μm in thickness.

A high dislocation density was also associated within these laths as shown in figure 100.

Figure 100:- Transmission electron micrograph of undeformed 1.25% Chromium Molybdenum alloy showing typical pocket of fine lath phase. (Magnification 68K)



Additionally, it appeared that the 25 and 50% deformed samples contained significantly more fine lath phase than the undeformed and 10% deformed sample. The 50% deformed microstructure given in figure 101 shows a large area of fine lath like phase. Massive regions of fine lath phase were not observed in the undeformed or 10% deformed sample, moreover they appeared as small “pockets” as shown previously in figure 100.

Figure 101:- Transmission electron micrograph of 50% deformed 1.25% chromium molybdenum alloy showing typical massive fine lath phase region. (Magnification 68K)



The dislocation density varied significantly depending upon the amount of prior cold work. Overall the undeformed and 10% deformed microstructure possessed a moderate dislocation density, however dense dislocation forests were observed especially within martensitic laths and at carbide interfaces. Figure 102 shows a bainitic lath packet with moderate dislocation density.

Figure 102:- Transmission electron micrograph of 10% deformed 1.25% chromium molybdenum alloy showing bainitic lath with moderate dislocation density.

Magnification 29.5K.



In contrast to the undeformed and 10% deformed, the 25 and 50% deformed microstructure was highly dislocated throughout, making it was quite difficult to clarify the exact morphology in some regions. Carbides appeared surround by dense forests of dislocations and in some cases appeared “sheared” as shown in figure 103 and 104.

Figure 103:- Bright field transmission electron micrograph of 1.25% chromium molybdenum alloy 50% deformed. Magnification 152K).

Sheared carbides within highly dislocated bainite lath.

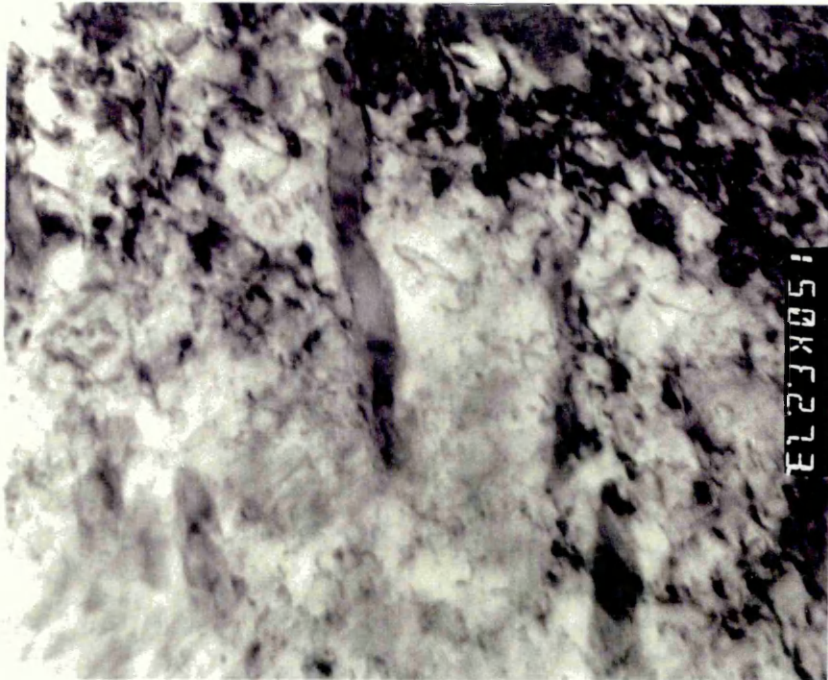


Figure 104:- Dark field transmission electron micrograph of 1.25% chromium molybdenum alloy 50% deformed. Magnification 152K).

Sheared carbides within highly dislocated bainite lath.



In addition to the frequent dense dislocation forests frequently observed within the martensitic laths of the 25 and 50% deformed alloy, occasional dislocation cellular arrays were observed in the bainitic laths. These cellular arrays were not as well defined or as frequently observed compared to the tempered alloys, however their existence did signify that some degree of cross slip was taking place in regions of comparatively lower dislocation density.

To summarise, the deformed microstructure was found to consist of heavily dislocated martensitic laths with extensive amounts of twinning and bainitic laths of lower dislocation density and occasional cellular arrays.

9.2 Morphological studies of 0.25% carbon, 0.5% chromium alloy.

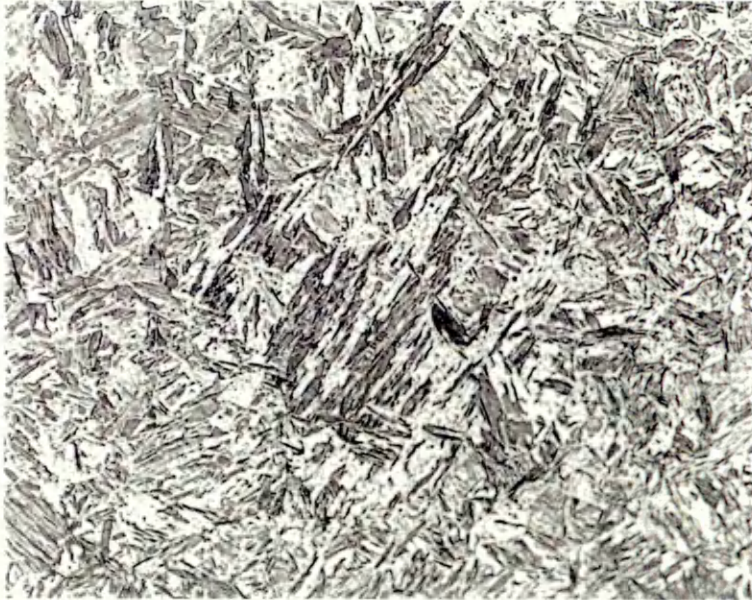
9.2.1 Optical microscopy

Optical microscopy revealed a uniform lath like microstructure for both undeformed and deformed samples. This lath morphology together with a hardness of 530 VPN and above suggested that these microstructures were predominantly martensitic with perhaps small amounts of lower bainite. Figures 105 and 106 show the undeformed and 10% deformed 0.25 mass% carbon 0.5 mass% chromium variant respectively. Earlier optical examinations of this alloy system (chapter 8), indicated large amounts of lower bainite existed alongside martensite. However this was due to the fact that the previous sample thickness was five times larger possessing a completely different cooling rate profile. As with the 1.25% chromium molybdenum alloy system, the orientation of laths towards the roll direction was observed in the 25 and 50% deformed microstructure only. Figure 107 shows the 25% deformed microstructure indicating a subtle degree of lath orientation. Figure 108 shows the 50% deformed microstructure with many distinctly aligned and in some cases banded laths.

Figure 105:- Optical micrograph of undeformed 0.25% carbon 0.5% chromium alloy. Water Quenched from 950°C. (Magnification 150X)

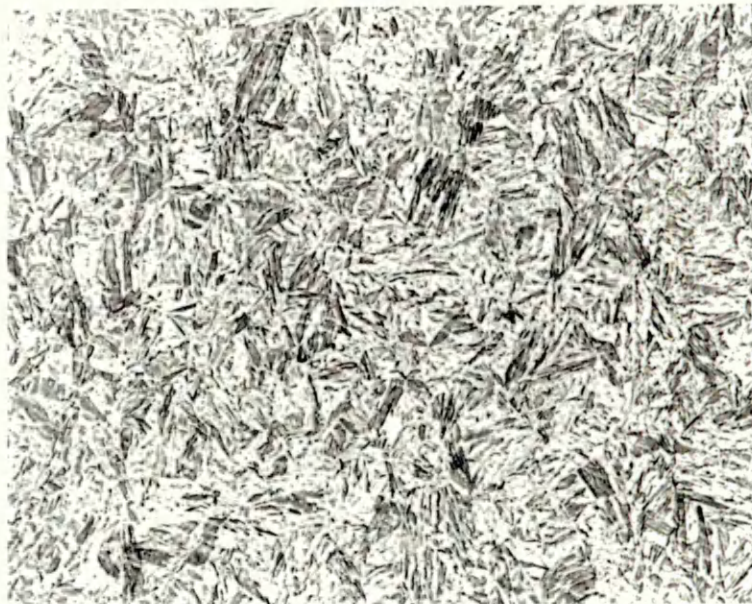


Figure 106:- Optical micrograph of 10% deformed 0.25% carbon 0.5% chromium alloy.
Water Quenched from 950°C. (Magnification 500x)



↓ roll direction

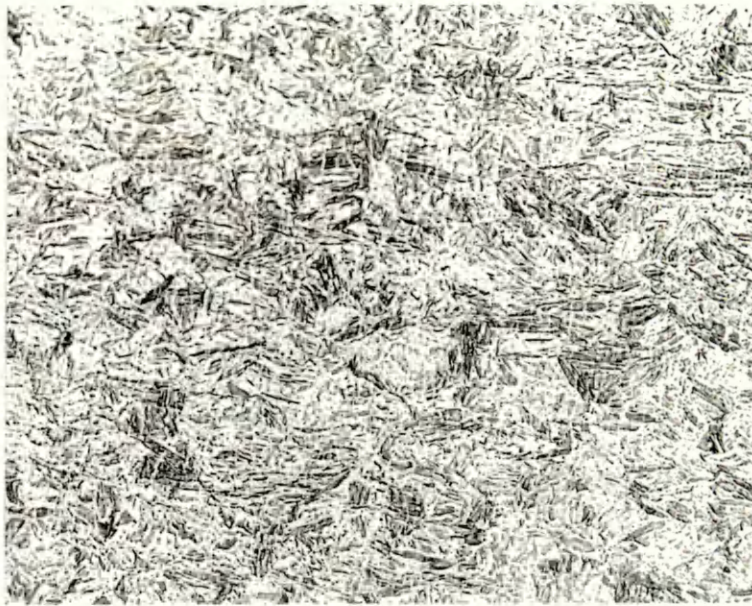
Figure 107:- Optical micrograph of 25% deformed 0.25% carbon 0.5% chromium alloy.
Water Quenched from 950°C. (Magnification 500X)



Banded / orientated laths

↓ roll direction

Figure 108:- Optical micrograph of 50% deformed 0.25% carbon 0.5% chromium alloy. Water Quenched from 950°C. (Magnification 375X)



Direction of rolling →
Broken / banded laths

9.2.2 Transmission electron microscopy

Transmission electron microscopy revealed packets of martensitic laths, the majority of which had a width between 0.15 to 0.25 μm (see figure 109). A fine internal lath structure was also observed within the martensitic laths, which were thought to be fine twins (figure 110, 111 and 112).

Even though the carbon content of this alloy system was quite low and a certain amount of autotempering was expected, no evidence of carbide precipitation with martensitic laths was found. However bainitic carbide rich laths were found in amongst martensitic packets as shown in figure 113 and 114. This phase was identified as lower bainite since these internal carbides were generally orientated 60° to the long axis of the lath. Additionally the lath width was much greater typically 0.6 to 1.25 μm .

Figure 109:- Transmission electron micrograph of 0.5% Chromium 0.25% carbon alloy system 10% deformed showing typical martensite packet. (Magnification 29.5K)



Figure 110:- Transmission electron micrograph of 0.5% Chromium 0.25% carbon alloy system 10% deformed showing typical martensite lath with internal lath structure. (Magnification 40K)

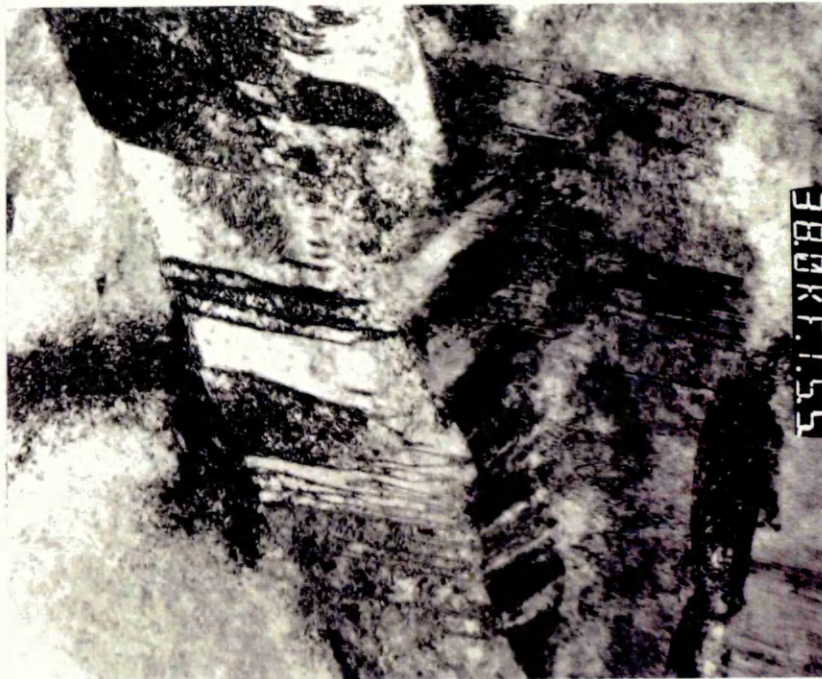


Figure 111:- Transmission electron micrograph of 0.5% Chromium 0.25% carbon alloy system 25% deformed showing typical martensite lath with internal lath structure.

(Magnification 90K)

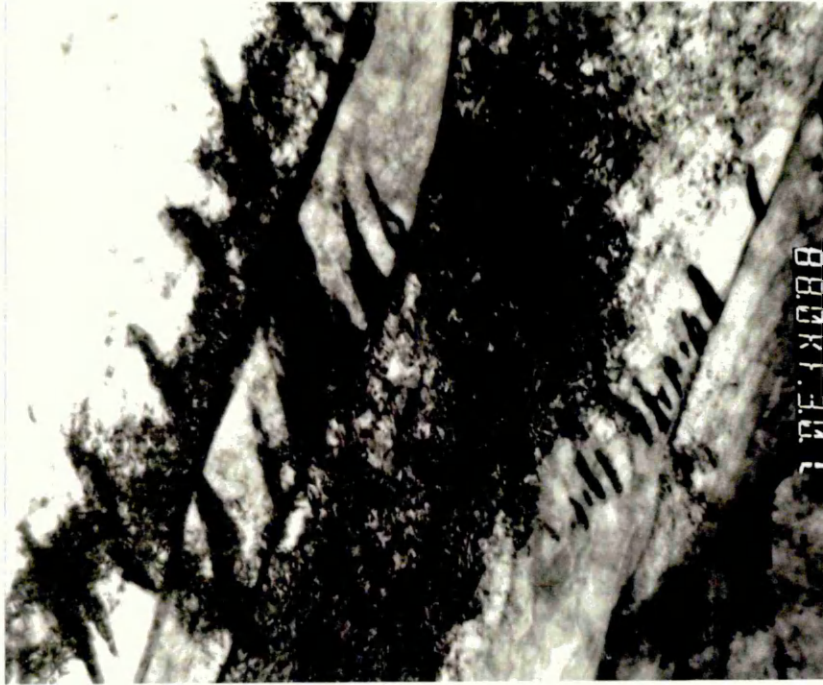


Figure 112:- Transmission electron micrograph of 0.5% Chromium 0.25% carbon alloy system 25% deformed showing typical internal lath structure.

(Magnification 117K)

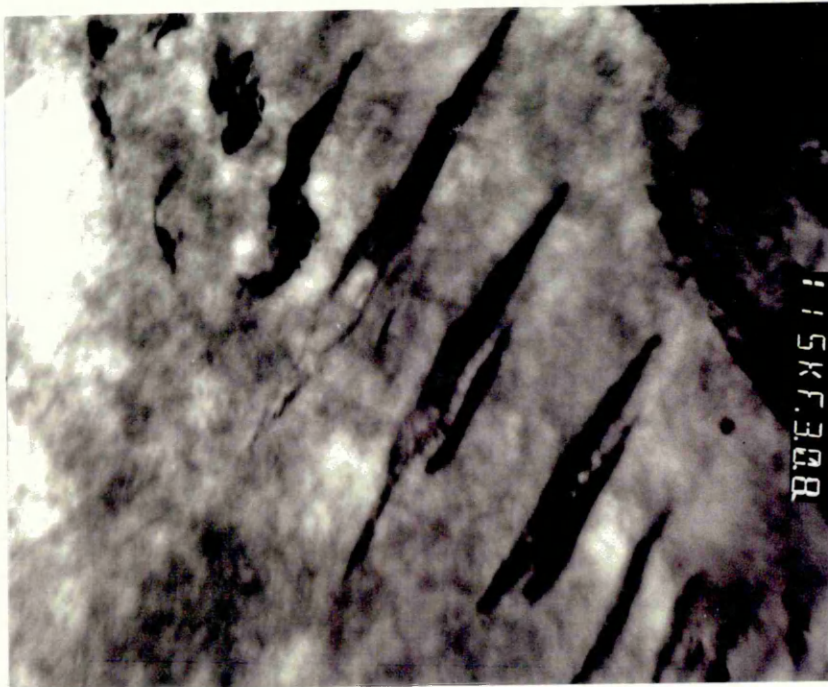


Figure 113:- Transmission electron micrograph of undeformed 0.5% Chromium 0.25% carbon alloy system showing bainitic lath (Magnification 68K)



Lath width = approximately $0.8 \mu\text{m}$

Figure 114:- Transmission electron micrograph of 10% deformed 0.5% Chromium 0.25% carbon alloy system showing bainitic lath (Magnification 68K)



Figure 114a :- 117K X magnification of region X showing fine carbides

The dislocation density of the undeformed alloy was on the whole moderate. This was in complete contrast to the 10, 25 and 50% deformed alloy. Even the slightest amount of cold work was enough to generate pockets of highly dislocated microstructure as shown in figure 115. Figure 116 shows a packet of martensitic (and possibly bainitic) laths from the 25% deformed alloy, with a highly dislocated substructure.

Figure 115:- Transmission electron micrograph of 0.25 mass% carbon 0.5 mass% chromium alloy deformed 10% showing pockets of highly dislocated substructure.

Magnification 29.5K



Figure 116:- Transmission electron micrograph of 0.25 mass% carbon 0.5 mass% chromium alloy deformed 25% showing martensitic and bainitic lath packet with high dislocation density. (Magnification 40Kx)



As well as the fine lath (twin) substructure observed within many martensite laths, appreciable amounts of this phase were also observed amongst dense dislocation forests and appeared unconfined to a specific lath. This microstructural feature was observed in both the undeformed and deformed alloy systems, examples of which are given in figures 117, 118 and 119.

Figure 117:- 0.25 mass% 0.5 mass% chromium alloy system, 10% deformed showing fine twin region within dislocation forest. (Magnification 40 KX)



Figure 118:- 0.25 mass% 0.5 mass% chromium alloy system, 25% deformed showing fine twin region within dislocation forest. (Magnification 40KX)

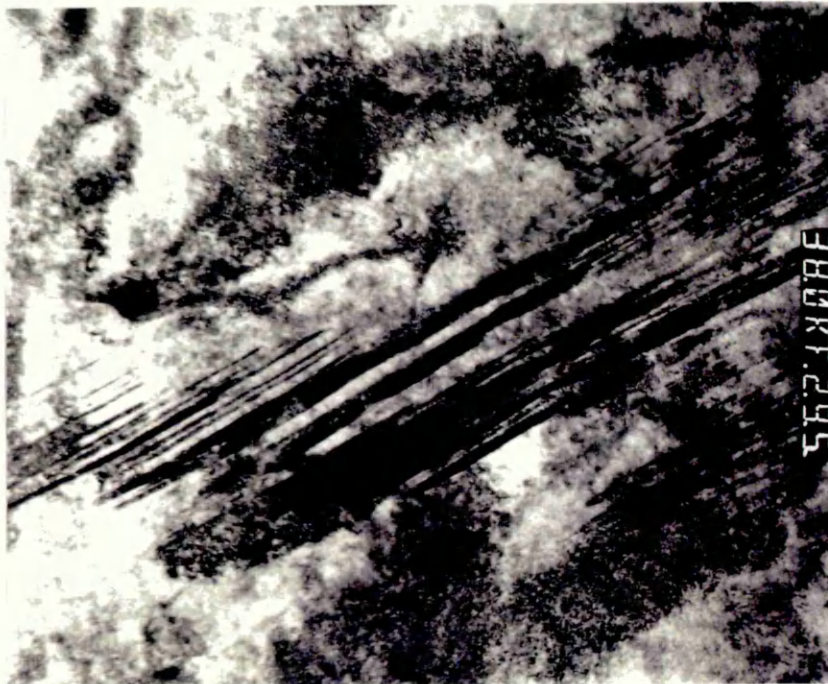


Figure 119:- 0.25 mass% 0.5 mass% chromium alloy system, undeformed showing fine twin region within dislocation forest. (Magnification 40 KX)



Within the occasional bainitic lath, dislocation cellular type arrays were observed. However, in general these arrays were somewhat limited bearing in mind that the proportion of bainitic type lath was also low.

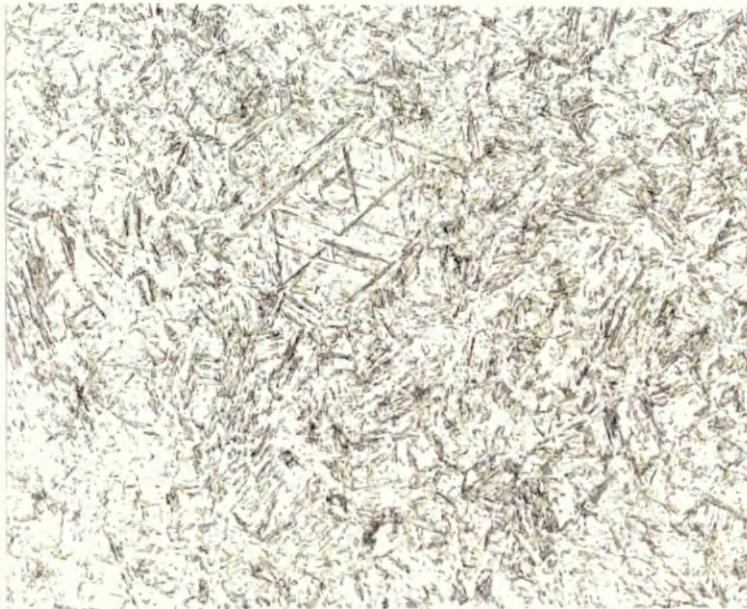
To summarise, the deformed 0.5 mass% chromium 0.25 mass% carbon variant generally consisted of dense dislocated martensitic type laths. Carbides were limited to the bainitic laths and often appeared sheared as a result of the plastic deformation.

9.3 Morphological studies of 0.3 mass% carbon boron alloy system

9.3.1 Optical microscopy

A uniform lath like microstructure for both undeformed and deformed samples was observed with an initial hardness of 550 rising rapidly to 660 VPN. This, together with thermal history and alloy chemistry suggested that these microstructures were primarily martensitic. The undeformed and 10% deformed microstructure contained several lath clusters at an approximate angle of 60° angle to one another (figure 120). No evidence of lath alignment in the direction of rolling was observed in the 10% deformed microstructure. However heavier deformation caused lath alignment and in the 50% deformed alloy many laths also appeared discontinuous or banded (figure 122). In general these microstructure were very similar to the 0.5 mass% chromium 0.25 mass % carbon alloy with well defined almost needle like laths as opposed to the “granular” lath like microstructure of the 1.25% chromium molybdenum alloy.

Figure 120:- Optical micrograph of 0.3 mass% carbon boron alloy system (undeformed)
Showing lath microstructure. Magnification 200X

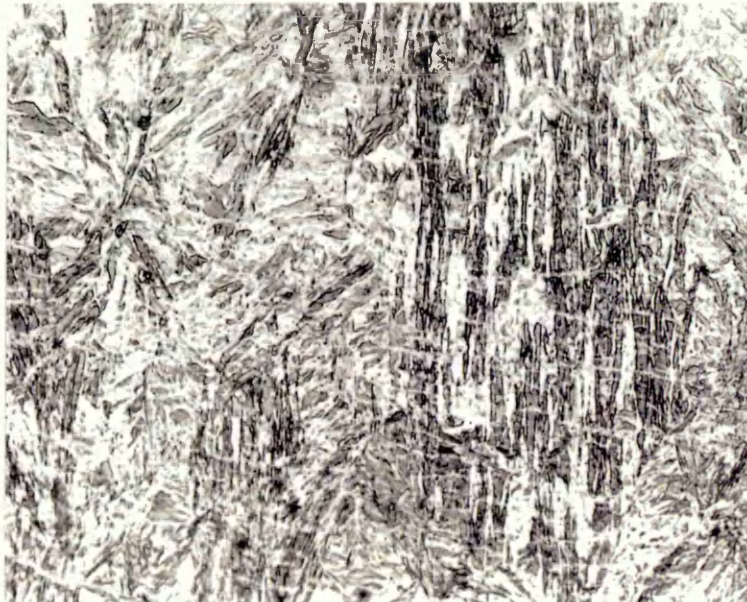


Laths orientated at 60° to one another

Figure 121:- Optical micrograph of 0.3 mass% carbon boron alloy system 10% deformed
Showing lath microstructure. Magnification 375X



Figure 122:- Optical micrograph of 0.3 mass% carbon boron alloy system (50% deformed)
Showing lath microstructure orientated towards direction of rolling and patches of
discontinuous laths. Magnification 500x



↓ Direction of rolling

9.3.2 Transmission electron microscopy of 0.3 mass% carbon boron alloy

Transmission electron microscopy revealed lath packets comprising of both martensitic and bainitic laths (figure 123, 124 and 125). Laths with a width greater than approximately $0.6\mu\text{m}$ containing fine internal carbides orientated 60° to the long axis were identified as lower bainite. Whilst martensitic laths were generally thinner and carbide free with a higher dislocation density and fine internal twin structure.

Figure 123:- Transmission electron micrograph of 0.3 mass% carbon boron alloy (10% deformed). Lath packet showing martensitic and bainitic laths. Magnification 22kx



Figure 124:- Transmission electron micrograph of 0.3 mass% carbon boron alloy (undeformed). Bainitic and martensitic laths in approximately equal proportions

Magnification 22K



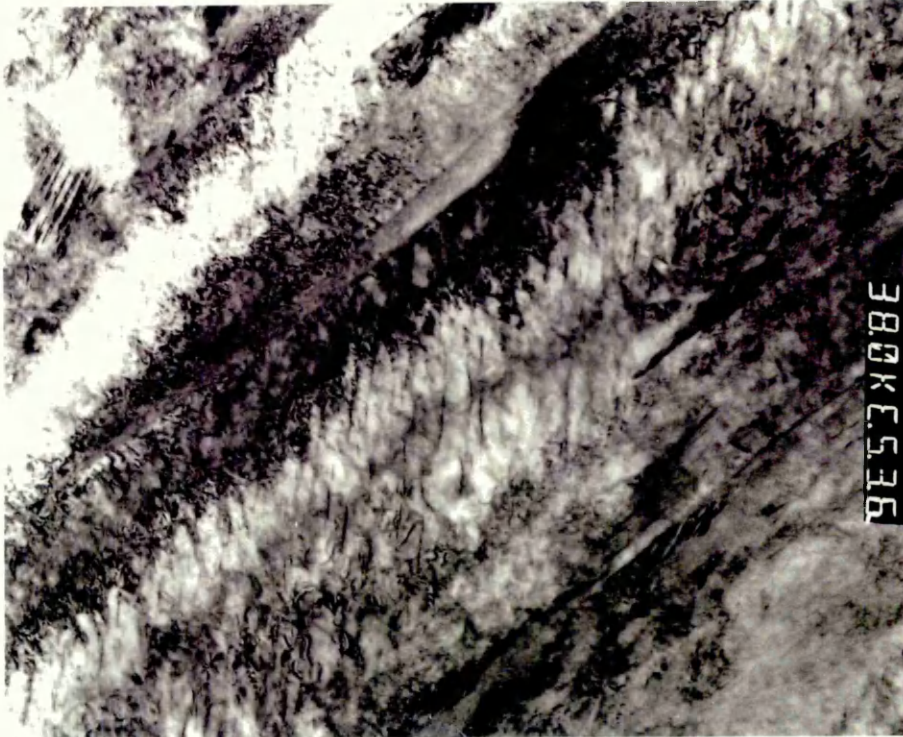
Figure 125:- Transmission electron micrograph of 0.3 mass% carbon boron alloy (25% deformed). Bainitic and martensitic laths in approximately equal proportions

Magnification 29.5K



Figure 126:- Transmission electron micrograph of 0.3 mass% carbon boron alloy (undeformed). Bainitic lath showing fine internal carbide structure.

Magnification 40K



Interestingly, these carbides (shown in figure 126) were quite different in morphology compared to those examined in the isothermally treated 1.25% chromium molybdenum alloy system which were much larger and disc like. Additionally even in the undeformed alloy system, these fine carbides were often surrounded by dense dislocation networks. whereas the disc shaped carbides in the undeformed 1.25 mass% chromium molybdenum alloy were relatively dislocation free.

The dislocation density ranged from moderate in the undeformed sample to extremely dense (figure 128). Perhaps the most dramatic increase in dislocation density was observed in the 10% deformed microstructure, and at low magnifications patches of exceptionally dense dislocation forests were frequently observed. Fine twins were also observed in both the undeformed and deformed microstructure, either appearing confined to a specific lath (figure 127) or amongst dense dislocation networks in the deformed microstructure (figure 128).

Figure 127:- Transmission electron micrograph of 0.3 mass% carbon boron alloy (undeformed). Bainitic and martensitic lath moderately dislocated with fine internal twin structure.

Magnification 29.5K.

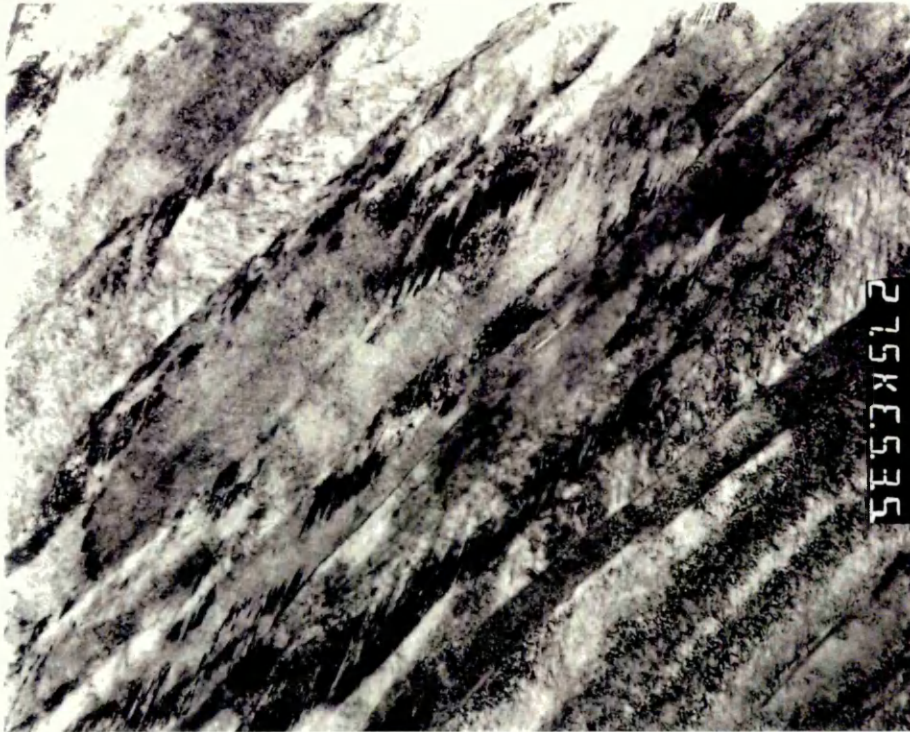


Figure 128:- Transmission electron micrograph of 0.3 mass% carbon boron alloy 10% deformed. Packet of martensitic and bainitic laths with dense dislocation forests

Magnification 13.5K



Examination of the effect of cold work on the morphology of carbides within the bainite lath was fraught with difficulties. For example, the extremity of the dislocation density in the deformed microstructure concealed the majority of microstructural features. Also the size and shape of these precipitates, with degrees of fineness similar to the contrast image produced from a dislocation line, made clarification within a moderately dense dislocation forest extremely difficult.

In addition to the dense dislocation forests observed within the martensitic laths of the deformed variants, occasional dislocation cellular arrays were observed, especially within regions of apparently lower dislocation density. e.g. bainitic laths (figures 129-131). However, their occurrence was not as frequent as the tempered alloy systems and the dislocation cell wall tended to be not as clearly defined compared to the tempered alloy variants.

To summarise, the effect of plastic deformation appeared to dramatically increase the dislocation density, with dense dislocation forest observed within the martensitic laths. Occasionally, dislocations within the bainitic laths were arranged into cellular type arrays as observed in the deformed 0.5 mass% chromium 0.25 mass% carbon variant.

Figure 129:- Transmission electron micrograph of 0.3 mass% carbon boron alloy 25% deformed. "Ragged" dislocation cell substructure.

Magnification 52K

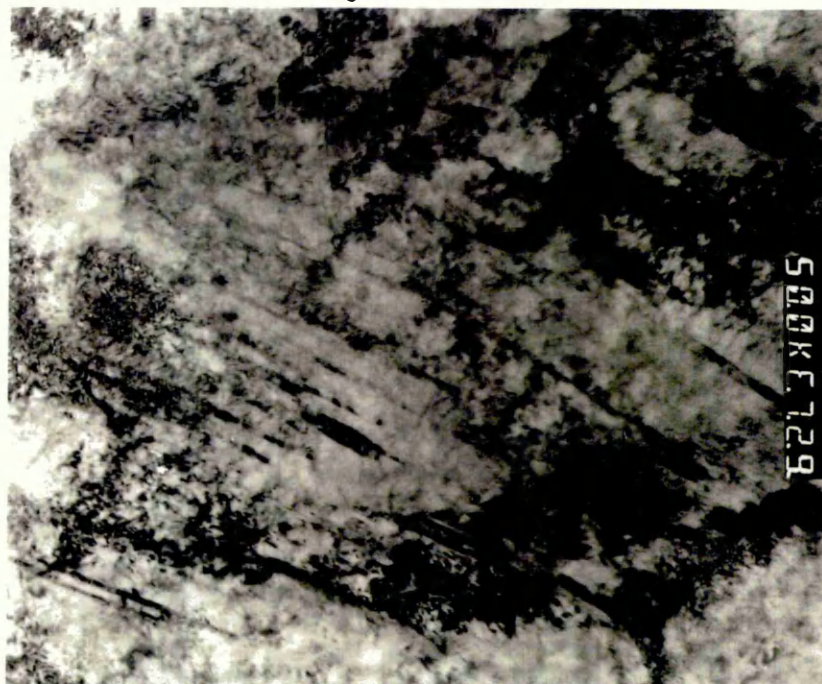


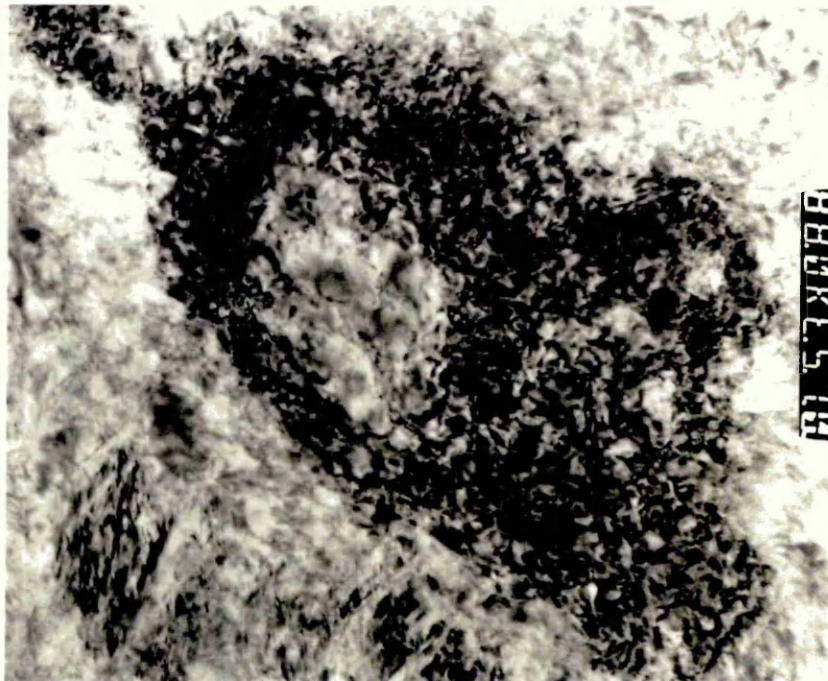
Figure 130:- Transmission electron micrograph of 0.3 mass% carbon boron alloy 10% deformed. "Ragged" dislocation cell substructure.

Magnification 68K



Figure 131:- Transmission electron micrograph of 0.3 mass% carbon boron alloy 50% deformed. Dislocation cell substructure.

Magnification 90K



9.4 Morphological studies of 0.3 mass% carbon boron (tempered 250°C)

9.4.1 Optical microscopy

Optical microscopy revealed a well defined but quite granular lath like microstructure reminiscent of both the untempered and high temperature tempered variants. In other terms, an irregular shaped lath morphology comparable to the untempered variant, but somewhat granular and therefore similar to the 400°C tempered alloy, was found (figure 132).

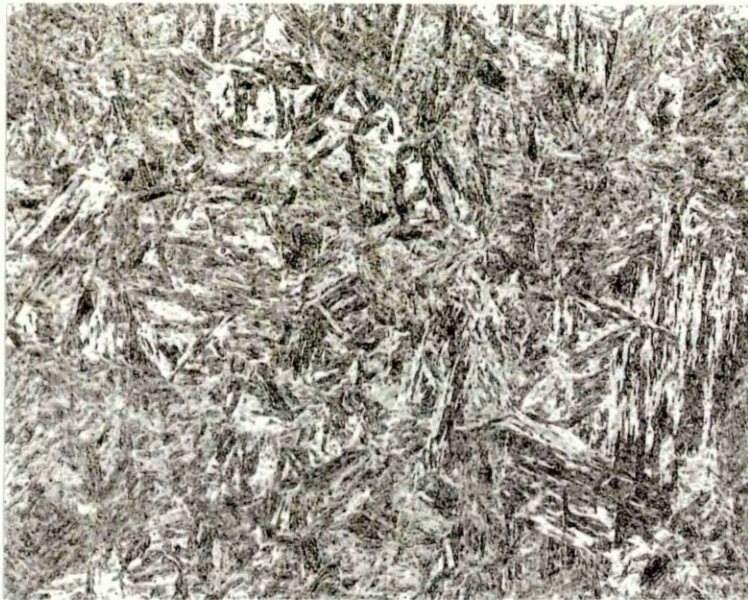
This lath morphology, together with an initial Vickers hardness of 500 VPN suggested that this microstructure was predominantly martensitic. In contrast to the higher temperature tempered variant, lath packet boundaries were not well defined, hence grain size determination was not possible.

Figure 132:- Optical micrograph of 0.3 mass% carbon boron alloy, water quenched from 950°C, tempered at 250°C, for 10 minutes, undeformed. Magnification 375 X.



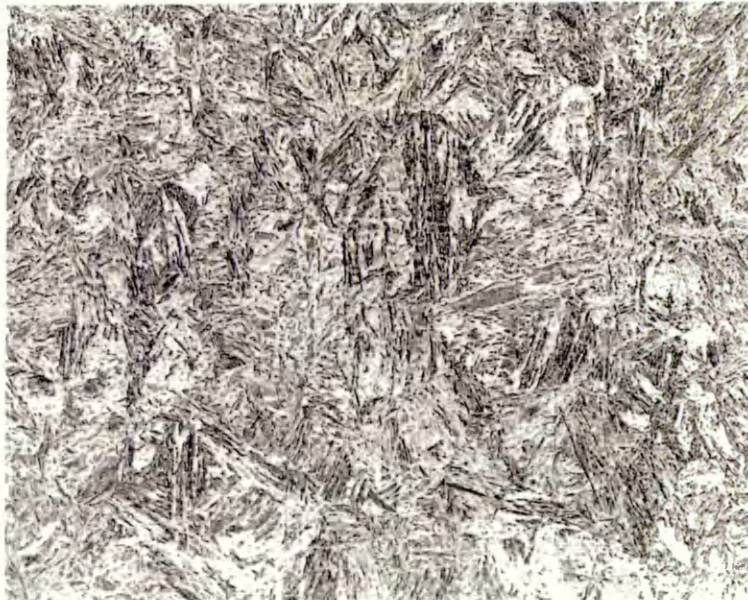
The 25 and 50% deformed microstructure consisted of packets of orientated and in some cases banded laths amongst a predominantly granular or particulate like matrix. A similar observation was made in the high temperature tempered 25 and 50% deformed alloy, but with less retention of a lath like morphology. Figure 133 shows the 10% deformed alloy system, with randomly orientated granular laths, identical to the undeformed variant. Figures 134 and 135 show the 25 and 50% deformed microstructure with broken / banded laths surrounded by a particulate like matrix.

Figure 133:- Optical micrograph of 0.3 mass% carbon boron alloy, water quenched from 950°C, tempered at 250°C, for 10 minutes, 10% deformed. Magnification 375 X.



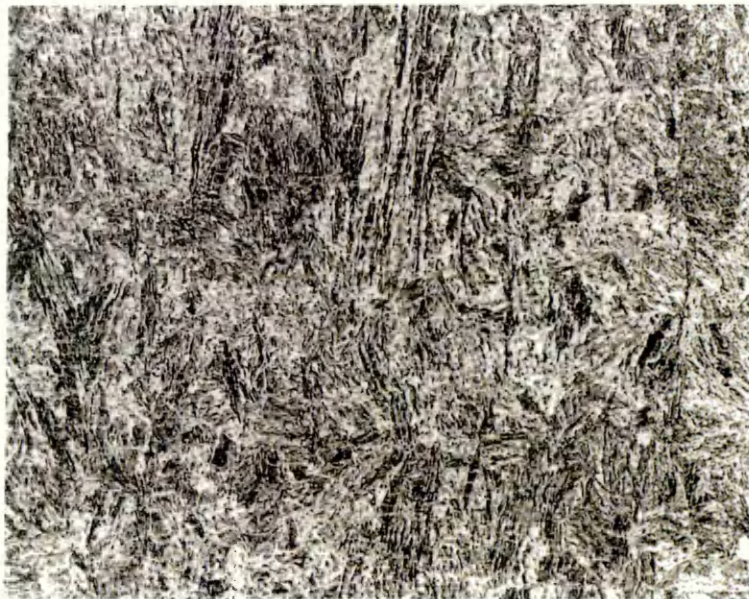
Roll direction →

Figure 134:- Optical micrograph of 0.3 mass% carbon boron alloy, water quenched from 950°C, tempered at 250°C, for 10 minutes, 25% deformed. Magnification 375 X.



Roll direction ↓

Figure 135:- Optical micrograph of 0.3 mass% carbon boron alloy, water quenched from 950°C, tempered at 250°C, for 10 minutes, 50% deformed. Magnification 375 X.



Roll direction ↓

9. 4. 2 Transmission electron microscopy

Examination of the 250°C tempered 0.3 mass% carbon boron alloy revealed packets of martensitic laths, the majority of which contained very few or no carbides, alongside relatively carbide rich, bainitic laths.

Figure 136 shows part of a martensite lath packet from the 25% deformed alloy system where the average lath width was determined at 0.25 μm .

Figure 136:- Transmission electron micrograph o 0.3 mass% carbon boron alloy, water quenched form 950°C, tempered at 250°C for 10 minutes, 25% cold deformed.
Moderate - heavily dislocated martensite packet. Magnification 52KX.



The dislocation density of the undeformed variant was described as moderate, appearing perhaps slightly lower than its untempered counterpart. As expected however, the dislocation density rose significantly after plastic deformation especially in the martensitic laths.

Patches of exceptionally fine laths were frequently observed in both the undeformed and deformed microstructure, figures 137 and 138 show bright and dark field micrographs of a series of fine laths with an average width of $0.07\ \mu\text{m}$. Interestingly this alloy system appeared to contain less fine laths when compared to the untempered counterpart. In addition the higher temperature tempered variant contained even less amounts of fine lath phase (see section 9.5.2)

Figure 137:- Transmission electron micrograph of 0.3 mass% carbon boron alloy, water quenched from 950°C , tempered at 250°C for 10 minutes, undeformed.

Bright field of Fine laths . Magnification 202KX.



Figure 138:- Transmission electron micrograph of 0.3 mass% carbon boron alloy, water quenched from 950°C, tempered at 250°C for 10 minutes, undeformed.

Dark field of Fine laths . Magnification 202KX.



In contrast to figure 136, figure 139 shows the much wider bainitic lath (1.3 μm) from the 10% deformed alloy system with internal carbides lying 60° to the long axis and lath boundary carbide. The fine particles observed on this micrograph were disregarded (contamination from sample preparation procedure).

Carbide morphology was found to be similar in many respects to the 450°C tempered microstructure, being quite needle / rod like. There was also significant amounts of spheroid shaped carbide as illustrated in figure 140.

The size of the rod shaped internal carbides varied quite considerably. However, unlike the precipitated carbides in the martensitic lath of the 450°C tempered microstructure, did not extend beyond approximately 40% of the lath width.

Figure 139:- Transmission electron micrograph of 0.3 mass% carbon boron alloy, water quenched from 950°C, tempered at 250°C for 10 minutes, 10% cold deformed.

Bainitic lath with internal and lath boundary carbides. Magnification 22KX



Figure 140:- Transmission electron micrograph of 0.3 mass% carbon boron alloy, water quenched from 950°C, tempered at 250°C, 10% cold deformed. Bainitic lath with internal rod and spheroid shaped carbides. Magnification 40KX



On close examination of the bainitic laths in the 25 and 50% deformed microstructure, many were found to contain irregular “stepped” shaped carbides as illustrated in figures 141, 142 and 143.

Figure 141:- Transmission electron micrograph of 0.3 mass% carbon boron alloy, water quenched from 950°C, tempered at 250°C, 25% cold deformed. Bainitic lath with irregular shaped internal carbides. Magnification 90KX

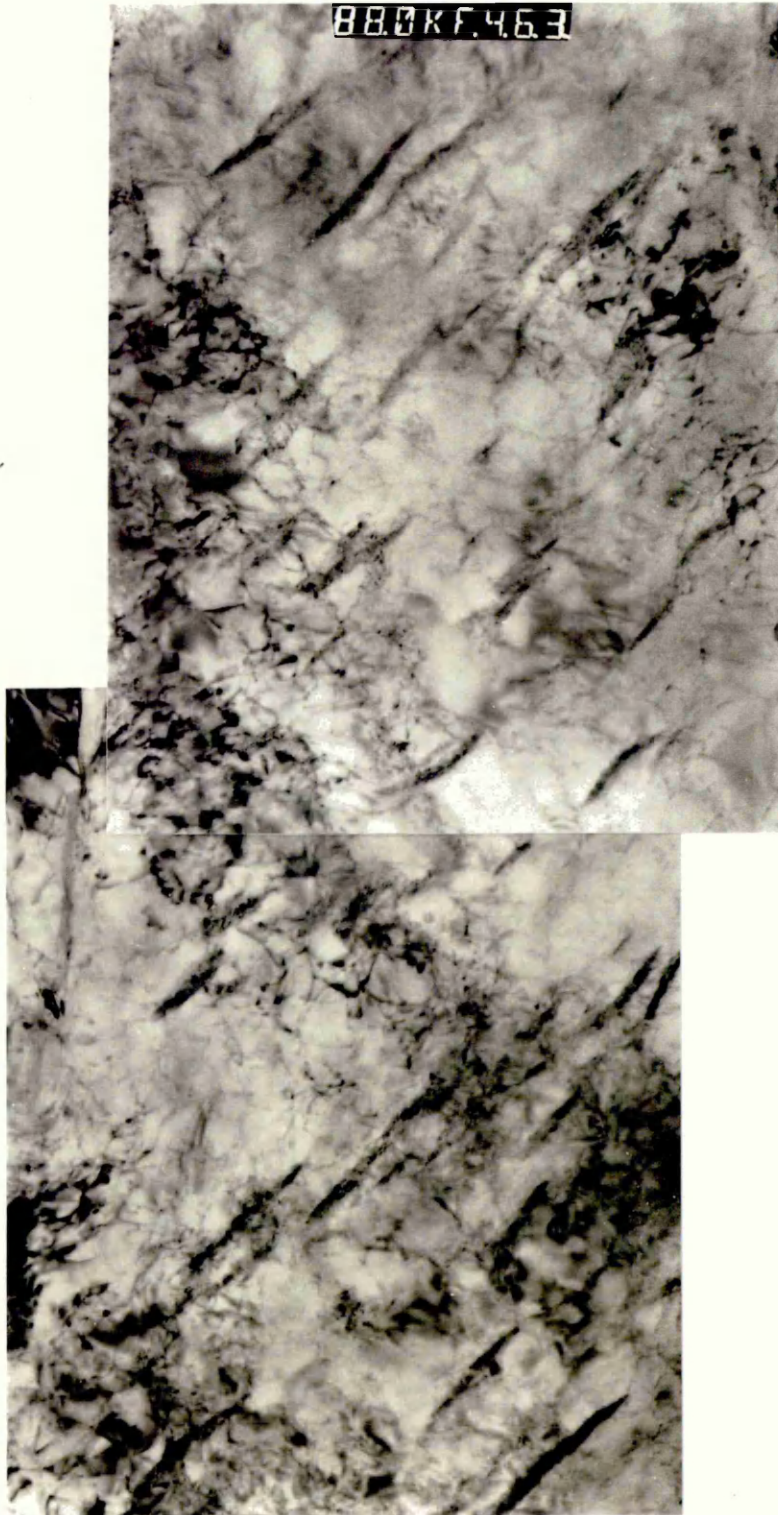


Figure 142:- Transmission electron micrograph of 0.3 mass% carbon boron alloy, water quenched from 950°C, tempered at 250°C, 25% cold deformed. Bainitic lath with irregular shaped internal carbides. Magnification 52KX

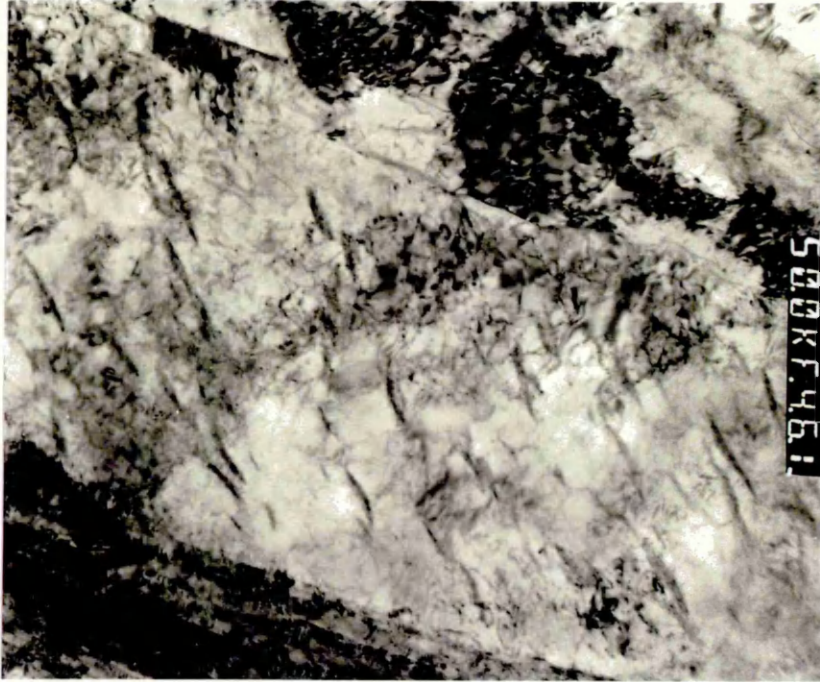
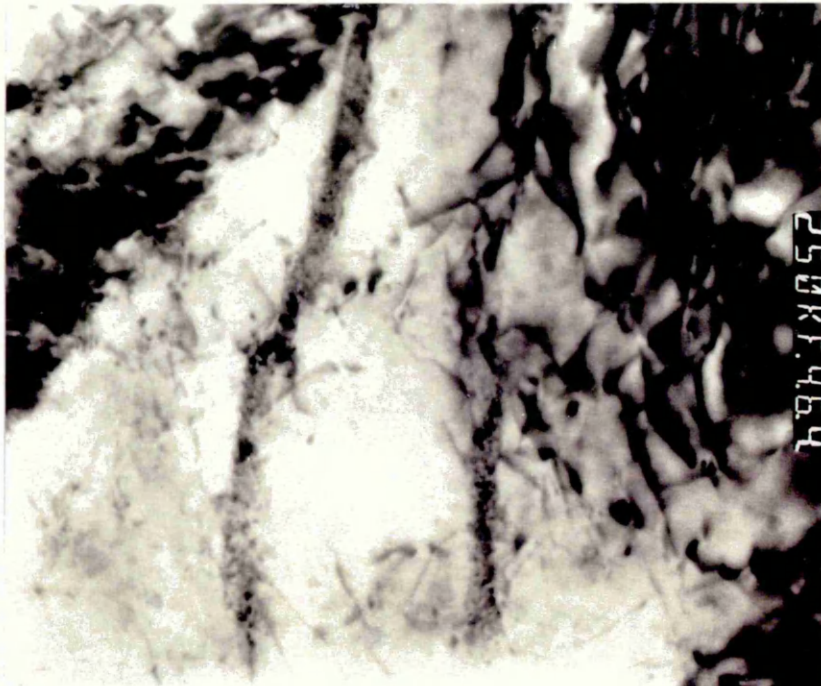


Figure 143:- Transmission electron micrograph of 0.3 mass% carbon boron alloy, water quenched from 950°C, tempered at 250°C, 25% cold deformed. Bainitic lath with irregular shaped internal carbides. Magnification 252KX



As anticipated, the amount of cold work / plastic deformation significantly effected overall dislocation density. The undeformed microstructure was generally found to be light to moderately dislocated, with the majority of dislocation forests amongst the martensitic laths. In the 25 and 50% deformed microstructures, dislocation clustering around bainitic carbides was often detected, along with an increase in dense dislocation forests.

Some degree of dislocation cell formation was also detected (figure 144) although this feature was not as prevalent as in the high temperature tempered microstructure.

Figure 144:- Transmission electron micrograph of 0.3 mass% carbon boron alloy, water quenched form 950°C, tempered at 250°C, 25% cold deformed. Dislocation cell formation. Magnification 40KX.



9.5 Morphological studies of 0.3 mass% carbon boron (tempered 400°C)

9.5.1 Optical microscopy

In contrast to the untempered microstructure (with needle like, irregular shaped but well defined laths), the tempered microstructure consisted of uneven / ragged shaped laths amongst an almost unresolvable particulate like region (figure 145). In some parts there was also evidence of a grain structure (i.e. an abrupt change in lath packet orientation) hence an approximate grain size of 40 μ m was determined (figure 146).

To summarise, optical microscopy revealed a predominantly particulate (granular) like microstructure with sporadic packets of ragged shaped laths within clearly defined grains.

The 10% deformed alloy appeared identical to the undeformed alloy under optical microscopy with randomly orientated lath packets amongst a particulate like granular region. However the 25 and 50% deformed microstructure was quite different with well defined texturing towards the direction of rolling (see figure 147). Additionally the deformed microstructure tended towards a predominantly granular / coarse particulate morphology with an occasional suggestion of a lath like phase as illustrated in figure 147.

Figure 145:- Optical micrograph of 0.3 mass% carbon boron alloy, water quenched from 950°C tempered at 400°C for 10 minutes. Undeformed.

Magnification approximately 250X



Figure 146:- Optical micrograph of 0.3 mass% carbon boron alloy, water quenched from 950°C tempered at 400°C for 10 minutes. Undeformed. Showing evidence of grain boundaries

Magnification approximately 500X

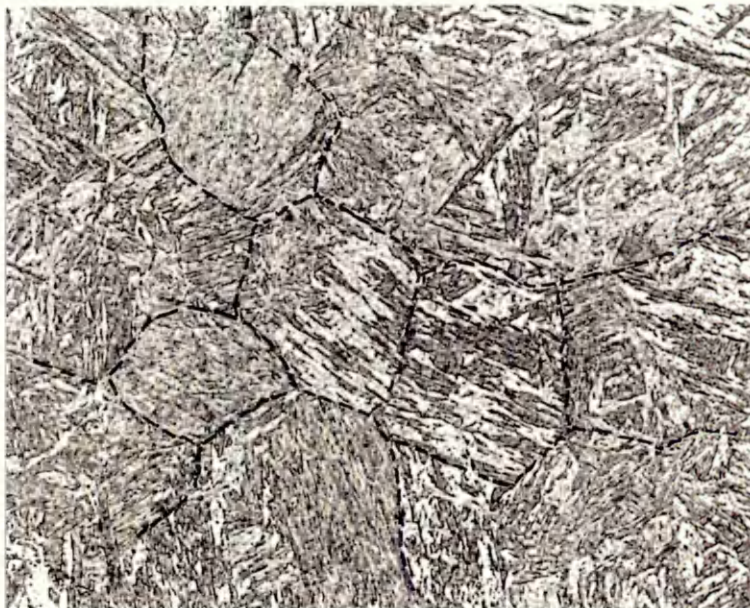


Figure 147:- Optical micrograph of 0.3 mass% carbon boron alloy, water quenched from 950°C tempered at 400°C for 10 minutes. 25% deformed. Showing texturing towards roll direction

Magnification approximately 375X



Roll direction

9.5.2 Transmission electron microscopy

Examination of the high temperature tempered 0.3 mass% carbon boron alloy under transmission electron microscopy revealed packets of martensitic and bainitic laths, together with substantial amounts of inter and intra lath carbides.

Large inter-lath carbides were easily observed at low magnification and were generally either at an angle of 60 or 90° to the long axis of the lath boundary.

Occasionally internal lath carbides lying almost parallel to the lath boundary impinged on perpendicular positioned carbides resulting in a “T” or cross shaped carbide as shown in figures 148 and 149.

Figure 148:- Transmission electron micrograph of 0.3 mass% carbon boron alloy. Water quenched from 950°C, tempered at 400°C for 10 minutes, undeformed. Packets of martensite laths with coarse carbides at 90° angle to the long axis of the lath plus “T” shaped carbides and lath boundary carbides. Magnification 22K.



Figure 149:- Transmission electron micrograph of 0.3 mass% carbon boron alloy. Water quenched from 950°C, tempered at 400°C for 10 minutes, undeformed. Packets of martensite laths with coarse carbides at 90° angle to the long axis of the lath plus lath boundary carbides and bainitic lath with carbides. Magnification 29.5KX.

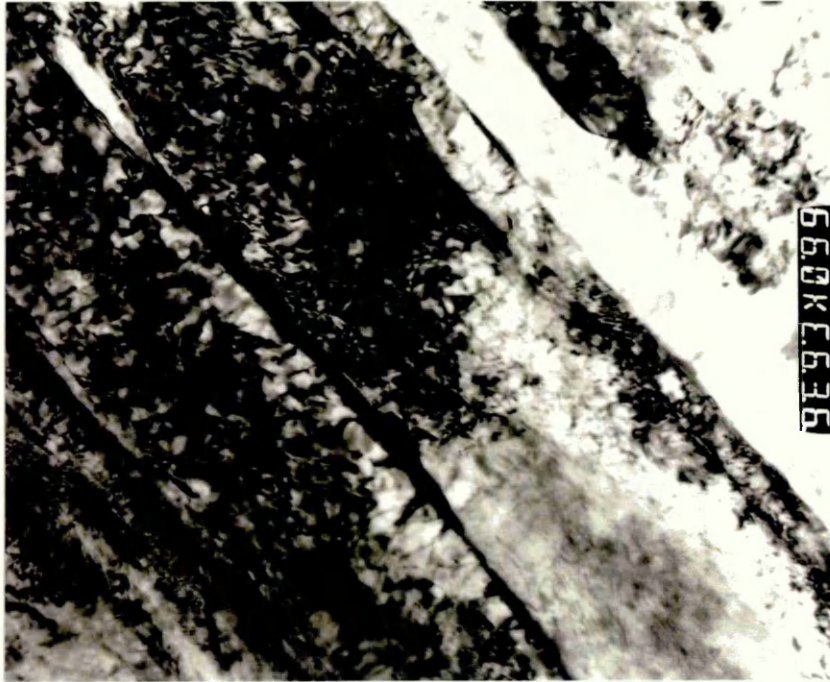


The size of the inter lath carbides varied from exceptionally fine (similar in morphology to those previously observed within the bainitic laths in the untempered variant), to quite coarse and blocky as shown in figures 150 and 151. Additionally the majority of the carbides within the martensitic lath extended well beyond 50% of the lath width.

Figure 150:- Transmission electron micrograph of 0.3 mass% carbon boron alloy. Water quenched from 950°C, tempered at 400°C for 10 minutes, undeformed. Bainitic lath surrounded by martensitic laths with coarse and fine carbides. Magnification 40KX.



Figure 151:- Transmission electron micrograph of 0.3 mass% carbon boron alloy. Water quenched from 950°C, tempered at 400°C for 10 minutes, undeformed. Large interlath carbide between martensitic laths. Magnification 68KX.



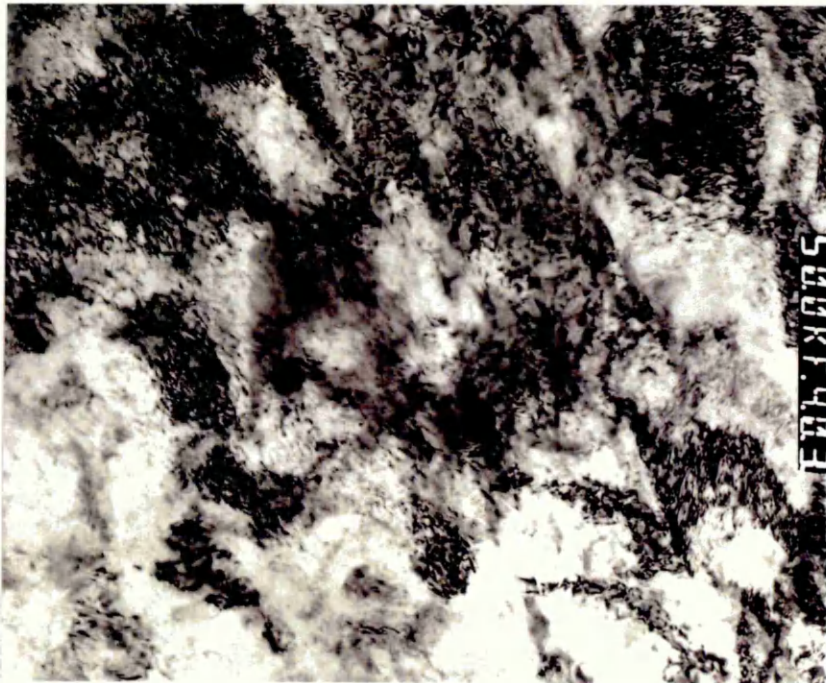
On the whole a moderate dislocation density was found in the undeformed alloy system. Occasional dense dislocation forests were observed within some of the finer martensitic laths (figure 150) and lath / grain boundary interfaces (figure 149).

The application of cold work on this tempered alloy system did not appear to significantly increase the dislocation density as previously observed in the untempered variants. Alternatively a cell like dislocation substructure was developed as illustrated in figures 152 and 153.

Figure 152:- Transmission electron micrograph of 0.3 mass% carbon boron alloy. Water quenched from 950°C, tempered at 400°C for 10 minutes, 25% deformed. Development of cell structure. Magnification 68KX.



Figure 153:- Transmission electron micrograph of 0.3 mass% carbon boron alloy. Water quenched from 950°C, tempered at 400°C for 10 minutes, 25% deformed. Development of cell structure. Magnification 52KX.



The carbide matrix interface and carbide morphology were examined in the undeformed and deformed alloy systems.

In the undeformed microstructure, low magnification electron microscopy revealed straight sided rod shaped carbides with a smooth well defined interface. At higher magnifications, light dislocation networks were observed amongst many of the interlath carbides interface. However occasional interfacial clustering was also found and produced a “spiked” matrix carbide interface as a result of contrast interference.

In contrast the deformed microstructure appeared to contain many more ledge shaped carbides (figures 154, 155 and 156). Dislocation clustering amongst interlath carbides was again observed, however there appeared to be no significant increase in the “inter-carbide” dislocation density with respect to the amount of deformation.

Figure 154:- Transmission electron micrograph of 0.3 mass% carbon boron alloy. Water quenched from 950°C, tempered at 400°C for 10 minutes, 10% deformed. Ledge shaped and rod shaped carbides. Magnification 90K

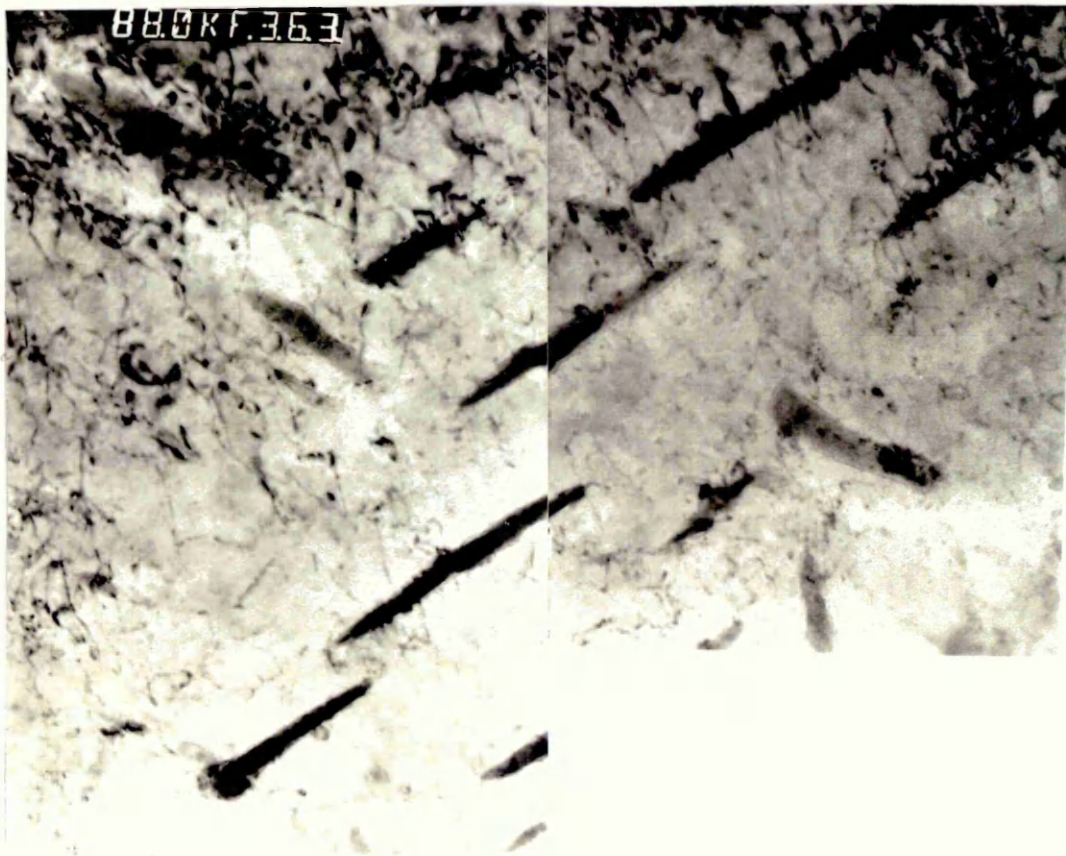


Figure 155:- Transmission electron micrograph of 0.3 mass% carbon boron alloy. Water quenched from 950°C, tempered at 400°C for 10 minutes, 10% deformed. Sheared carbide surrounded by few dislocations. Magnification 117 and 312KX

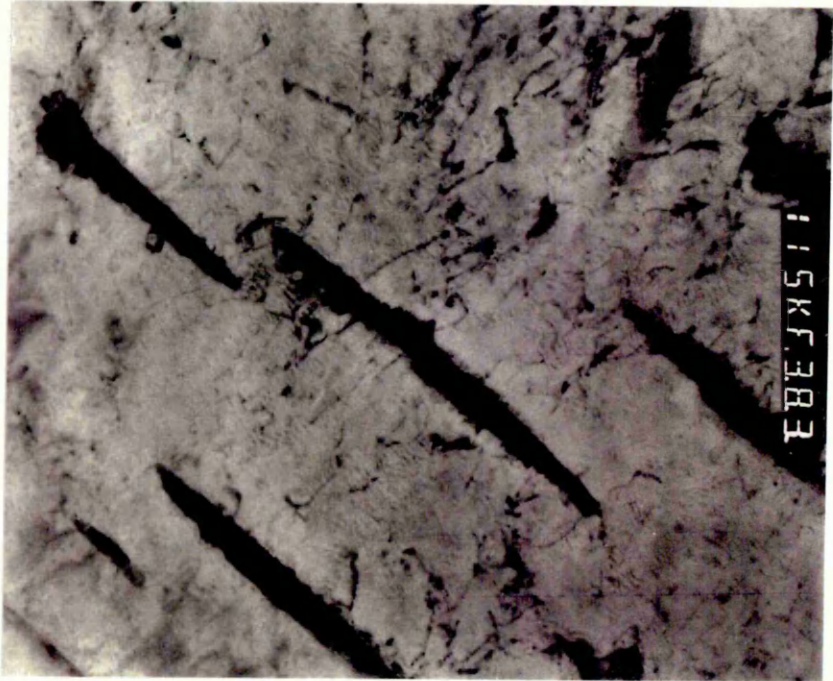
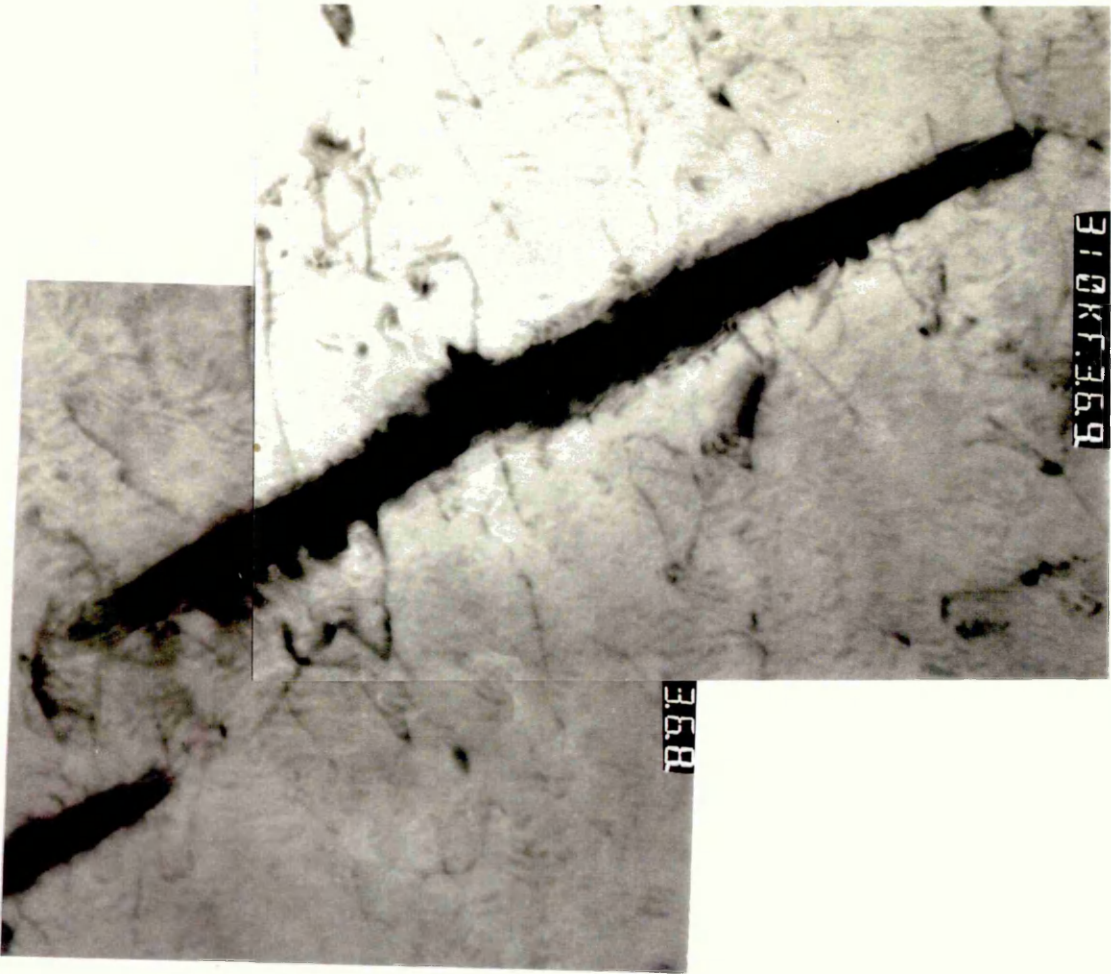


Figure 156:- Transmission electron micrograph of 0.3 mass% carbon boron alloy. Water quenched from 950°C, tempered at 400°C for 10 minutes, 10% deformed. Ledge shaped carbide surrounded by few dislocations. Magnification 90KX



To summarise, the 400°C tempered 0.3 mass% carbon boron alloy mass% carbon boron alloy comprised of martensitic and bainitic laths with relatively large carbides distributed throughout. Little evidence of twinning was found, even after significant amounts of plastic deformation and the dislocation density remained low - moderate. Dislocation cell arrays were well defined and quite prolific amongst both lath types. Carbide shearing was frequently observed after 25 - 50% plastic deformation.

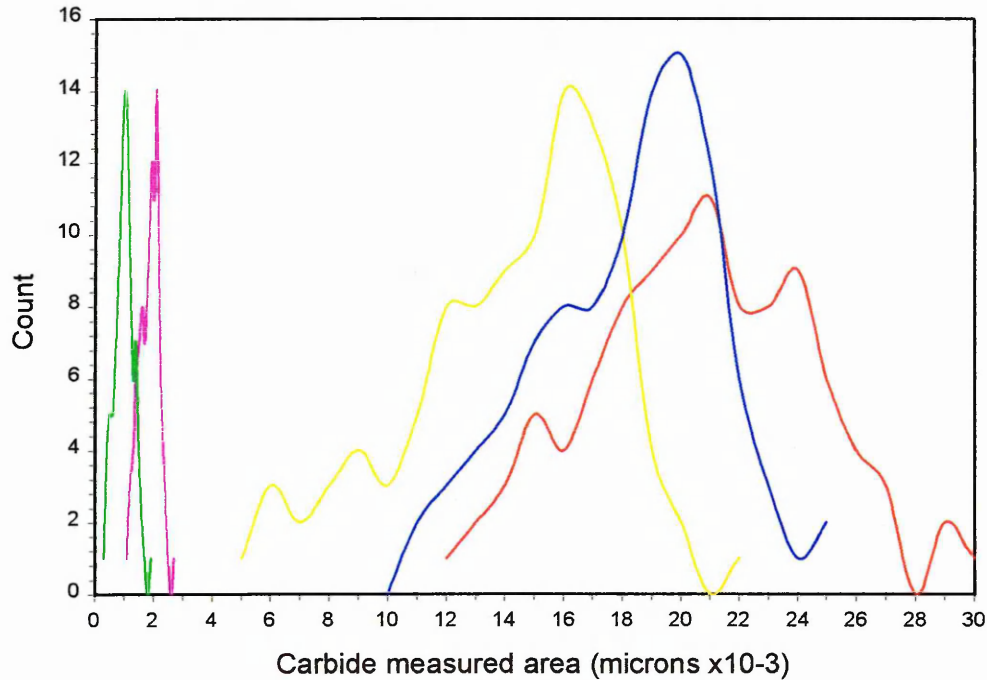
9.6 Precipitate size distribution and identification

9.6.1 Precipitate size distribution.

The carbide sizes for each particular alloy system varied significantly (especially in the tempered or isothermally treated alloy systems). Figure 157 shows the carbide distribution curve for each alloy system which was generated by randomly measuring 100 precipitates during Transmission Electron Microscopy. From figure 157 and the results discussed previously, it was noted that:-

- The 0.5 mass% chromium 0.25 mass% carbon variant contained the smallest carbides, closely followed by the 0.3 mass% carbon boron alloy, and were confined to the bainitic laths only.
- The 1.25 mass% chromium molybdenum variant possessed the largest carbides also confined to the bainitic laths.
- The effect of tempering was clearly observed with an increase in carbide size and population.
- The carbide distribution plot for the 0.3 mass% carbon boron alloy, tempered at 250 and 400°C were similar in profile (slightly skewed towards larger sizes).

Figure 157:- precipitate (carbide) distribution curve for each examined alloy system, measurements taken via TEM.



Key:-

Red:- 1.25 mass% chromium molybdenum variant, quenched into salt bath at 320°C.

Green:- 0.5 mass% chromium 0.25 mass% carbon variant, quenched into water from 950°C.

Magenta:- 0.3 mass% carbon boron variant, quenched into water from 950°C.

Yellow:- 0.3 mass% carbon boron variant, quenched into water from 950°C, tempered at 250°C.

Blue:- 0.3 mass% carbon boron variant, quenched into water from 950°C, tempered at 400°C.

Chapter 10

Mechanical evaluation of optimum alloy systems.

10.1 Mechanical evaluation of 1.25 mass% Cr. Mo alloy system.

10.1.1 Tensile and hardness test results

True stress strain graphs for all four alloy variants are provided in figure 158. From these results the tensile properties of the undeformed, 10, 25 and 50% deformed alloy system were noted (table 27). Measured values included the 0.2% proof strength, ultimate tensile strength with Vickers hardness noted prior the tensile test.

Note:- True stress strain as opposed to engineering stress strain measurements were taken where;

$$\text{True stress} = \frac{\text{Force}}{\text{Area}} \quad (10.1)$$

Area = cross sectional area measured at a specified loads throughout the tensile test as opposed to a single measurement prior to the tensile test (i.e. Engineering stress).

Also;

$$\text{True strain} = \ln\left(\frac{L}{L_0}\right) \quad (10.2)$$

With L (length) being the Length of the specimen at a given load and L_0 the original length. Engineering strain is the instantaneous change in length over the original length.

Figure 158:- True stress / Strain curve for 1% chromium molybdenum steel, austenitised at 950C salt bath quenched at 320C. Work hardened various amounts

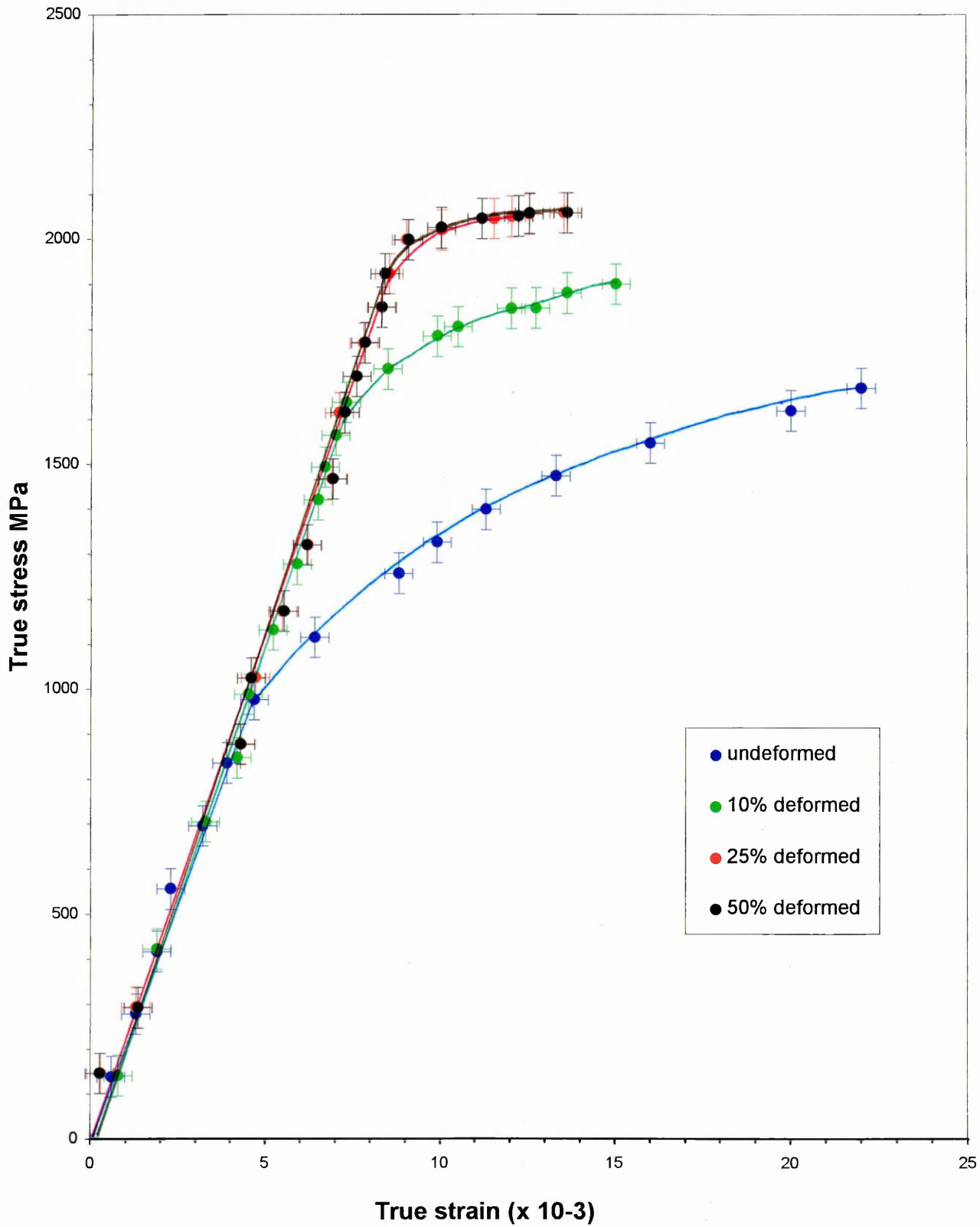


Table 27:- Mechanical results of 1.25 mass% Cr. Mo alloy salt bath quenched from austenitisation, cold deformed various amounts

Thermal treatment and % amount of deformation	0.2% Proof strength (MPa)	Ultimate tensile strength (MPa)	PS / UTS ratio (%)	Hardness (VPN)
Quench into salt bath from 950°C, hold at 320°C for 10 minutes.	1160	1669	69	464
Quench into salt bath from 950°C, hold at 320°C for 10 minutes. Cold deform 10%	1775	1900	93	534
Quench into salt bath from 950°C, hold at 320°C for 10 minutes. Cold deform 25%	2040	2058	99	562
Quench into salt bath from 950°C, hold at 320°C for 10 minutes. Cold deform 50%	2040	2058	99	574

10.1.1.1 Comparison of 0.2% proof strength and shape of flow curves

A rapid increase in the 0.2% true proof strength was observed between the undeformed and 10% deformed alloy variant indicating that a significant degree of work hardening had taken place during the cold rolling procedure. Additionally, on comparing the 10% and 25% deformed alloy curves, a moderate increase in the 0.2% proof strength was observed, thus indicating a small degree of work hardening also. However the 50% deformed system curve was nearly identical to the 25% deformed system, suggesting that strengthening via cold work was almost achieved.

It was also noticed that the undeformed alloy system possessed an initial high work hardening rate, lessening somewhat with increasing strain.

In contrast the plastic portion gradient for the 25 and 50% deformed alloy systems were uniform and quite shallow, suggesting a lower and consistent work hardening rate under the tensile test.

When examining the slope of all the flow curves at a true strain of 12×10^{-3} , a gradual decrease in the work hardening rate with increasing amount of prior plastic deformation was found. (section 10.1.2) A similar result was obtained on examining the change in hardness and 0.025% proof strength versus prior plastic deformation, except in the latter cases, the work contribution through the tensile test is obviously omitted.

10.1.2 Determination of work hardening during the tensile test

Essentially two techniques were utilised to describe the work hardening characteristics of each alloy under the tensile test. The first method involved simple gradient measurement at a specified strain. The second method makes use of the fact that the plastic flow of metal often obeys a power law relationship, with a work hardening exponent determinable from a log log plot of true stress strain.

10.1.2.1 Work hardening rate from gradient of the flow curve

Plastic flow gradients for each alloy system were measured at a true strain of 12×10^{-3} . Values corresponding to the work hardening rate are given in table 28, and indicate an initial sharp decrease between the undeformed and 10% deformed alloy. However, the difference in the work hardening rate between the 25 and 50% deformed alloy system was virtually nil.

Table 28:- Work hardening rates of 1.25 mass% Chromium molybdenum alloy systems, quenched from 950°C into salt bath at 320°C, cold deformed various amounts (values taken from figure 158).

Alloy type (amount of deformation)	Gradient at strain of 12×10^{-3} (Work hardening Rate) ($\times 10^3$)
Undeformed alloy	37.4
10% deformed alloy	27.7
25% deformed alloy	9.4
50% deformed alloy	9.4

10.1.2.2 Work hardening rate from power law relationships

The flow curve of many metals in the region of uniform plastic deformation can be expressed by the simple power curve relation;

$$\sigma = k\varepsilon^\eta \quad (10.3)$$

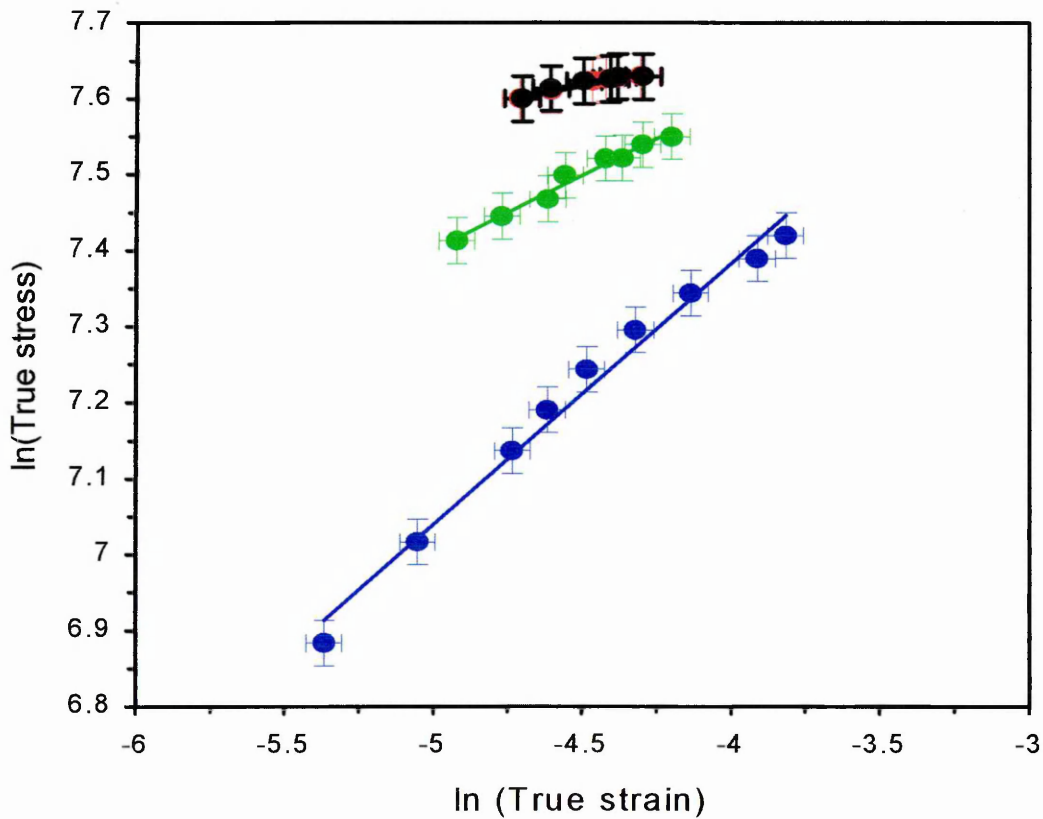
Where η is the strain hardening exponent and k is the strength coefficient.

A log log plot of true stress and true strain up to a maximum load will result in a straight line if equation (10.3) is satisfied, with the linear slope of this line being the strain hardening exponent.

Figures 159 show a log log plot of the true stress strain values taken from plastic portion of each true stress strain curve in figure 158.

Although it was appreciated that there were only few data points available, it was thought that some degree of linearity did exist hence these curves did obey the simple power curve relation (equation 10.3).

Figure 159:- Plot of Log True Stress versus Log True Strain (data taken from plastic portion of True Stress Strain curve). 1.25 mass% chromium molybdenum alloy quenched into salt bath at 320°C, deformed various amounts.



Key

- Blue Undeformed
- Green 10% deformed
- Red 25% deformed
- Black 50% deformed

The gradients from figure 159 are given in table 29 and correspond to the work hardening exponent. From these results it became evident that the strain hardening exponent decreased quite rapidly after 10% prior plastic deformation, tending towards $n = 0$ (perfectly plastic solid).

Table 29:- Work hardening exponent values taken from figure 159 gradients

Sample	Linear equation	Gradient (n)
Undeformed	$y = 0.3446X + 8.7613$	0.3446
10% deformed 1.25 mass% Cr Mo. alloy	$y = 0.1955X + 8.3776$	0.1955
25% deformed 1.25 mass% Cr Mo. alloy	$y = 0.0762X + 7.961$	0.0762
50% deformed 1.25 mass% Cr Mo. alloy	$y = 0.0728X + 7.946$	0.0728

A work hardening rate $d\theta/d\varepsilon$ was calculated from the strain hardening exponent by noting that:-

$$n = \frac{d(\log \theta)}{d(\log \varepsilon)} = \frac{d(\ln \theta)}{d(\ln \varepsilon)} = \frac{\varepsilon}{\theta} \times \frac{d\theta}{d\varepsilon} \quad (10.4)$$

hence;
$$\frac{d\theta}{d\varepsilon} = n \frac{\theta}{\varepsilon} \quad (10.5)$$

Hence at a given value of stress / strain and a knowledge of the strain hardening exponent, the strain hardening rate at that particular point was determined. Table 30 shows calculated values of the work hardening rate at a designated strain of 12×10^{-3} , and for comparison the work hardening rates determined by the previous method (10.1.2.1) are also given.

Table 30:- Work hardening rates of 1.25 mass% chromium molybdenum alloy, austenitised at 950°C, salt bath quenched at 320°C, cold deformed various amounts

Alloy (% deformation)	True stress measured (MPa)	True strain measured ($\times 10^{-3}$)	Work hardening rate determined from exponent / power method ($\times 10^3$)	Work hardening rate determined via gradient method ($\times 10^3$)
undeformed alloy	1410	12	40.9	37.4
10% deformed	1850	12	30.1	27.7
25% deformed	2010	12	13.0	9.4
50% deformed	2045	12	12.5	9.4

NB:- Work hardening rates calculated in table 30 incorporated a strengthening effect from the tensile test plus where applicable strengthening from the cold rolling procedure.

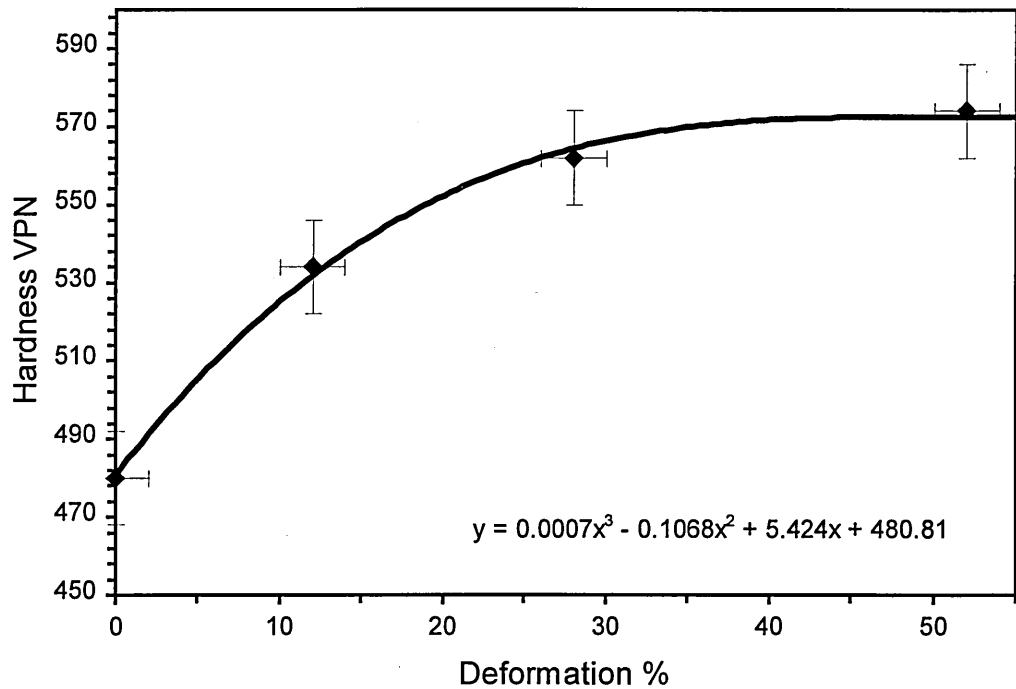
10.1.3 Determination of strengthening from the cold rolling procedure

Strengthening calculation from hardness measurement

To measure the amount of strengthening from the cold rolling procedure only plots of hardness versus amount of prior cold work were examined. Alternatively, plots of 0.025% proof strength versus plastic deformation can be used, i.e. a point at which little work hardening is incorporated into the test piece during the actual tensile test.

A plot of Vickers hardness versus the amount of prior cold work is shown in figure 160, and shows a rapid increase between the undeformed and 10% deformed alloy systems. However beyond a prior plastic deformation of approximately 25% no significant increase in hardness was observed.

Figure 160:-Hardness versus plastic deformation of 1.25 Mass% Chromium molybdenum alloy quenched into salt bath at 320°C



The relationship between hardness and deformation was described mathematically as being polynomial (10.6), which when differentiated provided a second equation (10.8), allowing the determination of curve gradient at specific plastic deformation amounts, for example:-

$$\text{Line equation } y = 0.0007X^3 - 0.1068X^2 + 5.424X + 480.81 \quad (10.6)$$

$$\text{hence gradient, } dy/dx = (3 \times 0.0007X^2) - (2 \times 0.1068X) + 5.424 \quad (10.7)$$

$$dy/dx = 0.0021X^2 - 0.2136X + 5.424 \quad (10.8)$$

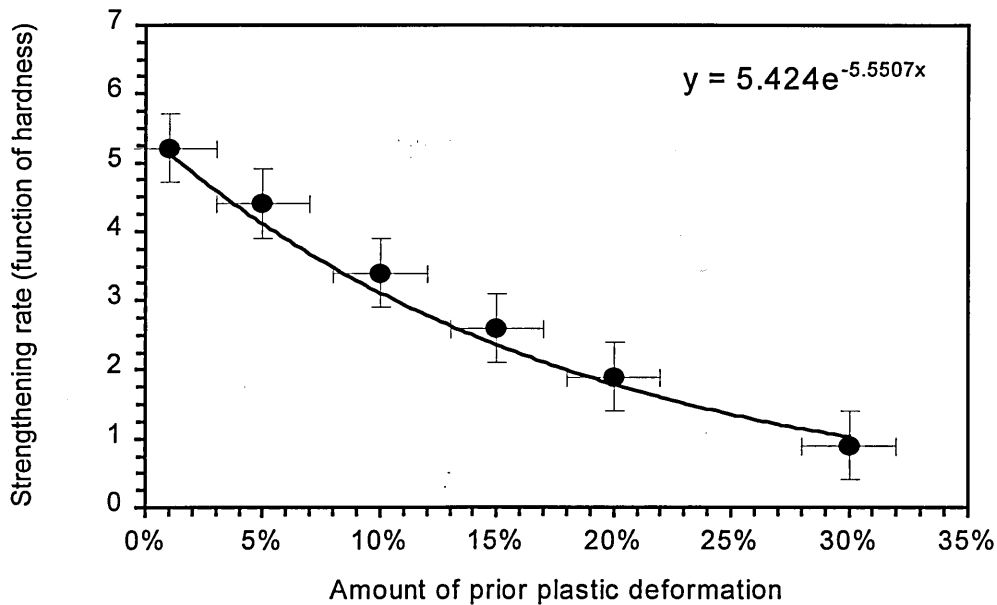
Gradient values (deformation strengthening) for specific amounts of plastic deformation are given in table 31 and figure 161. Note the equation given in figure 161 is essentially a simple analytic approximate best fit of equation 10.8.

Table 31:- Deformation strengthening as a function of hardness versus prior plastic deformation for 1.25 mass% chromium molybdenum alloy, austenitised at 950°C salt bath quenched at 320°C.

Amount of plastic deformation	strengthening rate (hardness / prior deformation) dVPN/dPS
1%	5.2
5%	4.4
10%	3.5
15%	2.7
20%	1.9
30%	0.9

A plot of prior plastic deformation versus the deformation strengthening rate (dVPN/ dPD) is illustrated in figure 161. The strengthening rate was found to decay in an exponential manner between 1 and 30% plastic deformation and an equation (noted on figure 161) was derived to describe this.

Figure 161:- Prior plastic deformation versus the hardening rate (dVPN / dPD) for 1.25 mass% chromium molybdenum alloy austenitised at 950°C, salt bath quenched at 320°C.



10.2 Mechanical evaluation of 0.5 mass% chromium 0.25 mass% carbon alloy system.

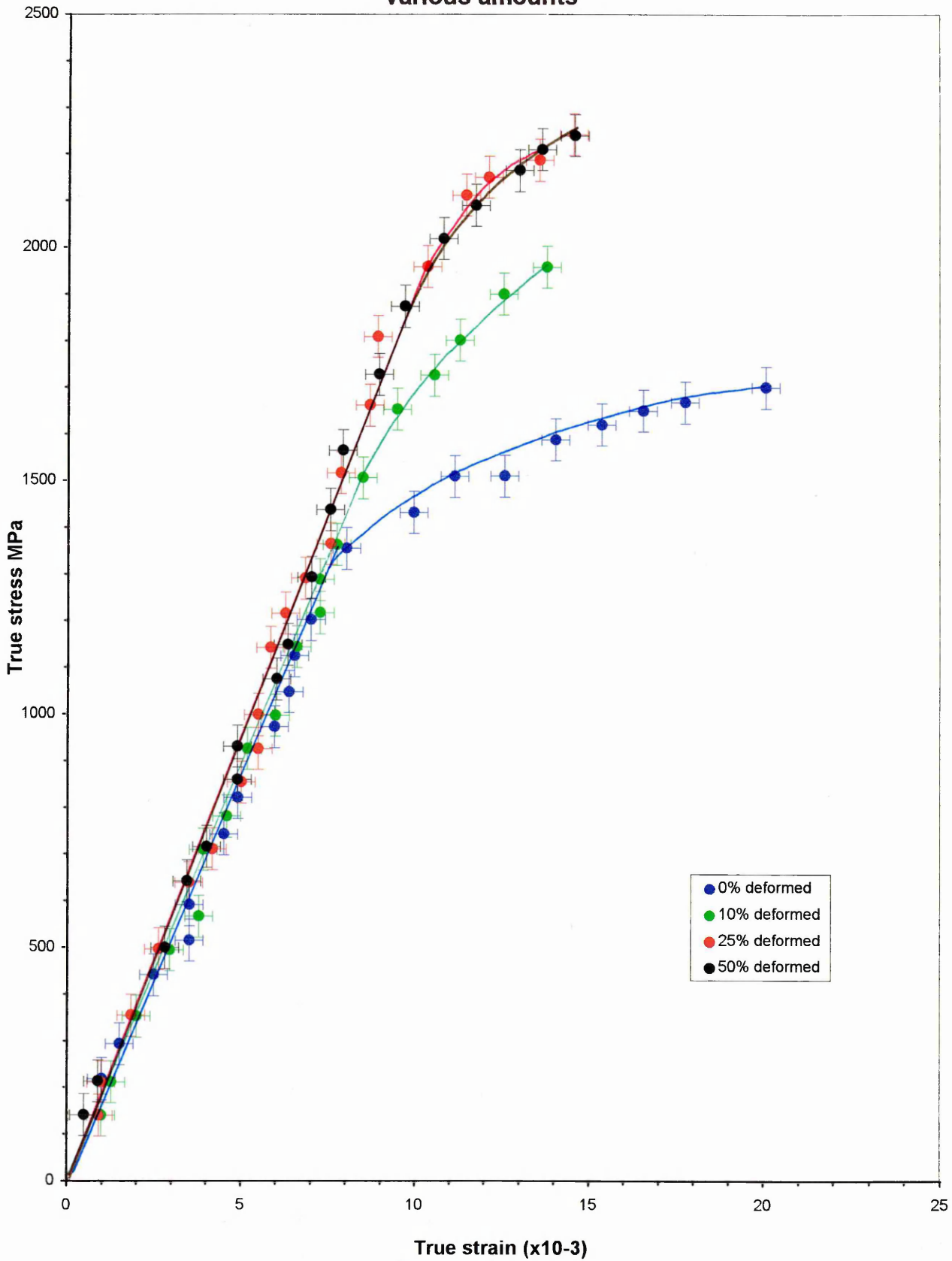
10.2.1 Tensile and hardness test results

Tensile and Vickers hardness results for the undeformed, 10, 25 and 50% deformed alloy systems are given in table 32. Corresponding true stress strain curves are illustrated in figure 162.

Table 32- Mechanical results of 0.25 mass% carbon, 0.5 mass% chromium alloy water quenched from austenitisation, cold deformed various amounts.

Thermal treatment and % amount of deformation	0.2% Proof strength (MPa)	Ultimate tensile strength (MPa)	PS / UTS ratio (%)	Hardness (VPN)
Quench into water from 950°C.	1475	1700	86	537
Quench into water from 950°C. Cold deform 10%	1850	1958	94	618
Quench into water from 950°C. Cold deform 25%	2140	2242	95	650
Quench into water from 950°C. Cold deform 50%	2140	2240	95	675

Figure 162:- True stress / Strain curve for 0.25 % chromium / 0.25% carbon alloy, water quenched from 950 C, work hardened various amounts



10.2.1.1 Comparison of 0.2% proof strength and shape of flow curve

On comparing mechanical strengths values provided in table 32, (taken from the flow curves in figure 162), a rapid increase in the 0.2% proof strength was noted between the undeformed and the 10% deformed alloy system. This suggested that a significant amount of strengthening had taken place during the cold rolling procedure. The 25% deformed alloy system possessed a superior 0.2% proof strength still, suggesting that the strengthening limit was not quite reached at the 10% deformation level. However the mechanical properties of the 25 and 50% deformed alloy system were almost identical indicating that the strengthening limit via cold work was achieved.

Each alloy system also work hardened quite differently during the tensile test, a concise summary of this is given as follows:-

- The undeformed alloy possessed a relatively low and consistent work hardening rate up to fracture.
- In contrast all deformed alloy systems possess very high but also consistent work hardening rate up to fracture. The plastic portion of this alloy system was also found to be somewhat reduced suggesting a tendency towards brittleness, and possible susceptibility to stress corrosion cracking.
- On comparing the deformed alloy flow curves at a true strain of 12×10^{-3} , a subtle decrease in the work hardening rate with respect to amount of prior plastic deformation was found.
- The flow curve for the 25 and 50% deformed alloy were almost identical with similar, relatively high work hardening rates and limited plastic flow portion hence high proof / ultimate tensile strength ratio.

10.2.2 Determination of work hardening during the tensile test

The first method employed to calculate the work hardening rate of each alloy during the tensile test was a simple gradient measurement from a nominated strain value. Method two included the use of power law relationships (i.e. using log log plots to estimate the work hardening exponent and then multiplying this by a nominated stress strain ratio). Work hardening rate results for both methods employed are provided in table 33, with figure 163 illustrating the work hardening exponent relationships used for method two.

Figure 163:- Plot of log True Stress versus Log True Strain (data taken from plastic portion of True Stress Strain curve). 0.5 mass% chromium 0.25 mass% carbon alloy water quenched from austenitisation, deformed various amounts

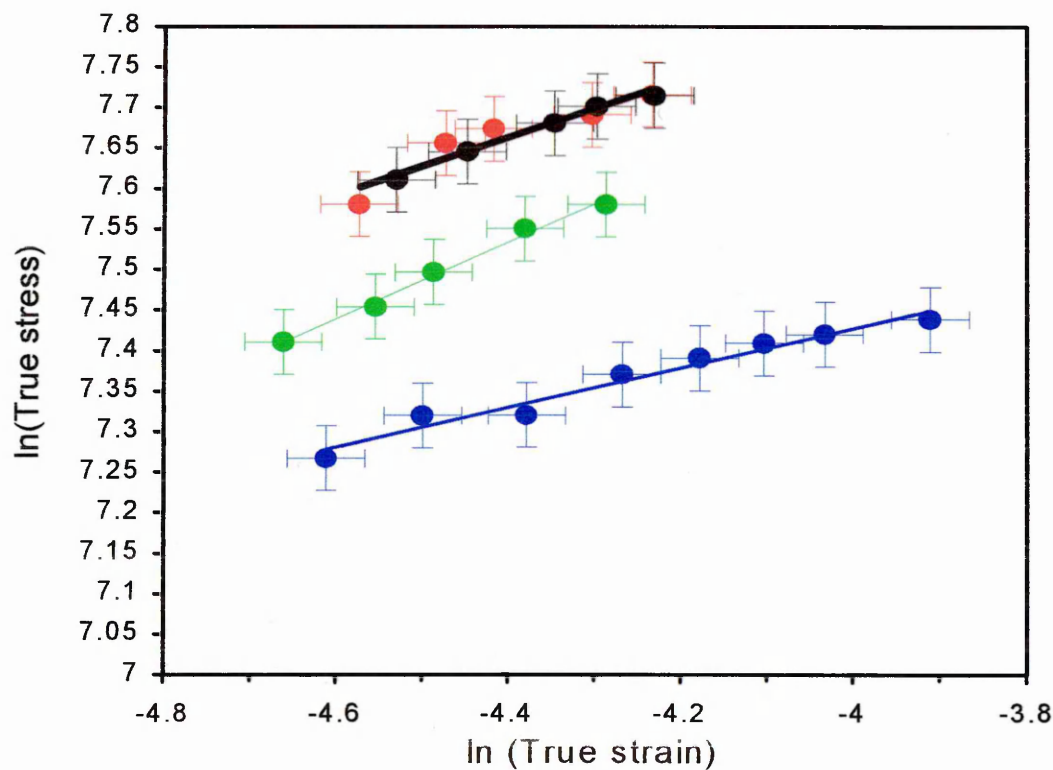


Table 33:- Work hardening rates (using both methods previously outlined) for 0.5 mass% Chromium 0.25 mass% carbon alloy systems, quenched from 950°C into water (15-18°C), cold deformed various amounts

Alloy type (amount of deformation)	Gradient at a strain of 12×10^{-3} Work hardening Rate measured directly from stress strain curve. ($\times 10^3$)	Work hardening rate measured using the gradient provided in figure 163 and a nominates stress strain ratio.
Undeformed alloy	33.4	30.5
10% deformed alloy	70.7	70.7
25% deformed alloy	60.0	60.0
50% deformed alloy	60.0	60.0

Table 33 shows reasonable agreement of work hardening values between the two methods employed. Apart from undeformed alloy system, the work hardening rate calculated from the power law relationship was found to be a little higher than the gradient method. This discrepancy was possibly due to the fact that only a limited number of data points were available although other error sources were also recognised and are discussed in further detail in appendix 2.

10.2.3 Determination of strengthening amount from cold rolling.

Strengthening evaluation from hardness measurement

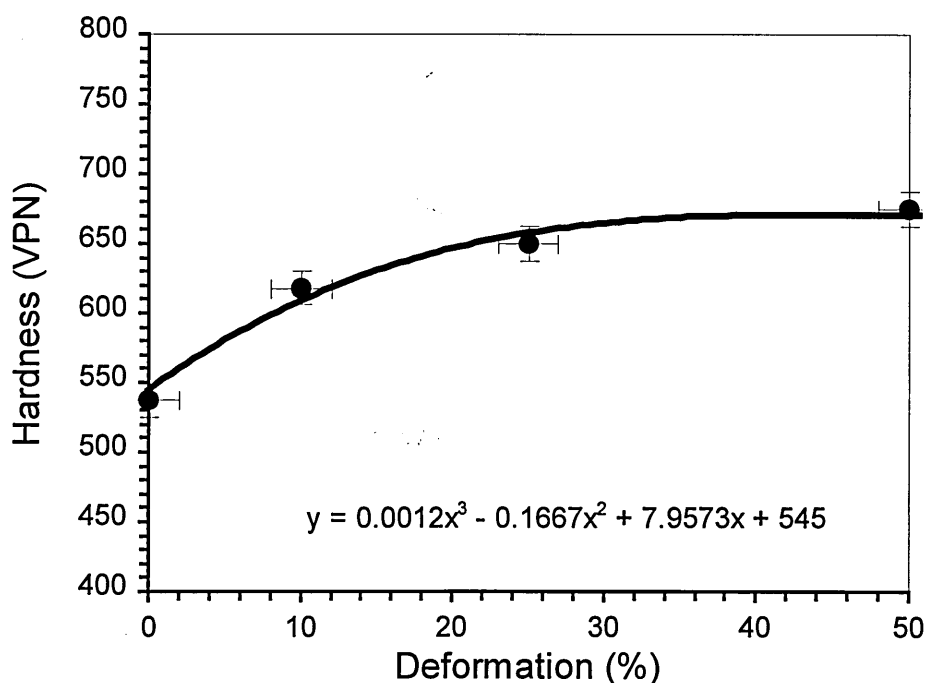
To examine the strengthening from the cold deformation procedure, plots of hardness versus amount of prior plastic deformation were examined.

The change in strengthening rate, as a function of hardness was then calculated from the gradient of the respective curve.

Figure 164 shows a plot of average hardness versus prior plastic deformation for the 0.5 mass% chromium 0.25 mass% carbon alloy system.

A sharp increase in hardness was found below approximately 15% deformation which correlated to a high rate of deformation strengthening. Beyond approximately 25% plastic deformation, measured hardness remained more or less constant equating to a very low deformation strengthening rate.

Figure 164:- Hardness versus amount of prior plastic deformation for 0.5 mass% chromium 0.25 mass% carbon alloy, water quenched from austenitisation



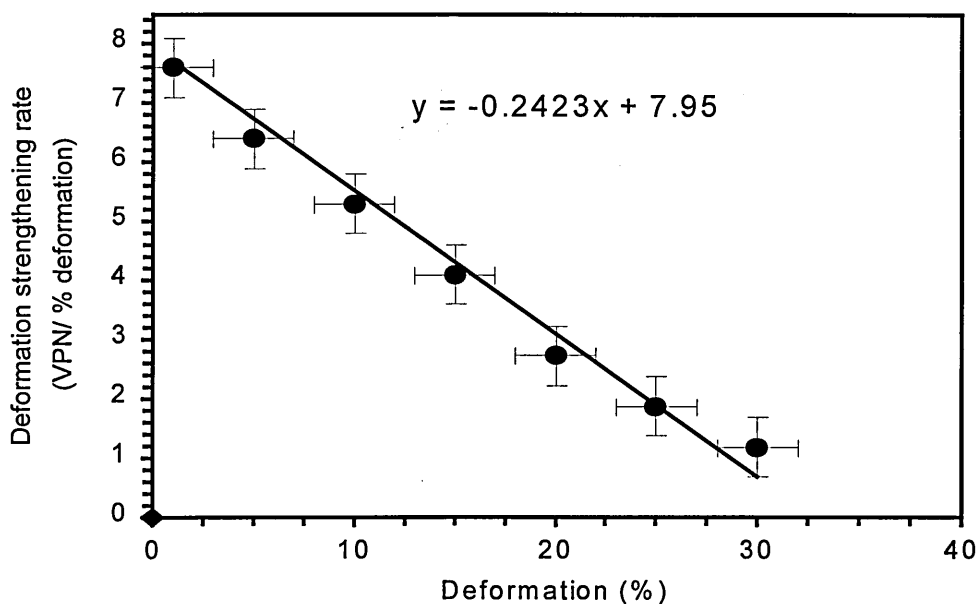
The relationship between hardness and deformation was described mathematically as being polynomial, which when differentiated provided a second equation, allowing the determination of curve gradient at specific plastic deformation amounts.

Theoretical values (amounts of plastic deformation) were then incorporated into the differentiated equation provided in figure 164 to obtain a plot of deformation strengthening rates as a function of hardness (table 34 and figure 165).

Table 34:- Deformation strengthening rate as a function of hardness for 0.5 mass% chromium, 0.25 mass% carbon alloy water quenched from austenitisation

Amount of plastic deformation	Hardening rate (hardness / prior deformation) $\frac{dVPN}{dPD}$
5%	6.38
10%	5.05
15%	4.14
20%	2.72
25%	1.87
30%	0.29

Figure 165:- Deformation strengthening rate (function of hardness) versus prior plastic deformation of 0.5 mass% chromium, 0.25 mass% carbon alloy water quenched from austenitisation



10.3 Mechanical evaluation of 0.3 mass% C, Boron alloy system

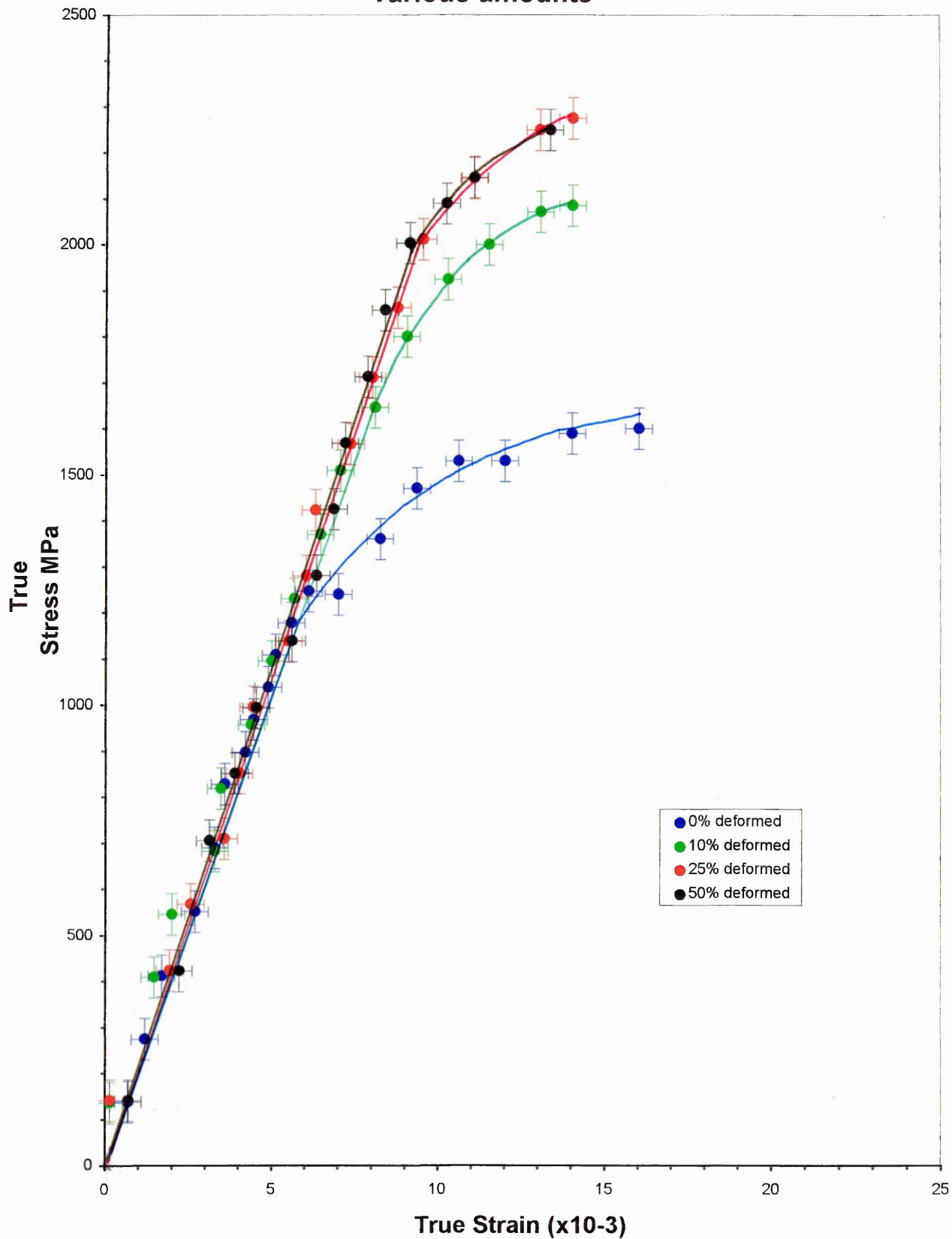
10.3.1 Tensile and hardness test results

Tensile and Vickers hardness results for the undeformed, 10, 25 and 50% deformed alloy systems are given in table 35. Corresponding true stress strain curves are illustrated in figure 166.

Table 35:- Mechanical results of 0.3 mass% carbon, boron alloy water quenched from austenitisation, cold deformed various amounts.

Thermal treatment and % amount of deformation	0.2% Proof strength (MPa)	Ultimate tensile strength (MPa)	PS / UTS ratio (%)	Hardness (VPN)
Quench into water from 950°C. Undeformed	1375	1558	88	548
Quench into water from 950°C. Cold deform 10%	1925	2085	92	619
Quench into water from 950°C. Cold deform 25%	2200	2275	97	652
Quench into water from 950°C. Cold deform 50%	2220	2250	98	664

Figure 166:- True stress / strain curve for 0.3 % carbon boron steel water quenched from 950C, work hardened various amounts



10.3.1.1 Comparison of 0.2% proof strength and shape of flow curves

On comparing mechanical strengths values provided in table 35, (taken from the flow curves in figure 166), a rapid increase in 0.2% proof strength and ultimate tensile strength ratio was noted between the undeformed and the 10% deformed alloy system. This suggested that a significant amount of strengthening had taken place during the cold rolling procedure.

The 25% deformed alloy system possessed a marginally greater 0.2% proof strength, suggesting that the strengthening limit was not quite reached at the 10% deformation level. However the mechanical properties of the 25 and 50% deformed alloy system were almost identical indicating that the strengthening limit via cold work was achieved.

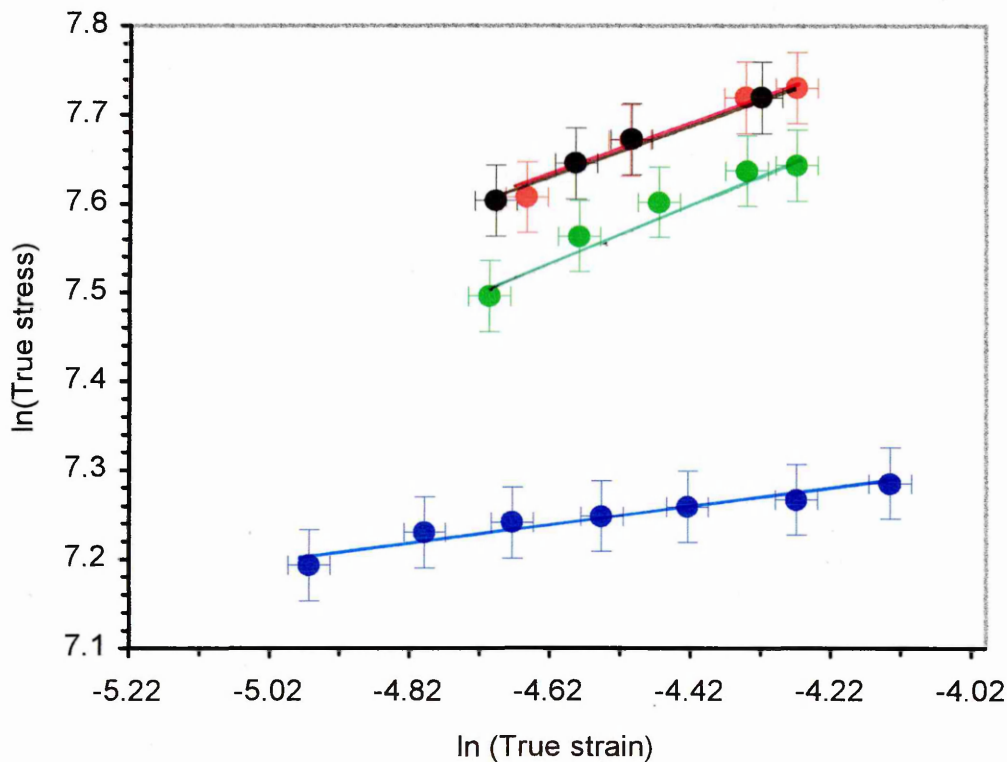
Each alloy system also work hardened quite differently during the tensile test, a concise summary of this is given as follows:-

- The undeformed alloy initially appeared to work harden quite rapidly up to a true strain of approximately 8×10^{-3} . However at larger strains a relatively low and consistent work hardening rate up was found.
- In contrast all deformed alloy systems possess a much higher rate of work hardening during the tensile test which diminished somewhat at high strains near the point of fracture.
- The plastic elastic ratios of the deformed alloy systems were also found to be somewhat reduced suggesting a tendency towards brittleness / loss in toughness.

10.3.2 Determination of work hardening rate during the tensile test

The first method employed to give an indication of the work hardening rate of each alloy during the tensile test included simple gradient measurement from a nominated strain value. Method two included the use of power law relationships (i.e. log log plots to estimate the work hardening exponent and then multiplying this value by a nominated stress strain ratio value). Work hardening rate results for both methods employed are provided in table 36, with figure 167 shows the work hardening exponent relationships used for method two.

Figure 167:- Plot of log True Stress versus Log True Strain (data taken from plastic portion of True Stress Strain curve). 0.3 mass% carbon boron alloy water quenched from austenitisation, deformed various amounts.



Key:- See figure 159

Table 36:- Work hardening rates (using both methods previously outlined) for 0.3 mass% carbon boron alloy, austenitised at 950°C, water quenched, cold deformed various amounts

Alloy (% deformation)	Gradient at a strain of 12×10^{-3} (work hardening rate $\times 10^3$) Measured directly from stress strain curve.	Work hardening rate measured via the gradient provided in figure 167 and nominated stress strain ratio.
undeformed alloy	10	11.3
10% deformed	54.5	55.1
25% deformed	56.6	55.7
50% deformed	56.6	54.3

Table 36 shows reasonable agreement of work hardening values between the two methods employed, with both approaches finding the most dramatic increase occurring between the undeformed and 10% deformed alloy system.

The 25 and 50% deformed alloy system were assumed to have near identical work hardening rates since the flow curves were more or less superimposed on one another.

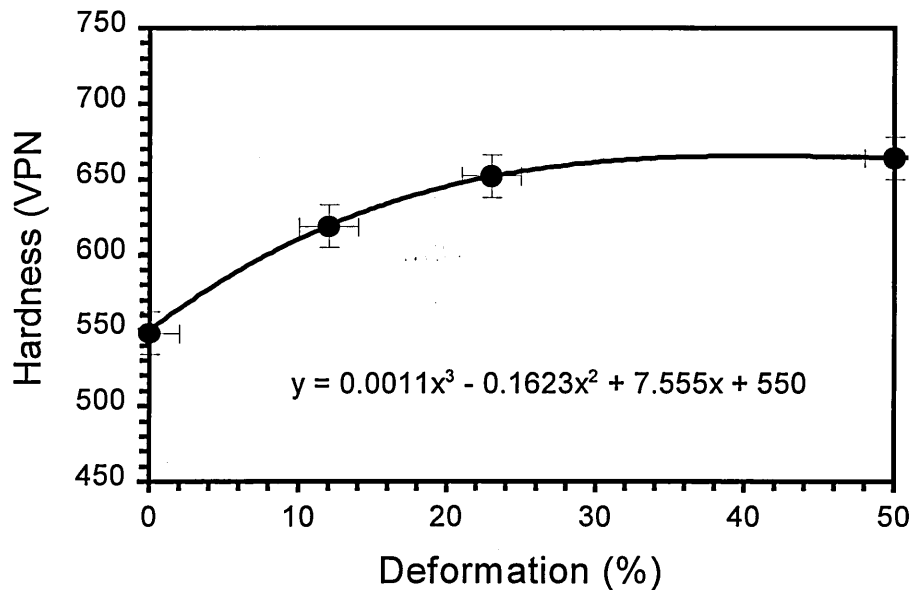
The slight difference in work hardening rate determined via power law method was not thought to be unreasonable considering the amount of data points available and possible sources of error.

10.3.3 Determination of strengthening from cold rolling procedure

Figure 168 shows a plot of average hardness versus prior plastic deformation for the 0.3 mass% carbon boron alloy system.

A rapid increase in hardness was found up to approximately 25% prior plastic deformation which correlated to a high rate of deformation strengthening. In contrast the measured hardness of the 25 and 50% deformed samples were more or less identical suggesting a very low work hardening rate.

Figure 168:- Hardness versus amount of prior plastic deformation for 0.3 mass% carbon boron alloy, water quenched from austenitisation

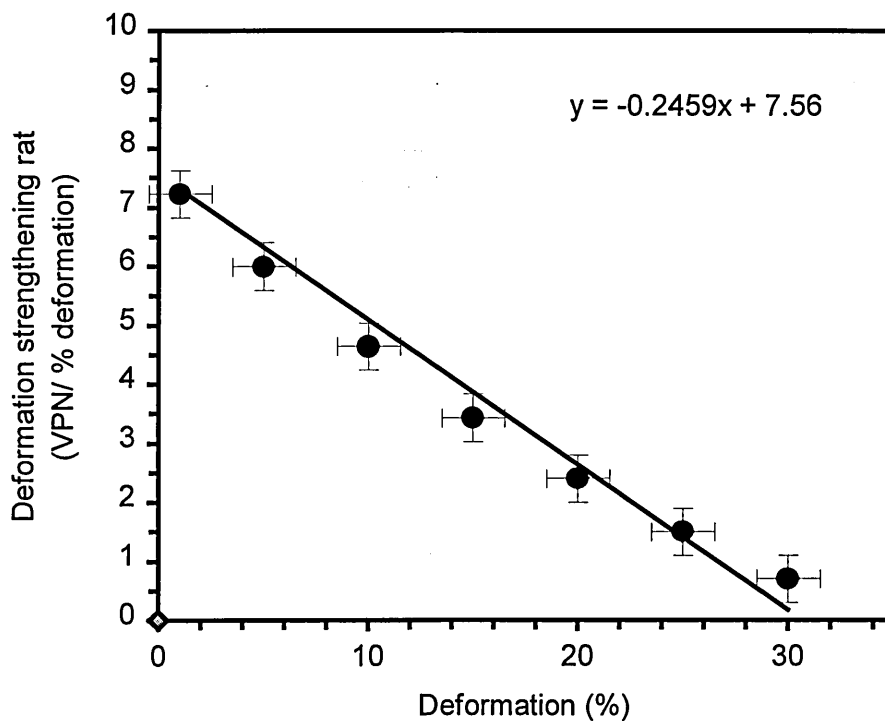


The hardness / plastic deformation function is also provided in figure 168, which when differentiated provided the gradient at specific plastic deformation amounts, and hence the deformation strengthening rate. Theoretical values (amounts of plastic deformation) were then incorporated into the differentiated equation provided in figure 168 to obtain plots of deformation strengthening rates as a function of hardness (table 37 and figure 169)

Table 37:- Deformation strengthening rate as a function of hardness for 0.5 mass% chromium, 0.25 mass% carbon alloy water quenched from austenitisation

Amount of plastic deformation	Deformation strengthening rate (hardness / prior deformation) $\frac{dVPN}{dPD}$
1%	7.23
5%	6.01
10%	4.64
15%	3.43
20%	2.38
25%	1.50
30%	0.78

Figure 169:- Work hardening rate (function of hardness) versus prior plastic deformation of 0.3 mass% carbon boron alloy water quenched from austenitisation



10.4 Mechanical evaluation of 0.3 mass % C, B alloy (tempered 250°C)

10.4.1 Tensile and hardness test results

The mechanical properties, including true stress strain and Vickers hardness of each variant are given in table 38, with corresponding true stress strain curves illustrated in figure 170.

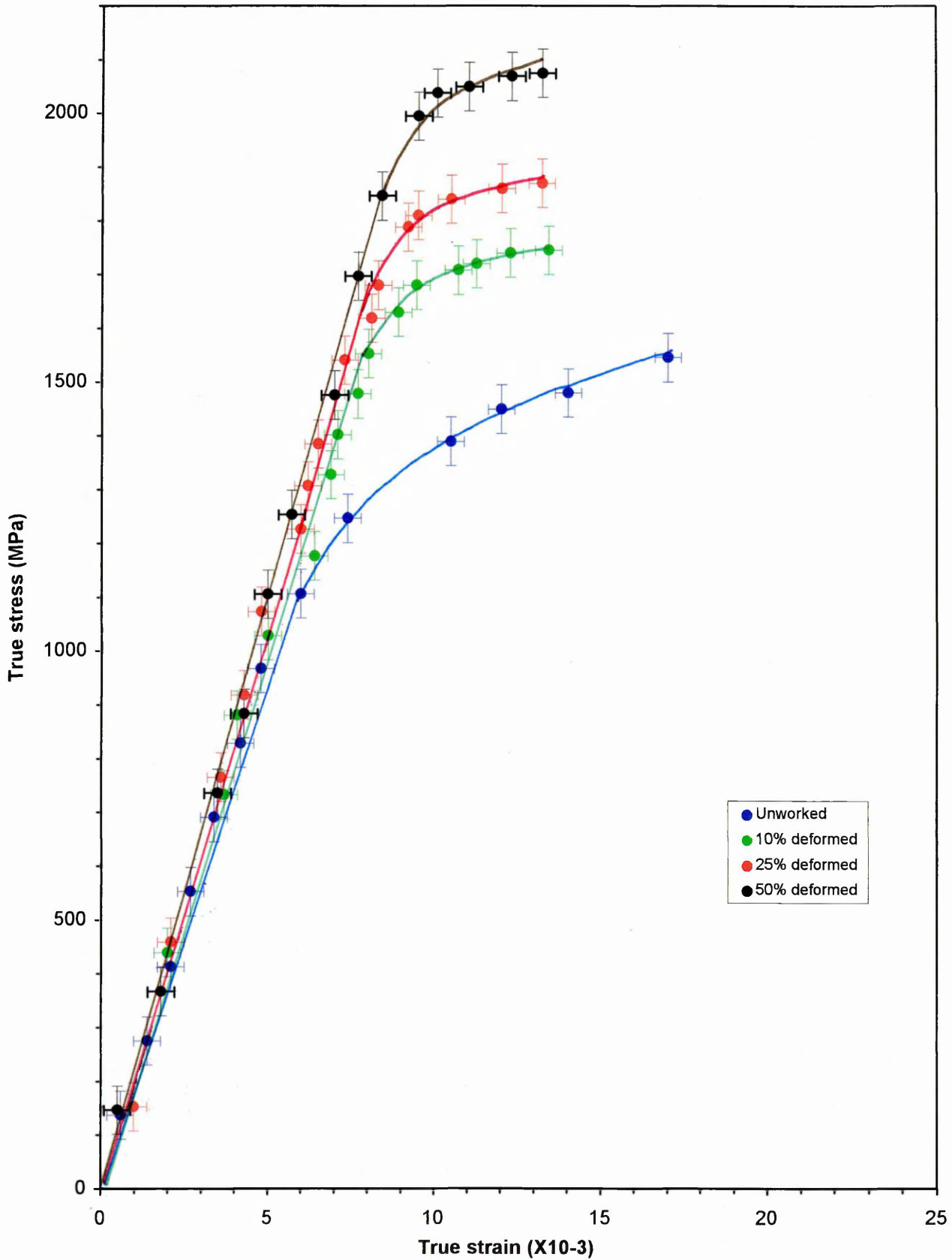
Table 38:- Mechanical results of 0.3 mass % Carbon, Boron alloy water quenched from austenitisation tempered at 250°C for 10 minutes, cold deformed various amounts.

Thermal treatment and % amount of deformation	0.2% Proof strength (MPa)	Ultimate tensile strength (MPa)	PS / UTS ratio (%)	Hardness (VPN)
Quench into water from 950°C.	1375	1546	89	499
Quench into water from 950°C. Cold deform 10%	1690	1745	97	532
Quench into water from 950°C. Cold deform 25%	1850	1871	99	560
Quench into water from 950°C. Cold deform 50%	2050	2069	99	576

10.4.1.1 Comparison of 0.2% proof strength and shape of flow curves

A significant increase in the 0.2% proof strength was observed between the undeformed and 10% deformed alloy variant indicating that a significant degree of strengthening had taken place during the cold rolling procedure.

Figure 170:- True stress / Strain curve for 0.3% carbon boron steel water quenched and tempered at 250 C, work hardened various amounts



The plastic portion of the stress strain curve for the undeformed variant was found to be quite uniform but with a slight gradient, exhibiting some degree of work hardening during the tensile test. The plastic portion gradient for the deformed variants were in comparison, less acute indicating a reduced work hardening rate during the tensile test (see section 10.5.2).

10.4.2 Determination of work hardening under the tensile test

Work hardening rates for both methods employed are provided in table 39, with figure 171 showing the work hardening exponent relationships used for method 2.

Figure 171:- Plot of log True stress versus Log True strain (data taken from plastic portion of True Stress Strain curve). 0.3 mass % carbon boron alloy water quenched from austenitisation, tempered at 250°C for 10 minutes , deformed various amounts

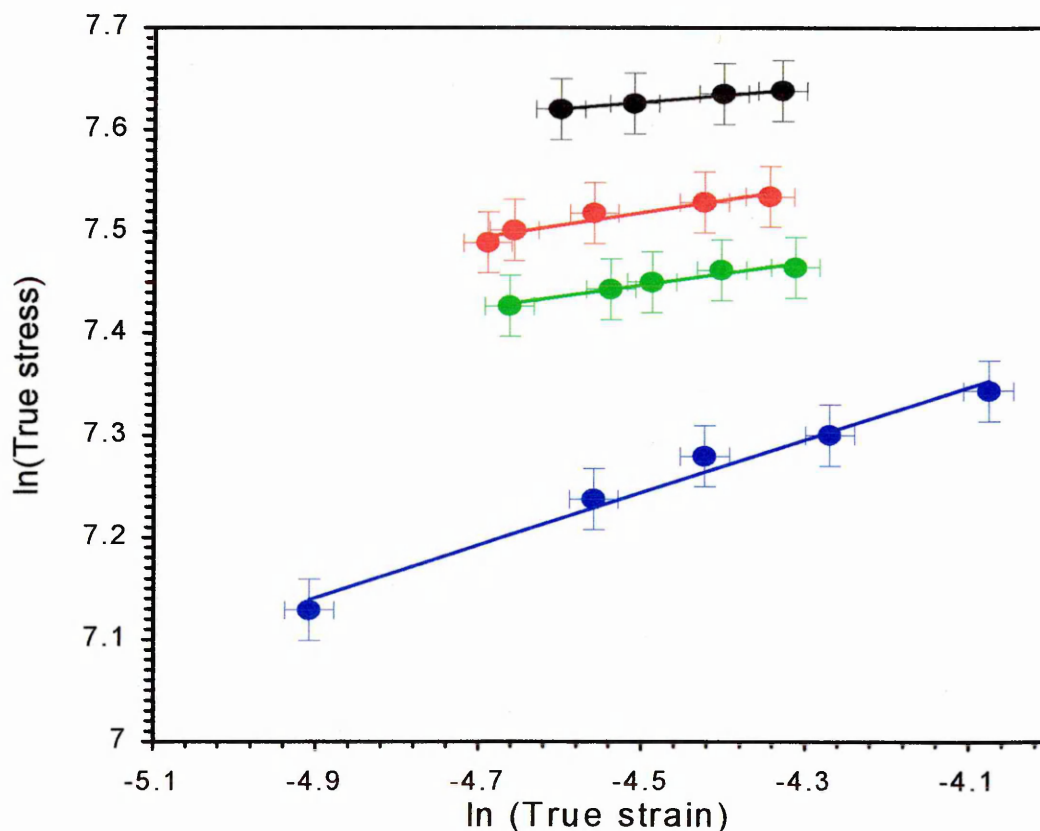


Table 39:- Work hardening rates (using both methods previously outlined)
for the 0.3 mass % carbon boron alloy, water quenched from
austenitisation, tempered at 250°C, cold deformed various amounts

Alloy (% deformation)	Gradient at a strain of 12×10^{-3} (work hardening rate measured directly from the stress strain curve)	Work hardening rate determined using the work hardening exponent from figure 171 ($\times 10^{-3}$)
undeformed alloy	28.0	30.6
10% deformed	14.7	16.4
25% deformed	17.0	18.9
50% deformed	10	11.9

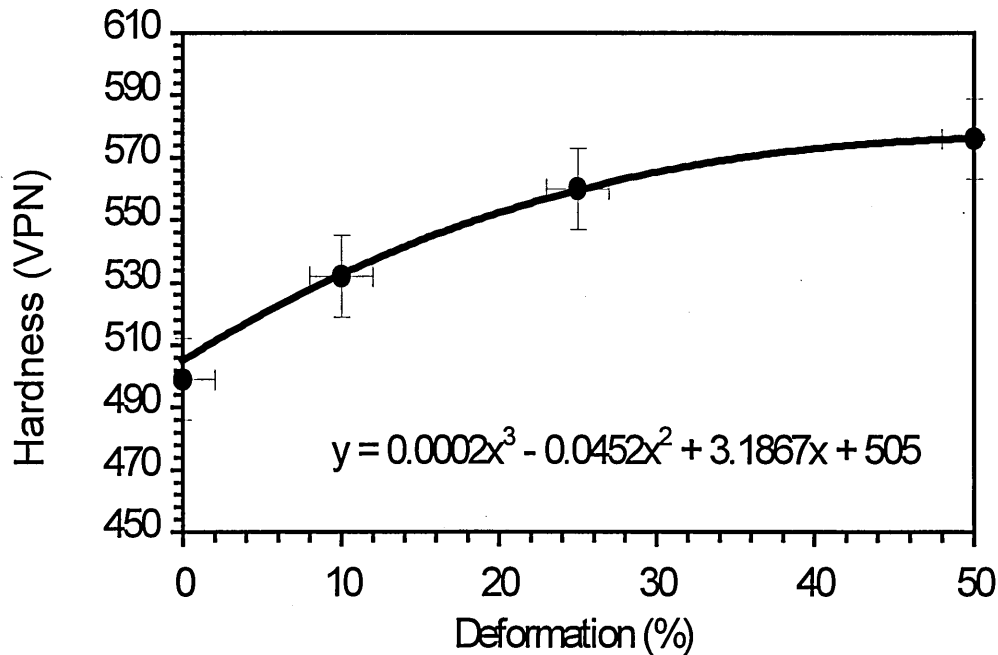
Table 39 shows good agreement between the two methods employed for the calculation of work hardening rate.

The undeformed alloy system possessed the highest work hardening rate at a true strain of 12×10^{-3} . This was also reflected in true stress strain curve gradients shown in figure 170. The work hardening rate of the 10 and 25% deformed alloy systems were found to be almost identical, with the stress strain curves shown in figure 170 almost identical also. The 50% deformed alloy possessed the lowest work hardening rate of all comparable with the 50% deformed 1.25 mass % chromium molybdenum alloy system.

10.4.3 Determination of strengthening from cold rolling procedure

Figure 172 shows a plot of average hardness versus prior plastic deformation for the 0.3 mass % carbon boron alloy tempered at 250°C.

Figure 172:- Hardness versus plastic deformation of 0.3 mass % carbon boron alloy quenched into water from austenitisation, tempered at 250°C for 10 minutes.

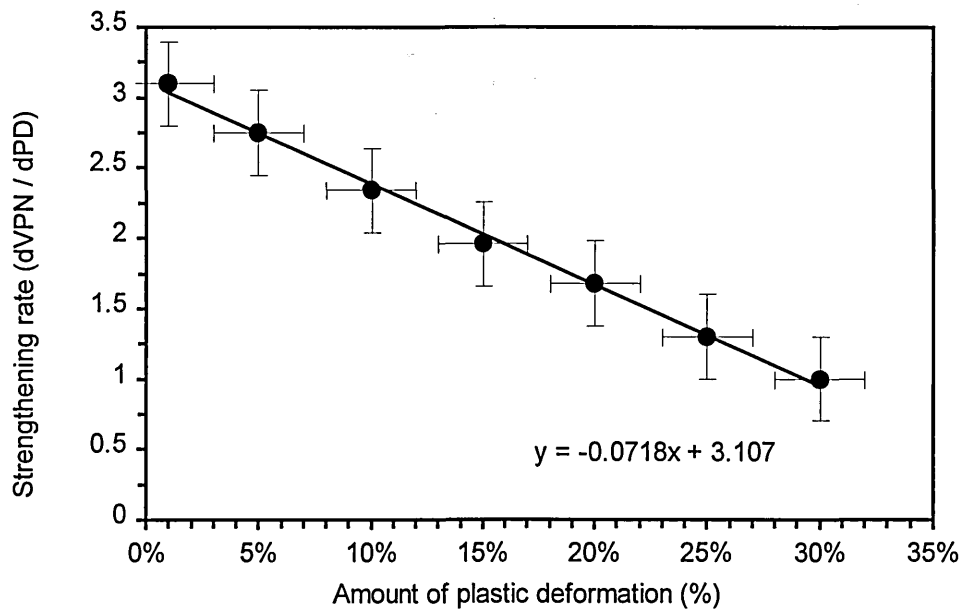


The relationship between hardness and deformation (given on figure 172) was differentiated to provide a second equation which allowed the determination of the curve gradient at specific plastic deformation amounts. Theoretical values (amount of plastic deformation) were then incorporated into the differentiated equation to provide a relationship of deformation strengthening rate as a function of hardness (see table 40 and figure 173).

Table 40:- Deformation strengthening rate as a function of hardness for 0.3 mass % carbon boron alloy water quenched from austenitisation, tempered at 250°C for 10 minutes.

Amount of plastic deformation	Strengthening rate (hardness / prior deformation) $\frac{dVPN}{dPD}$
1%	3.10
5%	2.75
10%	2.34
15%	1.96
20%	1.68
25%	1.3
30%	1.0

Figure 173:- Prior plastic deformation versus the hardening rate (dVPN / dPD) for 0.3 mass % carbon boron alloy water quenched from austenitisation, tempered at 250°C for 10 minutes.



10.5 Mechanical evaluation of 0.3 mass% C, B alloy (tempered 400°C)

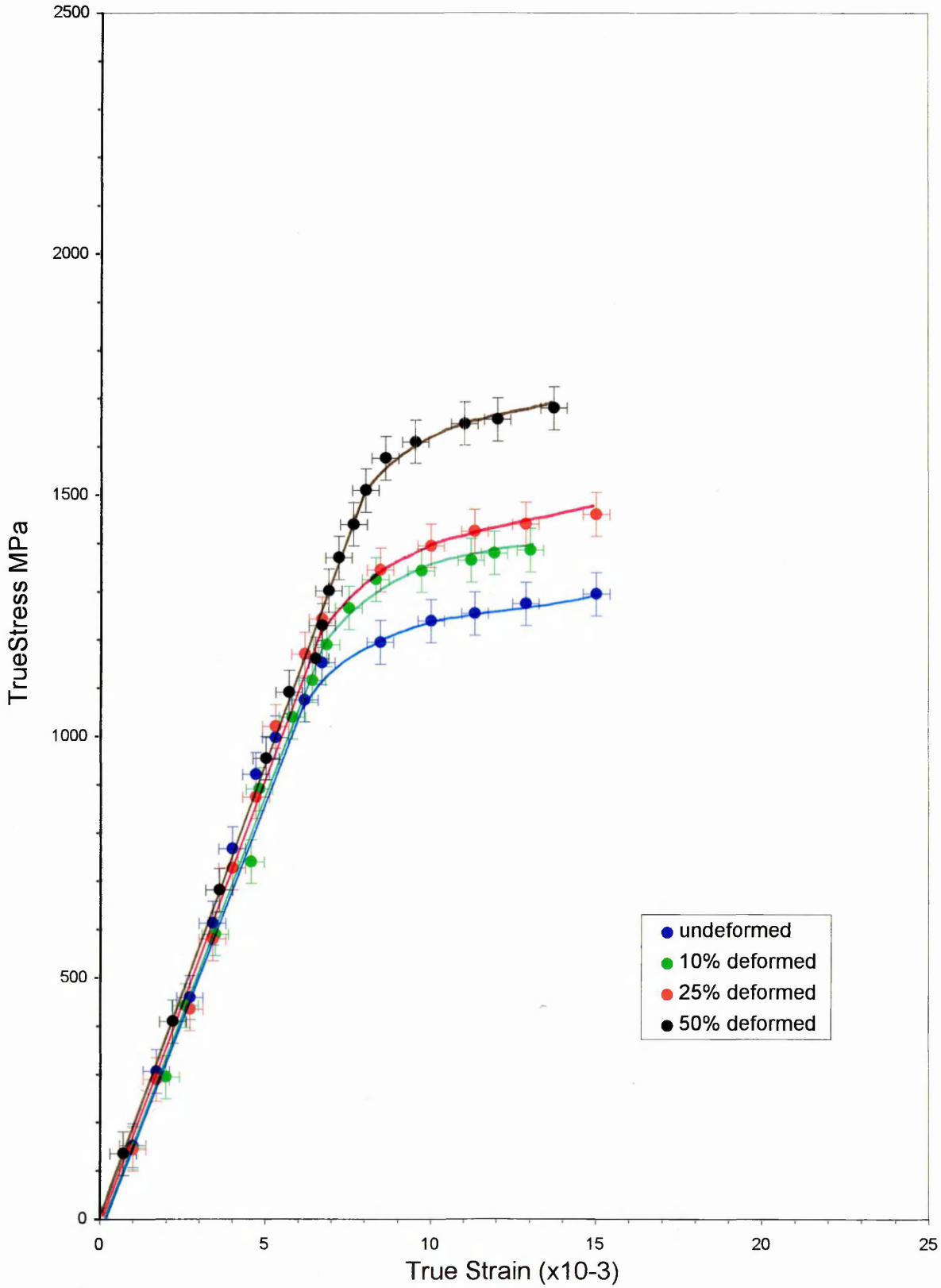
10.5.1 Tensile and hardness test results

The mechanical properties, including true stress strain and Vickers hardness of each variant are given in table 41. Corresponding true stress strain curves illustrated in figure 174.

Table 41:- Mechanical results of 0.3 mass% Carbon, Boron alloy water quenched from austenitisation tempered at 400°C for 10 minutes, cold deformed various amounts.

Thermal treatment and % amount of cold deformation	0.2% Proof strength (MPa)	Ultimate tensile strength (MPa)	PS / UTS ratio (%)	Hardness (VPN)
Quench into water from 950°C. Undeformed	1200	1295	93	407
Quench into water from 950°C. Cold deform 10%	1360	1386	98	420
Quench into water from 950°C. Cold deform 25%	1435	1450	99	432
Quench into water from 950°C. Cold deform 50%	1645	1680	98	464

Figure 174:- True stress / strain curve for 0.3% carbon boron alloy, water quenched from 950 C, tempered at 400C, work hardened various amounts.



10.5.1.1 Comparison of 0.2% proof strength and shape of flow curves

Characteristic features of all stress strain curves shown in figure 174 were:-

- Low rate of work hardening during the tensile test, with plastic portion of curve being uniformly “flat”.
- All round lower proof and ultimate tensile strength compared to the untempered variants.

On comparing the undeformed alloy with the 10% deformed, some strengthening had occurred from the rolling procedure since the proof strength was marginally higher. Interesting and somewhat puzzling aspects of this alloy series included the fact that the 25% deformed alloy mechanical properties were similar to the 10% deformed alloy system suggesting that maximum strengthening was almost attained. However the 50% deformed alloy system curve contradicted this with a significantly higher proof and ultimate tensile strength than the 25% deformed system.

10.5.2 Determination of work hardening under the tensile test

Work hardening rates for both methods employed are provided in table 42. Figure 175 shows the work hardening exponent relationships for all alloy variants, with the gradient from these plots multiplied by a nominated stress strain ratio to obtain a corresponding work hardening rate.

Figure 175:- Plot of log True stress versus Log True strain (data taken from plastic portion of True Stress Strain curve.) 0.3 mass% carbon boron alloy water quenched from austenitisation, tempered at 400°C for 10 minutes , deformed various amounts

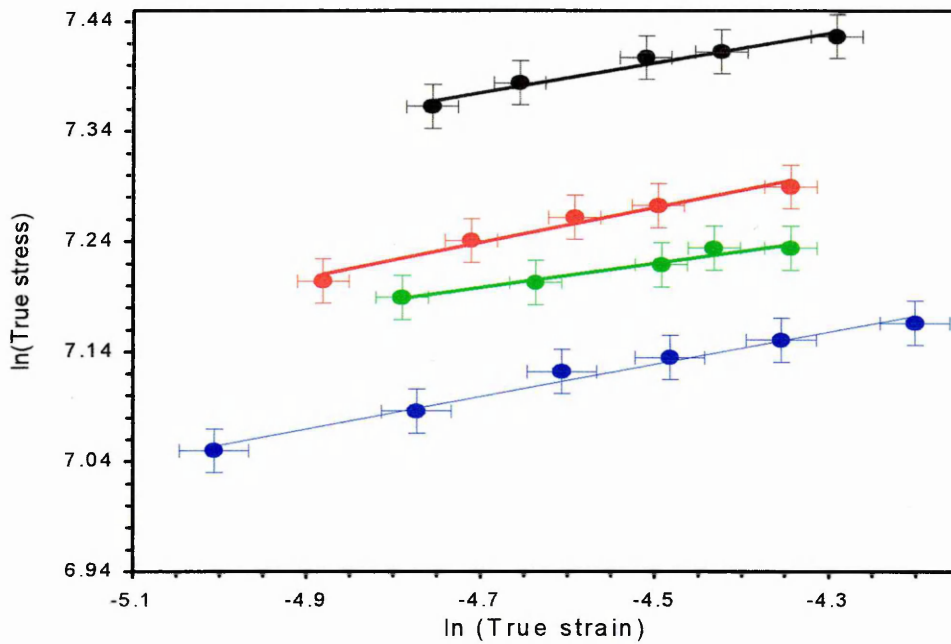


Table 42- Work hardening rate (using both methods previously outlined) for 0.3 mass% carbon boron alloy, water quenched from austenitisation, tempered at 400°C, cold deformed various amounts

Alloy (% deformation)	Gradient at a strain of 12×10^{-3} work hardening rate measured directly from the stress strain curve ($\times 10^3$)	Work hardening rate determined using the work hardening exponent from figure 175 ($\times 10^3$)
undeformed alloy	16	15.8
10% deformed	12.5	12.6
25% deformed	21.2	18.7
50% deformed	20	18.5

Table 42 shows good agreement between the two methods employed, with perhaps the power law method being the more accurate of the two since it removes some degree of measurement error. Interestingly, the work hardening rate for the undeformed alloy system is actually greater than the 10% deformed alloy. This fact is also clearly visible on the true stress strain curve (figure 174) However the difference between the two was only very subtle, unlike the untempered variants where the difference in work hardening rate was quite dramatic.

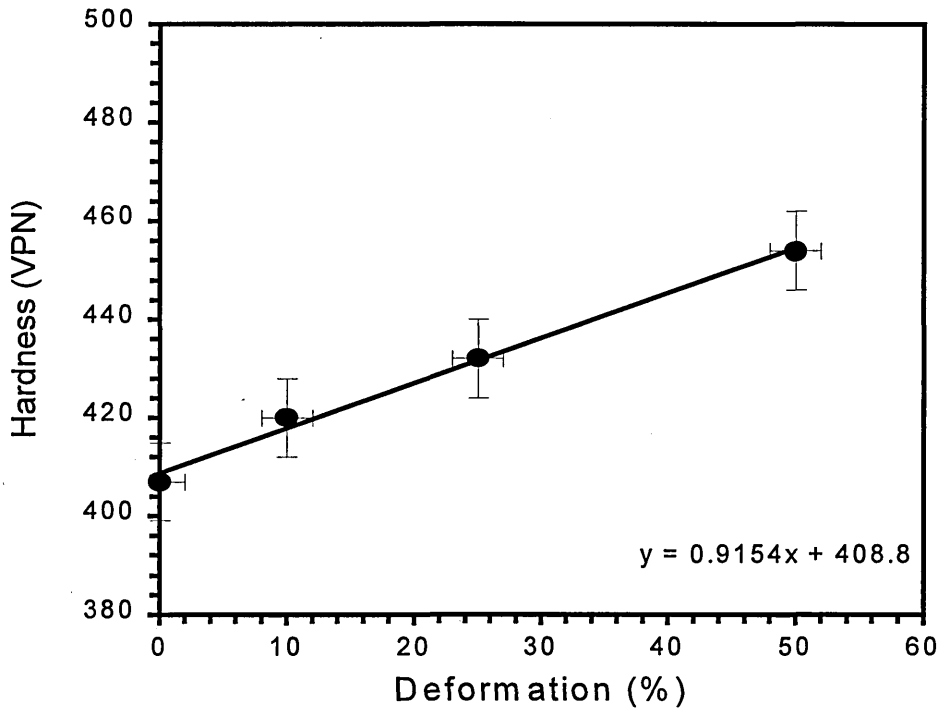
On comparing the 10 and 25% deformed alloy systems a small increase in the work hardening rate with increasing amounts of plastic deformation was found. This was in total contrast to the untempered variant (section 10.3.2.2) where the work hardening rate actually decreased between the same two variants. The 50% deformed tempered alloy was found to possess a slightly lower work hardening rate than the 25% deformed variant,. However, it was argued that these two alloys probably possessed similar work hardening rates after taking measurement and interpretation errors into consideration.

10.5.3 Determination of strengthening from cold rolling procedure

Figure 176 shows a plot of average hardness versus prior plastic deformation for the 0.3 mass% carbon boron alloy tempered at 400°C.

A linear relationship between hardness and deformation was found, which equated to a constant rate of strengthening up to 50% prior plastic deformation. The gradient of the line 0.9154 equates to deformation strengthening rate as a function of hardness from 0 to 50% prior plastic deformation.

Figure 176:- Hardness versus plastic deformation of 0.3 mass% carbon boron alloy quenched into water from austenitisation, tempered at 400°C for 10 minutes.

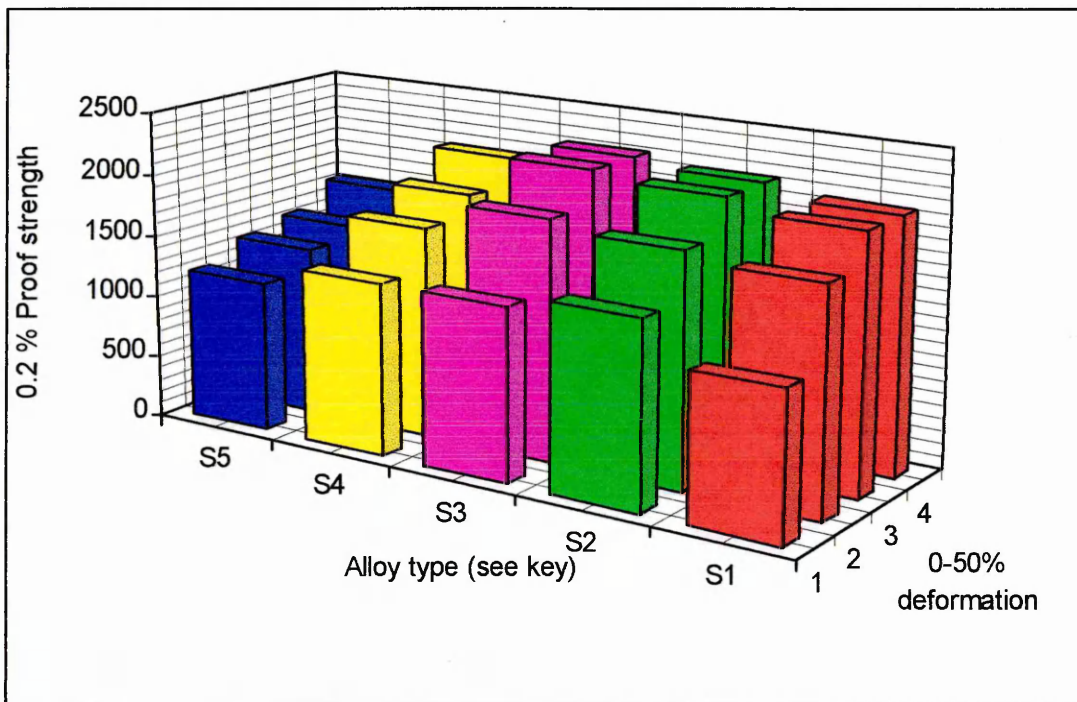


10.6 Summary of mechanical results for optimum alloy systems

10.6.1 True stress strain results (proof and ultimate tensile strength)

Figure 177 summarises the increase in 0.2% proof strength as a result of cold deformation for all the examined optimum alloy systems. Actual values are provided in tables 27, 32, 35, 38 and 41 were previously taken from true stress strain curves (figures 158, 162, 166, 170 and 174).

Figure 177 Comparison bar chart of 0.2% proof strength for all examined alloy systems in the undeformed, 10, 25 and 50% deformed condition



Key

S1 (red) = 1.25 mass% Cr Mo alloy quenched into salt bath from 320°C.

S2 (green) = 0.5 mass% Cr 0.25 mass% C alloy quenched into water from 950°C

S3 (magenta) = 0.3 mass% C, B alloy quenched into water from 950°C

S4 (yellow) = 0.3 mass% C, B alloy quenched into water from 950°C, tempered at 250°C

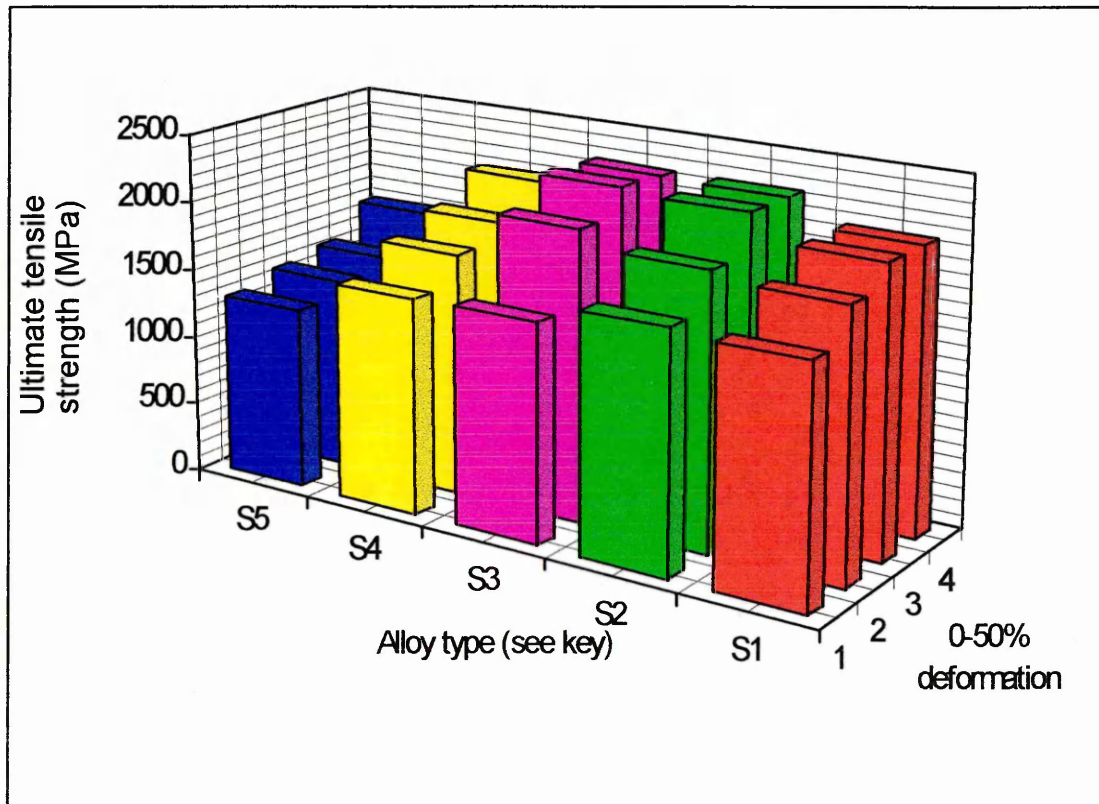
S5 (blue) = 0.3 mass% C, B alloy quenched into water from 950°C, tempered at 400°C

General observations with respect to figure 177 were noted as follows:-

- The most dramatic increase in 0.2% proof strength was found between the undeformed and 10% deformed alloy systems.
- In comparison, differences in 0.2% proof strength between the 25 and 50% deformed alloy systems were only slight.
- The 1.25 mass% chromium molybdenum alloy (salt bath quenched) and the straight water quenched 0.3 mass% carbon boron alloy possessed the largest increase in proof strength on 10% cold deformation.
- The 0.3 mass% carbon boron and the 0.5 mass% chromium 0.25 mass% carbon alloy possessed very similar proof strength profiles attaining similar strengths after cold deformation.
- On comparing the 0.3 mass% carbon boron alloy with its 250°C tempered counterpart, the 0.2% proof strengths in the undeformed condition were similar. However after 10% cold deformation the untempered variant possessed a significantly higher 0.2% proof strength.
- The effect of tempering (alloys S4 and S5) clearly affected the degree of mechanical strength improvement with only relatively slight increases in 0.2% proof strength observed.
- The 400°C tempered 0.3 mass% carbon boron alloy possessed the lowest initial 0.2% proof strength and the lowest degree of improvement with cold deformation.

Figure 178 surmises the increase in ultimate tensile strength for all examined optimum alloy systems. Actual values were previously taken from true stress strain curves (figures 158, 162, 166, 170 and 174).

Figure 178:- Comparison bar chart of ultimate tensile strength for all examined alloy systems in the undeformed, 10, 25 and 50% deformed condition



Key

S1 (red) = 1.25 mass% Cr Mo alloy quenched into salt bath from 320°C.

S2 (green) = 0.5 mass% Cr 0.25 mass% C alloy quenched into water from 950°C

S3 (magenta) = 0.3 mass% C, B alloy quenched into water from 950°C

S4 (yellow) = 0.3 mass% C, B alloy quenched into water from 950°C, tempered at 250°C

S5 (blue) = 0.3 mass% C, B alloy quenched into water from 950°C, tempered at 400°C

General observations with respect to figure 178 were noted as follows:-

- As with figure 177, the most dramatic increase in ultimate tensile strength was found between the undeformed and 10% deformed alloy systems.
- The 0.3 mass% carbon boron alloy in the straight water quenched condition possessed the largest increase in proof strength on 10% cold deformation.
- The increase in ultimate tensile strength of the 400°C tempered 0.3 mass% carbon boron alloy was found to be relatively slight with increasing amounts of plastic deformation.
- The ultimate tensile strength of all 25 and 50% deformed alloy systems were more or less identical.

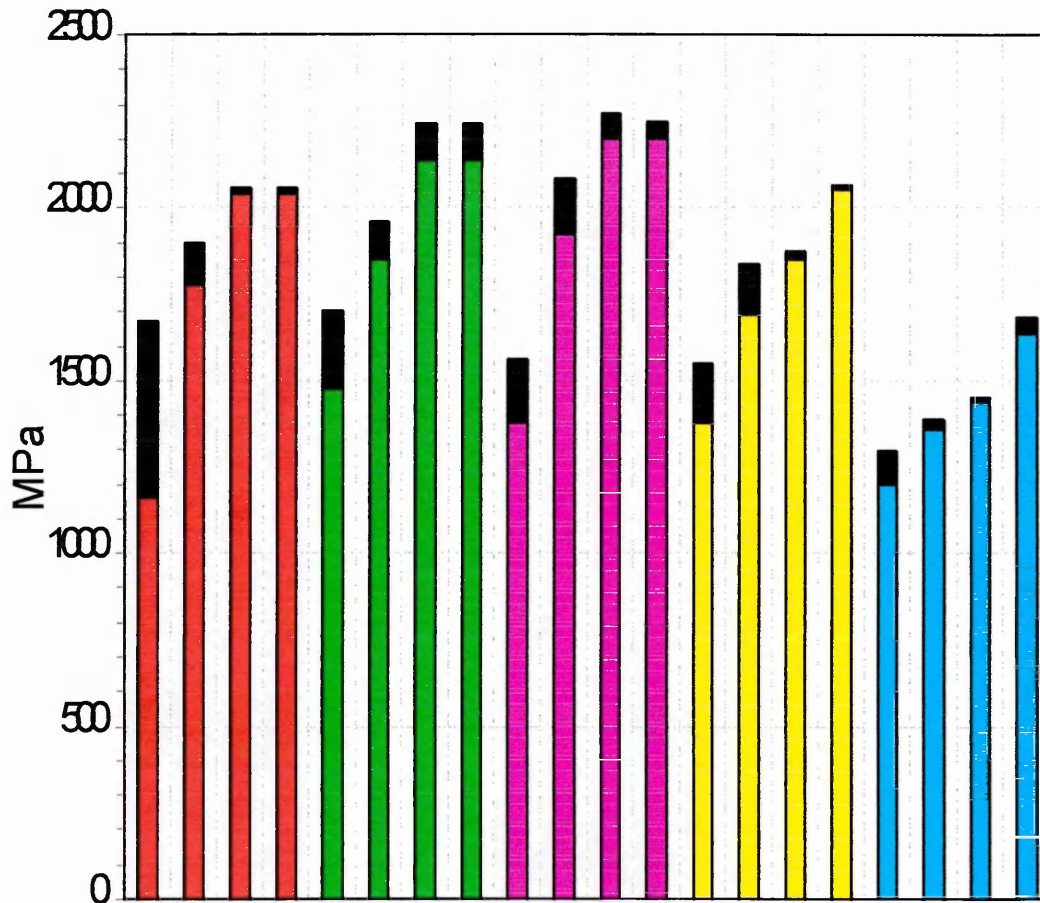
The ratio of 0.2% proof strength to ultimate tensile strength was also found to increase quite rapidly in all examined alloy systems. Figure 179 shows a bar chart with the black portion representing the difference between 0.2% proof strength and ultimate tensile strength. Additionally figure 180 illustrates proof / UTS ratios versus amount of plastic deformation.

Without exception the undeformed alloy possessed the lowest proof to ultimate tensile strength ratio, especially the 1.25 mass% chromium molybdenum system at 70%. In contrast, the 400°C tempered 0.3 mass% carbon boron alloy whose initial 0.2% proof strength was similar to the above mentioned, had a relatively initial high proof to UTS ratio.

Proof to UTS ratios above 95% were found in many of the examined alloy systems maximising at 25% cold deformation as illustrated in figure 180.

Alloys with initial low proof to UTS ratios (the salt bath quenched chromium molybdenum and the untempered variants) also finished with high proof to UTS ratios and therefore work hardened rapidly during cold deformation.

Figure 179:- 0.2% proof strength and ultimate tensile strength of all optimum alloy systems



Key

Black portion = proof to UTS ratio.

S1 (red) = 1.25 mass% Cr Mo alloy quenched into salt bath from 320°C.

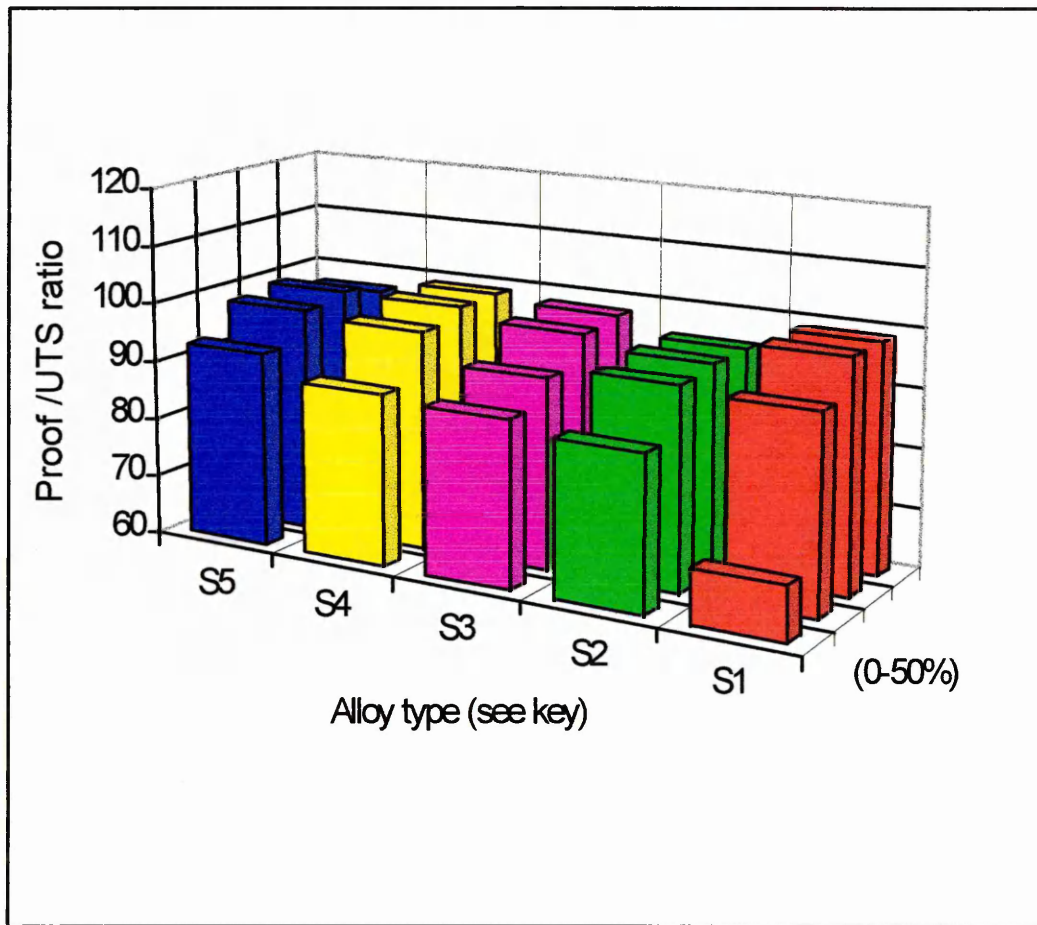
S2 (green) = 0.5 mass% Cr 0.25 mass% C alloy quenched into water from 950°C

S3 (magenta) = 0.3 mass% C, B alloy quenched into water from 950°C

S4 (yellow) = 0.3 mass% C, B alloy quenched into water from 950°C, tempered at 250°C

S5 (blue) = 0.3 mass% C, B alloy quenched into water from 950°C, tempered at 400°C

Figure 180:-Bar chart to show 0.2% proof strength / ultimate tensile strength ratio versus amount of cold deformation of all optimum alloy systems



Key

S1 (red) = 1.25 mass% Cr Mo alloy quenched into salt bath from 320°C.

S2 (green) = 0.5 mass% Cr 0.25 mass% C alloy quenched into water from 950°C

S3 (magenta) = 0.3 mass% C, B alloy quenched into water from 950°C

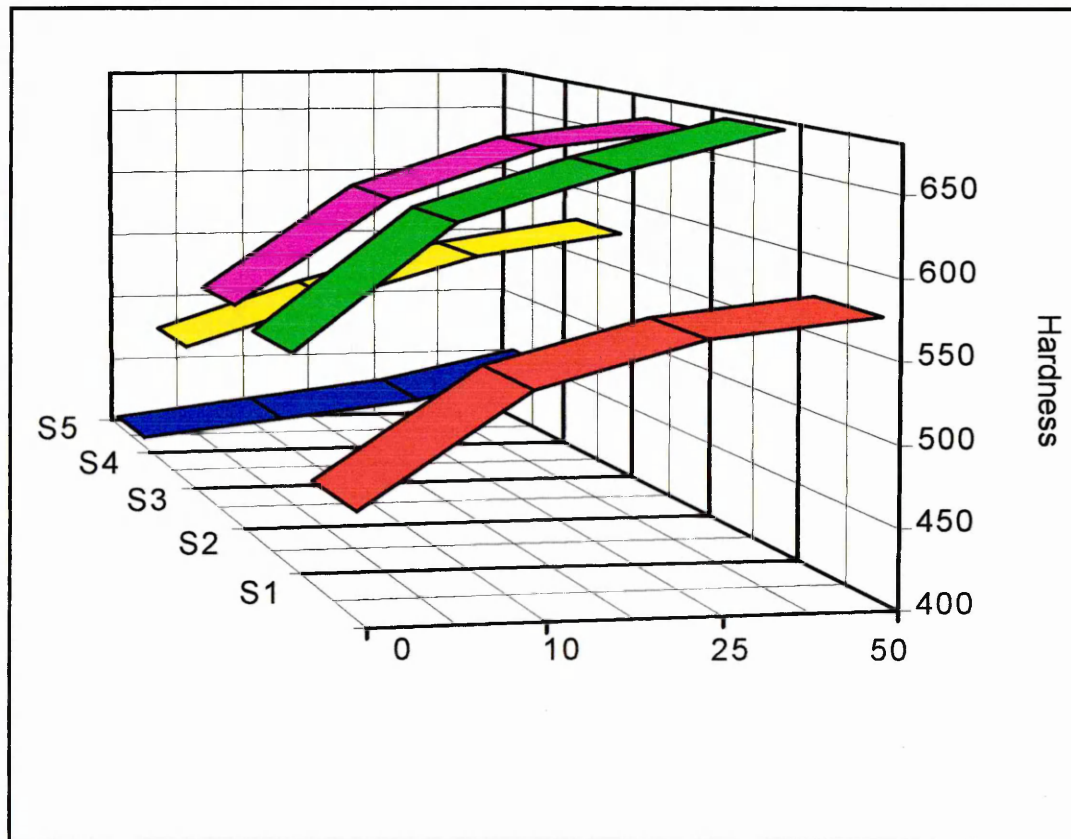
S4 (yellow) = 0.3 mass% C, B alloy quenched into water from 950°C, tempered at 250°C

S5 (blue) = 0.3 mass% C, B alloy quenched into water from 950°C, tempered at 400°C

10.6.2 Hardness results summary and comparison

The relationship between measured hardness and amount of cold deformation was found to be quite different for each type of alloy system. Figure 181 summarises hardness results versus amount of cold deformation for all examined alloy systems.

Figure 181:- Block line graph showing the relationship between hardness and cold deformation for optimum alloy systems examined



Key

S1 (red) = 1.25 mass% Cr Mo alloy quenched into salt bath from 320°C.

S2 (green) = 0.5 mass% Cr 0.25 mass% C alloy quenched into water from 950°C

S3 (magenta) = 0.3 mass% C, B alloy quenched into water from 950°C

S4 (yellow) = 0.3 mass% C, B alloy quenched into water from 950°C, tempered at 250°C

S5 (blue) = 0.3 mass% C, B alloy quenched into water from 950°C, tempered at 400°C

From figure 181 the following observations were made:-

- Similar to the 0.2% proof strength cold deformation relationship (figure 177), the most significant increase in hardness was detected between the undeformed and 10% deformed alloy system.
- With the exception of the 400°C tempered 0.3 mass% carbon boron system, an initial rapid increase in hardness was observed. However beyond approximately 20% cold deformation the increase in hardness was minimal.
- A polynomial type relationship described the relationship between hardness and cold deformation for all alloys except the 400°C tempered 0.3 mass% carbon boron system which was found to be linear.
- The 0.5 mass% chromium carbon alloy attained the highest hardness at maximum amount of deformation, closely followed by the 0.3 mass% carbon boron alloy both being untempered.
- The 400°C tempered 0.3 mass% carbon boron system possessed the lowest hardness range of all with even the hardness of the 50% deformed variant being lower than any of the other undeformed alloys.
- The 250°C tempered 0.3 mass% carbon boron alloy possessed a hardness range curve characteristic of both the higher temperature tempered and the straight water quenched variant. For example, the hardness versus cold deformation relationship only marginally deviated away from linearity, but the alloy attained relatively high hardness.
- Negligible increase in hardness was found beyond 25% plastic deformation, hence the deformation strengthening rate above this value was also assumed to be negligible.

Table 43:- Summary of hardness versus cold deformation relationships for
all examined optimum alloy systems

Alloy type	Curve equation	Relationship (0 - 50% cold deformation)
1.25 mass% Cr Mo alloy salt bath quenched at 320°C	$y = 0.0007x^3 - 0.1068x^2 + 5.424x + 480.81$	Polynomial
0.5 mass% Cr 0.25 mass% C alloy water quenched	$y = 0.0012x^3 - 0.1667x^2 + 7.957x + 545$	Polynomial
0.3 mass% Carbon Boron alloy water quenched	$y = 0.0011x^3 - 0.1623x^2 + 7.555x + 550$	Polynomial
0.3 mass% C B alloy water quenched tempered at 250°C	$y = 0.0002x^2 - 0.0452x^2 + 3.1867x + 505$	Polynomial
0.3 mass% C B alloy water quenched tempered at 400°C	$y = 0.9154x + 408.8$	Linear

10.6.3 Deformation strengthening from the cold rolling procedure

The deformation strengthening rate as a function of hardness (determined from the line equations provided in table 43) varied quite considerably between each alloy system. Figure 182 illustrates deformation strengthening curves as a function of hardness versus cold deformation for each examined alloy system.

Note:- The line equations / relationships are only valid up to 30% plastic deformation.

Figure 182:- A plot of deformation strengthening (dVPN / dPD) versus amount of plastic deformation for optimum alloy systems.

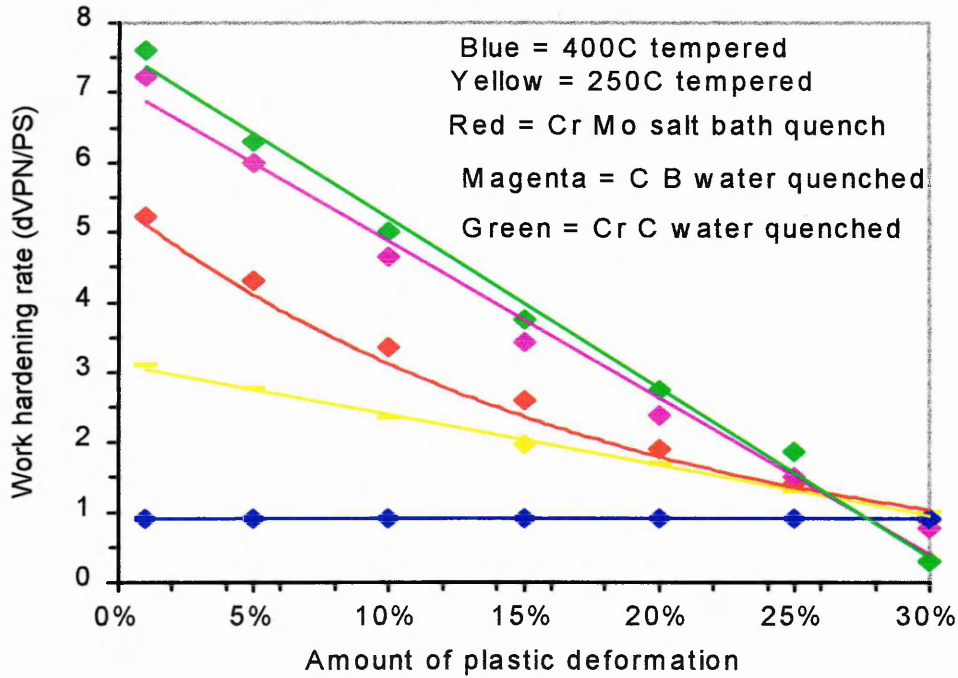


Table 44 summarises the line equations for deformation strengthening rates as a function of measured hardness / 0.025% proof strength. Hence from the given line equation the relationship between deformation strengthening and plastic deformation amount was determined.

Table 44:- Summary of work deformation strengthening rate as a function of hardness and 0.025% plastic deformation for all examined alloy systems.

Alloy type	Deformation strengthening rate (dVPN/PD) Line equation	Deformation strengthening rate relationship
1.25 mass% chromium molybdenum alloy salt bath quenched	$y = 5.424e^{-5.5507X}$	Exponential
0.5 mass% chromium 0.25 mass% carbon alloy water quenched	$y = -0.2423x + 7.95$	Linear
0.3 mass% carbon boron alloy water quenched	$y = -0.2459x + 7.56$	Linear
0.3 mass% carbon boron water quenched alloy tempered 250°C	$y = -0.0718x + 3.107$	Linear
0.3 mass% carbon boron water quenched alloy tempered 400°C	-	Constant

On considering the results provided in figures 181 and 182, (deformation strengthening rate versus prior plastic deformation), the following observations were made:-

The degree of strengthening for the 0.5 mass% chromium / 0.25 mass% carbon and the 0.3 mass% carbon boron 250°C tempered alloy linearly declined with increasing plastic deformation. Hence these alloys exhibited a constant decline in strengthening rate up to a maximum prior plastic deformation of 30%.

Alloy systems that possessed an initial high strengthening rate included the 0.5 mass% chromium molybdenum alloy and the 0.3 mass% carbon boron alloy system. This was due to the large difference in measured hardness between the undeformed and 10% deformed alloy variant.

In contrast, the 400°C tempered 0.3 mass% carbon boron alloy possessed an extremely low deformation strengthening rate independent of the degree of plastic deformation. Beyond approximately 30% plastic deformation the increase in hardness for all alloy systems was minimal, hence strengthening rate was assumed to be zero.

10.6.4 Work hardening results summary from the tensile test.

Work hardening rate evaluation during the tensile test were obtained by either;

- (a) considering the slope of the flow curve at a designated strain, or
- (b) calculation from the work hardening exponent from log log plots of true stress strain.

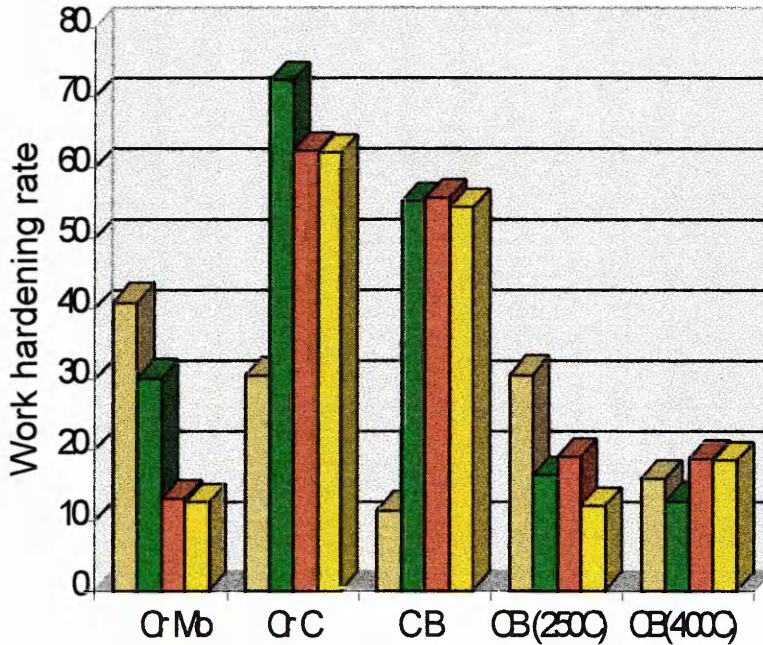
Note:- The total amount of work incorporated into these samples was:-

Work from tensile test + Work from cold rolling procedure* .

* This was obviously zero in the undeformed alloy systems.

Figure 183 summarises work hardening rates determined via the work hardening exponent method at a true strain of 12×10^{-3} . Determination of the work hardening rate via the gradient method produced a similar result and were therefore omitted in this summary.

**Figure 183:- Work hardening rates of optimum alloy systems in the 0,10, 25 and 50% deformed condition at a true strain of 12×10^{-3} .
(calculated via the work hardening exponent method).**



Key:-

Cr Mo = 1.25 mass% Cr Mo salt bath quenched from austenitisation.

Cr C = 0.5 mass% Cr 0.25 mass% C water quenched from austenitisation.

C B = 0.3 mass% C, B water quenched from austenitisation

CB(250C)= 0.3 mass% C, B water quenched from austenitisation, tempered at 250°C.

CB(400C)= 0.3 mass% C B water quenched from austenitisation, tempered at 400°C.

Colour key:-

Olive = Undeformed.

Dark green = 10% deformed.

Brown = 25% deformed.

Yellow = 50% deformed.

From figure 183 the following observations were made:-

- Both the 0.5 mass% Cr / 0.25 mass% C and the 0.3 mass% C B alloy possessed an exceptionally high work hardening rate after 10% plastic deformation.
- The 25 and 50% deformed alloy systems of the above two also rapidly work hardened under the tensile test, (high rate of work hardening). Additionally both alloys possessed similar work hardening rate profiles.
- Interestingly, the undeformed 1.25 mass% Cr Mo alloy and the 250°C tempered C B alloy work hardened rapidly under the tensile test, however after plastic deformation (10%), the work hardening rate dropped quite significantly.
- The work hardening rate profiles of the 1.25 mass% Cr Mo and the 250°C tempered C B alloy were found to be similar. The only a slight difference was a generally lower work hardening rate in the latter alloy, undeformed condition.
- The work hardening profile of the 400°C tempered C B alloy was found to be quite unusual. However, the overall change in the work hardening rate after plastic deformation was only very slight in comparison.
- A noticeable difference in the work hardening rate was found on comparing the undeformed untempered and tempered C B alloy systems.

Chapter 11

Discussion on mechanical and microstructural results

11.1 Basic microstructural strengtheners in optimum alloy systems

This chapter outlines the key microstructural strengthening mechanisms previously covered in the literature review and how they varied with each alloy system given the chemistry and thermal history. The second part of the discussion relates the observed microstructure to the mechanical properties of each alloy system in the undeformed and deformed condition.

The microstructural information gathered mainly via transmission electron microscopy was recognised as being more qualitative rather than quantitative.

Solid solution strengthening

The amount of solid solution strengthening incorporated into each alloy was described with the use of strengthening coefficient data. Additionally for low alloy concentrations there is an approximate linear dependence of solid solution strengthening on the mass% of the alloying element, i.e.

$$\text{Solid solution strengthening} = \text{Strengthening coefficient (mass\% alloy)}. \quad (11.1)$$

The effect of a number of alloying elements on the strengthening coefficient are provided in table 45. Hence the overall solid solution strengthening contribution was estimated by multiplying the alloy mass% (table 46) by the coefficient provided in table 45.

The contribution to strengthening via substitutional solid solution strengthening was thought to be extremely limited after considering the coefficient values and the alloy addition amount. For example, the most potential substitutional solute (Phosphorous) was deliberately kept to a low level because of the potential problem with low temperature temper embrittlement.

Table 45:- Effect of various elements on the solid solution strengthening coefficient for ferrite (Pickering²³)

Element	Coefficient in MPa per wt.% alloy
Mn	37
Si	83
Ni	33
Cr	-30
P	680
Cu	38
Mo	11
Sn	120
C and N	5000

Table 46:- Chemical composition of examined optimum alloy systems

Alloy	C	Mn	Si	P / S	Cr	Mo	Ni	Al	Ti	N	B
1.25 mass% Cr Mo salt bath quenched	0.48	0.59	0.25	0.005	1.21	0.52	0.18	0.005	-	-	-
0.5 mass% Cr 0.25 mass% C water quenched alloy	0.25	1.5	0.2	0.004	0.5	-	-	-	0.02	0.011	-
0.3 mass% carbon boron water quenched alloy	0.3	1.02	0.23	0.005	0.24	0.011	0.021	-	0.02	-	0.0029
0.3 mass% carbon boron water quenched alloy tempered at 250°C	0.3	1.02	0.23	0.005	0.24	0.011	0.021	-	0.02	-	0.0029
0.3 mass% carbon boron water quenched alloy tempered at 400°C	0.3	1.02	0.23	0.005	0.24	0.011	0.021	-	0.02	-	0.0029

The next most potential substitutional solute atom according to table 46 was silicon, however the mass% of silicon the majority of the examined alloys was at best only 0.25 mass%, giving a contribution of $(0.25 * 83) = 20\text{MPa}$. Chromium was noted as the least effective for solid solution strengthening due to its strong carbide forming characteristics.

In contrast interstitial solid solution strengthening was thought to contribute markedly to the overall strengthening of all examined alloy systems. Solid solution hardening by carbon and / or nitrogen was thought to be linearly related to a power function of the concentration (Pickering²³) :-

$$\sigma_y = \sigma_0 \kappa (\text{wt.}\% \text{ C})^n \quad (11.2)$$

where σ_0 , κ and n are constants, with n varying from 0.33 and 1.0.

Precipitation strengthening

When the solid solubility of an alloy element was exceeded, a new phase was formed to accommodate the increased atomic concentration. For example in the case of when carbon solid solubility in b.c.c iron was exceeded, accommodation was in the form of cementite precipitation. The amount of strengthening resulting from precipitates depends upon the size, shape and distribution in the matrix. Essentially dislocation glide is hindered by the precipitate, with further motion only occurring after sharp changes in dislocation curvature. Alternatively in the case of coherent precipitation the dislocation must first actually shear through the particle before further glide can commence, although this requires a much higher stress level than normally required for glide.

Precipitate morphology was very much dependant on chemistry / thermal history and varied significantly between each alloy system. The 1.25 mass% chromium molybdenum alloy system contained a large population of exceptionally large lenticular shaped Fe_3C precipitates confined to the bainitic lath only. These large precipitates were positioned at a 60° angle to the long axis of the lath, with an average size of $20 \times 10^{-3} \mu\text{m}$ (surface area). The formation of such large precipitates was thought to be as a result of the isothermal treatment, where both time and sufficient energy was provided for precipitate growth. In contrast, the martensitic regions of the 1.25 mass% chromium molybdenum alloy microstructure appeared precipitate free, suggesting that this phase had formed during the air cool stage after the isothermal treatment.

Hence precipitation within the martensite would have only been expected on subsequent tempering. Overall, the cementite precipitate morphology / distribution was thought to have reduced the strengthening potential. For example, cementite precipitated in such a coarse form without substantial coherency strains meant that dislocations were more likely to by pass at lower levels of stress rather than cut through them. Extensive dislocation glide was therefore expected to take place at relatively low stresses, with effective pinning lost from precipitate growth, and associated interstitial solid solution removal.

The 0.5 mass% chromium 0.25 mass% carbon alloy microstructure consisted of mainly carbide free martensitic laths with smaller proportions of lower bainitic laths containing exceptionally fine long carbides positioned at 60° angle to the long axis. The fineness of these carbides was attributed to the thermal history of the alloy system, where the fast water quench did not permit extensive growth of the precipitated carbides as compared with the isothermally treated 1.25 mass% chromium molybdenum alloy.

Surprisingly no evidence of carbide precipitation was found within the martensite laths which was expected due to the predicted high martensite start temperature (hence expected auto tempering). Overall, the microstructural carbide population of the 0.5 mass% chromium 0.25 mass% carbon alloy was described as low with approximately 20% of the laths containing carbides (bainitic portion).

Hence although a fine carbide size was achieved, the distribution and population was not ideal, and the contribution to strengthening via precipitates was somewhat limited.

The 0.3 mass% carbon boron alloy precipitates were found to be slightly larger in size compared to the 0.5 mass% chromium 0.25 mass% carbon alloy and again were confined to the bainitic laths. No evidence of carbide precipitation within the martensitic laths was found even though the predicted martensite start temperature was high. In comparison to the 0.5 mass% chromium 0.25 mass% carbon variant, the carbide population within the bainitic portion also appeared to be slightly higher.

This, coupled with the fact that there appeared to be more bainitic laths present throughout the structure, indicated that the carbide population and distribution was, as a whole closer to ideal. As with the 0.5 mass% chromium 0.25 mass% carbon variant, the degree of fineness of the carbide precipitate was thought to be due to the thermal history, where the fast water quench did not allow significant amounts of precipitate growth. The higher carbon content, and possible additional segregation effects were thought to be partly responsible for the observed higher carbide population. Alternatively, the bainite start temperature may have been higher in the 0.3 mass% carbon boron alloy, thereby effectively allowing more time for cementite precipitation and growth.

The carbide shape, size and distribution was dramatically altered on tempering the 0.3 mass% carbon boron alloy system. Large rod shaped cementite carbides were detected in the 400°C tempered 0.3 mass% carbon boron alloy system, lying parallel and at 90° to the long axis in the martensitic laths, or at 60° to the long axis in the bainitic lath. Additionally a large amount of interlath carbide was detected in the 400°C tempered 0.3 mass% carbon boron alloy. The size of carbide within both the bainitic and martensitic laths were quite similar however the carbide within martensitic laths did extend almost fully across the lath due to the relative lath thinness. The carbide population was also quite extensive, with carbide “overlap” occurring in many regions giving the appearance of “T” shaped carbides.

The carbide size was attributed to the relatively high temperature temper treatment imposed on this alloy system. It was thought that fine bainitic interlath carbides were present prior to tempering, and that on subsequent isothermal treatment at 400°C, these fine carbides coarsened to produce large rod shaped precipitates. Similarly, during isothermal treatment carbide precipitation within the martensitic laths took place growing to a similar size as the bainitic carbides. To summarise, although this alloy contained a homogeneously distributed array of carbides, the carbide coarseness reduced this alloys strengthening potential. In contrast to the 400°C 0.3 mass% carbon boron alloy, the 250°C tempered variant contained very few carbides within the martensitic laths. Instead, a large number of carbides ranging from quite fine to rod like were found within the bainitic portion with unusual carbide clusters precipitated between bainitic laths.

The lower temperature tempering operation had therefore appeared to have promoted growth of pre-existing bainitic carbides, but prohibited the significant nucleation and growth of carbide within the martensitic lath.

The overall result, therefore was a heterogeneous distribution of moderately sized carbides confined to the bainitic lath with the largest carbides still somewhat smaller than the ones observed in the higher temperature tempered variant.

Table 47 summarises the size, shape and distribution of the iron carbide precipitates found in all examined alloy systems, additionally, the carbide size distribution graph, in chapter 9 should also be referred to.

Table 47:- Summary of carbide shape, average size and distribution
in optimum alloy systems

Alloy type	Carbide average size and shape	Carbide location	General comments
1.25 mass% chromium molybdenum alloy system, isothermally treated at 320°C	very large rod shaped carbides averaging at $23 \times 10^{-3} \mu\text{m}$ in surface area.	Present within the bainitic laths only , however approximately 60 -70% of the microstructure estimated as being bainitic.	Very large carbide size not ideal in terms of strengthening, although carbides were found to be distributed well throughout the bainitic laths. Bainitic portion found to be the most prolific hence overall carbide population very high.
0.5 mass% chromium 0.25 mass% carbon alloy system water quenched.	Exceptionally fine long carbides averaging at $0.5 \times 10^{-3} \mu\text{m}$ in surface area.	Moderate population within the occasional bainitic lath, lower population within the majority of the bainitic laths. No carbides observed within the martensitic laths.	Fine carbide size. Bainitic portion approximately 20% maximum therefore overall carbide population very low.
0.3 mass% carbon boron alloy system, water quenched.	Very fine long carbides averaging at $1.5 \times 10^{-3} \mu\text{m}$ in surface area.	Predominantly within the bainitic laths, very occasionally found within the martensitic laths also.	Fine carbides , distributed well throughout the bainitic laths promoting strengthening. Bainitic portion estimated at 40- 45 %. therefore overall population quite high but still heterogeneously distributed within the general microstructure .
0.3 mass% carbon boron alloy, water quenched and tempered at 250°C.	Moderate sized long rod shaped carbides averaging at $16 \times 10^{-3} \mu\text{m}$ in surface area.	Predominantly within the bainitic laths and clustering along bainite lath boundary, very occasionally found within the martensitic laths also.	moderate - larger sized carbides , distributed well throughout the bainitic laths promoting some strengthening. Bainitic portion estimated at 40- 45 %. therefore overall population quite high but still heterogeneously distributed within the general microstructure .
0.3 mass% carbon boron alloy, water quenched and tempered at 400°C.	Large rod shaped carbides averaging at $20 \times 10^{-3} \mu\text{m}$ in surface area.	Present within bainitic and martensitic laths.	Homogeneously distributed, but size of carbide far from ideal for strengthening, especially large carbides in martensitic phase extending full width of lath.

Dislocation density.

In alloys with higher carbon contents, the degree of lattice distortion associated with the trapped carbon atoms is conversely greater, the martensite start temperature is much lower and the morphology is rather plate like as opposed to lath like. The finer structure of plate martensite is often composed of very fine transformation twins or screw dislocation arrays consistent with plastic deformation modes characteristic of body centred structures deformed at low temperatures. In addition it was also recognised that dislocation nucleation occurred at other stress concentration sites such as precipitate - matrix boundaries, when a precipitate loses coherency. When inclusions and precipitates have a complex shape, the associated strain field and resultant dislocation distribution is correspondingly more complex and tangled arrays of dislocations are produced. Previous electron microscopy literature has revealed that dislocation density generally decreases from martensitic, lower bainitic to upper bainitic microstructures of similar composition. This presumably is due to differences in plastic accommodation and transformation temperature. The dislocation density was thought to contribute markedly to the mechanical properties and was found to be quite different for each alloy system. Bush and Kelly⁹⁹ have described the contribution of strengthening with respect to dislocation density:-

$$\sigma_d = 1.2 \times 10^{-3} (\varphi)^{1/2} \quad (11.3)$$

Where φ is the dislocation density in lines cm^{-2} .

The 1.25 mass% chromium molybdenum alloy system dislocation density was described as moderate, with tightly packed dislocation forests confined to the martensitic laths. The relatively high dislocation density associated with bainitic ferrite was thought to be associated with the plastic accommodation in the austenite / bainite phases.

The dislocation density of bainite is also suggested to increase with decreasing transformation temperature, hence a higher isothermal treatment temperature would have produced an alloy with lower proof strength because of the lower dislocation density. Frequent dislocation tangles were observed around larger cementite precipitates within the bainitic laths that could well have nucleated at the precipitate matrix interface. In contrast the martensitic laths within the 1.25 mass% chromium molybdenum variant were found to contain a number of dense dislocation forests and were carbide free, suggesting transformation had occurred below 320°C. On the commencement of plastic deformation, it was envisaged that many dislocations within the martensitic laths would rapidly become immobilised as tangles formed or were pinned at the associated twin boundaries. In contrast, dislocation glide within the bainitic laths was achieved at relatively low stresses, partly from the lower dislocation density. The overall mechanical properties were thought to have been controlled predominantly by the lower dislocation density bainitic laths.

The 0.5 mass% chromium 0.25 mass% carbon and the 0.3 mass% carbon boron alloy were interesting since both alloy systems possessed identical martensite start temperatures. Both alloys were water quenched from austenitisation hence, dislocation densities was expected to be similar.

The dislocation density within the martensitic laths were found to be quite variable between one lath and another presumably due to the range of temperatures at which the martensite reaction had occurred. For example, martensitic laths formed at higher temperatures were expected to contain fewer dislocations whilst lower temperature martensitic laths possessed characteristic fine internal twins with higher dislocation density. This effect could have been further compounded by subtle segregation of alloying elements or carbon thereby depressing the martensite start temperature.

Overall it was thought that the 0.3 mass% carbon boron alloy contained less dislocations compared to the 0.5 mass% chromium 0.25 mass% carbon variant. The lower dislocation density of the 0.3 mass% carbon boron alloy was as a direct result of increased proportion of the lower bainite and partly explained to the lower proof strength obtained.

The dislocation density / transformation temperature relationship proposed by Pickering²³ with respect to bainitic microstructures was found to be valid for martensitic microstructures also. For example, the difference in dislocation density between the martensitic laths of the 1.25 mass% chromium molybdenum and the 0.3 mass% carbon boron alloy were quite dramatic. In the former alloy system dense dislocation tangles coupled with fine twinning suggested a low martensite start (higher carbon content). Whereas in the 0.3 mass% carbon boron alloy, the dislocation density within the martensitic laths was much less suggesting a higher martensite start temperature (lower carbon content).

As well as encouraging the precipitation and growth of cementite precipitates, the tempering process also decreases the dislocation density of the microstructure. This in turn will effect the mechanical properties of the alloy system, in particular proof strength and work hardening characteristics. The dislocation density of 250⁰C tempered 0.3 mass% carbon boron alloy was found to be significantly lower than the untempered counterpart, although strength was maintained from additional cementite precipitation. The flow curve characteristics on the other hand, suggested easier dislocation glide probably as a result of cross slip.

Dislocation density after plastic deformation

When a material is plastically deformed, the change in shape is accomplished by dislocation glide on preferred closest packed system. In addition the dislocation density increases rapidly. Dislocation multiplication may take place via Frank-Read mechanism or grain boundary mismatch (see proceeding section). Hence a high initial dislocation density and fine grain size should encourage a high dislocation generation rate through cold work.

Generally speaking, the most rapid increase in dislocation density was observed in the straight water quenched variants. Frequent dense dislocation tangles were observed reminiscent of those observed in the martensitic portion of the 1.25 mass% chromium molybdenum variant.

In contrast the dislocation arrangement in the tempered alloy system was quite regular with little indication of forest formation. Instead the majority of the dislocations arranged themselves into cellular type arrays suggesting that a significant amount of cross slip was maintained (Yan and Men²⁰⁶).

Grain, Lath and Packet boundary strengthening

It has been established (Pickering²³) that the grain boundaries:-

- Provide barriers for the movement of dislocations during plastic deformation .
- Act as dislocation “emitters” during external plastic deformation via a miss match effect.

In addition, a fine austenite grain size will also affect the product phase crystal size (i.e. martensite packet size), with the packet boundary also considered as a potential barrier for dislocation movement.

Early models to describe the effect of bainitic ferrite grain size on strengthening were based on the observation that the proof strength more or less increased linearly with $d^{-1/2}$ where d was the mean linear intercept of the bainitic ferrite grain size.. It was also recognised that the bainitic ferrite lath width should also be considered as a strengthening contributo (Pickering²³).

However, the bainitic ferritic lath width in a Hall-Petch type equation gives much too high a strength contribution, instead the bainitic ferrite “packet” dimensions may produce a more reasonable result .

Evidence in the literature suggested that the grain size within the martensitic microstructure only accounts for some 25 - 30% of the proof strength. Variations in the prior austenite grain size have been shown to produce significant changes in the strength of the as quenched alloy martensite). However it is thought that the prior austenite grain size controls the martensite packet size and that it is this that effect the proof strength (Pickering²³).

With the exception of the 1.25 mass% chromium molybdenum variant, grain refining additives were specified in the alloy chemistry, hence the strengthening via high angle boundaries (grain and packet lath size) were maximised as far as possible. Due to such microstructural complexity it was difficult to ascertain the effect of grain, packet and lath size with respect to mechanical strength. However general observations included:-

- 1.25 mass% chromium molybdenum variant contained relatively large packets of bainite type laths. Martensitic laths were frequently observed in discrete smaller packets or intermittent between bainitic laths.
- 0.5 mass% chromium 0.25 mass% carbon alloy contained very small packets of martensitic laths with occasional bainitic laths.
- 0.3 mass% carbon boron alloy contained small packets of martensitic laths also, however this alloy contained increased amounts of bainitic type laths.

The inferior mechanical strength of the 1.25 mass% chromium molybdenum variant was therefore thought to be partly due to the generally larger packet sizes. In contrast, the lath packet sizes were much finer in both water quenched alloy systems, hence the superior mechanical properties.

A subtle difference in martensite packet size was observed on examining the microstructure of the 0.5 mass% chromium 0.25 mass% carbon and 0.3 mass% carbon boron alloy.

The packet size of the latter alloy system appeared slightly larger, and contained more bainitic type laths, thereby explaining the subtly lower proof strength obtained. Finally, it was suggested in the literature that the lath boundary act as potential barriers to the movement of dislocations. The microstructural observations in general confirmed this with dislocation cellular arrays often confined to one particular lath. However, in some instances (especially in the tempered and 50% deformed variant), cellular type dislocation arrays appeared to cross a lath boundary. Such observations have also been reported in the literature (Yan and Men²⁰⁶), where it is suggested that given the high state of stresses involved it is possible for a low angle boundary to be overcome to allow dislocation cell growth.

11.2 Microstructural observations mechanical property relationships

11.2.1 1.25 mass% Cr Mo alloy

To recap, this alloy system was austenitised at 950°C then immediately quenched into a salt bath at 320°C and held at this temperature for approximately ten minutes. This heat treatment regime was used since the objective was to produce a near fully bainitic microstructure. Hence with a knowledge of alloy chemistry together with relevant continuous cooling and time temperature transformation diagrams (Atkins¹¹²) it was anticipated that the major microstructural constituent would be bainitic. Additionally, preliminary dilatometry investigations with 20 mm bar material suggested that the martensite start temperature was approximately 290°C. This confirmed the predicted value from empirical relationships in the available literature (Andrews¹²³), i.e.:-

$$M_s = 539 - 423(\text{wt.\% C}) - 30.4(\text{wt.\% Mn}) - 17.7(\text{wt.\%Ni}) - 12.1(\text{wt.\% Cr}) - 7.5(\text{wt.\% Mo}) \quad (11.4)$$

$$M_s = 539 - 423(0.48) - 30.4(0.59) - 17.7(0.18) - 12.1(1.21) - 7.5(0.52)$$

$$M_s = 539 - 203 - 17.9 - 3.2 - 14.6 - 3.9$$

$$M_s = 296^\circ\text{C}$$

The addition of chromium and molybdenum markedly retard the transformation curve, hence were added to ensure that the bainite shelf of the continuous cooling transformation diagram was extended as far as possible. From the following quantitative formulae, the bainite transformation range was also determined (Steven and Haynes⁴⁵):-

$$B_s = 830 - 270(\% \text{ C}) - 90(\% \text{ Mn}) - 37(\% \text{ Ni}) - 70(\% \text{ Cr}) - 83(\% \text{ Mo}) \quad (11.5)$$

$$B_s = 830 - 270(0.48) - 90(0.59) - 37(0.18) - 70(1.21) - 83(0.52)$$

$$B_s = 512^\circ\text{C}.$$

NB:- % is given as mass

Hence the temperature at which bainite would start to form in this alloy system was estimated at 512°C (upper bainite). Lower bainite was estimated to form nearer the M_s hence an isothermal treatment at 320°C was chosen. Optical and transmission electron microscopy indicated that the microstructure consisted of mixture of lower bainite and martensite. Transmission electron microscopy results suggested that the bainitic phase was perhaps the most predominant constituent (approximately 60 - 70%). Although it was appreciated that the sample area for this technique is exceptionally small, therefore this estimation was treated with some caution. Bainitic laths were identified from lath width measurement coupled with the observation of inter-lath carbides lying at a 60° angle to the long axis of the lath. In contrast the martensite laths were much thinner and appeared carbide free, occasionally with fine internal twins approximately 1 μm thick.

Significant amounts of martensite were found in this alloy system because some degree of elemental segregation had taken place during manufacture. Segregated elements within the martensitic region included chromium, molybdenum and silicon, alongside a subtle decrease in iron. The segregation of these elements effectively modified alloy hardenability encouraging martensite formation. Segregation of chromium, molybdenum and silicon also suppresses the martensite start temperature, thereby reducing the possibility of carbide precipitation during the air cool.

Given the sensitivity of the technique used for segregation analysis, it was concluded that carbon was more or less homogeneously distributed throughout. If this had not been the case, it was anticipated that increased amounts of carbon would have been detected within the martensitic region. This was because if the martensitic laths would have been depleted in carbon the M_s of region would have then coincided with the isothermal treatment temperature hence cementite precipitates would have been observed. These martensitic laths would have also contained less dislocations, since this is thought to be related to transformation temperature.

On a finer scale, (under transmission electron microscopy), it was suspected that some of the martensitic laths were actually enriched in carbon, with a respectively lower M_s temperature. This was because some of the martensitic laths were very densely dislocated often containing fine internal twins which are usually associated with higher carbon grade alloy systems.

Mechanical and microstructural properties in the undeformed condition

The microstructural and mechanical properties of the undeformed variant were compared to the other alloy systems:-

- Lowest proof strength, ultimate tensile strength and hardness.
- Low proof to ultimate tensile strength ratio.
- Varying rates of work hardening during the tensile test, initially high progressing to low at higher strains.
- Large cementite precipitates confined to the bainitic laths only.
- Low dislocation density within bainitic laths, higher dislocation density in martensitic laths.
- Occasional fine twinning within martensite observed..

The onset of plastic deformation during the tensile test signifies the point at which a significant number of dislocations are able to move (slip) after exceeding a critical stress. The magnitude of this critical stress is therefore determined by the interaction of its population of dislocations with each other and with microstructural barriers e.g. precipitates. The 1.25 mass% chromium molybdenum alloy in the undeformed condition possessed the lowest proof strength (1160 MPa) when compared to all other examined systems. The relatively low yield strength of the undeformed variant was thought to be partly due to the inability of the coarser cementite precipitates to effectively lock up dislocations.

The absence of precipitates within the martensitic region of the microstructure also encouraged dislocation glide, however these laths were also quite heavily dislocated thereby increasing the chances of sessile forest formation. Altogether, the yield strength of the undeformed variant was thought to have been dictated partly by the low to moderate dislocation density in the bainitic portion, with morphology and distribution characteristics of the cementite also reducing the alloy potential. The large amounts of cementite precipitation also removed much of the strengthening incorporated from interstitial solid solution.

The work hardening rate varied quite significantly during the tensile test and was quite high in the earlier stages of plastic flow. This indicated that a significant number of dislocations were initially rendered immobile, probably after interacting with one another and the finer sized cementite precipitates. Additionally twin, lath and grain boundaries acted as barriers to dislocation movement. Towards the end of the tensile test, the lower work hardening rate observed indicated easier dislocation glide possibly accomplished by the loss of the pinning effect at finer precipitates. Additionally, the relatively large number of slip systems available would promote cross slip allowing a previously locked up dislocation to move onto another slip plane.

To summarise, the plastic flow during the tensile test of the undeformed alloy variant induced the following reactions:-

- On exceeding the critical stress (yield stress) dislocations proceed to glide on preferable slip planes, a low proof strength indicated limited dislocation locking capability probably due to the initial dislocation density and the carbide morphology.
- Additional dislocations were also generated during plastic flow and proceeded to glide within the closest packed system.
- At low stress levels the work hardening rate was relatively high with dislocation immobilisation via interaction with fine precipitates, twin, lath and grain boundaries and sessile network formation.
- At increasing values of stress, the work hardening rate decreased, due to dislocation cross slip on higher energy slip systems.
- At higher stresses, a lower work hardening rate suggested loss of carbide pinning effects via dislocation by pass or shearing through carbides.

On comparing this alloy system to the water quenched variants in the undeformed condition, the dislocation density and carbide morphology appeared to play a critical role in determining the mechanical properties. For example, a higher dislocation density in the 0.25 mass% carbon 0.5 mass% chromium alloy explained the superior proof strength obtained. In contrast, the lower dislocation density and similar carbide morphology of the 400°C tempered carbon boron variant explained the similar mechanical properties. Further comparisons are drawn later in this chapter.

Mechanical and microstructural properties of the deformed variants

Prior to plastic deformation, the optically examined microstructure consisted of randomly orientated “macropackets” of laths. The prior austenite grain structure was not clearly visible although it was expected that these were equiaxed in shape. However, after extensive plastic deformation a distinct degree of “macropacket” alignment had taken place with preferred orientation towards the direction of rolling. The development of this preferred orientation during cold deformation was thought to be due to the rotation of crystallographic planes to the direction of maximum strain. The type of preferred orientation or texture developed, depends primarily on the number and type of available slip systems and on the principle strain. Hence the important planes and directions for the body centred cubic system are {100} and $\langle 110 \rangle$, i.e. the closest packed planes and directions for slip. Since a well developed texture (microstructural) was developed at moderate deformations in the 1.25 mass% chromium molybdenum alloy system, it was concluded that there must have been a significant number of systems available for twinning or slip.

At larger deformations (50%) , the texturing appeared no different to that of the 25% deformed sample, which was also reflected in the mechanical properties. The effect of cold work on microstructural observations and mechanical properties were summarised in chapters 9 and 10 respectively and included:-

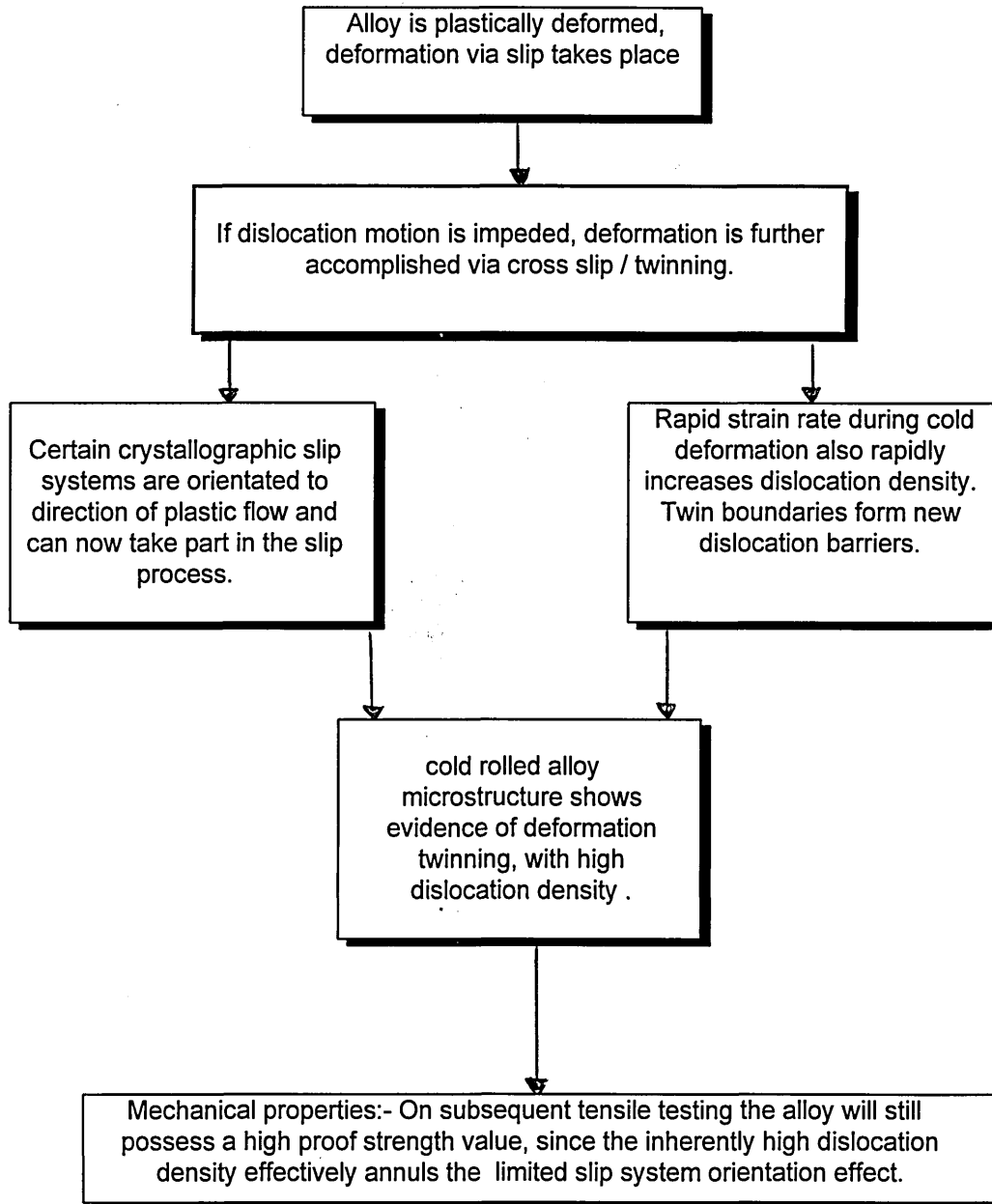
- A dramatic increase in the dislocation density, especially within the martensitic laths.

- Limited evidence of dislocation cell type structure formation within some of the bainitic laths.
- Apparent increase in the amount of twin phase and sheared carbides above 25% plastic deformation.
- An increase in the hardness, proof strength, ultimate tensile strength and hence proof to UTS ratio.
- A general decrease in the work hardening rate during the tensile test with increasing amounts of plastic deformation.
- A gradual decrease in the strengthening rate (e.g. change in hardness versus plastic deformation) decaying in an exponential manner.

The rapid increase in dislocation density was thought to be as a result of the miss-match effect between the individual grains rather than from the Frank Read mechanism. This high dislocation density was also reflected in the mechanical properties, i.e. high proof strength. In addition, the 25 and 50% deformed microstructure appeared to contain large amounts of twinned martensitic laths that were assumed to have originated from the cold rolling procedure. This assumption was treated with some caution since the detection of internal twinning on such a fine scale with the aid of an electron microscope is very dependant on the orientation of the martensite plate with respect to the electron beam (Kelly and Nutting²¹³). Nevertheless, after several repetitive investigations it was thought that the amount of twinned microstructure did increase with plastic deformation. This therefore indicated that dislocation motion via slip on the closest packed planes was severely hindered and that some of the deformation had been accomplished via a twinning mechanism.

An important feature of the twinning process during plastic deformation is the orientation changes to place new slip systems in a favourable orientation with respect to the stress axis so that additional stress can take place. However, it is thought that only a relatively small fraction of the total volume of crystal is reoriented by twinning. Moreover, twin boundaries act as barriers to further dislocation. In addition, it was expected that the dislocation multiplication rate would be high given the rapid strain rate employed. The proposed mechanism is illustrated in figure 184.

Figure 184:- Proposed theory for the deformation behaviour of 1.25 mass% chromium molybdenum alloy during cold rolling



Concurrent to the strengthening effect brought about by plastic deformation, these alloy variants were also found to possess a low rate of work hardening during the tensile test. In contrast, the undeformed alloy possessed a higher rate of work hardening due to dislocation reactions with various microstructural barriers.

Although at higher levels of stress (near to fracture) a lower rate of work hardening ensued from the cross slip of dislocations. A similar effect was probably responsible for the lower rates of work hardening in the deformed variants where significant amounts of cross slip allowed further dislocation glide hence lower rates of work hardening at these higher levels of stress.

Dislocation cellular type arrays were observed within the bainitic laths after large amounts of plastic deformation. This indicated that a significant amount of dislocations were able to cross slip hence the respective rate of work hardening was lower. A summary of the predicted dislocation reactions during the tensile test for the deformed alloy system are as follows:-

- Below the yield point dislocations are effectively pinned predominantly through the formation of sessile networks. Some of these dislocations were previously glissile and operated within the lowest energy slip system (closest packed plane and direction).
- Hence only as the stress level is increased, dislocations in less favourable closest packed slip planes may begin to move. (i.e. higher yield strength).
- At a high level of stress, a certain amount of cross slip will take place to reduce the work hardening rate. Some additional deformation twinning may reorientate additional slip systems.

The minimal difference in yield strength for the 25 and 50% suggested that the critical stress for dislocation movement in both alloy systems were identical. It was difficult to tell whether the amount of twin phase and dislocation density in the 50% deformed alloy system was greater. However because the stress strain curves were so similar, it was assumed that the cold rolling had simply introduced a few more dislocations into an already densely dislocated microstructure.

The mechanical strengths and microstructural characteristics of the deformed 1.25 mass% chromium molybdenum variant were compared with other examined deformed variants in the untempered condition. Consistent with the hardness results, the proof strength was always lower after equal amounts of plastic deformation.

For example, after 10% plastic deformation, the proof strength of the 1.25 mass% chromium molybdenum, 0.5 mass% chromium 0.25 mass% carbon and the 0.3 mass% carbon boron alloy were 1775, 1850 and 1851 MPa respectively. Additionally the work hardening rate was much higher in the later two alloy systems. These differences in mechanical strength and behaviour during the tensile test were due to several microstructural features, for example, dislocation density, grain and lath boundaries and carbide morphology. For example, the overall dislocation density within the 10% deformed 1.25 mass% chromium molybdenum variant was somewhat lower than the 0.5 mass% chromium 0.25 mass% carbon variant. Additionally a lower number of lath boundaries coupled with the possibility of lower numbers of grain boundaries effectively reduces the number of dislocation sources. Hence after deformation, the dislocation density was expected to be lower in the 1.25 mass% chromium molybdenum variant than the 0.5 mass% chromium 0.25 mass% carbon alloy. In addition to this, although the 1.25 mass% chromium molybdenum variant contained more carbon, the majority of this was thought to be precipitated as coarse cementite thereby reducing the solid solution strengthening effect.

The consequence of lower dislocation density and reduced carbon solid solution strengthening alongside other microstructural effects was to reduce the proof strength and also to promote dislocation glide during the tensile test (lower rate of work hardening). The observed dislocation cell structure in the 1.25 mass% chromium molybdenum variants, contrasting with dense dislocation tangles within the deformed untempered variants also reflected the work hardening results. The various microstructural strengthening effects for the 1.25 mass% chromium molybdenum variant based on a Hall-Petch type relationship were summarised as follows:-

$$\sigma_{ps} = \sigma_{dis} + \sigma_{Gb} + \sigma_{Twin} + \sigma_{lath} + \sigma_{Ssh} + \sigma_{Ppts} \quad (11.6)$$

σ_{ps} = Obtained proof strength.

σ_{dis} = Strengthening due to dislocation density.

σ_{Gb} = Strengthening due to grain boundaries.

σ_{Twin} = Strengthening due to twin boundaries.

σ_{Lath} = Strengthening due to lath boundaries.

σ_{SSH} = strengthening due to solid solution strengthening.

σ_{Ppts} = Strengthening due to fine precipitates.

General comparisons between the 1.25 mass% chromium molybdenum variant, with the 0.5 mass% chromium 0.25 mass% carbon alloy, considering equation 11.6 were also drawn, noting that:-

σ_{dis} = Generally lower in the 1.25 mass% chromium molybdenum variant

σ_{Gb} = Lower in the 1.25 mass% chromium molybdenum variant

σ_{Twin} = More martensite appeared twinned in the 1.25 mass% chromium molybdenum variant, however the proportion of martensite was lower.

σ_{lath} = Lower in the 1.25 mass% chromium molybdenum variant, with more of the microstructure consisting of bainite.

σ_{SSH} = Probably lower in the 1.25 mass% chromium molybdenum variant, with the majority of carbon precipitated as coarse cementite.

σ_{Ppts} = Not definable since although the carbide size is fine within the 0.5 mass% chromium 0.25 mass% carbon alloy, the population was rather low.

The increase in hardness or alternatively 0.025% proof strength with respect to amount of cold work was found to be greatest at smaller amounts of deformation and was thought to correlate to a high mobile dislocation exhaustion rate. After large amounts of plastic deformation, insignificant increases in hardness were observed hence the hardness versus plastic deformation curve flattened off.

From plots of hardness versus plastic deformation (figure 185), a second plot was obtained to describe the rate at which the potential strengthening decayed (figure 186).

Figure 185:- Typical curve of 0.1% proof strength versus plastic deformation.

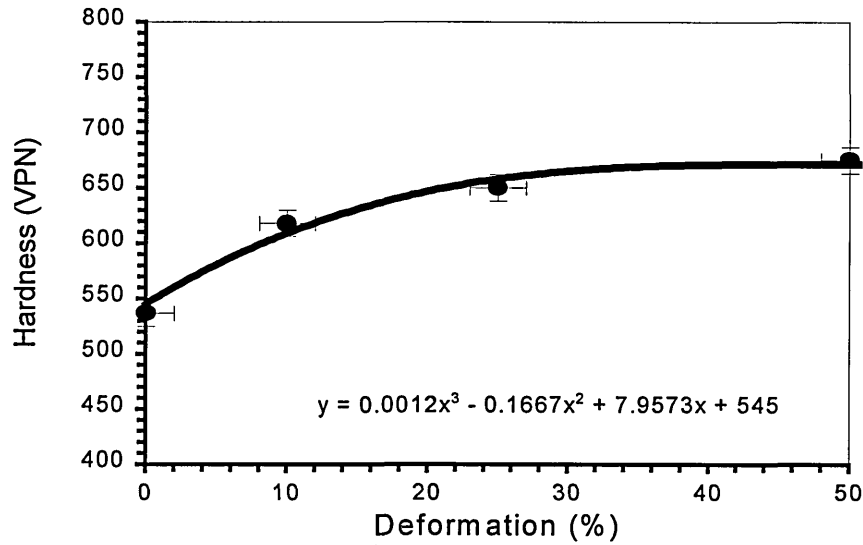
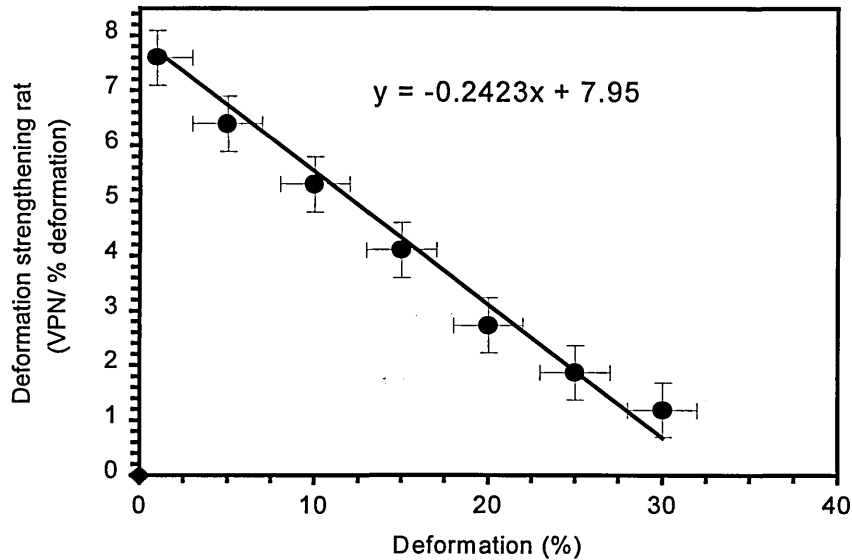


Figure 186 - Typical plot to describe the decay of the potential strengthening with plastic deformation (calculated by differentiating the equation provided in figure 185).



This decay in the rate of strengthening for 1.25 mass% chromium molybdenum variant was described by an exponential function, and was termed the strengthening loss coefficient (μ). In contrast a linear type function described the strengthening loss coefficient for the water quenched variants with the plot gradient apparently related to the tempering temperature.

Hence it was thought that the strengthening loss coefficient was related to several key microstructural features, including dislocation density, carbide morphology, and the type of dislocation arrays formed after cold work.

Turning to the 1.25 mass% chromium molybdenum variant, a high potential strengthening gain after small amounts of plastic deformation signified high dislocation interaction, formation of sessiles etc.. After large amounts of plastic deformation, the rate at which dislocations were rendered immobile was thought to be low through a cross slip mechanism rather than glissile dislocation exhaustion via forest formation. This was because of the observed low rates of work hardening and dislocation cellular type arrays after excessive plastic deformation. The rate of strengthening between the 25 and 50% deformed alloy systems was measured at almost zero, or in other terms, no increase in proof strength or hardness was observed after plastic deformation. This result mirrored the tensile test results where the extra amount of cold rolling was thought to have simply introduced more dislocations into an already densely dislocated microstructure. Further cold rolling beyond 50% would have probably resulted in brittle failure. The effect of plastic deformation on the carbide morphology highlighted the fact that some of the interlath cementite, although coarse, incorporated some degree of coherency strain on the surrounding ferrite matrix. This was because evidence of carbide shearing was clearly found in the 25% and 50% plastically deformed microstructure. Hence once a critical level of stress was attained dislocation motion by precipitate shear as well as precipitate by pass probably took place thereby allowing further slip. Even though this alloy system had been isothermally heat treated, no evidence of dislocation cell array formation was found within the martensitic portion. This was because the martensite was thought to have formed below 320°C (the isothermal temperature), being carbide free and therefore effectively untempered. The formation of cell type dislocation networks after plastic deformation of tempered martensitic microstructures has been reported by a number of authors (Yan and Men²⁰⁶). However, after extensive research no evidence of dislocation cell structures within deformed bainitic microstructures were referenced in the available literature.

11.2.2 The 0.5 mass% chromium, 0.25 mass% carbon alloy system.

The chemistry and heat treatment of this alloy system was devised to produce a through hardened (martensitic) microstructure. Hardenability data was utilised to determine the ideal critical diameter where through hardening to 40 mm was specified. Additionally the carbon content was kept low to encourage auto-tempering, i.e. the lower the carbon content, the higher the M_S and therefore the greater the opportunity for precipitation during the quench. The predicted martensite start temperature from empirical relationships available in the literature was (Andrews¹²³) :-

$$M_S = 539 - 423(\text{wt.\% C}) - 30.4 (\text{wt.\%Mn}) - 17.7(\text{wt.\%Cr}) - 7.5(\text{wt.\%Mo}) \quad (11.7)$$

$$M_S = 539 - 423(0.25) - 30.4(1.5) - 17.7(0.5) - 7.5(0)$$

$$M_S = 539 - 106 - 45.6 - 8.9$$

$$M_S = 378.5^\circ\text{C}$$

On examining the microstructure optically, a relatively fine and uniform lath like structure was observed. In contrast to the 1.25 mass% chromium molybdenum alloy, no evidence of distinct banding through element segregation was found.

Transmission electron microscopy results showed that the microstructure consisted of a mixture of martensite with some bainite. Additionally these results suggested that the martensitic phase was by far the most predominant constituent (approximately 80%). Virtually no carbide precipitation within the martensitic region was found, instead fine carbides limited to the bainitic region was observed (hence low overall carbide population). The occurrence of small amounts of lower bainite within this microstructure was thought to be as a result of exceptionally limited amounts of elemental segregation rather than inaccuracies in hardenability calculations. This was because the sample size used in this experiment was very small (4 mm thick maximum), almost ten times smaller than the ideal critical diameter.

The lack of significant amounts of autotempered martensite was surprising since the M_s temperature was thought to be sufficiently high enough to encourage carbide precipitation and temper during the quench. The absence of autotempered martensite combined with significant amounts of bainite were possibly due to limited amounts of segregation. For example, carbon depleted regions, having lower hardenability would be expected to transform to bainite. Whilst the carbon enriched regions would be expected to transform to martensite, and if the martensite start temperature is also sufficiently suppressed, the degree of auto tempering will be somewhat limited.

Three types of lath were observed in the 0.5 mass% chromium 0.25 mass% carbon microstructure, they were:-

- Moderately dislocated bainitic with exceptionally fine internal carbides, possibly carbon depleted regions.
- Moderately dislocated martensite without carbides.
- Densely dislocated martensite with fine internal twins also without carbides, possibly carbon enriched regions.

Mechanical / microstructural properties in the undeformed condition

The general microstructure of the undeformed alloy system was found to contain moderate amounts of dislocations, together with fine internal lath twins formed from the shear nature of the martensite transformation. The occurrence of twin phase may also indicate that limited amount of carbon segregation had occurred since twin phase is usually associated with higher carbon content alloys. Twinned martensite has also been observed in 0.14 mass% carbon alloys hence the detection of small amounts of twin phase in this particular alloy was not surprising (Kelly and Nutting²¹³). Martensitic laths containing fine twins also appeared to be more densely dislocated than the non twinned martensite laths. This indicated a localised lower M_s temperature and therefore a slightly higher carbon / alloy content.

A distinct difference in dislocation density was observed on comparing the majority (untwinned) laths of this alloy with those found in the 1.25 mass% chromium molybdenum system. This was in agreement with the dislocation density transformation temperature relationship, since it was believed that the localised M_s for the later alloy would be have been at least 100°C less than the 0.5 mass% chromium molybdenum system. The amount of twinned martensitic laths also varied significantly on comparing both undeformed variants. This was probably as a direct result of carbon content since it is thought that the relative number of twinned martensitic laths increase with carbon content (Kelly and Nutting²¹³).

The proof strength of this alloy system in the undeformed condition was the highest compared to all other examined systems at 1475 MPa. Such strength was attributed to the interaction of dislocations with each other within the martensitic laths and the fine carbide morphology within the bainitic laths.

The flow curve profile of the undeformed alloy were typical in shape with an initial high work hardening rate suggesting rapid dislocation interaction, proceeded by a region of lower strain hardening due to dislocation reactions that were originally suppressed (i.e. cross slip).

At a true strain rate of 12×10^{-3} the work hardening rate of this alloy system was found to be lower than the 1.25 mass% chromium molybdenum variant (see figure 211). However, these results were not taken to singularly represent the overall work hardening behaviour. Moreover, these results described the alloy flow stage at the strain of 12×10^{-3} . For example, when the stress strain curves for single crystals are plotted as resolved shear stress versus shear strain, the flow curve can be divided into three stages. Stage one is the region of easy glide, where the dislocations are able to move over relatively large distances without encountering barriers and hence the work hardening rate is low. Stage one is thought to be virtually non existent in the case of polycrystalline materials since it is assumed that no dislocation is able to move without encountering a precipitate or second dislocation.

In the second stage the strain hardening rate of the material increases rapidly. Slip is thought to occur on more than one set of planes and as a result dislocation tangles begin to develop.

Stage three is the region of decreasing rate of strain hardening. The processes occurring in this stage are often called dynamic recovery and the stresses are high enough so that dislocations can take part in processes that were previously suppressed. Cross slip is believed to be the main process by which dislocations piled up at obstacles during stage two can escape. Alternatively, if the stress is sufficiently high, twinning may occur to orientate new slip systems with respect to the stress axis so that additional slip can take place. Although some authors suggest that twin boundaries actually serve as barriers to further dislocation motion (Kelly and Nutting²¹³) thereby increasing the work hardening rate.

In comparison with the 1.25 mass% chromium molybdenum alloy at a strain of 12×10^{-3} , the lower rate of work hardening was thought to actually suggest that this alloy was nearer to stage three with respect to the plastic flow model. In other terms at a true strain of 12×10^{-3} , mechanisms to reduce the strain hardening rate were further advanced (i.e. cross slip). This was perhaps as expected since at the nominated strain the true stress was much higher in the 0.5 mass% chromium 0.25 mass% carbon alloy with the cross slip phenomena probably more prevalent.

On comparing this alloy the 1.25 mass% chromium molybdenum variants, the differences during the tensile test were noted and attributed to:-

- Higher proof strength due to overall higher dislocation density, and finer carbide morphology etc.
- Higher initial work hardening rate due to higher initial dislocation density also smaller packet size (larger percentage of martensite) hence more barriers to dislocation glide.
- Increased work hardening rate also due to higher dislocation generation through higher number of dislocation sources (hence higher dislocation density).

- Lower rate of work hardening at true strain of 12×10^{-3} , due to rapid approach of stage three (flow mechanism). Higher levels of stress ensure cross slip is more favourable.

A definite and positive effect on the yield strength was also attributed to increased effects from interstitial solid solution strengthening and finer interlath cementite carbides. However strengthening from carbides was thought to be somewhat limited since the carbide population was low being confined to the bainitic laths only.

Mechanical and microstructural properties of the deformed variants

As like the 1.25 mass% chromium molybdenum variant, the optically examined microstructure of the 0.5 mass% chromium 0.25 mass% carbon alloy consisted of randomly orientated “macropackets” of laths. However, after extensive plastic deformation a distinct degree of “macropacket” alignment had taken place with preferred orientation towards the direction of rolling. The amount of alignment however did not appear to change after 25% plastic deformation, consequently the mechanical properties of the 25 and 50% deformed alloy were also found to be identical. The effect of cold work on the microstructural observations and mechanical properties were summarised in chapters 9 and 10 respectively and included:-

- A rapid increase in dislocation density, together with apparent increase in the amount of twin phase.
- An increase in the hardness, proof strength, ultimate tensile strength and hence proof to UTS ratio.
- A dramatic increase in the overall work hardening rate during the tensile test up to 10% plastic deformation, but then remaining relatively unchanged.
- A gradual decrease in the potential strengthening rate (e.g. change in hardness versus plastic deformation) decaying in a linear manner.

The microstructure of all deformed variants consisted of dense dislocation networks obscuring the majority of the cementite precipitates. Because of this, carbide morphology assessment was very difficult and it was impossible to determine pinning loss (via shearing).

A rapid increase in dislocation density was observed after relatively small amounts of deformation and were thought to be due to the number of dislocation emitters available (grain / lath boundaries). Additionally, the initial / start dislocation density was quite high thereby increasing the number of Frank-Read sources. Although, precise grain size measurement was not available for these alloy systems it was assumed that this system possessed a finer grain size than the former. This was because the 1.25 mass% chromium molybdenum alloy did not contain grain size controlling titanium nitride particles whereas the 0.5 mass% chromium 0.25 mass% carbon variant did. The finer grain size, effectively increases the number of dislocation emitters in the microstructure and will therefore effect the resultant dislocation density. In addition a finer grain size is also known to affect packet size which in turn will affect the mechanical strength.

The obtained mechanical properties of the 10% deformed 0.5 mass% chromium 0.25 mass% carbon alloy were attributed chiefly to the high dislocation density. Hence the relatively high proof strength and exceptionally high rate of work hardening indicated rapid dislocation lock up probably from the formation of dense sessile networks. Dislocation lock up at fine interlath carbides probably also took place, however, this strengthening mechanism was thought to be rather limited due to the relatively low precipitate population. A high work hardening rate was observed even at very high amounts of stress / strain indicating that even after limited cross slip, the relatively few mobile dislocations soon became locked up.

After 25% plastic deformation, the proof strength was raised again, correlating to a further increase in the dislocation density. However, the overall work hardening rate remained relatively unchanged (high) and indicated that as soon as these dislocations did move probably via cross slip, they became locked up.

A subtle decrease in the overall work hardening rate between the 10 and 25% deformed system was possibly due to the fact that some dislocation locking was lost from the carbide shearing effect. Although this was impossible to quantify due to the high dislocation density obscuring these fine carbides. Alternatively, with dislocation glide via slip being hindered, deformation via a twinning mechanism could have taken place thereby increasing the number of available slip systems and reducing the overall work hardening rates also (very limited effect).

As with the 1.25 mass% chromium molybdenum variant, no increase in mechanical strength was observed beyond 25% plastic deformation. Additionally the work hardening rates were alike, hence the true stress strain curves were described as being identical. The extra amount of cold work had therefore simply introduced more dislocations into an already densely dislocated microstructure. In contrast to the 1.25 mass% chromium molybdenum alloy no cellular dislocation type substructure was found within any of the laths, however observations of such dislocation arrangements are thought to be associated with tempered alloys, whose overall dislocation density is lower and cross slip is achieved with relative ease.

Comparisons between the 1.25 mass% chromium molybdenum alloy system and the 0.5 mass% chromium 0.25 mass% carbon alloy are as follows:-

- After 10% plastic deformation, both alloys possessed similar proof strengths (the 1.25 mass% chromium molybdenum alloy always fell a little short probably due to the slightly lower dislocation density and larger carbide size.
- After plastic deformation, the overall work hardening rate of the 0.5 mass% chromium 0.25 mass% carbon alloy was much greater indicating rapid dislocation lock up even after dislocation slip / cross slip.
- The difference in work hardening characteristics were attributed chiefly to different dislocation densities and cementite precipitate morphology.
- Microstructural observations also indicated that extensive cross slip was somewhat limited in the 0.5 mass% chromium 0.25 mass% carbon alloy with little evidence of dislocation cellular arrays.

The difference in overall mechanical properties was also described via a Hall-Petch type equation (see section 11.2.1).

The degree of strengthening imparted from plastic deformation was measured by first plotting hardness versus the amount of plastic deformation. As with the 1.25 mass% chromium molybdenum variant, a polynomial relationship was obtained where an initial sharp increase in hardness was observed, flattening off after approximately 25% plastic deformation. The plot obtained was also described mathematically and differentiated to produce a second plot, to describe the degree of strengthening imparted versus plastic deformation.

In contrast to the 1.25 mass% chromium molybdenum variant, the amount of strengthening procured through plastic deformation was found to decay in a linear manner with increasing amounts of plastic deformation. In addition to this, the 10 and 25% plastic deformed alloy systems possessed an exceptionally high work hardening rate and the observed dislocation arrays were extremely dense. The gradual loss of potential strengthening after large amounts of plastic deformation was thought to be related to the exhaustion of glissile dislocations and the formation of dense sessile networks. Cross slip was thought to be somewhat limited, hence further plastic deformation may have been supplemented via twinning mechanisms. This was supported by microstructural observations (i.e. twinned laths, dense dislocation patches and no cellular dislocation arrays after large amounts of plastic deformation).

The gradient of the deformation strengthening plot, termed the deformation strengthening loss coefficient (μ), was thought to be related to the work hardening characteristics and the material microstructure. The 0.5 mass% chromium 0.25 mass% carbon alloy, being effectively untempered, contained dense patches of dislocations after small amounts of plastic deformation. In conjunction with this, a high rate of work hardening / high strengthening loss coefficient suggested rapid dislocation sessile formation and exhaustion of glissile dislocations with limited cross slip.

11.2.3 0.3 mass% carbon boron alloy system

Hardenability data was utilised to determine the correct alloy chemistry required to produce a fully martensitic microstructure on water quenching from austenitisation. The carbon content was kept low to firstly encourage auto tempering, and secondly to maintain optimum hardenability effects from boron. The carbon / boron content was therefore specified to ensure adequate hardenability but at the same time maximising the boron and auto tempering effect.

The predicted martensite start temperature from empirical relationships available in the literature was:-

$$M_s = 539 - 423(\text{wt.}\% \text{C}) - 30.4 (\text{wt.}\% \text{Mn}) - 17.7(\text{wt.}\% \text{Cr}) - 7.5(\text{wt.}\% \text{Mo}) \quad (11.8)$$

$$M_s = 539 - 423(0.30) - 30.4(1.02) - 17.7(0.24) - 7.5(0)$$

$$M_s = 539 - 127 - 30.0 - 4.3$$

$$M_s = 378^\circ\text{C}$$

The results obtained showed that the microstructure consisted of a mixture of martensite with some bainite. Transmission Electron Microscopy suggested that the martensitic phase was the most predominant, although in some areas as much as 40 - 50% bainite was observed.

As with the 0.5 mass% chromium 0.25 mass% carbon variant, only limited amounts of carbide precipitation were observed within the martensitic laths. Instead, the majority of the cementite precipitates were found within the bainitic laths, were exceptionally fine, and located at an angle of 60° to the long axis.

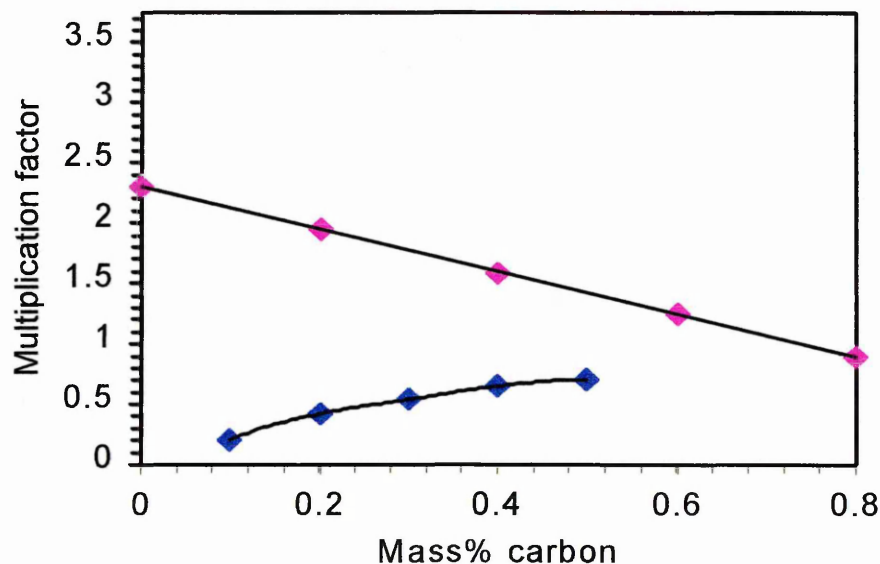
In contrast to the previously mentioned alloy however, because the percentage of bainitic laths was much greater, it was concluded that the overall carbide population was higher.

The occurrence of significant amounts of bainite within the microstructure was thought to be due to limited amounts of segregation rather than inaccuracies in hardenability data.

For example, a subtle depletion in boron or localised increases in carbon (making boron less effective) could result in some of the microstructure transforming to bainite as opposed to martensite. However a subtle depletion of carbon within a boron containing steel was not thought to significantly reduce the hardenability and encourage the formation of bainite. This was because lowering the carbon content would actually increase the boron effectiveness thereby outweighing any loss of hardenability.

Figure 187 below shows the effect of increasing carbon on hardenability in terms of its own multiplication factor and the boron multiplication factor (Siebert et al¹³²). The linear plot effectively shows a decrease in the Boron multiplication factor with increasing amounts of carbon (i.e. a boron containing steel with increasing amounts of carbon). The increased potency of boron over carbon is clearly shown, hence subtle increases in carbon would actually decrease overall hardenability. Figure 188 combines both multiplication factors (added) to show that increasing carbon content does indeed lead to an overall decrease in multiplication factor and therefore hardenability.

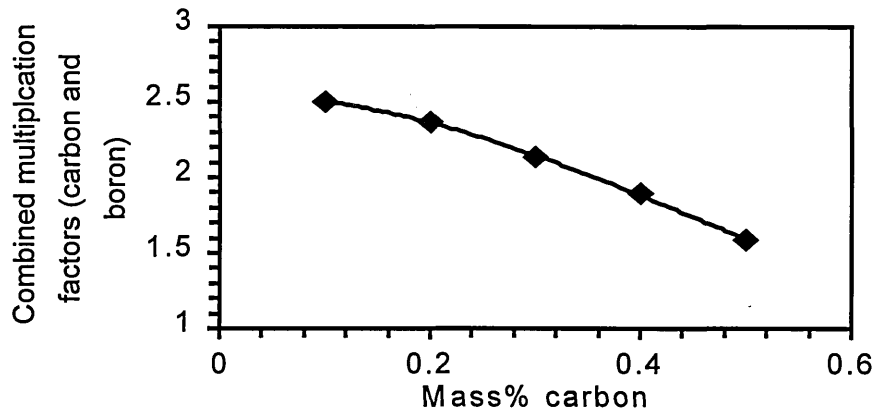
Figure 187:- The relationship between carbon content and the multiplication factors for carbon and boron. (Siebert et. al.¹³²)



Key = Pink Boron Multiplication (boron containing steel)

Blue = Carbon Multiplication (boron free steel)

Figure 188:- The relationship between carbon content and combined multiplication factors for carbon and boron.



The main microstructural differences between this alloy system and the 0.5 mass% chromium 0.25 mass% carbon alloy was the amount of bainite and carbide population, although the carbide sizes were quite similar. Overall, it appeared that the dislocation density in the martensitic laths were lower in comparison to the 0.5 mass% chromium 0.25 mass% carbon variant. This was not initially as expected since the predicted martensite start temperature for both alloy systems were very similar 378°C. This lower than expected dislocation density was possibly due to a subtle depletion of carbon or other alloying additions thereby increasing the martensite start temperature. This effect would also explain the occurrence of significant amounts of bainite through loss of boron effectiveness, as well as the lower dislocation density in the martensite phase. Four types of lath were observed in the 0.3 mass% carbon boron alloy microstructure, they were:-

- Bainitic laths with moderate - low dislocation density without internal carbides (upper bainite) possibly as a result of carbon enrichment.
- Bainitic laths with moderate - low dislocation density with quite fine internal carbides possibly as a result of carbon enrichment.
- Moderately dislocated martensitic with occasional carbides.
- Very occasional densely dislocated martensitic with fine internal twins also without carbides, probably with localised lower martensite start temperature.

Mechanical and microstructure properties in the undeformed condition

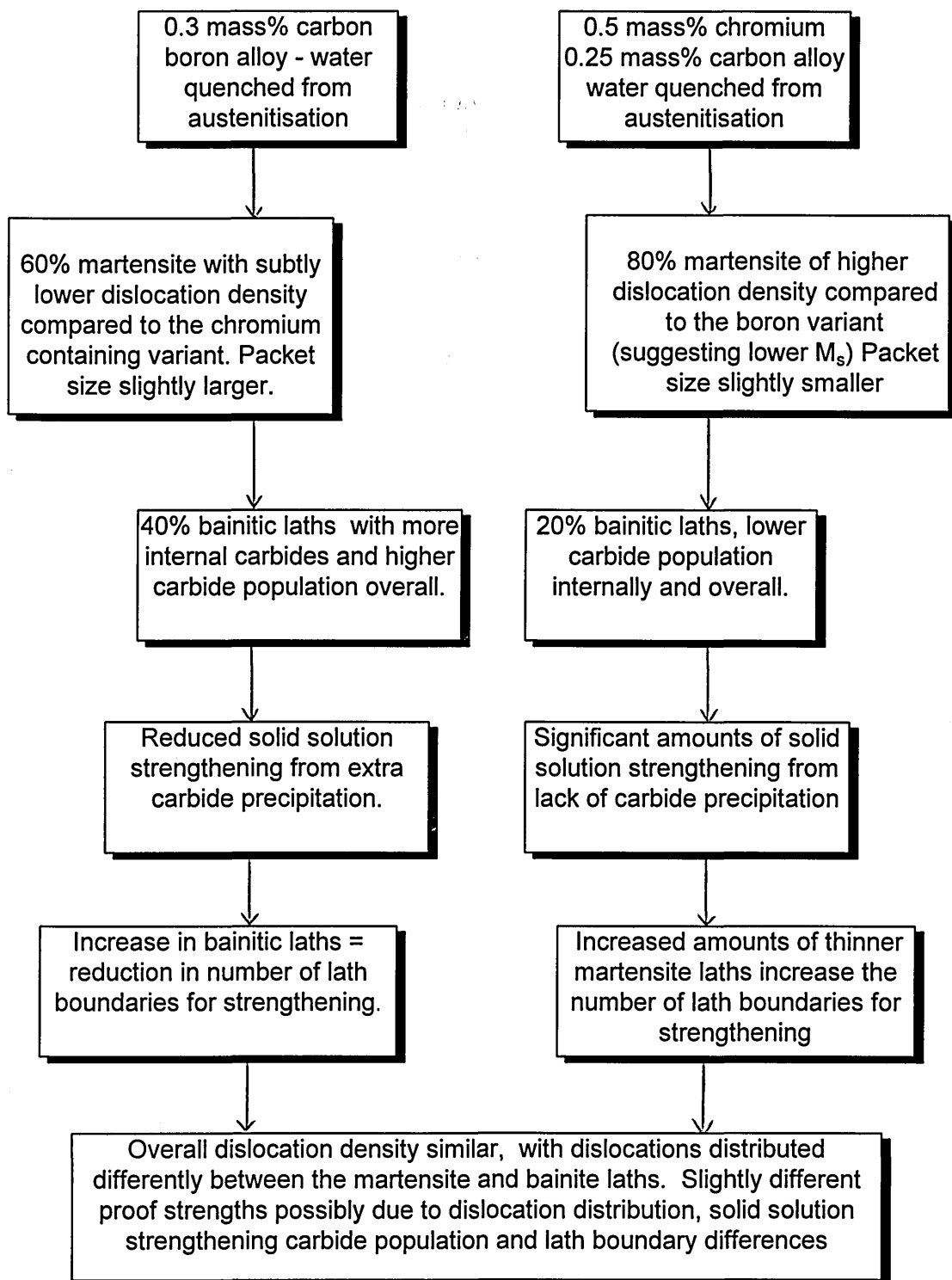
The tensile and microstructural properties of the undeformed 0.3 mass% carbon boron alloy were compared to the other examined alloy systems:-

- Slightly lower proof strength compared to the 0.25 mass% carbon 0.5 mass% chromium alloy but higher than the 1.25 mass% chromium molybdenum alloy.
- Larger proportion of bainitic laths compared to the 0.5 mass% chromium 0.25 mass% carbon variant, but less bainitic laths than the 1.25 mass% chromium molybdenum variant.
- Martensitic laths in the 0.3 mass% carbon boron alloy appeared to contain less dislocations compared to the 1.25 mass% chromium molybdenum and the 0.5 mass% chromium 0.25 mass% carbon variant.
- Slightly larger packet size (martensitic / bainitic lath packet) compared to the 0.5 mass% chromium 0.25 mass% carbon variant.
- Similar amounts of twinned martensitic laths compared to the 0.25 mass% carbon 0.5 mass% chromium alloy.
- Similar true stress strain curve compared to the 0.25 mass% carbon 0.5 mass% chromium alloy. High initial work hardening rate, reducing to a constant low rate of work hardening at higher strains.
- Slightly larger carbide size compared to the 0.5 mass% chromium 0.25 mass% carbon variant.

Overall, the undeformed alloy system was found to contain moderate amounts of dislocations with occasional twinned martensite laths formed due to the shear nature of the transformation. The twinned martensitic laths also appeared to be more densely dislocated than the non twinned laths suggesting localised lower M_s . Subtle differences in the dislocation distribution, bainitic proportion, carbide morphology and packet size were thought to be responsible for the slightly lower proof strength obtained in this alloy system.

Additionally the contribution via carbon in solid solution was probably higher in the 0.5 mass% chromium 0.25 mass% carbon variant thereby promoting a higher proof strength. A comparison between the 0.3 mass% carbon boron alloy and the 0.5 mass% chromium 0.25 mass% carbon alloy is shown in figure 189.

Figure 189:- Microstructural comparison between 0.3 mass% carbon boron alloy and the 0.5 mass% chromium 0.25 mass% carbon variant to account for difference in proof strengths (undeformed condition)



During the true stress strain test, the plastic flow of the 0.3 mass% carbon boron alloy behaved in a similar manner to the 0.5 mass% chromium 0.25 mass% carbon alloy. An initial high rate of work hardening suggested rapid dislocation lock up at fine precipitates and dislocation sessile formation. Towards the end of the tensile test, the work hardening rate decreased somewhat and further dislocation motion was again allowed after, for example cross slip.

Turning to the work hardening rate measurements (figure 183), a moderate to low rate of work hardening was measured at a true strain of 12×10^{-3} . This indicated that at this given strain, this alloy was well within stage three of plastic flow, with cross slip taking place to reduce the work hardening rate. A similar rate of work hardening was observed at the same strain in the 0.5 mass% chromium 0.25 mass% carbon. At the same strain, the work hardening rate of the 1.25 mass% chromium molybdenum variant was found to be slightly higher than both of the water quenched variants. However, this was taken to represent the tensile flow stage at the given stress / strain rather than as a direct comparison. Hence at a true strain of 12×10^{-3} , the 0.3 mass% carbon boron alloy was thought to be nearer to stage 3 (easier flow from cross slip) than the 1.25 mass% chromium molybdenum variant.

Mechanical and microstructural properties of the deformed variants

The effect of plastic deformation on the optically examined microstructure was to align previously random orientated "macropackets" of laths to the cold rolling direction. As with the 1.25 mass% chromium molybdenum and 0.5 mass% chromium 0.25 mass% carbon variants, little change in this alignment was observed after 25% deformation which was reflected in the mechanical results.

The effect of cold work on the microstructural observations and the mechanical properties were summarised in chapters 9 and 10 respectively and included:-

- A rapid increase in the dislocation density, with slight apparent increase in the amount of twin phase.
- An increase in hardness, proof strength, ultimate tensile strength and hence proof to UTS ratio.
- An increase in the overall work hardening rate during the tensile test up to 10% plastic deformation, but then remaining relatively unchanged.
- A gradual decrease in the potential strengthening rate (e.g. change in hardness versus plastic deformation decaying in a linear manner).

The mechanical properties of the 10% deformed 0.3 mass% carbon boron alloy were found to be very similar to the 10% deformed 0.5 mass% chromium 0.25 mass% carbon variant. After plastic deformation, both alloys possessed similar proof strength values, together with similar flow curves during the tensile test. This perhaps indicated that the dislocation density of the two alloy systems after plastic deformation were similar, which in turn suggested that the start dislocation density and degree of dislocation multiplication were also alike. Dislocation multiplication through plastic deformation can take place via a Frank-Read mechanism, other sources include high angle boundaries (e.g. grain boundaries). Unfortunately the grain boundary strengthening effect was not determined at this stage, however it was assumed that the grain size of the 0.3 mass% carbon boron alloy was quite fine due to the addition of grain refining additives.

The high dislocation density of the 10% deformed alloy system also effected the work hardening characteristics during the tensile test. A high rate of work hardening was observed even at very high amounts of stress / strain indicating that even after limited cross slip, the relatively few glissile dislocations became locked up. After 25% plastic deformation, the proof strength was raised again correlating to a further increase in dislocation density with the overall work hardening rate still remaining relatively high. As like the 1.25 mass% chromium molybdenum and the 0.5 mass% chromium 0.25 mass% carbon variant, no additional increase in mechanical strength was observed beyond 25% plastic deformation.

In contrast to the tempered variants, little cellular dislocation type substructure was observed after plastic deformation. Instead dense dislocation networks formed which were thought to contain mainly sessile dislocations, which in turn dictated the work hardening characteristics.

The rate of strengthening measured by plotting the rate of change of hardness or proof strength versus plastic deformation was in many respects similar to that of the 0.5 mass% chromium 0.25 mass% carbon alloy. A high initial strengthening (dramatic increase in proof strength or hardness) after light amounts of plastic deformation signified a high exhaustion rate in the number of glissile dislocations. In contrast after large amounts of plastic deformation, although the dislocation density had increased significantly, it was imagined that the majority of these would be sessile hence the potential for strengthening was reduced.

11.2.4 0.3 mass% carbon boron alloy, tempered at 250°C.

In the as quenched condition, the 0.3 mass% carbon boron alloy consisted of a mixture of carbide free martensite, martensite with few carbides and carbide rich bainite. The ratio of bainite to martensite was estimated from limited transmission electron microscopy at approximately 35 / 65. It was anticipated that the 250°C temper treatment would increase the number of precipitates throughout the structure, especially in the martensitic laths. The actual size of the precipitates is also greatly influenced by temper treatment temperature and since a relatively low temperature was used it was expected that the cementite precipitates would not significantly coarsen. The overall microstructure was therefore expected to consist of homogeneously distributed, and relatively fine precipitates to effectively pin dislocations.

The microstructure consisted of bainitic laths with moderately sized carbides and martensitic laths either with occasional carbides or carbide free. The newly formed carbides within the martensitic laths were identified as cementite (Fe_3C) which was as expected since the temperature at which the transitional carbide transforms to cementite is around 200°C. Carbides formed from the water quench within the bainitic laths were also of the type Fe_3C but were generally larger and more prolific. A certain amount of interlath cementite was found, although it was not established whether this had transformed from interlath retained austenite.

A lower dislocation density in comparison to the untempered variant was also observed indicating that some dislocations were annihilated during the temper treatment. However, the dislocation density was not thought to be as low as the higher temperature tempered variant. This was in agreement with recovery mechanisms where dislocation reduction is established as being temperature dependant.

Small amounts of twin phase were frequently observed, and although difficult to quantify it was estimated that the amount of twinned martensite was not as high as the untempered variant but higher than the 400°C variant.

Mechanical and microstructural properties of the undeformed variant.

The mechanical and microstructural properties of the undeformed 0.3 mass% carbon boron alloy tempered at 250°C were compared to the other alloy systems, observations included:-

- Identical proof strength as the untempered 0.3 mass% carbon boron alloy. (Second highest overall).
- Moderate work hardening rate during the tensile test (similar to the untempered 0.3 mass% carbon boron alloy).
- Moderately sized cementite carbides in bainitic lath, few carbides in martensitic lath.
- Moderate dislocation density and twinned martensite, being lower than the untempered but higher than the high temperature tempered variant.

Interestingly, the 0.2% proof strength of the low temperature tempered 0.3 mass% carbon boron alloy was the same as its untempered counterpart. Identical proof strength values for these two alloy systems transcribed to an identical critical stress to initiate significant dislocation glide. Nevertheless, the untempered and 250°C tempered microstructures were quite different as were the strengthening contributions from each particular phase. Microstructural differences between this alloy and the untempered variant included a larger carbide size, increased carbide population and lower overall dislocation density. With additional precipitation, the contribution to strengthening via solid solution was also reduced.

Contributions to microstructural strengthening were defined as dislocation density, carbide size, carbide population and solid solution carbon and were described by a Hall - Petch type equation:-

$$\sigma_{Ys} = \rho_{dd} + \phi_{ppt} + \sigma_{ssh} + \sigma_{Boundary} \quad (11.6)$$

Where σ_{Ys} is the yield strength.

ρ_{dd} is the strengthening contribution due to dislocation density.

ϕ_{ppt} is the contribution from precipitated carbides

σ_{ssh} is the contribution from solid solution strengthening.

$\sigma_{Boundary}$ is the contribution from grain and lath boundaries.

Table 48 compares the untempered and 250°C tempered 0.3 mass% carbon boron alloy. It was assumed that the precipitated carbides did not coarsen to an extent as to reduce their ability to pin dislocations. Hence although this alloy possessed a lower dislocation density, the extra carbide precipitation counteracted this potential strengthening loss.

Table 48 :-comparison of strengthening systems in the untempered and 250°C tempered 0.3 mass% carbon boron alloy.

Alloy →	0.3 mass% carbon boron alloy untempered	0.3 mass% carbon boron alloy tempered at 250°C
Strengthening ↓		
Dislocation density	↑	↓
Precipitated carbide size	↓	↑
Precipitated carbide population	↓	↑
Solid solution strengthening	↑	↓
Lath and grain boundaries	unchanged	unchanged

The work hardening characteristics of the 0.3 mass% carbon boron alloy in the untempered and 250°C tempered condition were also similar. An initial high rate of work hardening suggested mutual interaction of dislocations with one another and the cementite precipitates. Towards the end of the tensile test, a lower rate of work hardening suggested significant amount of dislocation glide probably via cross slip or even deformation twinning. Hence, the overall lower dislocation density did not appear to effect the work hardening characteristics, and dislocations were pinned just as effectively at the cementite precipitates.

Mechanical and microstructural properties of the deformed variants

The effect of plastic deformation on the microstructural and mechanical properties provided in chapters 9 and 10 respectively were compared to the other examined alloy systems:-

- Moderate increases in proof strength, ultimate tensile strength and hardness with increasing amounts of cold rolling.
- Formation of dislocation cell structures after large amounts of plastic deformation with occasional dense dislocation forests.
- All deformed variants possessed a lower rate of work hardening compared to the untempered variant.
- “Sheared” carbides observed after extensive plastic deformation.

The low temperature temper treatment was found to significantly effect the strengthening potential of this alloy system. For example, both the untempered and 250°C tempered 0.3 mass% carbon boron alloy started with identical proof strengths (1430 MPa), but after 10% plastic deformation the proof strengths were 1850 and 1740 MPa respectively. In addition to this the rate of work hardening under the tensile test was much lower in the tempered alloy, indicating a greater ability for dislocation glide and cross slip.

Transmission electron microscopy revealed that after significant amounts of plastic deformation, the dislocation density increased significantly thereby increasing proof strength. However, the way in which the new dislocations were arranged was neither totally cellular like (i.e. the 400°C tempered counterpart) or like the untempered variant, as dense randomly placed forests. Instead, the dislocation substructure tended to fall in between the two with:-

- Occasional dense forests of dislocations, often found near twinned microstructure.
- Partly formed dislocation cells which have a “ragged appearance” i.e. not totally cellular in shape.
- Laths containing well developed dislocation cellular arrays.

Dislocation cellular structures are thought to play an important role in the work hardening behaviour of tempered steels (Yan and Men²⁰⁶). After small amounts of plastic deformation dislocations gather to form tangles which then go on to form dislocation substructures with increasing amounts of plastic deformation. In the 10% deformed variant, the dislocation substructures were not particularly well defined and the majority of the microstructure appeared to consist of more randomly placed dislocation tangles. The flow curve of the 10% deformed variant perhaps mirrored this, with a large proportion of the flow curve indicating quite a high rate of work hardening. In contrast the 50% deformed sample contained quite a few well developed dislocation cellular arrays (indicating cross slip) and was thought to explain the generally larger proportion of easier plastic flow during the tensile test.

Compared to the untempered and deformed 0.3 mass% carbon boron alloy, The lower rate of work hardening of the 250°C tempered variant, was attributed to the generally lower dislocation density and the ability of some of the glissile dislocations to cross slip and form dislocation cell arrays. Additionally at such high levels of stress, it was expected that some of the dislocations would bypass the cementite precipitates, and indeed evidence of this was found. The work hardening rate of the 400°C tempered 0.3 mass% carbon boron alloy was found to be even lower than this alloy due to the even lower dislocation density, enhanced ability to cross slip and pinning loss due to over ageing of cementite precipitates. Hence after plastic deformation, a much larger proportion of the dislocation arrays were cellular like (see section 11.3.2).

Deformation strengthening versus plastic deformation was measured by first plotting the 0.01% proof strength or hardness versus plastic deformation. A polynomial type curve was obtained, flattening off after large amounts of plastic deformation. This curve therefore illustrated that the largest increases in proof strength or hardness were obtained after small amounts of plastic deformation.

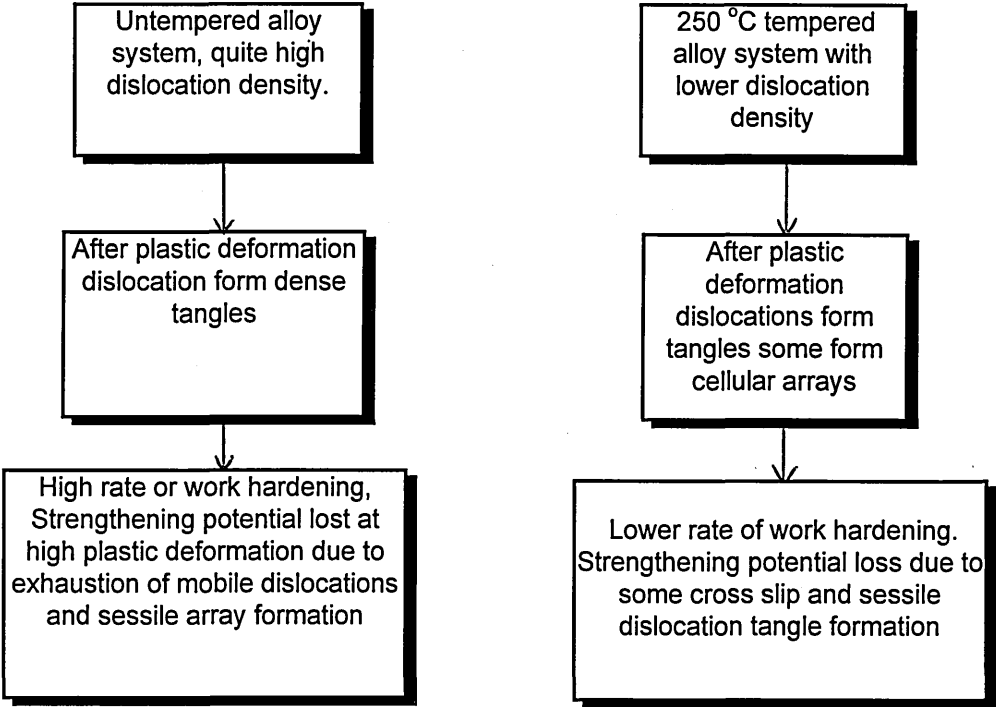
After determining a mathematical function to describe the hardness proof strength versus plastic deformation curve a second linear plot was obtained giving the deformation strengthening loss coefficient.

On comparing each 0.3 mass% carbon boron alloy variants in the untempered and tempered condition, It was found that increasing the tempering temperature reduced the extent of strengthening potential loss versus plastic deformation. This in turn was related to the ease at which mobile dislocations were pinned and the exhaustion of glissile dislocations at higher stresses. For example, in the undeformed alloy system, the majority of the glissile dislocations were soon locked up after relatively small amounts of plastic deformation. The higher dislocation density, coupled with finer carbide size supported a high rate of work hardening, hence high potential strengthening loss (coefficient). This effect was obviously lost in the 400°C temperature tempered alloy system, where a lower dislocation density , coarse carbide size promoted cross slip and dislocation cell formation, hence the number of mobile dislocations remained somewhat constant.

The 250°C tempered alloy system was found to possess a strengthening coefficient in-between the untempered and 400°C tempered variant which was as expected since the microstructural characteristic were described as being hybrid of the two mentioned above.

Figure 190 summarises the effect of tempering on the potential strengthening loss coefficient (μ) for the untempered and 250°C tempered 0.3 mass% carbon boron alloy.

Figure 190:- Effect of tempering on the strengthening coefficient for 0.3 mass% carbon boron alloy systems.



11.2.5 0.3 mass% carbon boron alloy, tempered at 400°C.

Carbide size, population and type is known to be related to the diffusion of carbon and hence temper treatment temperature. It was anticipated that the 400°C tempering treatment would significantly increase the number of precipitates throughout the structure, especially in the martensitic laths. Additionally the cementite precipitates were expected to be quite large and of the type Fe₃C (cementite).

On examination of this tempered alloy, an array of large cementite precipitates were found indicating that this alloy had been effectively heat treated at the third stage of tempering. The carbides within the martensitic laths often extended across the lath width, and the carbides within the bainitic lath had also coarsened to a similar size. Prior to the third temper stage, transformation of retained austenite to a mixture of ferrite and cementite, with the cementite constrained between martensite laths takes place. Indeed, interlath cementite was observed in this alloy system although it was not established whether austenite was present prior to the temper treatment.

A lower dislocation density in comparison to the untempered variant was also observed indicating that a number of dislocations had been annihilated during the temper treatment. This was in agreement with well established recovery mechanisms that cause the elimination of low angle interlath boundaries and reduction of high dislocation density of the as quenched lath martensite .

Any remaining dislocations within the tempered martensite in the very late stages of tempering can align themselves into low angle grain polygonisation boundaries. Such a process probably required a higher temper temperature than 400°C, since little evidence of polygonisation was found.

Mechanical and microstructural properties in the undeformed condition.

The mechanical and microstructural properties of the undeformed variant were compared to the other alloy systems and are summarised as follows:-

- Low proof strength, ultimate tensile strength and hardness.
- Low proof to ultimate tensile strength ratio.
- Consistently low rate of work hardening during the tensile test.
- Large cementite carbides in both martensitic and bainitic laths.
- Low dislocation density, no evidence of twin phase.

This alloy possessed the second lowest proof strength, being marginally higher than the 1.25 mass% chromium molybdenum variant. In both cases lower proof strengths were attributed to the coarseness of the precipitated cementite, lower dislocation density, and reduced solid solution strengthening effect. Figure 157 showed that the average cementite precipitate size was approximately 20 microns (based on measured surface area). In comparison, the carbides within the 1.25 mass% chromium molybdenum variant were generally larger with several measuring in excess of 24 μm . This subtle difference in carbide size therefore partly explained the obtained proof strengths.

Although the undeformed high temperature tempered alloy possessed a slightly higher proof strength than the 1.25 mass% chromium molybdenum variant, the latter appeared to work harden more during the tensile test. In other words, dislocation glide appeared to be hindered to a greater extent in the 1.2 mass% chromium molybdenum alloy. Both alloy systems appeared to possess similar dislocation densities hence it was difficult to attribute the difference in work hardening behaviour to this. However the way in which dislocations arranged themselves in the deformed microstructures were quite different for each alloy, and to this end the work hardening behaviour during the tensile test was partly explained.

For example, after moderate amounts of plastic deformation in the 1.25 mass% chromium molybdenum alloy, the dislocation density increased, but on the whole dislocations were homogeneously distributed throughout.

This contrasted with the high temperature tempered carbon boron alloy, where after plastic deformation, dislocations arranged themselves into cell like substructures. The type of dislocation array formed after plastic deformation is thought to be dependant on crystal structure, temperature of deformation, strain and strain rate. A stable cellular like dislocation configuration can develop if the generation of sessile dislocations due to multiple slip is allowed and cross slip can take place. Dislocations within the high temperature tempered carbon boron alloy were therefore allowed to cross slip with some ease, form cell substructures and maintain a low rate of work hardening. The development of cellular type dislocation arrays are also associated with microstructures of lower stored energy, brought about by a tempering operation.

In contrast the 1.25 mass% chromium molybdenum variant, contained significant amounts of twin boundaries that block dislocation movement and reduce the number of available slip systems. This amount of cross slip was therefore reduced, hence random dislocation tangles generally formed instead, hence a higher rate of work hardening was observed.

On comparing the true stress strain curves of the high and low temperature tempered variants, the work hardening characteristics were also found to be quite different. The high temperature tempered alloy possessed a curve indicating a high work hardening rate at a limited range of strain which rapidly degenerates to a lower rate for the majority of the test. In comparison, the low temperature tempered variant possessed a higher rate of work hardening over a wider spectrum of strains. Additionally, the extent to which the work hardening rate decreased during the tensile test was much less in the lower temperature tempered alloy. The difference in proof strength and work hardening rate were attributed to dissimilar carbide size and dislocation density and contribution from solid solution strengthening, which were characteristic of the tempering temperature used. On comparing the carbide distribution curves of the low and high temperature tempered 0.3 mass% carbon boron alloy, it was interesting to note that the shape of these curves were almost identical.

In both cases the carbide distribution was skewed towards smaller values although a shift of approximately 5 microns in average carbide size was enough to dramatically reduce the proof strength. To summarise, the point at which dislocation glide commences was thought to start in the region of lowest dislocation density or around coarse carbides where pinning is minimal. This microstructure contained significant amounts of low dislocation density laths, as well as coarse carbide size resulting in a low proof strength. In addition the rate at which the microstructure work hardens, was thought to be related to the ability of the dislocation to cross slip. For the high temperature tempered carbon boron alloy, a low rate of work hardening together with formation of dislocation cell like substructure indicated that significant amounts of cross slip had indeed taken place.

Mechanical and microstructural properties of the deformed variants

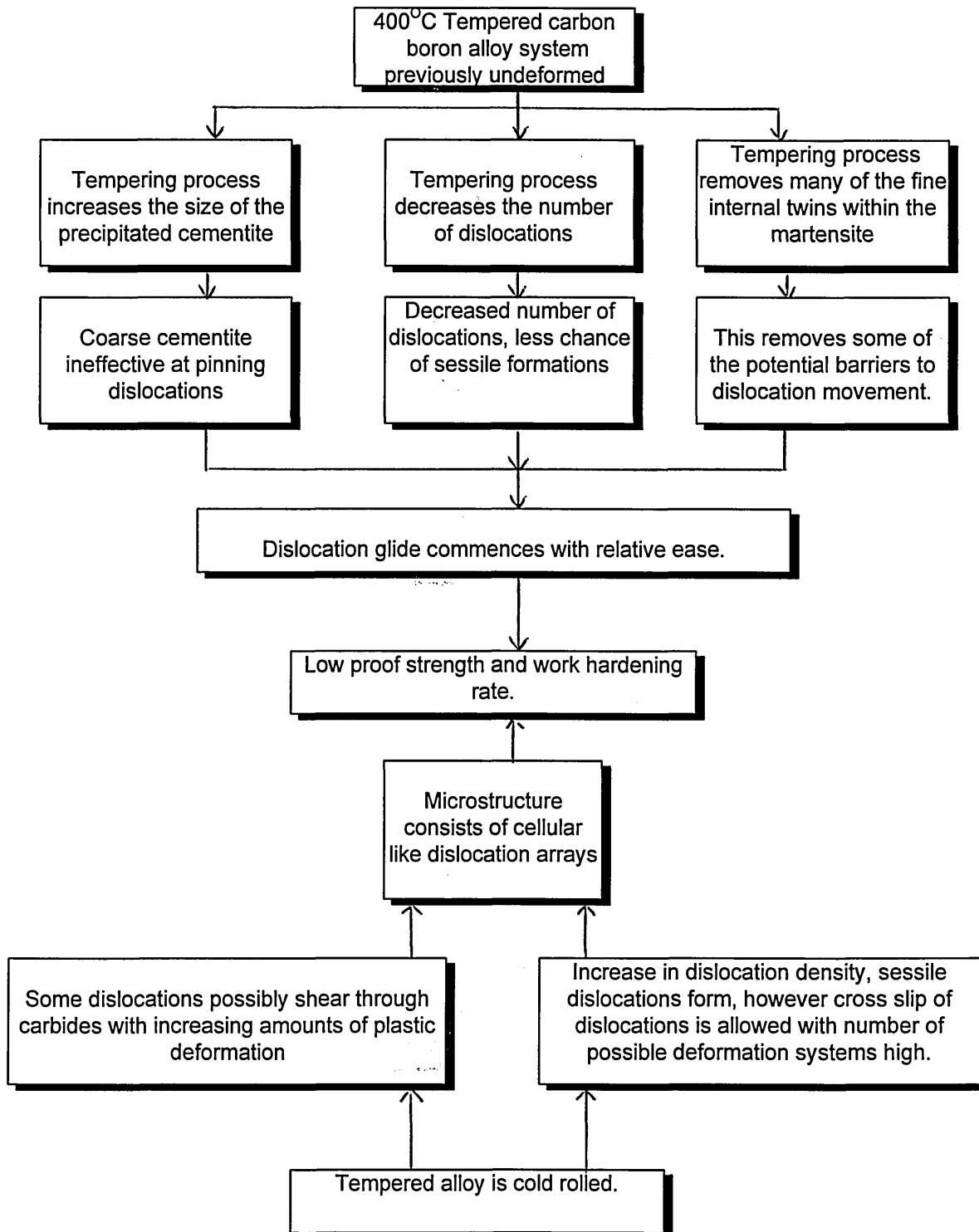
The optical microstructure in the undeformed condition consisted of packets of randomly orientated laths of granular appearance. The grain structure was also visible presumably due to additional carbide precipitation during the temper. The effect of cold work was also observed optically with macropacket alignment and grain boundary orientation towards the direction of rolling. The microstructural and mechanical properties provided in chapters 9 and 10 were compared to other alloy systems:-

- Very slight increases in proof strength, ultimate tensile strength and hardness, all deformed variants possessed a low rate of work hardening.
- Apparent increase in the amount of dislocation cell formation with increasing amounts of plastic deformation.
- Apparent increase in amount of "sheared " carbides with increasing amounts of deformation.
- Little observed twin phase, or densely dislocated patches within martensitic or bainitic laths.

The stress strain curves of all cold rolled variants in this high temperature tempered condition were very similar. On attaining a relatively low critical stress, plastic flow commenced and dislocation glide proceeded with relative ease transcribing to a low rate of work hardening. Transmission Electron Microscopy revealed that after significant amounts of plastic deformation, cellular like dislocation networks developed throughout the microstructure as opposed to the dense forest type previously observed in the untempered variants. Such dislocation cell substructures are thought to develop via a multi-stage process, each one of which plays an important role in the work hardening behaviour. At the initial stage, dislocations gather to form tangles which then go on to form dislocation sub structures at increasing amounts of strain. Different dislocation substructures form after different amounts of deformation resulting in different work hardening characteristics of the steel. Small amounts of dislocation substructure were observed in the 10% deformed variant. The remaining dislocations tended to form quite tight tangles within the martensitic laths whilst the bainitic laths remained lightly dislocated. After 25% deformation a dislocation cell structure was clearly evident and always confined to particular laths. With increased amounts of plastic deformation (50%) increased refinement of the dislocation cells were observed with perhaps elongated alignment towards the direction of rolling. Additionally some of the dislocation cells appeared to cross the lath boundary, indicating that some of the moving dislocations could overcome the obstruction of this boundary. The large amount of plastic deformation incorporated into this alloy system therefore appeared to refine the cellular like dislocation substructure. This, together with the low rates of work hardening indicated that significant amounts of cross slip were taking place even after 50% plastic deformation. The increase in proof strength was also extremely limited due to loss of pinning from large and sheared carbides. The 50% deformed alloy dislocation density was described as moderate and contrasted markedly with the untempered 50% deformed counterpart.

Such difference in dislocation density attributed to the lower initial dislocation density and internal stress reduction due to carbide precipitation, as summarised in figure 191.

Figure 191:- Summary of mechanical microstructural attributes of the 400°C tempered 0.3 mass% carbon boron alloy mass% carbon boron alloy in the undeformed and deformed condition.



The 400°C tempering treatment was found to have a distinct effect on the strengthening ability of the microstructure via cold work. Figure 182 showed that for all other alloy systems, the amount of strengthening imparted decreased with increasing amounts of plastic deformation. In other words, the microstructures were strengthened the most at smaller deformations where the number of glissile dislocations were greatest. For the 400°C tempered 0.3 mass% carbon boron alloy however, little strengthening was imparted from cold work. This implied that the majority of added dislocations from cold rolling remained quite mobile and were allowed to cross slip with some ease. This was supported by microstructural results, i.e. frequent observation of dislocation cellular type arrays, a prerequisite feature of excessive cross slip.

11.3 Discussion summary

The rationale behind this research programme was to develop a new alloy system which could replace an oil quenched and tempered variant currently used by Pandrol. Requirements included the ability to attain adequate mechanical strength and resilience via a relatively easy production route (i.e. air cool or straight quench). Several alternative alloy systems were developed with a chosen few identified as suitable candidates for the industrial application. In particular the water quenched low carbon boron and the chromium low carbon alloys were considered promising. Initial work suggested that microstructural strengthening of the above mentioned alloys were partly due to auto tempered carbide within the martensitic laths. However subsequent research has shown that these microstructures contain little or no autotempered martensite. Instead a fine dispersion of carbide precipitated within relatively large amounts of bainite were found. In order to induce further mechanical strength into these alloys, the use of cold work was utilised with great success. However, such increases in strength have been shown to be applicable when the alloy is in the untempered condition.

To conclude, this programme of research has successfully developed an alternative alloy system suitable for the Pandrol spring clip application. A novel straight water quench plus cold work production route was used to produce a spring with adequate mechanical strength. The contribution to knowledge that has emerged from this work has included:-

- Development of a new series of alloys via a novel and hybrid production route suitable for the industrial application.
- Identification that an alloy with a high M_s does not necessarily lead to an autotempered martensitic microstructure.
- Understanding that b.c.c metals (martensitic / bainitic microstructures) can appreciably work harden.
- The tempering of these new alloys will reduce the work hardening ability, with dislocations able to cross slip once more.

Chapter 12:- Conclusions

Defining the microstructure

- The results found reasonable agreement with hardenability data used to predict ideal critical diameter hence microstructure, however subtle segregation resulted in significant amounts of the microstructure transforming to bainite.
- Utilising lower carbon contents did not appear to promote significant amounts of auto tempering, even though the predicted M_s was sufficiently high.
- The 1.25 mass% chromium molybdenum alloy microstructure results were in good agreement with the continuous cooling transformation curves. The presence of martensite was attributed to chromium, molybdenum and silicon segregation.
- The effect of tempering the 0.3 mass% carbon boron alloy was established, altering the carbide size, dislocation density and amount of twinned martensite.

Mechanical and microstructure properties of undeformed alloy

- The proof strength in the undeformed condition was found to be related to carbide size and distribution and dislocation density.
- The proof strength was found to decrease on tempering above approx. 300°C due to excessive carbide growth, loss of solid solution strengthening, decrease in dislocation density and removal of twin boundaries.
- Microstructures containing large amounts of twin phase and sessile dislocations work hardened rapidly, whereas microstructures with little amounts of twin phase and lower dislocation densities possessed a lower rate of work hardening.
- Hence the work hardening characteristics were determined by the general dislocation mobility, in particular their ability to cross slip.

Mechanical microstructure properties after cold work

- The dislocation structures formed after cold work were influenced by the initial dislocation density and the amount of twinned martensite present.
- The high temperature tempered microstructure, contained very little twinned martensite forming cellular type dislocation arrays after plastic deformation. In contrast microstructures containing large amounts of twin phase possessed dense dislocation tangles after plastic deformation.
- This in turn then effected the increment of proof strength with cold work, i.e. microstructures tending to form dislocation cellular structures possessed low proof strengths and rates of work hardening.

Industrial Application

- Achievement of desired mechanical strength was possible after small amounts of strengthening through cold work.
- Strengthening achieved through dislocation interactions with fine precipitates, boundaries and one another to form dislocation tangles.
- Spring clip manufacture incorporating small amounts of plastic deformation is possible in house or during insertion onto track environment.
- A realistic alternative to traditional oil quenched and tempered silicon manganese grade alloy was found.

Appendix 1

Calculation of Retained Austenite

The basic equations used are:-

$$\text{Concentration (Cx)} = \frac{Pi}{R} \quad (13.1)$$

where Cx is the concentration of phase x.

Pi is the peak intensity.

$$R = \frac{1}{v} \times F^2 \times LP \times M \times e^{-2m} \quad (13.2)$$

where v = Volume of a unit cell (a^3)

F = Structure factor

LP = Lorentz Polarisation factor

M = Multiplicity factor

e^{-2m} = Temperature factor

$$\text{Retained austenite (\%)} = \frac{1}{1 + (Ca / Cb)} \times 100 \quad (13.3)$$

where Ca and Cb are concentrations of phase a and b .

Hence once peak heights are known, the R value must also be calculated for each (hkl). Equation 13.1 contains several complicated parameters described as follows:-

v , the volume of a unit cell

$$\text{Now } v = a^3 \text{ where } a \text{ is the lattice parameter} \quad (13.4)$$

$$\text{Now } d = \frac{a}{\sqrt{h^2 + k^2 + l^2}} \quad (13.5)$$

$$\text{and } \lambda = 2d \sin \theta \quad (13.6)$$

Using given values of λ (for copper = 1.5405Å) and measured values of θ , it is possible to calculate d . The lattice parameter and hence volume (v) is then calculated using equation (13.4)

F = Structure factor

$$\text{For b.c.c structures:-} \quad F^2 = 4f^2 \quad (13.7)$$

$$\text{For f.c.c structures:-} \quad F^2 = 16f^2 \quad (13.8)$$

where f is the atomic scattering factor which is determined from International tables for crystallography, volume 4. The chemical composition of the alloy must also be taken into consideration, especially in the case of multi-alloy systems containing elements with large atomic differences. In such cases an average atomic scattering factor must be used as given in equation 13.9.

$$f_{av} = \sum (\text{atomic fraction of element A}) \times (\text{scattering factor for A}) \quad (13.9)$$

The scattering factor values for each element are presented versus $\sin\theta/\lambda$, and are listed in tables of crystallography, a correction factor is also applied depending on the type of radiation used (International tables of crystallography, volume 4 pages 148-151) and the average scattering factor is then determined using equation 13.9.

Lorentz Polarisation factor

If a monochromator is used in XRD then the Lorentz Polarisation factor is given as equation (13.10)

$$LP = \frac{1 + \cos^2 2\alpha \times \cos^2 2\theta}{\sin^2 \theta \times \cos \theta} \quad (13.10)$$

Where α is the

θ is the measured peak angle

Multiplicity factor

For example if $hkl = (211)$ then the multiplication factor = 24

Temperature factor

is given by equation (13.11)

$$e^{-2m} = e^{-B \sin^2 \frac{\theta}{\lambda}} \quad (13.11)$$

Where B = Thermal vibration + Zero point energy of element under investigation (Ferrite), Thermal Debye parameters are given in tables of crystallography.

θ = measured angle

Appendix 2

Errors in the measurement of true stress strain

Standard errors from machinery, measurement gauges etc., were noted and are provided in table A.

Table A Errors identified in mechanical testing

Machine / gauge	Measurement parameter	Error
Digital micrometer	length / cross sectional area	+/- 0.01 mm
Laser micrometer	Instantaneous change in length for true strain	+/- 0.001 mm
Tensile machine at Sheffield testing laboratories	Newton	+/- 1.0%

Errors on true stress strain graphs

$$\text{True stress measured by :- } = \frac{\text{Force}}{\text{Area}} \quad (10.1)$$

Area = cross sectional area measured at a specified loads throughout the tensile test as opposed to a single measurement prior to the tensile test (i.e. Engineering stress).

$$\text{Also; True strain} = \ln\left(\frac{L}{L_0}\right) \quad (10.2)$$

sources of error were identified:-

- Load cell (tensile machine).
- Two readings from the digital micrometer to obtain cross sectional area.
- Laser micrometer gauge reading, initial and subsequent.

By using the error values quote in table 1, a maximum deviation from each specific reading was obtained over a range of values. Due to the inability to use individual error bars for each point, the maximum possible error reading was used throughout.

Errors in the measurement of hardness versus plastic deformation.

Hardness measurement errors were minimised by ensuring that all necessary calibration checks had been carried out prior to commencement of testing.

A block standard with a hardness of 453VPN was used which consistently gave hardness readings +/- 12VPN, which was then used as the error for subsequent readings.

Appendix 3

Spark Erosion Cutter operation

Settings as table 9.

1. Secure cutting electrode fro particular application in armature.
2. Switch on power.
3. Switch hydraulics on
4. Switch pump on.
5. Unscrew oil stopper ensuring plug is down.
6. Mount sample to be cut in clamp.
7. Once oil bath is full, set flow rate (manifold) to 4.6.
- 8.M/C (machine) switch to set.
9. Adjust head fine to achieve slow downward movement.
10. Switch M/C switch from set to machine.
11. Engage large red light machining button
12. Increase feed rate for head (outer dial).
13. Reset feed gauge to zero at start of sparking to gauge cutting depth.
14. Depress large red button to stop machining.

After spark erosion cutting is complete, the machine is left as follows:-

1. Pull out oil stopper
2. Close oil manifold
3. Switch off pump.
4. Switch off Hydraulics
5. Switch off power.

Appendix 4

Philips CM20 TEM calibration of magnification

The correct magnification was determined by using a silicon monoxide cross grating with 2.160 lines per μm .

Hence the true magnification = Line spacing measured from TEM plate / Actual line spacing.

From the silicon monoxide results:-

Nominal Magnification	Actual magnification
20K	20042K
38K	38224K
66K	66789K
88K	88875K
150K	15103K
200K	20140K

In addition, the magnification was adjusted after enlargement during plate printing.

References

- (1) G.E Dieter, Mechanical metallurgy, Mc Graw-Hill Book Co. Tokyo, Japan, (1988) pp 282- 283
- (2) H.C Keysor, Product Eng., Vol. 17 (1946) pp 86 - 89
- (3) A.S Kenneford and G..C Ellis, J Iron Steel Inst., Vol 164 Chapter 1 (1950) pp 265 - 267.
- (4) K Kuo, J Iron Steel Inst., Vol 184, (1956) pp 258 - 268
- (5) R.W.K Honeycombe and A.K Seal, Precipitation processes in steels, Iron and Steel Inst., Spec. Report No. 64, (1959), pp 44 - 56
- (6) F.B Pickering Physical Metallurgy and the Design of Steels, Applied Science Publishers Ltd., London U.K. (1978), pp 127 - 162.
- (7) R.O Ritchie, Met. Trans. A., Vol.8A, (July 1977), pp 1131 - 1140.
- (8) J.R Low, D.F Stein, A.M Turkalo and R.P LaForce,. Met. Trans. A., 242, Jan. (1868) , pp. 14-24.
- (9) R.W.K Honeycombe Steels- Microstructure and properties, Edward Arnold Publishers Ltd, London, U.K (1981).
- (10) G. Krauss, Materials Science and Technology, Published by VCH Publishers Inc., New York, USA (1992). Vol 7, chpater 1, pp. 3-40
- (11) T. Gladman, Materials Science and Technology, Published by VCH Publishers Inc., New York, USA (1992), Vol 7, Chapter 9, pp 403-432.
- (12) H.W Rayson, Materials Science and Technology, Published by VCH Publishers Inc., New York 1992, USA, (1992), Vol 7 chapter 13, pp 586-638
- (13) E.C Bain and H.W Paxton, Functions of the Alloying Elements in Steels. Metals Park, American Society for Metals, Metals Park, Ohio, USA (1966)
- (14) B.Garbarz Microalloyed Vanadium Steels (Edited by M. Korchynsky, S. Gorczyca, M. Blicharski). Krakow: Assoc. Of Polish Engineers and Strategic Minerals Corporation, Poland (1990) p. 193.
- (15) A.R Marder and B.L Bramfitt, Met. Trans. 7A, (1976), pp. 365-372
- (16) R.F Mehl, Hardenability of alloy steels, American Society for Metals, Metals Park, Ohio, USA (1939)
- (17) F.H.Samuel and A.A.Hussein, Trans. Iron Steel Inst. Jpn. 23, (1) (Jan 1983). pp 65-70.

- (18) G.E Pelissier, M.F Hawkes, W.A Johnson and R.F Mehl, Trans. ASM 30, (1942). p. 1049
- (19) I.D McIvor, Symp. Chemical Metallurgy of Iron and Steel. British Steel / Sheffield University, Sheffield, U.K (1974) pp 272-274.
- (20) G.Nadkami, M McCormick, J.D Boyd. Int. Conf Proc. Microstructure and properties of Microalloyed and other Modern High Strength Low Alloy Steels. (Pittsburgh, USA, 1991) Published by Iron and steel Soc. Warrendale (USA). (1988)
- (21) N. Ridley Phase transformations in ferrous Alloys (Edited by A.R Marder, J.I Goldstein) Warrendale, USA TMS-AIME (1984). pp 201-236
- (22) L.J DeMoe and S.V Subramanian, Transformation and Precipitation behaviour of Vanadium bearing Eutectoid Steels. Research Dept. Dofasco inc. Hamilton, Ontario. Published by Mc Master University, Hamilton, Ontario (1987).
- (23) F.B Pickering Materials Science and Technology, Published by VCH Publishers Inc., New York, USA (1992). Vol 7, chapter 2, pp 45-94
- (24) T. Gladman, I.D. Mcivor, F.B Pickering. J. Iron Steel Inst. London Vol. 210, (1972) p.196.
- (25) M. Gensamer, E.B. Pearsall, W.S Pellini, J.R Low (Jr.) Trans AMS 35, (1942), p. 383
- (26) G. Krauss, Principles of Heat treatment of Steels. American Society for Metals, Metals Park, Ohio, USA: (1980)
- (27) J.M Hyak and I.M Bernstein. Met. Trans. 74A, (1976) p. 1217
- (28) F.B Pickering and T.Gladman Iron and Steel Institute Spec. Rep. No 81, (1963) p.10.
- (29) M.F. Ashby, Oxide dispersion strengthening. Warrendale : AIME, 143. (1966).
- (30) T. George and J.J Irani, J. Aust. Inst. Metals 13, (1968) p.94
- (31) F.B Pickering. Vanadium Microalloyed Steels; Proc. Of Int. Symp. Krakow / Krinica, Poland : Edited by M. Korchynsky, S. Gorczyca, M. Blicharski. Association of Metallurgical Engineers and Strategic Minerals Corporation, USA. (1990) pp 79-104.
- (32) J. Brogran and I.D McIvor, Quantitative Relationships Between the Structure and Tensile Properties of High carbon Pearlitic Rod, Conf. Proc. "Steel wire in the 80's. Stratford-upon-Avon. U.K (1980).
- (33) F.P.L. Kavishe and T.J. Baker. Materials Science and Technology, 2 (Aug. 1986), pp 816-822.
- (34) N. Ridley, M.T. Lewis, W.B Morrison, in Advances in the Physical Metallurgy and Applications of Steels. The Metals Society, London (1982) p. 199.

- (35) T.Retí, A. Roosz, G.F. Vander Voort. Comparative Analysis of the Stereological Methods for Determining the Distribution of the True Interlamellar Spacing. Int. Conf. Proc. "Electron Microscopy 1984. Hungary Budapest. Published by Programme committee of the 8th European Congress on Electron Microscopy. (1984).
- (36) B.D. Fowler, A method of Determining the Interlamellar Spacing of pearlite Using Digital Image Analysis. Int. Conf. Proc. "Image Analysis and Metallography. Toronto Canada. Published by ASM International. (July 1988)
- (37) A. Roosz et. Al. Metallography, 13, (1980), p. 299
- (38) A. Roosz and Z. Gacsi, Metallography, 14, (1981), p. 129
- (39) G.F Vander Voort and A. Roosz. Metallography 17 (Feb. 1984), pp 1-17
- (40) T. Retí, Referenced as" To be Published In Bányász Kohász Lapok (1984),. Metallography 17, (Feb. 1984), pp 1-17.
- (41) J.W Christian and D.V Edmonds, Phase transformations in Ferrous Alloys. Edited by A.R Marder and J.I Goldstein. Warrendale, PA TMS-AIME (1984) pp 293-326.
- (42) H.I Aaronson, Mechanism of Phase Transformation in Crystalline Solids. Institute of Metals, London, U.K (1969), p270.
- (43) H,I Aaronson and C. Wells, Trans. AIME,236, (1966) pp 781-796.
- (44) H.K.D.H Bhadeshia, Bainite in steels, Published by The Institute of Materials. London, U.K. (1992)
- (45) W. Steven and A.G Haynes, J. Iron and Steel Inst. 183, (1956), p. 349
- (46) R.F Mehl, Hardenability of alloy Steels. Metals Park, American Society for Metals, Ohio, USA Metal Park, (1939) p.1-54.
- (47) R.F Hehemann, Phase Transformations, Metals Park, American Society for Metals, Metals Park, Ohio, USA (1970) pp 387-432.
- (48) S.J Matas and R.F Hehemann: Trans. AIME, 221, (1961), pp 179-185.
- (49) F.B Pickering, Transformations and Hardenability is Steels, Published by Ann Arbor, MI, Climax Molybdenum, (1967), pp 109-132
- (50) M. Takahashi, H.K.D.H Bhadeshia, Materials Science and Technology, Published by VCH Publishers Inc., New York, USA, (1990) Vol 6, Chapt 7, pp 592-603.
- (51) F. Wever and K. Mathieu, Mitt, Kaiser-Wilhelm-Inst. Eisenforsch 22 (1940),. p. 9.
- (52) T. Lyman and A.R. Toriano, TRANS. ASM, 37 (1946), pp 402-448.
- (53) A. Hultgren, Trans. ASM. 39, (1947), pp 915-1005

- (54) A.E Austen and C.M Schwartz, Proc. ASTM., 55, (1955) pp 523-625.
- (55) O. Kriesement and F. Wever, Mechanism of Phase Trans. In Met., Institute of Metals. Monograph and Rep, London, Ser. No. 18, (1956) p. 253.
- (56) B.P.J Sanvik, Metall. Trans A, 13, (1982), pp 789-800.
- (57) T. Naakamura and S.Nagakura, Int. Conf. On Martensitic Transformations INCOMAT 86, Japan Inst. Met., Japan, (1968), pp 386-391.
- (58) R.M Fisher, Proc. Int. Conf. On Electron Microscopy, Springer Verlag OHG, Berlin, (1958), pp 579-588.
- (59) G. Spanos, H.S. Fang and H.I Aaronson, Int. Conf. Proc. "Bainite II". Chicago, USA, Metall, Trans A. 21A, (1988), pp 1381-1390.
- (60) J.M Oblak and R.F. Hehemann, Transformations and hardenability in Steels. Climax Molybdenum Co., Ann Arbor, M1, (1967), pp 15-38.
- (61) H. Yada and T. Ooka. J. Metall. Soc. Jpn. 31, (1967), pp 771-776.
- (62) Y.Ohmori, H. Ohtani and T. Kunitake: Trans. Iron Steel Inst. Jpn. 11, (1971), pp 250-259.
- (63) T. Ko and S.A Cottrel, J. Iron Steel Inst. 172, (1952), pp 307-313.
- (64) K.J Irvine and F.B Pickering, J. Iron and Steel Inst. 188, (1958), p. 101.
- (65) G. R. Speich, Decomposition of Austenite by Diffusional Processes, Interscience, New York, USA (1962), pp 353-369.
- (66) K. Shimizu and Z. Nishiyama, Mem. Inst. Sci. Ind. Res., Osaka University, 20, (1963), p.42.
- (67) K. Simizu, T. Ko, and Z Nishiyama, Trans. Japan Inst. Met. 5, (1964), pp 223-228.
- (68) F. Wever and H. Lange Mitt, Kaiser-Wilhelm-Inst. Eisenforsch. 14, (1932), p. 71.
- (69) N.P Allen, L.B. Pfeil and W.T. Griffiths, Iron and Steel Inst. Special Rep. 24, London, (1939) pp 369-390,
- (70) D.P. Antia, A. Fletcher and M. Cohen, M. Trans. ASM. 32, (1944), p. 290.
- (71) A.E. Austen and C.M Schwartz, Proc. ASTM, 52, (1952), pp 592-596
- (72) J. Deliry, Mem. Sci. Rev. Metall. 62, (1965), pp 527-550.
- (73) J. Pomey Mem. Sci. Rev. Metall. 63, (1966) pp 507-532.
- (74) V.T.T Miihkinen and D.V Edmonds, Mater. Sci. And Technol. (1987), pp 422-431.
- (75) V. Franetovic, A.K Sachdev, and E.F. Ryntz, Mater. Metallography, 20, (1987), pp 15-37.
- (76) G.V. Kurdjimov and G. Sachs, Z. Phys. 64, (1930), p. 325.

- (77) Z. Nishiyama, *Sci. Rep. Tohoku Univ*, 23, (1934), p.325.
- (78) E.C. Bain, *Trans. AIMME*, 70, (1924), pp 25-46.
- (79) A.Crosky, P.G. McDougall, J.S Bowles, *Acta Metall.* 28, (1980), pp 1495-1504.
- (80) H.K.D.H Bhadeshia and D.V Edmonds, *Acta Metall.* 28, (1980), pp 1265-1273
- (81) M. Sarikaya, H. Tokushige and G Thomas, *Int. Conf. On Martensitic Transformations INCOMAT 86'*, Japan Inst. Of Metals, Tokyo, Japan, (1986), pp 613-618.
- (82) G.R Srinvasen and C.M. Wayman, *Acta Metall* 16, (1968), pp 609-620
- (83) B.P.J. Sandvik and C.M. Wayman, *Metall. Trans. A* 14A, (1983), pp 809- 822.
- (84) K.H. Jack, *Acta Cryst* 3, (1950), p. 392.
- (85) Hofer, E.M Cohn, W.C. Pebbles. *J. Amer. Chem. Soc.* 71 (1949) p. 189.
- (86) G.Z. Hägg, *Kristallogr.* 89, (1934), p. 92.
- (87) K.C.S. Hirotsu and S.Nagakura, *Acta Metall.* 20, (1972), pp 645-655.
- (88) J.Morniroli, E. Grosse, M. Gantois, *Phil. Mag. A* 48, (1983), p. 311.
- (89) G. Knoval, L. Zwell, L.A Gorman, W.C. Leslie, *Nature* 184, (1959), pp 1862-1863.
- (90) J.M. Schissler, J. Arnould, G. Metauer, *Mem. Sci. Rev. Metallurgie* 6, (1975), pp 779-793.
- (91) Y.A. Bagaryatski, *Dokl. Akad. Nauk. SSSR* 73, (1950), p. 1161.
- (92) D.N. Shackleton and P.M. Kelly, *Iron Steel Inst. Special Rep.* 93, London, (1965) pp 126-134.
- (93) I.VIsaichev, *Zhur Teekhn. Fiziki.*17, (1947), p. 835.
- (94) T. Ohmori, *Trans. Iron Steel Inst. Jpn.* 11, (1971), pp 95-101
- (95) D.H.Huang and G. Thomas, *Metall. Trans.* 8A, (1977). p. 1661.
- (96) R.W.K. Honeycombe and F.B Pickering, *Met. Trans.* 3A, (1972) p. 1099
- (97) K.J.Irvine and F.B. Pickering, *Iron Steel Inst. Spec. Rep.* 93, London, (1965), pp 110-125.
- (98) A. Kamada, N. Koshizuka, T. Funakoshi, *Trans. Iron Steel Inst.* 16, (1976), p. 407.
- (99) M.E. Bush and P.M. Kelly, *Acta Met* 19, (1971), p. 1363.
- (100) T. Gladman, B. Holmes, I.D Mclvor, *The effect of Second Phase Particles on the Mechanical Properties of Steel.* London: The Iron and Steel Institute, (1971) p. 68.
- (101) P.O. Kettunen and U.F. Kocks, *Acta Metall.*, 20, (1972), pp 95-103.
- (102) P.O. Kettunen and T. Lepistö, *Trans. Japan Inst Mat.* 17, (1976), p. 63.

- (103) R.F. Hehemann, V.J. Luhan, A.R. Troiano. *Trans. ASM.* 40, (1957), pp 409-426.
- (104) Y. Tomota, K. Kuroki, T. Mori and I Tamura, *Mater. Sci. Eng.* 24, (1976), p. 85.
- (105) F.B Pickering. *Int. Conf. On Electron Microscopy*, Springer Verlag OHG, Berlin (1958), pp 628 - 637.
- (106) D.B McCutcheon, T.W Trumper, J.D. Embury. *Revue de Metallurgie*, (Feb. 1976), pp 143-174.
- (107) G. Deep and W.M. Williams. *Canadian Metall. Quart* 14, (1965), pp 85-96.
- (108) K.J Irvine and F.B. Pickering, *J. Iron Steel Inst.* 201, (1963), pp 518-531
- (109) F.B Pickering, *Physical Metallurgy and the Design of Steels*, Applied Science Publishers, Essex. UK, (1978), p.104.
- (110) W.B. Morrison in *Controlled Processing of HSLA steels. Proc. Of British Steel Corporation Conference*, York. Sheffield: British Steel Corporation, paper 1. (1976)
- (111) M. Umemoto, T.Furuhara and I. Tamura, *Acta Metall.* 34, (1986), pp. 2235-2245.
- (112) M. Atkins, *Atlas of Continuous Cooling Transformation Diagrams for Engineering Steels*. Published by British Steel Corporation, Sheffield UK. (1977)
- (113) M.S Wechsler, D.S Lieberman and T.A Read, *Trans. TMS AIME* 197, (1953) p. 1503.
- (114) J.S Bowles and J.K Mackenzie, *Acta Metall* (1954), Vol. 2, p. 129..
- (115) B.A Bilby and J.W. Christian, *J. Iron and Steel Institute* 197, (1961) p. 122.
- (116) C.M. Wayman, *Introduction to the Crystallography of Martensite Transformations*. MacMillan, New York, USA. (1964)
- (117) J. W. Christian, *Martensite Fundamentals and Technology*. Edited by E.R Petty, Longman, London, U.K (1970), pp 11-42.
- (118) A.B. Greniger and A.R. Troiano, *Trans. TMS-AIME* 185, (1949) p. 590.
- (119) Naylor and Cook, *Materials Science and Technology*, Published by VCH Publishers Inc., New York (1992). Vol 7. (10) pp 433-488,
- (120) R.A. Grange and H.M. Stewart, *Trans. AIME*, 167, (1946) p. 467.
- (121) P. Payson and C.H. Savage, *Trans. ASM* 33, (1944) p. 261.
- (122) E Hornbogen, *Acta Metall.* 33, (Apr. 1985), pp 595-601.
- (123) K.W. Andrews, *J. Iron and Steel Inst.* 203, (1965) p.721.
- (124) T.G. Diggs, *Trans ASM* 28, (1940) p. 606
- (125) E.R. Petty, *Martensite Fundamentals and Technology*. Edited by E.R. petty. Longmans. London U.K. (1970).

- (126) W.W.Gerberich, P.L. Hemmings and V.F. Zackay, Conf. Fracture 69. London: Chapman and Hall, (1969) p. 288.
- (127) J.L. Burns, T.L. Moore and R.S Archer, Trans ASM 26, (1938) p.1
- (128) J.M Hodge and M.A. Orehoski. Trans AIME, 167, (1946), pp. 502-512.
- (129) A.E. Nehrenberg, P. Payson and P. Lilys. Trans. ASM, 47,(1955), pp. 785-793.
- (130) L.C. Boyd and J. Field, Calculation of the standard end quench hardenability curve from the chemical composition and grain size. AISI Contribution to the metallurgy of steel., (1945), No. 12.
- (131) M.A. Grossman, M. Asimow and S.F. Urban. Hardenability and its relation to quenching, some quantitative data, In Hardenability of alloy steels (1939), Cleveland (ASM). P. 124
- (132) C.A Siebert, V.D. Doane and D.H. Breen. The Hardenability of Steels- Concepts, Metallurgical Influences and Industrial Applications. Published by The American Society for Metals, Metals Park, Ohio, USA: (1977).
- (133) I.R. Kramer, S. Siegel and J.G. Brooks. Trans. AIME, 167, (1946), p. 670.
- (134) W. Crafts and J.L. Lamont. Trans. AIME., 158, (1944) pp. 157-167.
- (135) R.A. Grange and T.M. Garvey. Trans. ASM, 37 (1946), p. 136.
- (136) B.M. Kapadia, R.M. Brown and W.J. Murphy. Trans. SM, 242, (1946) p. 1689.
- (137) D.T. Lewellyn and W.T. Cook. Metals Tech., (Dec 1974), p. 517
- (138) G.F. Melloy, P.R. Slimmon and P.P. Podgursky, Met.Trans., 4, (1973), p.2279.
- (139) D.H. Breen and G.H. Walter, Metals Progress, 102, (Dec 1972), p. 42.
- (140) W.C. Leslie, Strengthening mechanisms. Syracuse University Press 43, Sytacuse. (1966)
- (141) R.A Grange, trans ASM, 59, (1966) p.26
- (142) L.F. Porter and D.S. Dabrowski, Ultra Fine Grain Metals: Edited by J.J Burke, V. Weiss, Syracuse University Press, (1970). p. 133
- (143) T. Swarr and G. Krauss, Met. Trans. 7A,, (1976). p.41
- (144) A. Brownrigg, Scripta Metall. 7, (1973), pp 1139-1142.
- (145) T. Kunitake and S. Sugisawa, The Sumitomo Search 5, May, 16. (1971).
- (146) M. Kusunoki and S. Nagakura, J. Appl. Cryst. 14,. (1981). p.329.
- (147) D.W. Hoffman, Acta Metall. 13, (1970). p. 819
- (148) J.M.R. Glenin and P.A. Flinn, Trans. AIME 242,(1968) p. 1419.
- (149) Y. Hirotsu and S. Nakazawa, Acta Metall. 20, (1972) p. 645.
- (150) D.L. Willianson, K. Nakazawa, G. Krauss, Metall. Trans. 10A, (1979), p. 1351
- (151) J.H. Holloman, Trans. ASM 36, (1946). p. 473

- (152) B.C. Woodfine, J. Iron Steel Inst. London 173, (1953). p. 229
- (153) J.R. Low (Jr.) Fracture of Engineering Materials; ASM 147 (1964).
- (154) C.J. McMahon (Jr.) Temper Embrittlement in Steel; ASM STP. 407. (1967)
- (155) Y. Ohmori, H. Ohtani and T Kunitake, Met. Sci 8, (1974) p. 357.
- (156) G.E Dieter, Mechanical metallurgy, Mc Graw-Hill Book Co.,Tokyo, Japan, (1988) pp 184-240.
- (157) G.E Dieter, Mechanical metallurgy, Mc Graw-Hill Book Co.,Tokyo, Japan, (1988) pp 103 - 183.
- (158) A.H Cottrell, An introduction to Metallurgy, Edward Arnold Publishers Ltd. London (1967) pp 261-295.
- (159) E. Orowan, Z. Phys., Vol. 89, (1934) pp 605, 614, 634.
- (160) M. Polanyi, Z. Phys. Vol. 89,(1934) p. 660.
- (161) G.I. Taylor, Proc. R. Soc. London, Vol. 145A, (1934) p. 362.
- (162) D. Hull and D.J. Bacon, Introduction to Dislocations, Pergamon press (3rd.Ed), Oxford, U.K. (1984) pp 1 - 24.
- (163) G.W Groves and A. Kelly, Change of Shape due to dislocation climb, Phil. Mag. 19, (1969). P. 977.
- (164) D. Hull and D.J. Bacon, Introduction to Dislocations, Pergamon press (3rd.Ed), Oxford, U.K, (1984), pp 47 - 70.
- (165) R.E Reed-Hill, Physical metallurgy Principles, Edited by W.W.Hagerty, Published by D.Van Nostrand Company Inc. (1964) pp. 95 - 154.
- (166) M. Abe, Materials Science and Technology, Published by VCH Publishers Inc., New York (1992). Vol 7. (7) pp 285 - 334.
- (167) D. Hull and D.J. Bacon, Introduction to Dislocations, Pergamon press (3rd.Ed), Oxford, U.K, (1984), pp 91 - 111.
- (168) A. Seeger, Dislocations and Mechanical Properties of Crystals, Published by Wiley and Sons (1957). p. 243.
- (169) D. Hull and D.J. Bacon, Introduction to Dislocations, Pergamon press (3rd.Ed), Oxford, U.K (1984) pp 112 - 140.
- (170) R.W Hertzberg, Deformation and Fracture Mechanics of Engineering materials, 2nd Edition, John Wiley and Sons (1983), Chapter 4.
- (171) R.E Reed-Hill, Physical metallurgy Principles, Edited by W.W.Hagerty, Published by D.Van Nostrand Company Inc. (1964) pp. 399 -438.
- (172) R.L Bell and R.W Cahn, Proc. Roy. Soc. (London), 239, (1957), p. 494.

- (173) R.L Fleischer, Solid Solution Hardening in D. Peckner (ed.), "The strength of Metals," Reinhold Publishing Corporation, New York, (1964).
- (174) R.E Reed-Hill, Physical metallurgy Principles, Edited by W.W.Hagerty, Published by D.Van Nostrand Company Inc.(1964) pp. 220-235.
- (175) A.H. Cottrell, S.C Hunter and F.R.N Nabarro, Phil. Mag., Vol. 44, (1953) p 1064.
- (176) N.F Mott and F.R.N Nabarro, "Report on Conference on the Strength of Solids", Phys. Soc., London (1948). p.1
- (177) R. Labusch, Phy. Stat. Sol., vol. 41, (1970) p. 659..
- (178) J.W. Martin, Precipitation Hardening. Pergamon press, New York, USA (1968).
- (179) P.B. Hirsch and A. Kelly, Phil. Mag., vol. 12, (1965) p. 881.
- (180) A. Kelly and R.B. Nicholson, Prog. Mater. Sci., vol 10, no. 3, (1963) p. 151.
- (181) H. Gleiter and E. Hornbogen, Mater. Sci. Eng., vol. 2 (1967) pp. 285-302..
- (182) C.W. Corti, P. Cotterill and G. Fitzpatrick, Int. Met. Rev., vol. 19, (June 1974) pp. 77-88.
- (183) E. Orowan, discussion in "Symposium on internal Stresses"., Institute of Metals, London, (1947). p.451
- (184) D. Hull and D.J. Bacon, Introduction to Dislocations, Pergamon press (3rd.Ed), Oxford. U.K (1984) pp 210 - 250.
- (185) E.O Hall, Proc. Phys. Soc. London, vol. 643, (1951) p. 747..
- (186) N.J. Petch, J. Iron Steel Inst. London, vol. 173, (1953) p. 25.
- (187) J.C.M. Li, Trans. Metall. Soc. AIME, vol. 227, (1963) pp. 239-247.
- (188) D. Hull and D.J. Bacon, Introduction to Dislocations, Pergamon press (3rd.Ed), Oxford, U.K, (1984) pp 141 -160
- (189) A.H. Cottrell, trans. Metall. Soc. AIME, vol 212, (1958) p. 192.
- (190) F.C Frank and W.T Read, Phys. Rev., vol. 79, (1950) pp 722-723.
- (191) D. Hull and D.J. Bacon, Introduction to Dislocations, Pergamon press (3rd.Ed), Oxford, U.K (1984) pp 161- 174
- (192) J.J. Gilman and W.G. Johnston, Solid State Physics, 13, (1962) p. 147.
- (193) H. Hu, The Nature and behaviour of Grain Boundaries, Plenum Press, New York, USA. (1972)
- (194) M.F. Ashby, Phil. Mag., ser. 8, vol 21 (1970), pp 399-424.
- (195) D. McLean, Mechanical Properties of Metals. Published by Wiley and Sons Inc., New York, (1962) pp. 153-161.

- (196) M.A. Meyers and K.K. Chawla, Mechanical Metallurgy, Prentice Hall, Inc., Englewood Cliffs, N.J., (1984). Chapter 9.
- (197) G.E Dieter, Mechanical metallurgy, Mc Graw-Hill Book Co. Tokyo, Japan, (1988), pp 275-324.
- (198) J.L. Duncan, Sheer Met. Ind., (July 1967), pp. 483-489.
- (199) J. Datsko, Material Properties and manufacturing Processes, pp. 18-20. Published by Wiley and Sons Inc. New York, (1966).
- (200) D.C. Ludwigson, Metall. Trans., vol.2, (1971) pp. 2825-2828.
- (201) H.E Peterson, Metal Prog. Vol 90, no. 1, (July 1966), pp 79-81.
- (202) G.E Dieter, Strain rate effects in deformation Processing, W.A. Backofen (Ed.) Fundamentals Deformation Processing, Syracuse University Press, (1964). Chap. 7
- (203) N. Hansen and D. Kuhlmann-Wilsdorf. Mater. Sci. Eng., 81, (1968) pp. 141-161.
- (204) J.L. Martin and A.S. Argon. Mater. Sci. Eng., A113, (1986) pp. 337-348.
- (205) C.Y. Barlow, B. Bay and N. Hansen. Philos. Mag., 51, (1985) pp. 253-275.
- (206) L. Yan and L.Y. Men, The work hardening of high tempered 0.14%C 1.96%Cr-3.6%Ni steel during the tensile test. Int. Conf. "Mechanical behaviour of Materials - VI vol. 3. Kyoto, Japan. 29 July - 2 Aug 1991.
- (207) J.G. Sevillano, P.V. Houtte and E. Aernoudt,. Mater. Sci. Eng., 25. (1980) pp. 69-80.
- (208) G.I. Taylor, The mechanism of plastic deformation of crystals. Pro. R. Soc. London, Ser. A, 145,(1934) pp 362-415.
- (209) D.L. Holt. J. Appl. Phys., 41, (1970) pp. 3197-3201.
- (210) M.B. Bever, D.L. Holt and A.L. Titchener, Prog. Mater. Sci. Vol 17, Pergamon Press Ltd. London (1973).
- (211) S. Ryalls, Private Communication, Swindon Laboratories Ltd. (1995).
- (212) K.W. Andrews, D.J. Dyson and S.R. Keown. Interpretation of diffraction patterns (2nd Ed) Published by Adam Hilger Ltd. London. (1968)
- (213) P.M. Kelly and J. Nutting. Journal of the Iron and Steel Institute, (March 1961), pp 199-210.
- (214) H. Ohtani Materials Science and Technology, Published by VCH Publishers Inc., New York 1992. Vol 7. (4) pp 147 - 182.
- (215) Y. Ohmori and R.W.K Honeycombe Suppl. Trans. Iron and Steel Inst. Jpn. (1971) pp 1160-1164.
- (216) W. Pitsch Acta Metall. 10 (1962) p. 897.